UNIVERSITY COLLEGE LONDON

DEPARTMENT OF ELECTRONIC & ELECTRICAL ENGINEERING

NanoSQUIDs for Millikelvin Magnetometry

Author:
Arnaud Bertrand Bernard BLOIS

Supervisor:
Dr. Edward J. ROMANS

April 15, 2014

Thesis submitted in partial fulfillment of the requirements for the Degree of Doctor of Philosophy of University College London

I, Arnaud Bertrand Bernard Blois, confirm that the work presented in this thesis is my own. Where information has been derived from other sources, I confirm that this has been indicated in the thesis

Abstract

Nanoscale Superconducting QUantum Interference Devices (SQUIDs) have spin sensitivities approaching that required to detect the flip of a single spin in close proximity. There is considerable interest in developing them for measuring the properties of small spin populations in magnetic systems. It is desirable that such measurements can be realised at sub-kelvin temperatures thereby allowing the study of magnetic systems that undergo phase changes at such temperatures. However, most nanoscale SQUIDs use nanobridges as the Josephson elements which limits the operating range to temperatures close to the transition temperature of the device. Well below this, the current-phase relation can become non-sinusoidal, and hot spots arising from the large critical current lead to hysteretic I-V characteristics. To extend the temperature range downwards, we have developed a range of nanoSQUIDs fabricated from alternative materials with lower transition temperatures including Ti/Au and Al/Ag bilayers patterned using lift-off and e-beam lithography (EBL). We report on their I-V characteristics, noise performance and behaviour in applied magnetic fields at temperatures down to 60 mK. We discuss theoretical analysis and computer modelling of the heat flow in the nanobridge structure, and consider the effects of bank geometry and kinetic inductance on the overall device performance. Finally, we present measurements of several magnetic systems: control lines, superconducting islands and ground planes and discuss the feasibility of magnetic measurements of novel materials of interest, including the heterointerface between lanthanium aluminate and strontium titanate.

Acknowledgements

I would like to express my gratitude to my supervisor Dr Edward J. Romans for giving me the opportunity to work on this project and for his kind guidance throughout the course of this thesis. Although he once said that our relation "will be exactly like the relation between the Emperor and Darth Vader", he has been more than just a mentor, he has also been a friend. I am very thankful to Dr Sergiy Rozhko for his invaluable help with the low-temperature measurements with the ADR and the interesting discussions I had with him about many subjects, mostly scientific but sometimes drifting to hypo-allergenic cats or coffee. I am also indebted to Dr Ling Hao and Dr John Gallop for their precious advices and feedbacks regarding my measurements. I also thank Dr Paul Warburton for introducing me to the fantastic world of SQUIDs during my MSc project and Dr Jon Fenton for the enlightening conversations we shared. I acknowledge my gratitude to Dr Peter Petrov and his team: Clementine Walker, Dr Kevin Zou, Dr Sean McMitchell for providing LAO/STO samples, and to all the cleanroom staff: Steve Etienne, Mike Creswell, David Malone and Suguo Huo for their constant efforts into maintaining the equipment and their expertises in the different processes. I would like to thank Thuong Thuong Nguyen aka Tchoutchou, Nick Constantino, Ivan Isakov, Huan Wang, Nuno Braz, Marina Panfilova and Dr Ed Osley who have been very nice colleagues to work with and, as importantly, good friends that helped me cope with the stress of the thesis with their contagious good mood. Special thanks to Mostapha Osman for the overly generous supply of coffee capsules he gave me when he learnt I was writing up (better wired than tired!). On a more personal level, I would like to thank all my family and dedicate them this thesis for their continuous encouragements, love and attention, with extra thanks to my parents Éric and Frédérique for the support at the end of the project. Finally, I would like to thank Marion Sourribes, an exceptional scientist and also my beautiful girlfriend, for everything she did to help me during this project.

Contents

List of Figures

Chapter 1

Introduction & Theoretical Background

1.1 Introduction

Superconducting QUantum Interference Devices (SQUIDs) are small superconducting loops intersected by one or two regions of weakened superconductivity called the Josephson elements, or weak links. They are used mainly for their unrivalled magnetic flux sensitivity and recently the main trend has been to develop ever smaller nanoscale SQUIDs (nanoSQUIDs) to reach a spin sensitivity[1] – which scales with the loop size [1] – sufficient to detect the flip of one or more spins in close proximity. Potential applications include fundamental science (e.g. for investigating small spin populations in magnetic nanoparticles [2] or molecules [3]), and quantum device applications (e.g. as readouts for flux qubits in quantum computing or for spintronic devices [4]). The Josephson elements for SQUIDs were originally Superconductor - Insulator - Superconductor (S-I-S) junctions which tended to be relatively large (several microns). Diverse alternative techniques to create smaller Josephson elements for nanoSQUIDs have been reported: using DNA-templated nanowires [5], films deposited on fine tips [6] and carbon nan-

---

[1] In this thesis, "spin sensitivity" refers to the electronic spin. The nuclear spin is typically two thousand times smaller and measuring it is not a realistic aim for nanoSQUIDs at present.

otubes [7], etc. However, the main part of research towards nanoSQUIDs relies on the use of "nanobridges" – constrictions in the superconducting thin films patterned using Electron Beam Lithography (EBL) [8, 9] or Focussed Ion Beam (FIB) lithography [10, 11], which behave as Josephson elements due to their reduced dimensions comparable to the Ginzburg-Landau coherence length ξ_{GL}. The theory for this will be given in Section 1.2, including the properties of superconductors, and description of Josephson junctions and SQUID operation with a focus on the different parameters that characterise them.

In Chapter 2 we will review different reported state-of-the-art nanoSQUIDs developed for high spin sensitivity, as low as a few spins/$\sqrt{\mathrm{Hz}}$. However, operating such devices somewhat below their T_{c} (9.2 K for niobium, 1.2 K for aluminium) generally leads to hysteretic I-V characteristics and renders their operation extremely difficult. A remaining goal for nanobridge-based SQUIDs is therefore to extend their operation range to millikelvin temperatures, both to take advantage of the lower noise floor this would provide, but also to be able to use the SQUIDs to characterise phase transitions and other quantum phenomena at ultra-low temperatures in coupled magnetic or superconducting systems, such as topological insulators or some perovskite heterointerfaces. The aim of the present thesis is therefore the fabrication and study of nanoSQUIDs that can be operated in a conventional way down to millikelvin temperatures and which are optimised towards high spin sensitivity, so that they could be in the future integrated on magnetic samples of interest.

After a description of the apparatus and method we used to fabricate and measure our nanoSQUIDs in Chapter 3, including initial design considerations, we will focus in Chapter 4 on the reasons for the hysteresis in other groups' devices at millikelvin temperatures. Skocpol *et al.* published a model in the 1970s attributing this to the creation of a self-sustaining normal hot spot in each bridge when current-biasing the SQUID [12]. This model was later refined by Hazra *et al.* to account for the reduced thermal conductivity in superconductors [13]. However both these models assumed a radial temperature distribution in the banks which as we will show is not accurate in the millikelvin regime. In Chapter 4, we describe two new thermal models we developed, referred to as Models M-1 and M-2 in the following, and which are based on more realistic assumptions.

Other groups have already used a noble metal shunt in conjunction with the superconducting material to improve the heat conduction and partially solve the hot spot issue for a limited range of temperature. However, in the present work we used the combination normal metal/superconductor bilayers not only to increase the thermal conductivity but also as a way to suppress T_c thanks to the proximity effect. This novel aspect allowed us to achieve non-hysteretic operation of our nanoSQUIDs down to millikelvin temperature. We describe how we adapted our thermal models M-1 and M-2 to bilayers, which enabled us to predict the hysteresis for any arbitrary bilayers and bridge dimensions and allowed us to model and fabricate non-hysteretic devices down to 60 mK. However, as we will discuss, this alone was not enough to guarantee the excellent performance we expected due to two further issues: a large inductance and excess heat. In Chapter 5, we discuss how we were able to solve both these issues by adapting to our nanoSQUIDs a shadow evaporation technique introduced by Vijay *et al.* [14]. The resulting devices, having a “3D” profile with banks much thicker than the nanobridges, were not affected by either issues and performed properly. Their magnetic responses were measured and we discuss their noises and spin sensitivities.

We then consider in Chapter 6 the feasibility of using our SQUIDs for measurements down to millikelvin temperatures of actual systems with weak magnetic signatures. To examine this, we started with the measurement of fabricated test systems with a deliberately larger signal, including a control line and a superconducting plane, and finally superconducting islands. Using the characteristics we determined from these experiments, we move on to discuss the integration of nanoSQUIDs onto ultrathin samples of interest: e.g. topological insulators, heterointerfaces between perovskites, especially the example of $\mathrm{LaAlO_3/SrTiO_3}$

among other similar systems.

We draw our final conclusions in Chapter 7 and consider several possible avenues for future work, including using techniques such as neon-helium FIB to fabricate non-hysteretic nanoSQUIDs of alternative materials with very reduced dimensions ($< 50\,\mathrm{nm}$ radius) which we predict would have a spin sensitivity several orders of magnitude better than $1\,\mathrm{spin}/\sqrt{\mathrm{Hz}}$.

1.2 Theoretical Background

1.2.1 Superconductivity

Superconductivity, discovered one century ago, is the disappearance of any electrical resistivity below a critical temperature T_c. Its development led to the discovery of several effects that proved crucial for science but also that have successfully found commercial applications.

Discovery

In 1908, there were several schools of thought regarding the evolution of the electrical resistivity of a pure metal as a function of temperature. Lord Kelvin's theory was that the resistivity would start increasing as the temperature tends to the absolute zero because the "electrions", or conduction electrons, would condense on the atoms making the metal perfectly insulating [15]. Dewar predicted the opposite behaviour: the resistivity should converge towards zero as there are less and less scattering from phonons [16]. In between lay Matthiessen's prediction, derived from his study of the resistivity of alloys as a function of temperature [17], which is known nowadays as Matthiessen's rule, $\rho = \rho_\mathrm{impurities} + \rho_\mathrm{phonons}(T)$. At low temperature, the component of resistivity due to the existence of phonons ρ_phonons tends to zero but there is still the constant residual value $\rho_\mathrm{impurities}$. These three theories are summarised in Figure 1.1.

In order to study these theories, Heike Kamerlingh Onnes, a renowned Dutch physicist in Leiden specialised in cryogenics, achieved for the first time the liquefaction of helium in 1908. Onnes was a follower of Dewar's theory and decided to

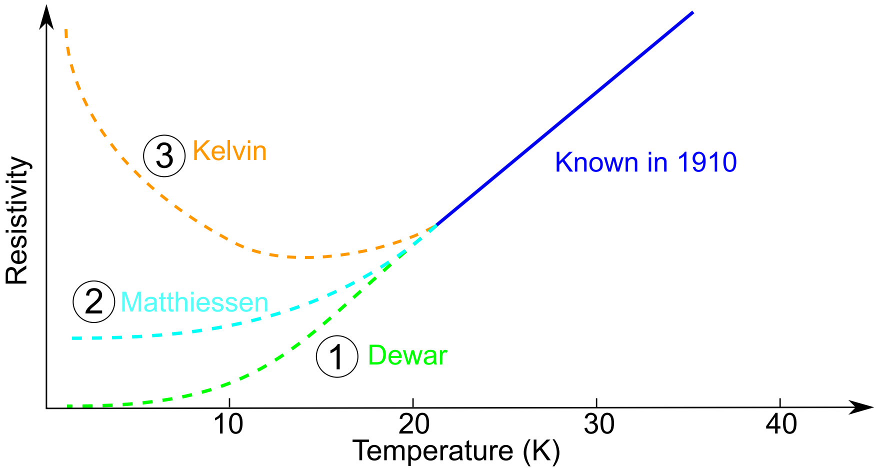

Figure 1.1: The three historical theories predicting the evolution of the resistivity of a metal as a function of decreasing temperature. Adapted from Ireson [15].

measure the resistivity down to liquid helium temperatures of mercury that was easy to purify thanks to its liquid phase at room temperature and pressure. On the 8th of April 1911, he saw a sudden drop of the resistance at 4.2 K and the same year also observed superconductivity in tin and lead [18]. He received the Nobel Prize in Physics for this discovery in 1913.

The Meisser-Ochsenfeld Effect and the London' Equations

For twenty-two years after Onnes' observation, scientists thought that superconductors were not different from perfectly conducting metals. For such materials[2], infinitely flowing screening currents prevent any magnetic field from entering its bulk, this property being referred to as perfect diamagnetism. For a density of superconducting electrons n_s, the circulating current flows only on the surface of the superconductor to a depth $\lambda = \sqrt{m/\mu_0 n_\mathrm{s} e^2}$, where m and e are respectively the mass and charge of an electron and μ_0 the magnetic constant. λ is called the penetration depth and represents the thickness over which the magnetic field can penetrate the superconductor. This result can be found by applying the Drude model [19] for an electron of mass m, charge e and speed $\mathbf{v_s}$ in an electric field $\mathbf{E}$. Its motion follows the equation $m\,\mathrm{d}\mathbf{v}_\mathrm{s}/\mathrm{d}t = e\mathbf{E} - m\,\mathbf{v}_\mathrm{s}/\tau$ where τ is the time

---

[2] Assuming that they can be considered as bulk materials, i.e. their dimensions are long in direction of the film.

constant between two elastic collisions of the electron with the fixed ions. For a superconductor, we can neglect this effect and consider $\tau = +\infty$. Taking the derivative of the current density $\mathbf{J}_\mathrm{s} = n_\mathrm{s} e \mathbf{v}_\mathrm{s}$ with respect to time yields the first of the London equations:

$$\frac{\partial \mathbf{J}_\mathrm{s}}{\partial t} = \frac{n_\mathrm{s} e^2}{m} \mathbf{E}. \tag{1.1}$$

By inserting this value into the Maxwell equation $\dot{\mathbf{B}} = -\nabla \times E$, we find

$$\dot{\mathbf{B}}_\mathrm{s} = -\frac{m}{n_\mathrm{s} e^2} \nabla \times \dot{\mathbf{J}}_\mathrm{s}. \tag{1.2}$$

Assuming the displacement current $\dot{\mathbf{D}}$ is negligible compared to $\mathbf{J}_\mathrm{s}$ and that superconductors have a relative magnetic permeability $\mu_\mathrm{r} = 1$, we can rewrite the Maxwell equation $\nabla \times \mathbf{H} = \mathbf{J} + \dot{\mathbf{D}}$ in the form $\nabla \times \mathbf{B} = \mu_0 \mathbf{J}$. By using its time derivative $\nabla \times \dot{\mathbf{B}} = \mu_0 \dot{\mathbf{J}}$, Equation 1.2 becomes

$$-\frac{1}{\lambda^2} \dot{\mathbf{B}} = \nabla \times \nabla \times \dot{\mathbf{B}}. \tag{1.3}$$

By definition of the Laplacian, we have $\nabla^2 \dot{\mathbf{B}} = \nabla(\nabla . \dot{\mathbf{B}}) - \nabla \times \nabla \times \dot{\mathbf{B}}$. As $\nabla . \mathbf{B} = 0$, we get

$$\nabla^2 \dot{\mathbf{B}} = \frac{1}{\lambda^2} \dot{\mathbf{B}} \tag{1.4}$$

where n_s is the density of “superconducting electrons”, which are in fact two bound electrons called a Cooper pair. Solving Equation 1.4 at the boundaries of the superconductor gives $\dot{\mathbf{B}} = \dot{\mathbf{B}}_\mathbf{s} \exp^{-x/\lambda}$ where $\mathbf{B_s}$ is the applied magnetic field at the surface. This classical result shows that a time-dependent field is decaying exponentially over the penetration depth. By performing magnetic field measurements on tin and lead samples, the German scientists Ochsenfeld and Meissner discovered that the magnetic field is not only screened but also expelled from the inside during the superconducting transition [20]. This led Fritz and Heinz London in 1935 [21] to propose that Equation 1.4 was valid for time-independent fields as well:

$$\nabla^2 \mathbf{B} = \frac{1}{\lambda^2}\mathbf{B}. \tag{1.5}$$

By retracing back through all the previous equations with this hypothesis, they obtained the second London equation:

$$\nabla \times \mathbf{j_s} = -\frac{n_s e^2}{m}\mathbf{B}. \tag{1.6}$$

While the classical model allowed the existence of fields frozen in the superconductor during the transition, this model predicts that even time-independent fields are expelled from the bulk, successfully explaining the Meissner effect. Experimentally [22], the penetration depth is often found to follow the two-fluid temperature dependence that was modelled by Gorter and Casimir in 1934 [23]: $\lambda(T) \approx \lambda_0/\sqrt{1-(T/T_c)^4}$. However, while these equations successfully take into account part of the behaviour of superconductors, they stem from an entirely phenomenological approach and do not provide any explanation of the phenomenon. Also, whilst in theory the penetration depth of most materials should be in the range of 20–50 nm, some experiments [24] have shown that it can be much longer, up to one order of magnitude. This result was only explained by the introduction of the coherence length in the Ginzburg-Landau theory.

The BCS Theory

The Bardeen Cooper Schrieffer (BCS) theory, published in 1957, was the first microscopic theory of superconductivity, successfully explaining many experimental results at the atomic scale. A complete description of this theory is beyond the scope of this thesis and is explained in the original paper [25]. Its starting point is the fact that in the presence of an attractive potential between electron pairs below a certain temperature T_c, a phase change occurs where the formation of electron pairs is energetically more favourable than the existence of single electrons. This attraction had been postulated by Fröhlich [26] and originates from the interaction of two electrons with the crystal lattice vibrations, or phonons, that leads to a weak attraction arising between them. Electrons of opposite spins then form pairs of correlated electrons, called Cooper pairs which are bosons and are not limited by Pauli's exclusion principle. They all condense to the same quantum ground state which gives them superfluidic properties. In order to break a pair, an energy 2Δ, where Δ is the energy gap, has to be applied. We can therefore draw an energy level diagram for a superconductor, shown in Figure 1.2. The absence of scattering means there is no electric resistance in that state. Δ is maximum at $T = 0$ and stays almost constant as the temperature rises until the thermal excitation has decorrelated a large enough number of Cooper pairs. Then, it rapidly drops to zero as the temperature approaches the transition temperature T_c at which point the sample is no longer superconducting. Close to T_c in most classic superconductors[3] such as aluminium [29] or niobium, the energy gap can be approximated by:

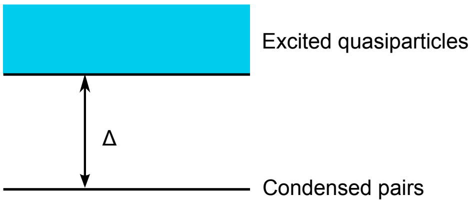

Figure 1.2: Energy band diagram for a superconductor. Adapted from Rose-Innes *et al.* [27].

$$\frac{\Delta(T)}{\Delta(0)} \approx 1.74\sqrt{1-\frac{T}{T_\mathrm{c}}}. \tag{1.7}$$

The energy gap at $T = 0$ can itself be approximated in the BCS theory by:

$$\frac{\Delta(0)}{k_\mathrm{B}T_\mathrm{c}} = 1.764. \tag{1.8}$$

This coefficient has been shown to be in good agreement with the experimental results obtained for several low-T_c superconductors [30, 31]. These equations are

---

[3] For which the weak-coupled approximation $N(0)V \ll 1$ is true where V is the interaction potential and $N(0)$ the density of states at the Fermi level for the electrons sharing the same spin [28].

not valid for strong-coupling superconductors such as lead or mercury, nor for high-T_c superconductors as they do not follow the BCS theory [32]. The BCS theory introduces the coherence length ξ_0 which can be seen as the length over which the electrons in a Cooper pair would be correlated at $T = 0\,\mathrm{K}$. In a clean superconductor, i.e. for which the mean free path tends towards infinity, it is defined by $\xi_0 = \hbar v_\mathrm{F}/\pi\Delta(0)$ where v_F is the Fermi velocity. As v_F is very similar for typical weakly-coupled superconductors ($v_\mathrm{F} \approx 10^6\,\mathrm{m/s}$), ξ_0 can be considered a function of T_c such that the product $\xi_0 T_c = 1.5\,\mu\mathrm{m\ K}$ is a good approximation in most cases [33].

In 1986, at a time where most scientists had started to think that everything was known about superconductivity, Karl Müller and Johannes Bednorz discovered a type of material ($\mathrm{Ba}_x\mathrm{La}_{5-x}\mathrm{Cu}_5\mathrm{O}_{5(3-y)}$) whose critical temperature was higher than the maximum value predicted by the BCS theory [34]. Since then, many similar materials have been discovered. While the object of intensive research for two decades, this phenomenon is still not completely understood and part of the scientific interest is now moving back to devices made of low-T_c superconductors for the much lower level of thermal noise they offer. High-T_c superconductors have typically multi-layered crystalline structures close to perovskites. Their fabrication requires a lattice matched substrate heated at about 800°C which eliminates many substrate choices. For this reason, we will only consider low-T_c superconductors in this thesis.

The Ginzburg-Landau Theory

The BCS theory provides a complete microscopic explanation for low-temperature superconductivity but is too complex to model macroscopic effects practically. The theory developed by Ginzburg and Landau (GL theory) provides an easier and more convenient way to describe the phenomena. Though GL theory is purely phenomenological, Gor'kov [35] proved that it is in fact a limiting case of the BCS theory for temperatures close to T_c and small changes of the order parameter $\psi(x)$ (explained below) and magnetic vector potential $\mathbf{A}$, which explained its success.

GL theory stems from the observation in 1932 by Keesom of the unusual phase transition of helium I to helium II at 2.19 K without any latent heat [36]. Ehrenfest classified this as a second-order phase transition because the first derivatives of the Gibbs free energy G of the system were continuous. This is not the case for first-order transitions which exhibit a discontinuity in the thermodynamic characteristics of the system, such as the volume $V = (\partial G/\partial P)_T$ and entropy $S = (\partial G/\partial T)_P$ for the liquid-vapour or solid-liquid transitions, and some latent heat is either absorbed or released [37, 38]. In 1937, Landau published a theory describing systems undergoing a second-order phase transition by introducing an order parameter going from zero in the disordered phase to a non-zero value for ordered phases [39]. Ginzburg and Landau [40] saw in the experimental measurements of the penetration depth versus temperature the signs of such a transition and introduced a complex wavefunction ψ as an order parameter for the system describing the density of Cooper pairs by $n_\mathrm{s} = |\psi(x)|^2$. Close to the critical temperature, ψ is small enough to apply a series expansion to the free energy of the system which is of the form:

$$f = f_{\mathrm{n}0} + \alpha|\psi|^2 + \frac{\beta}{2}|\psi|^4 + \frac{1}{2m^*}\left|\left(\frac{\hbar}{i}\nabla - \frac{e^*}{c}\mathbf{A}\right)\psi\right|^2 + \frac{h^2}{8\pi} \tag{1.9}$$

where $f_{\mathrm{n}0}$ is the free energy at the normal state, $\mathbf{A}$ the vector potential and m^* and e^* the effective electronic mass and charge, i.e. $e^* = 2e$ and $m^* \approx 2m$. The constants α and β are two coefficients that can be expressed as a function of the critical field H_c of the superconductor and the effective penetration depth $\lambda_\mathrm{eff} = \sqrt{m^* c^2/4\pi|\psi|^2 e^{*2}}$ which is nearly similar to the London penetration depth λ_L discussed previously. However, for superconductors in the “dirty” limit, i.e. for which the mean free path l is shorter than the BCS coherence length ξ_0, or close to T_c, it deviates from this value and we have

$$\lambda_\mathrm{eff} = \lambda_\mathrm{L}(T)\sqrt{1 + \xi_0'/l} \tag{1.10}$$

where $\xi' = \xi$ at $T = 0$ and $\xi' = 0.75\,\xi$ near T_c. The coefficient β in Equation 1.9 is always positive for the theory to hold. The coefficient α is positive above T_c in which case f_n reaches its minimum and $|\psi|^2 = 0$, and negative below T_c in which case $|\psi|^2 = -\alpha/\beta$. Ginzburg and Landau worked out the expressions for these coefficients at temperatures close to T_c:

$$\alpha(T) = -\frac{2\mathrm{e}^2}{mc^2}\; H_\mathrm{c}^2(T)\; \lambda_\mathrm{eff}^2(T) \tag{1.11}$$

$$\beta(T) = -\frac{16\pi\mathrm{e}^4}{m^2c^4}\; H_\mathrm{c}^2(T)\; \lambda_\mathrm{eff}^4(T). \tag{1.12}$$

When perturbations such as currents or magnetic fluxes are applied, the system will adopt the wavefunction configuration that minimises the free energy. By minimising Equation 1.9, it can be shown we obtain the Ginzburg-Landau differential equations:

$$\alpha\psi + \beta|\psi^2|\psi + \frac{1}{2m^*}\left(\frac{\hbar}{i}\nabla - \frac{e^*}{c}A\right)^2 \psi = 0 \tag{1.13}$$

$$J = \frac{e^*}{m^*}|\psi|^2\left(\hbar\nabla\psi - \frac{e^*}{c}A\right). \tag{1.14}$$

These equations can be simplified and solved to predict the behaviour of Josephson junctions or weak links (see Section 1.2.5). In absence of any magnetic field ($\mathbf{A} = 0$) and by normalizing the wavefunction using $f = \psi/\psi_\infty$ where $\psi_\infty^2 = -\alpha/\beta$, Equation 1.13 can be written:

$$\frac{\hbar^2}{2m^*|\alpha|}\frac{\mathrm{d}^2 f}{\mathrm{d}x^2} + f - f^3 = 0. \tag{1.15}$$

Introducing $\xi(T)$ which is the Ginzburg-Landau (GL) coherence length equal to

$$\xi(T)^2 = \frac{\hbar^2}{2m^*|\alpha|} = \frac{\Phi_0}{2\sqrt{2}H_\mathrm{c}(T)\lambda_\mathrm{eff}(T)}. \tag{1.16}$$

Equation 1.15 can be rewritten:

$$\xi^2(T)\frac{\mathrm{d}^2 f}{\mathrm{d}x^2} + f - f^3 = 0. \tag{1.17}$$

Using the BCS theory, the expression for the GL coherence length can be approximated to be:

$$\xi(T) = 0.74 \frac{\xi_0}{\sqrt{1 - T/T_\mathrm{c}}} \text{ in the clean limit } (l \gg \xi_0) \tag{1.18}$$

$$\xi(T) = 0.855 \sqrt{\frac{\xi_0 l}{1 - T/T_\mathrm{c}}} \text{ in the dirty limit } (l \ll \xi_0). \tag{1.19}$$

The ratio $\kappa = \lambda_\mathrm{eff}/\xi(T)$, called the dimensionless GL parameter, is an important parameter to determine the behaviour of the superconductor in a magnetic field (see Section 1.2.1).

Important Properties of Superconductors

The theories we presented above successfully model several properties of superconductors.

(i) Type I and Type II Superconductors Superconductors can be of two types depending on their behaviours in an applied magnetic field. For most low-T_c superconductors with the notable exception of niobium, the penetration depth λ is shorter than the coherence length ξ. These materials are known as type I. As shown in Figure 1.3, a magnetic field cannot penetrate the superconductor bulk up to a critical field H_c at which point it goes into normal state and becomes permeable to the applied magnetic field. In 1957, Abrikosov [41] studied what would happen in the case $\lambda > \xi$. According to his theory, the superconductor is said to be of type II if $\kappa = \lambda/\xi$ is bigger than $\sqrt{2}/2$. In this case, above its lower critical field H_c1 the superconductor enters an intermediate state where the magnetic field can penetrate in the form of vortices of quantised flux $\Phi_0 = h/2e$ called Abrikosov vortices. As the magnetic field increases, more and more vortices will penetrate the superconductor until the superconductivity is completely destroyed at the upper critical field $H_\mathrm{c2} = \Phi_0/2\pi\xi^2$.

(ii) The Proximity Effect The proximity effect is the diffusion of the Cooper pairs from a superconducting material into a contacting normal material through

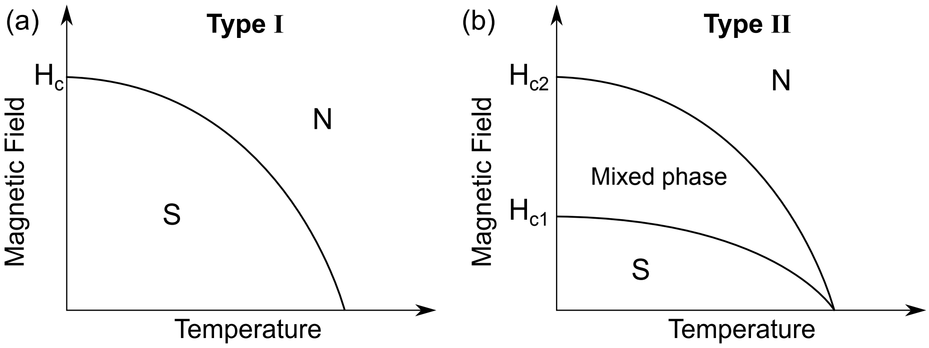

Figure 1.3: General shape of the critical field as a function of temperature for bulk superconductors of type I (a) and type II (b).

their common interface. As it affects the density of carriers in the superconductor, it effectively reduces its critical temperature [42]. This effect was hypothesised by Meissner after he measured the resistance of superconducting tin wires plated with different normal metals and observed that the critical temperature was lower [43]. At the interface between a superconductor and a normal metal (S-N), the order parameter in the S part is lowered and exponentially decays in the normal metal. The length scale of this effect is set by the normal metal coherence length ξ_{N}. In the clean limit, we have $\xi_{\mathrm{N}} \equiv \xi_{\mathrm{N},0} = \hbar v_{\mathrm{F}}/2\pi \mathrm{k_B} T_{\mathrm{c}}$ whereas in the dirty limit it becomes $\sqrt{l\xi_{\mathrm{N},0}/3}$ where l is the mean-free path of electrons in the metal. Depending on the quality of the interface, there can be an abrupt drop of the order parameter at the interface. This discontinuity is the macroscopic effect of complex pairing-depairing of Cooper pairs called Andreev reflections occurring between the two materials. The proximity effect has two practical applications. First, it allows the tuning of the critical temperature of a superconductor by adjusting the thickness of the contacting normal metal layer. This was theoretically analysed by de Gennes and others [44, 45] in the 1960s and more recently has been important for research on Transition Edge Sensors (TES) [46]. This aspect will be developed in more detail in Section 4.2.2. The proximity effect can also be used to weakly couple two superconductors using a normal metal layer forming what is called a S-N-S junction which is a type of weak link displaying Josephson effects.

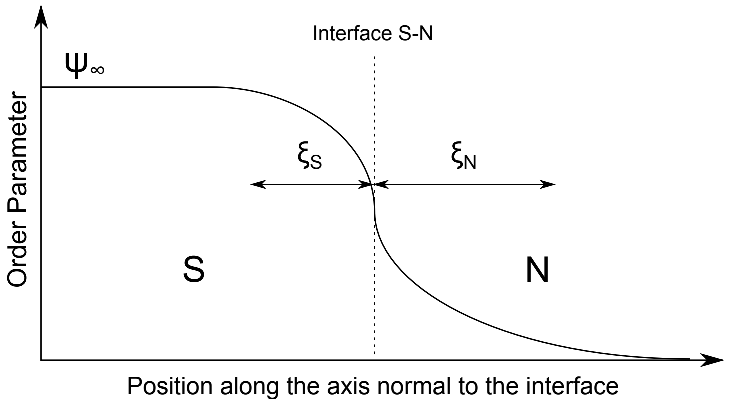

Figure 1.4: Order parameter at the interface between a superconductor S and a normal metal N. In the normal metal the wavefunction decays over a length of ξ_{N}.

1.2.2 Josephson Junctions

A Josephson junction is the junction of two weakly-coupled superconductors. It is named after Brian Josephson who predicted the tunnelling of Cooper pairs across an insulating barrier for a Superconductor-Insulator-Superconductor (SIS) junctions in 1962 [47]. This was later experimentally observed by Anderson and Rowell [48]. It was subsequently demonstrated that this model can be adapted to a variety of weak couplings including Superconductor-Normal metal-Superconductor (SNS) junctions, point-contact or film constrictions (also called S-s-S junctions).

Josephson Equations Following the then new BCS theory and inspired both by Gor'kov's microscopic derivation of the GL equations [35] and Giaever's supercurrent tunnelling experiments across aluminium oxide [30], Josephson wrote down equations describing what happens at the interface between two weakly coupled superconducting regions [49]. Noting φ the difference in phases of the macroscopic wavefunction on either side of the junction, I the current flowing through the junction and V the potential difference between the two superconducting regions, we have:

$$\frac{\mathrm{d}\varphi}{\mathrm{d}t} = \frac{2eV(t)}{\hbar} \tag{1.20}$$

$$I = I_\mathrm{c} \times \sin(\varphi). \tag{1.21}$$

I_c is called the critical current of the junction and is the maximum current applicable whilst keeping the junction in superconducting state. It is a parameter dependent on a variety of factors: the area of the junction, the quality of the film, its structure, the temperature and the magnetic field applied on the junction. Equation 1.20 is always true, but Equation 1.21 is only strictly valid for an ideal Josephson junction. However, it was later demonstrated that the latter is a good approximation of the behaviour of a superconducting nanobridge, assuming the length of this bridge is much shorter than the coherence length [50]. If that is not the case, the current-phase relationship (CPR) starts showing some distortions and can even become multivalued (see Section 1.2.6), although it can remain a periodic function of φ.

The Josephson equations give rise to several interesting properties which are described below.

(i) Josephson Inductance Considering small changes around I_0 and φ_0, the current and phase across a junction, from $I_0 = I_\mathrm{c} \sin\varphi_0$ we have $\mathrm{d}I = I_\mathrm{c}\cos\varphi_0 \mathrm{d}\varphi$. Replacing $\mathrm{d}\varphi$ using Equation 1.20, we have

$$V = \frac{\hbar}{2eI_\mathrm{c}\cos\varphi_0}\frac{\mathrm{d}I}{\mathrm{d}t} = L_\mathrm{J}(\varphi_0)\frac{\mathrm{d}I}{\mathrm{d}t}. \tag{1.22}$$

A Josephson junction behaves therefore as a phase-sensitive inductance of value $L_\mathrm{J}(\varphi)$ called the Josephson inductance.

(ii) Response to DC voltage: The AC Josephson Effect If we apply a finite dc voltage V_dc across a Josephson junction, we can integrate Equation 1.20 to get $\varphi = \varphi_0 + \frac{2e}{\hbar}V_\mathrm{dc}t$. Noting $\omega_\mathrm{J} = 2eV_\mathrm{dc}/\hbar$ and substituting for φ in Equation

1.21, we notice the Josephson current is oscillating:

$$I_{\mathrm{s}} = I_{\mathrm{c}} \sin\left(\varphi_0 + \omega_{\mathrm{J}} t\right). \tag{1.23}$$

The frequency $f_{\mathrm{J}} = \omega_{\mathrm{J}}/2\pi = V/\Phi_0$ is called the Josephson frequency and is used chiefly in metrology to define the volt.

(iii) Response to AC signals Considering a Josephson junction which is voltage-biased with a voltage $V_{\mathrm{ac}} = V_0 + V_{\mathrm{rf}} \cos(\omega_{\mathrm{rf}} t)$, the phase becomes

$$\varphi = \varphi_0 + \omega_{\mathrm{J,dc}} t + \frac{\omega_{\mathrm{J,rf}}}{\omega_{\mathrm{rf}}} \sin\left(\omega_{\mathrm{rf}} t\right) \tag{1.24}$$

where $\omega_{\mathrm{J,dc}} = 2eV_{\mathrm{dc}}/\hbar$ and $\omega_{\mathrm{J,rf}} = 2eV_{\mathrm{rf}}/\hbar$. Substituting Equation 1.24 into Equation 1.21 and using a Fourier-Bessel expansion, it can be found that the expression for the supercurrent is:

$$I_{\mathrm{s}}(t) = I_{\mathrm{c}} \sum_{-\infty}^{+\infty} (-1)^n \mathcal{J}_n \left(\frac{\omega_{\mathrm{J,rf}}}{\omega_{\mathrm{rf}}}\right) \sin\left(\phi_0 + \omega_{\mathrm{J,dc}} t + n\omega_{\mathrm{J,rf}} t\right) \tag{1.25}$$

If $\omega_1 = n\omega_{\mathrm{J}}$ or $V_{\mathrm{dc}} = n\omega_1 \Phi_0/2\pi$ where n is an integer, we obtain a dc current response with an amplitude set by the corresponding Bessel function. These supercurrent features are called Shapiro spikes. Otherwise, the response is $\langle I \rangle = V_{\mathrm{dc}}/R_{\mathrm{n}}$. This gives the I-V characteristics shown in Figure 1.5 [51]. When the junction is instead current-biased, the spikes become Shapiro steps in the I-V curve.

The Resistively and Capacitively Shunted Junction (RCSJ) Model To model an actual, non-ideal Josephson junction, in addition to the phase-dependent current given by Equation 1.21, we have to consider the contributions from the displacement current I_{d} due to the change in the electric field and the normal current I_{qp} (due to quasiparticles in the case of tunnel junctions, or bridge resistance for constrictions). A precise estimation of these currents is extremely complex but

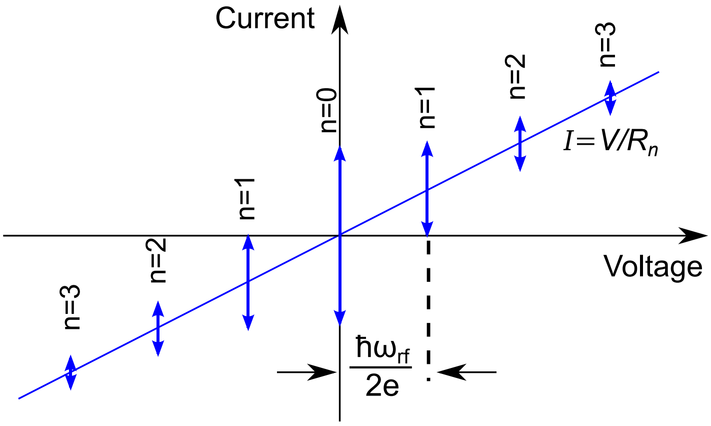

Figure 1.5: The dc component of I_s versus the applied dc voltage for a junction biased by a voltage $V_{ac} = V_0 + V_{rf}\cos(\omega_{rf}t)$. Adapted from Enss and Hunklinger [52].

they can be respectively approximated by the currents going through a capacitor and a resistor in parallel with an ideal junction in good approximation [53, 54]. This model, known as the Resistively and Capacitively Shunted Junction (RCSJ) model, is schematised in Figure 1.6. These factors ignore any spatial variations such as possible effects due to the edges or inhomogeneities across the junction. Kirchhoff's circuit law can be used to give the total current I as a function of potential V across the parallel combination of these devices. This gives

$$I = C\dot{V} + \frac{V}{R} + I_c \sin(\varphi) \tag{1.26}$$

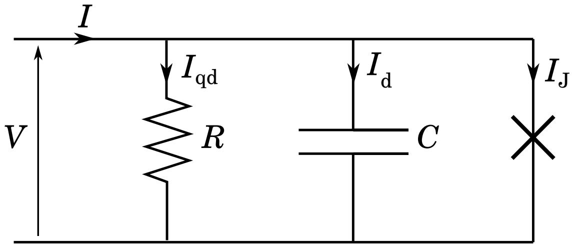

Figure 1.6: The RCSJ model for a real Josephson junction.

Using Josephson's Equation 1.20 to rewrite Equation 1.26, and normalizing the current by I_c, we get:

$$\frac{I}{I_\mathrm{c}} = \frac{C\Phi_0}{2\pi I_\mathrm{c}}\ddot{\varphi} + \frac{\Phi_0}{2\pi R I_c}\dot{\varphi} + \sin(\varphi) \tag{1.27}$$

which can be rewritten more simply as:

$$\frac{I}{I_c} - \sin(\varphi) = \frac{1}{\omega_p^2}\ddot{\varphi} + \frac{1}{\omega_p Q}\dot{\varphi} \tag{1.28}$$

by introducing the parameters $\omega_\mathrm{p} = \sqrt{2\pi I_\mathrm{c}/C\Phi_0}$ and $Q = \omega_\mathrm{p} RC = \sqrt{\beta_\mathrm{c}}$. ω_p is called the plasma frequency of the junction and Q its quality factor. Another parameter of interest is the Stewart-McCumber parameter $\beta_c = 2\pi I_\mathrm{c} R^2 C/\Phi_0$ which is often used along with Q to determine the quality of the junction and therefore its behaviour. Depending on the value of the quality factor Q, it is possible to distinguish two limiting types of junctions.

If Q $\ll$ 1 then the junction is said to be overdamped. The capacitance of the junction can be neglected in the electrical circuit and we can ignore the $\ddot{\varphi}$ term in Equation 1.28 which becomes

$$\dot{\varphi} = Q\,\omega_\mathrm{p}\left(\frac{I}{I_c} - \sin(\varphi)\right) \tag{1.29}$$

Solving this equation for currents above I_c gives $V = R\left(I^2 - I_c^2\right)^{1/2}$. The I-V characteristics of an overdamped junction are non-hysteretic, as illustrated in Figure 1.7(a).

If Q $\gg$ 1 the junction is then said to be underdamped and the I-V characteristics become hysteretic as shown in Figure 1.7(b). It can be explained by the fact that the relaxation constant of the RC components is much greater than the Josephson response, effectively limiting the dynamics of the junction.

It should be noted that the I-V characteristics show the time average voltage across the junction as there is in fact an ac current flowing in voltage state.

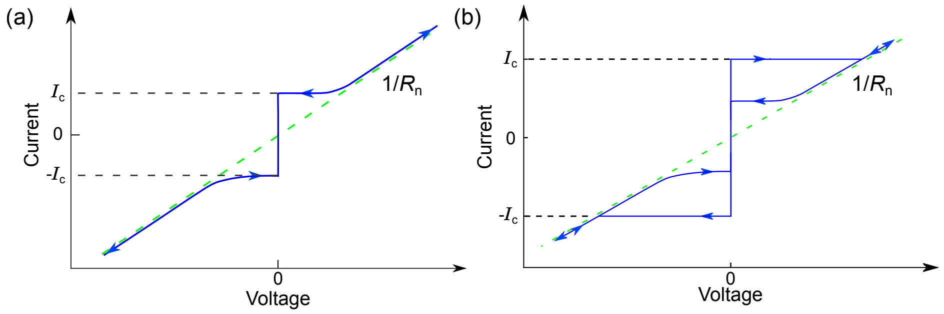

Figure 1.7: (a) (blue line) Generic shape for the I-V characteristics of an overdamped junction. The junction superconducts up to I_c and then the voltage approaches an asymptote (green line) which defines R_n. (b) I-V characteristics for an underdamped junction which shows hysteresis.

The washboard model The equation of motion along the x-axis for a mass m in a potential U and subject to a viscous drag ν is

$$m\frac{\mathrm{d}x^2}{\mathrm{d}t^2} + \nu\frac{\mathrm{d}x}{\mathrm{d}t} + \frac{\mathrm{d}U}{\mathrm{d}x} = 0. \tag{1.30}$$

By comparing Equation 1.30 with Equation 1.27 written in the form

$$\left(\frac{\hbar}{2e}\right)^2 C\frac{\mathrm{d}^2\varphi}{\mathrm{d}t^2} + \left(\frac{\hbar}{2e}\right)\frac{1}{R}\frac{\mathrm{d}\varphi}{\mathrm{d}t} + \frac{\mathrm{d}}{\mathrm{d}\varphi}\left(E_\mathrm{J}\left(1-\cos\varphi-\frac{I}{I_\mathrm{c}}\right)\right) = 0 \tag{1.31}$$

where E_J is the Josephson coupling energy $E_\mathrm{J} = \hbar I_\mathrm{c}/2e$, we can easily see the analogy between the motion of the ball and the RCSJ model. The analogy between the variables of the two models are summarised in Table 1.1.

Junction	Tilted washboard	Relation
Capacitance C	Mass m	$m \leftrightarrow (\hbar/2e)^2 C$
Phase φ	Position x	$x \leftrightarrow \varphi$
Tunnelling conductance $1/R$	Viscous damping ν	$\nu \leftrightarrow \left(\frac{\hbar}{2e}\right)\frac{1}{R}$
Bias current I	Tilt θ	$I \leftrightarrow \theta$
Potential energy U	Potential energy U	$U \leftrightarrow E_J\left(1-\cos\varphi-\frac{I}{I_\mathrm{c}}\right)$

Table 1.1: Analogy between the different variables of the RCSJ model for a Josephson junction and its mechanical analogue: the washboard potential.

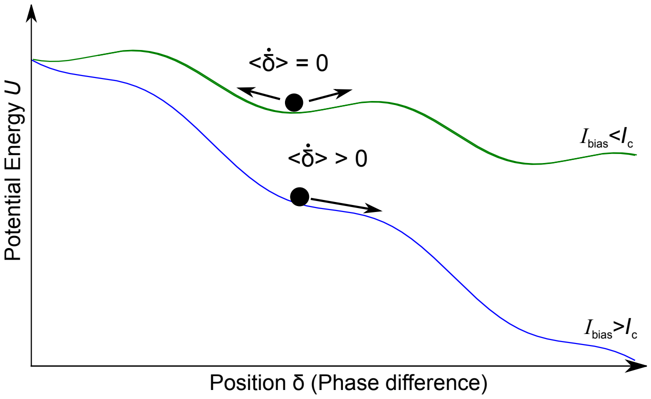

Figure 1.8: The washboard model, mechanical analogue of a Josephson junction. Potential energy as a function of the phase difference across a Josephson junction in two cases: $I_{\text{bias}} < I_{\text{c}}$ and $I_{\text{bias}} > I_{\text{c}}$.

If $I_{\text{bias}} < I_{\text{c}}$, the ball is oscillating at the plasma frequency inside one of the potential valleys. If $I_{\text{bias}} > I_{\text{c}}$, the ball starts rolling down the washboard. The average value for $\dot{\varphi}$ is therefore non-zero and following Josephson's equation a voltage arises across the junction. The two limiting behaviours can be understood by considering the viscous drag which is a function of the quality factor described earlier. An overdamped junction ($Q \ll 1$) would translate into a very high damping, if $I_{\text{bias}} < I_{\text{c}}$, meaning the tilt is reduced and the potential presents valleys again, the ball will get re-trapped instantly. For an underdamped junction, the drag is negligible and the ball will have enough kinetic energy to escape the valleys even when the tilt is lowered and will keep on rolling.

1.2.3 Noise Analysis

All the considerations above were made in the absence of any noise, at zero kelvin. Noise appears as an additional current source in the Josephson electrical circuit. It has several components: the thermal noise due to phonon excitation causing a voltage across the resistance of the junction and the so-called "flicker" noise.

Thermal noise Assuming the junction parameters are independent of the frequency, the Nyquist-Johnson formula predicts a power spectral density of

$S_\mathrm{V} = 4\mathrm{k_B}TR_\mathrm{n}$ over the whole frequency range, i.e white noise. In order to have the junction working correctly, it is necessary to have the Josephson coupling energy larger than the thermal energy. This condition is equivalent to having the noise parameter Γ of a junction, defined by $\Gamma = \mathrm{k_B}T/E_\mathrm{J}$, smaller than unity.

Flicker noise This is also called the $1/f$ noise because of its frequency dependence. Its origin is not as clear as that of the thermal noise. The possible main sources could be due to small temperature fluctuations between banks or unpaired spins due to the interaction with the substrate [55]. The study of this noise is especially important for research on Josephson qubits as it is a major source of decoherence, although it does not affect measurements at higher frequencies such as magnetisation reversal of molecules which are typically performed at frequencies above 100 kHz.

1.2.4 Flux Modulation

The flux going through a Josephson junction modulates its supercurrent. Assuming the current flow across the junction is uniform, it is possible to express the critical current as a function of the applied flux Φ:

$$I_\mathrm{c} = \left| \frac{I_\mathrm{c0} \sin(\pi\Phi/\Phi_0)}{\pi\Phi/\Phi_0} \right| \tag{1.32}$$

The pattern obtained from this equation is shown in Figure 1.9 and is similar to the Fraunhofer pattern in optics which is the intensity distribution of light diffracted through a single slit.

1.2.5 Weak Links

As we mentioned earlier, Josephson's theory was initially developed for tunnel junctions but it can be extended in good approximation to weak links in general, assuming the dimensions of the links are of the order of the coherence length [56]. In the following, we consider the case of a Dayem bridge, which is a constriction whose thickness t and width w are constant over its length L. The bridge is a weak link between two larger superconducting parts on either side that are referred to

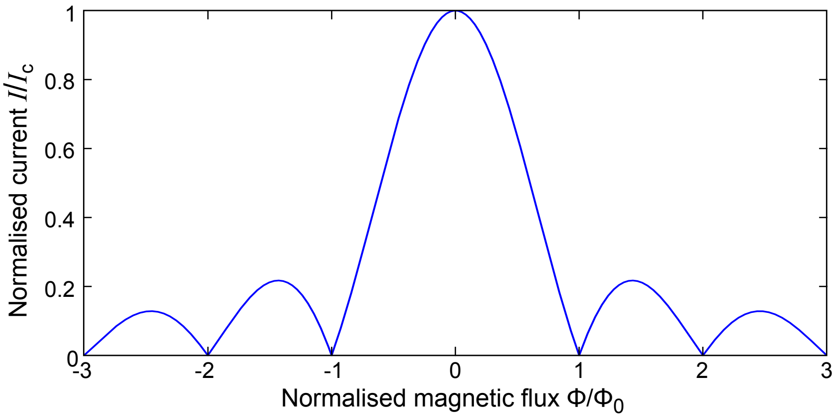

Figure 1.9: Normalised critical current as a function of the normalised magnetic flux for a Josephson junction, showing the Fraunhofer pattern.

as the banks in the literature. If we assume $L \gg t$ and $L \gg w$ and in the absence of any magnetic field, we can use the 1D-Ginzburg-Landau equation introduced earlier:

$$\xi^2 \frac{\mathrm{d}^2 f}{\mathrm{d}x^2} + f - f^3 = 0 \tag{1.33}$$

In the case of a short ($L \ll \xi$) Dayem bridge between two banks of the same superconductor in equilibrium, it was shown by Aslamazov and Larkin [57] that the derivative dominates the other terms so that Equation 1.33 can be written

$$\frac{\mathrm{d}^2 f}{\mathrm{d}x^2} = 0. \tag{1.34}$$

This equation can be easily solved over the length of the bridge by considering that the banks are massive enough to be in equilibrium $|f_{\mathrm{bank}}| = 1$ with a phase difference $\Delta\varphi$ in the order parameter between the two. The solution is of the form

$$f = (1 - x/L) + (x/L)e^{i\Delta\varphi} \tag{1.35}$$

where L is the length of the weak link. Considering the area of the junction $\mathcal{A} = wt$, inserting Equation 1.35 in the Ginzburg-Landau expression for the current

(Equation 1.14) gives the general form that Josephson predicted :

$$I_{\mathrm{s}} = \underbrace{\frac{2e\hbar\psi_{\infty}^{2}}{m^{*}}\frac{\mathcal{A}}{L}}_{I_c} \sin \Delta\varphi. \tag{1.36}$$

As $R_{\mathrm{n}} = \rho L/\mathcal{A}$, it should be noted that the $I_{\mathrm{c}}R_{\mathrm{n}}$ product does not depend on the dimensions of the nanobridge but only on the superconductor and the temperature. It is therefore a very useful parameter to analyse the behaviour and performance of weak links. Three main models have been developed to predict the value of the $I_{\mathrm{c}}R_{\mathrm{n}}$ product in different situations.

a) Ambegaokar and Baratoff (AB) model Ambegaokar and Baratoff [58] were able to generalise the Josephson effect for a tunnel junction using an alternative method based on thermodynamic Green's functions and Gor'kov's theory. From this development, they were able to work an exact analytical value for the $I_{\mathrm{c}}R_{\mathrm{n}}$ product over the whole temperature range of the junction:

$$I_{\mathrm{s}}(\varphi)R_{\mathrm{n}} = \frac{\pi\Delta}{2e}\tanh\left(\frac{\Delta}{2\mathrm{k_B}T}\right). \tag{1.37}$$

Close to T_{c}, this formula is valid for short metallic weak links as well, assuming their dimensions are much less than the coherence length.

b) KO-1 model A more advanced model, valid all the way down to $T = 0$, was suggested by Kulik and Omelyanchuk [59] to describe the phase current across a metallic weak link in the dirty limit. Based on Usadel's theory [141], which is a microscopic theory of superconductivity that extends the equations of the BCS theory assuming the electrons travels diffusively in the film, the KO-1 theory deviates from the AB theory as T tends towards zero. In this theory, the $I_{\mathrm{c}}R_{\mathrm{n}}$ product is the maximum of the product:

$$I_{\mathrm{s}}(\varphi)R_{\mathrm{n}} = \frac{2\pi k_{\mathrm{B}}T}{e}\sum_{\omega_n>0}\frac{2\Delta\cos(\varphi/2)}{\delta_n}\arctan\left(\frac{\Delta\sin(\varphi/2)}{\delta_n}\right) \tag{1.38}$$

where $\delta_n = \sqrt{\Delta^2 \cos(\varphi/2)^2 + \omega_n^2}$, and $\omega_n = \pi k_B T(2n+1)$ (called the n^{th} Matsubara frequency in the original paper).

c) KO-2 model Kulik and Omelyanchuk described in a later publication [60] that in the clean limit where electrons are travelling in a ballistic mode, the $I_s(\varphi)R_\text{n}$ product is higher and equal to:

$$I_s(\varphi)R_\text{n} = \frac{\pi\Delta}{e}\sin(\varphi/2)\tanh\left(\frac{\Delta\cos(\varphi/2)}{2k_\text{B}T}\right) \tag{1.39}$$

The three theories are represented in Figure 1.10. The $I_\text{c}R_\text{n}$ product is normalised by $\pi\Delta(0)/2e$ and the temperature by T_c.

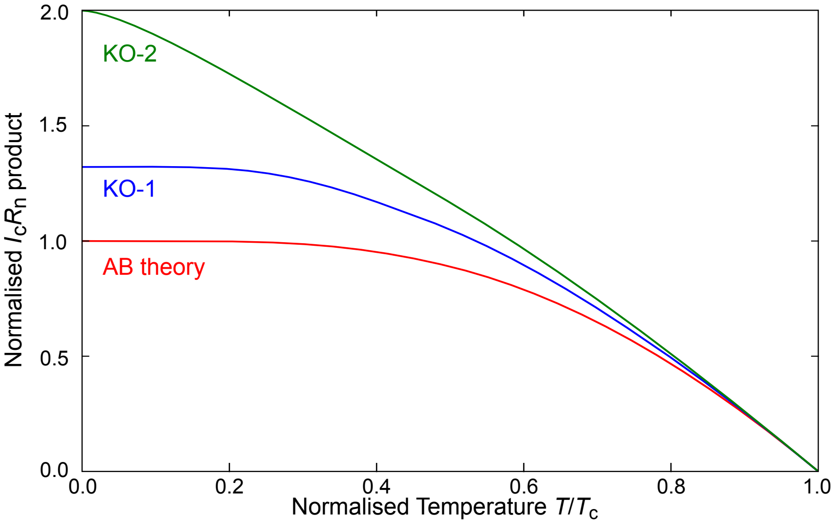

Figure 1.10: $I_\text{c}R_\text{n}$ product of a Josephson junction, normalised by $\pi\Delta(0)/2e$, as a function of reduced temperature shown for the three main theories presented in the text: Ambegaokar and Baratoff (AB) is shown in green, Kulik and Omelyanchuk (KO-1) in red and KO-2 in blue.

1.2.6 Dimensions of the Bridges

Critical Length L_c By performing numerical simulations based on the Usadel equations, Likharev and Yakobson [61] estimated the current-phase relationship (CPR) for several values of $L/\xi(T)$ as shown in Figure 1.11. As L increases, the CPR deviates from a sinusoid whilst staying single-valued up to $L_\text{c} \approx 3.5\,\xi(T)$ where it then becomes multi-valued. At this point the nanobridge no longer acts as

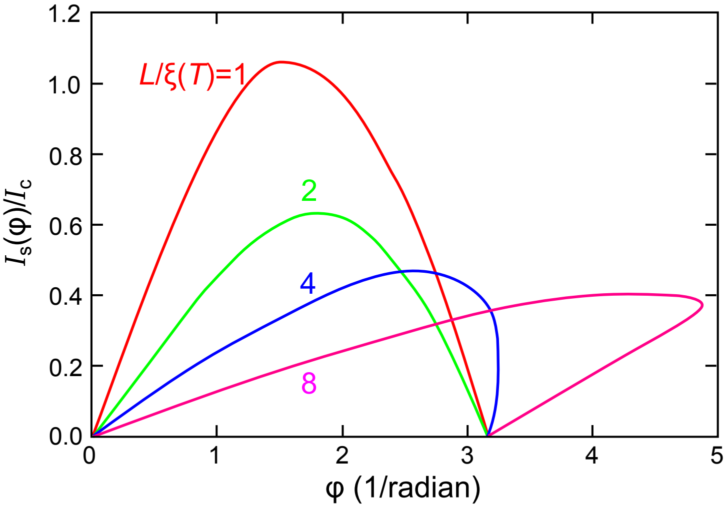

Figure 1.11: Current-phase relation (CPR) for nanobridges of different $L/\xi(T)$ ratios. If $L > 3.5\,\xi(T)$, the CPR become multivalued. Adapted from Likharev [56].

a Josephson junction even though the CPR may still be periodic depending on the width W of the bridge. Further numerical simulations showed two different regimes having periodic CPRs. If $W < W_c$ where $W_c \approx 4.44\,\xi(T)$, then 1D depairing starts occurring due to phase slips. If $W_c < W < \lambda$, the vortex motion is coherent enough to keep long-range order. If $W > \lambda$ there is no phase coherence and the CPR is no longer periodic. These different regimes are summarised in Figure 1.12.

Effective Length L_{eff} All the models mentioned above are valid in the hypothesis of what Likharev refers to his review [56] as the One-Dimensional Structure with Electrodes in Equilibrium (ODSEE) model. However, in reality the nanobridges affect the order parameter in the banks which are therefore involved as well in the non-linear effects. Theoretically these models would have to be completely reconsidered, but assuming the effect extends in the banks over a length δ, Likharev suggests it is a good enough approximation to apply the ODSEE results on a structure of effective length $L_{\text{eff}} = L + 2\delta$ where L is the geometrical length. For a Dayem bridge, the effective length is $L_{\text{eff}} \approx \max(L, W)$. This is shown in Figure 1.13. For a variable-thickness bridge, L_{eff} will be close to the geometric length when the banks are thick enough to hold the phase.

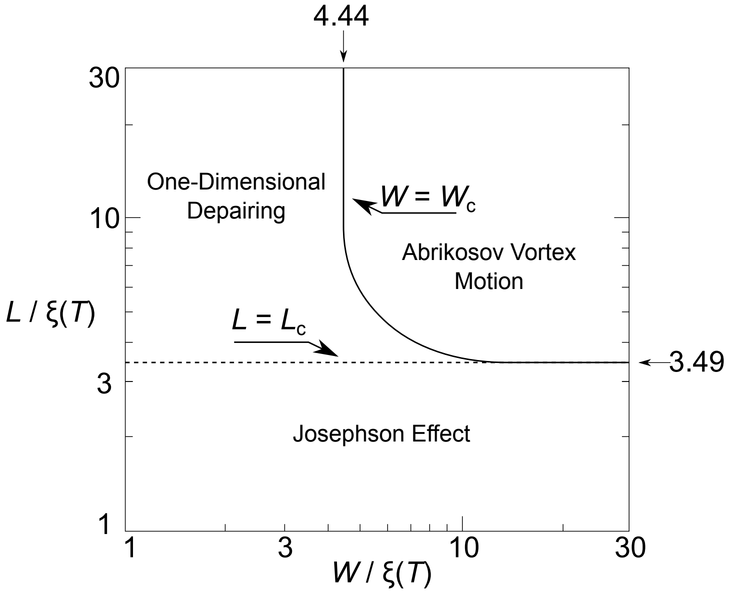

Figure 1.12: Schematic diagram showing the different regimes regarding the CPR depending on the normalised length L/ξ and width W/ξ of a bridge. Adapted from Likharev [56].

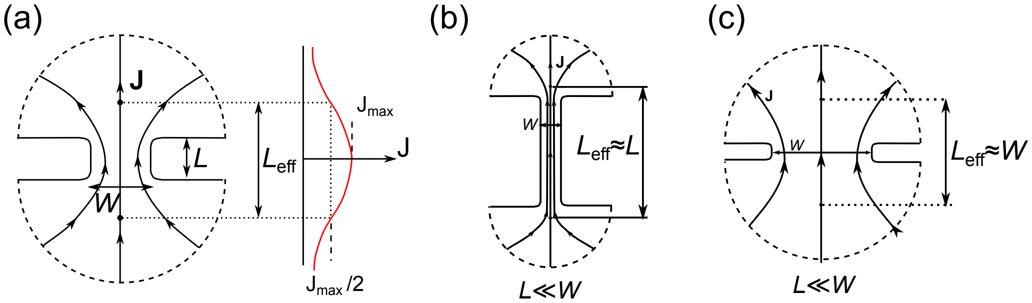

Figure 1.13: Current density for Dayem bridges with various lengths L and widths W. The current density falls off to half its maximum value at $L_{\text{eff}} \approx \max(L, W)$. Adapted from Likharev and Yakobson [61].

1.2.7 SQUIDs

A SQUID is a superconducting loop intersected by one or two Josephson elements (see schematic Figure 1.14a). I_c is modulated by the magnetic flux going through the loop and is Φ_0-periodic. It took only one year after the fabrication of the first Josephson junction for the first SQUID to be developed [62]. It was soon confirmed that SQUIDs were characterised by their extreme sensitivity to magnetic fluxes. With the addition of a larger pick-up loop, they can be used as powerful magnetometers with noise levels as low as $3\,\mathrm{fT}/\sqrt{\mathrm{Hz}}$ [63]. This means they have the ability to detect magnetic fields such as those we find in organic tissues including brain activity. Two sorts of SQUIDs can be distinguished depending on the sort of bias needed to operate them: direct-current (dc) SQUIDs that involve two junctions and radio-frequency (rf) SQUIDs that only involve one junction. The first SQUIDs were dc SQUIDs and rf SQUIDs appeared later. The fact that the latter can work with only one junction made them desirable in the early 1970s when the production of Josephson junctions was difficult. However, their reduced sensitivity has made their use much scarcer, especially since the development of better dc SQUIDs in the later 1970s. In the following, we will only consider dc-SQUIDs.

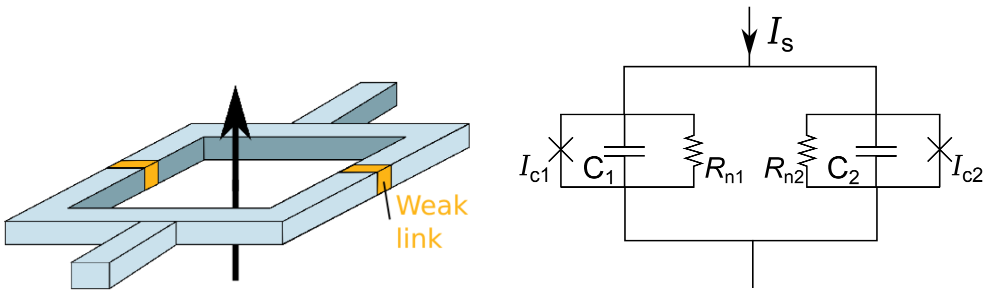

(a) Schematic

(b) Equivalent circuit

Figure 1.14: Schematic diagram of a dc SQUID and its RCSJ equivalent. An rf SQUID is similar but contains only one weak link.

DC-SQUIDs Description and Operation

If we consider a dc SQUID as shown in Figure 1.14, the supercurrent I_s is the sum of the contribution of the currents of two Josephson junctions: $I_\mathrm{s} =$

$I_{\mathrm{c1}} \sin(\varphi_1) + I_{\mathrm{c2}} \sin(\varphi_2)$. The junctions can be asymmetrical, this is quantified by a coefficient α so that we can write $I_{\mathrm{c1}} = (1+\alpha)I_0$ and $I_{\mathrm{c2}} = (1-\alpha)I_0$. For an ideal device we assume $\alpha \ll 1$.

Modelling the response of a SQUID requires the use of the vector potential $\mathbf{A}$ and the phase difference $\Delta\varphi$, which are non-observable quantities linked to observable physical parameters such as the magnetic field $\mathbf{B}$ or the supercurrent density $\mathbf{J}_{\mathrm{s}}$. Without gauge fixing, there is an infinite number of such quantities that could correspond to the observable values. For instance, the vector potential $\mathbf{A}$ and $\mathbf{A} + \nabla X$, where X can be any scalar field, both satisfy Maxwell's law $\mathbf{B} = \nabla \times \mathbf{A} = \nabla \times (\mathbf{A} + \nabla X)$. To allow for the existence of only one current value in a Josephson junction, we have to introduce the gauge-invariant phase difference γ. In the absence of any magnetic field ($\mathbf{A} = 0$), $\Delta\varphi$ and γ can be used interchangeably. However, the distinction has to be maintained to understand the response of SQUIDs and Josephson junctions to applied magnetic flux. In a bulk superconductor, $\nabla\gamma = 2\pi/\Phi_0(\mu_0\lambda^2\mathbf{J}_{\mathrm{S}} + \mathbf{A})$. In junctions, we often assume that the supercurrent density is uniform and then the gauge-invariant phase-difference across junctions 1 or 2 can be written

$$\gamma_{1,2} = \varphi_{1,2} - \frac{2\pi}{\Phi_0} \int \mathbf{A}.d\mathbf{l}. \tag{1.40}$$

The flux going through a superconducting loop is quantised, so over the whole contour C of the SQUID the condition $\oint_{\mathrm{C}} \nabla\gamma.dl = 2\pi n$ has to be satisfied. By summing the contribution of the two junctions and the loop body, we then have

$$2\pi n = \varphi_2 - \varphi_1 + \frac{2\pi\Phi}{\Phi_0} + \frac{2\pi}{\Phi_0} \int_{\mathrm{body}} \mu_0\lambda^2 \boldsymbol{J}_{\mathrm{S}}.dl \tag{1.41}$$

Assuming the film is thick enough compared to the penetration depth, we can find an integration path deep enough in the body where the supercurrent density is negligible. This allows us to give a simpler form of the relationship linking the phase differences across the two junctions as they have to satisfy the flux quantisation in the superconducting loop:

$$\varphi_2 - \varphi_1 = 2\pi n + \frac{2\pi\Phi}{\Phi_0} \tag{1.42}$$

If we assume the SQUID is ideal with symmetrical junctions ($\alpha = 0$, $I_{\mathrm{c1}} = I_{\mathrm{c2}} = I_{\mathrm{cjj}}$) we can use a trigonometric identity[4] to get:

$$I_{\mathrm{s}} = 2I_{\mathrm{cjj}} \sin\left(\varphi_1 + \frac{\pi\Phi}{\Phi_0}\right) \cos\left(\frac{\pi\Phi}{\Phi_0}\right) \tag{1.44}$$

It should be noted that in the above the flux Φ threading the loop is the sum of the flux Φ_{ext} due to the externally applied magnetic field and the flux Φ_L due to the inductance of the loop L[5] and the circulating current I_{circ}: $\Phi = \Phi_{\mathrm{ext}} + LI_{\mathrm{circ}}$. As $I_{\mathrm{circ}} = (I_{j1} - I_{j2})/2 = 0.5 I_{\mathrm{cjj}}(\sin\varphi_1 - \sin\varphi_2)$, using Equation 1.42 it can be shown that

$$\Phi = \Phi_{\mathrm{ext}} - LI_{\mathrm{c}} \sin\left(\frac{\pi\Phi}{\Phi_0}\right) \cos\left(\varphi_1 + \frac{\pi\Phi}{\Phi_0}\right) \tag{1.45}$$

At a given Φ_{ext}, the maximum supercurrent that can be applied through the SQUID has to be found self-consistently using Equations 1.44 and 1.45 [64].

A useful parameter to discuss the different limiting cases is the screening parameter $\beta_{\mathrm{L}} = 2I_{\mathrm{c}}L/\Phi_0$. It is the ratio of the magnetic flux generated by the maximum circulating current, i.e. $I_{\mathrm{circ}} = I_{\mathrm{c}}$, and $\Phi_0/2$. If $\beta_L \ll 1$, i.e. the inductance L is negligible, we have $\Phi \approx \Phi_{\mathrm{ext}}$. By maximising Equation 1.44 with respect to φ_1, it can be shown that the supercurrent is:

$$I_{\mathrm{s}} = 2I_{\mathrm{cjj}} \left|\cos\left(\frac{\pi\Phi}{\Phi_0}\right)\right| \tag{1.46}$$

---

[4] $2\sin a \cos b = \sin(a+b) + \sin(a-b)$ with

$$a = \varphi_1 + \frac{\pi\Phi}{\Phi_0} \text{ and } b = \frac{\pi\Phi}{\Phi_0} \tag{1.43}$$

[5] Our nanoSQUIDs are optimised towards high spin sensitivity and therefore do not include input coils such as what can be found for other applications. The inductance L in this thesis always refers to the inductance of the SQUID loop itself.

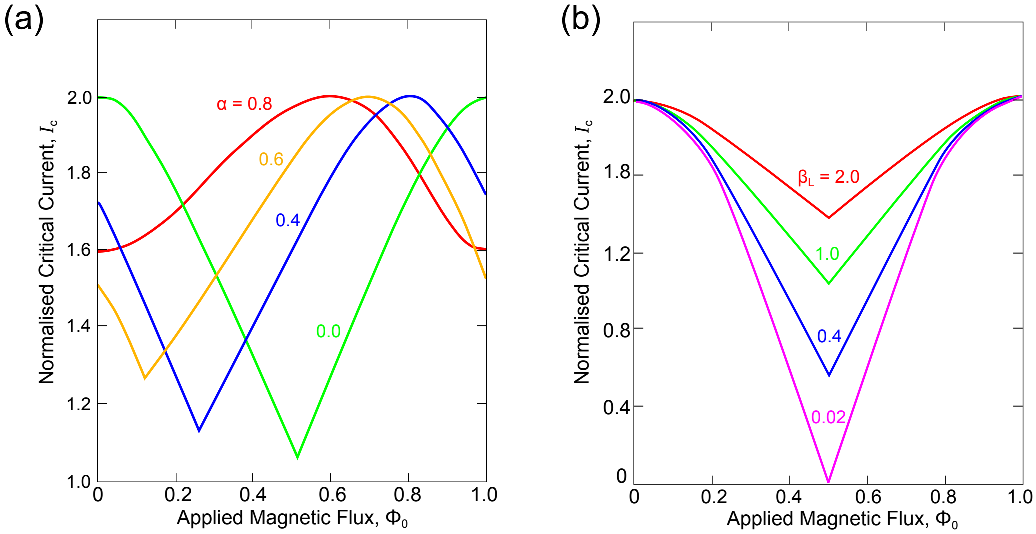

Figure 1.15: (a) Calculated normalised critical current I_c of a dc SQUID with strong damping $\beta_\mathrm{c} \ll 1$ versus the applied magnetic flux Φ_ext for various α. The screening coefficient β_L is set to 1. (b) Normalised critical current of a SQUID as a function of applied flux demonstrating quantum interference for several values of β_L for symmetrical junctions ($\alpha = 0$) with strong damping $\beta_\mathrm{c} \ll 1$. Adapted from Tesche and Clarke [65].

The other limiting case is for a strong magnetic screening $\beta_\mathrm{L} \gg 1$. The circulating current tends to compensate the magnetic flux in such a way that the total flux is quantised $\Phi = \Phi_\mathrm{ext} + LI_\mathrm{circ} \approx n\Phi_0$. It can be shown that:

$$I_\mathrm{s} = 2I_\mathrm{c}\left(1 - \frac{2}{\beta_\mathrm{L}}\frac{\Phi_\mathrm{ext}}{\Phi_0}\right) \tag{1.47}$$

The supercurrent for several values of α and β_L is shown in Figure 1.15. I_c can be read directly by increasing the current until a voltage arises across the device. This principle is used in some read-out electronics [66] but this affects the overall noise performance and increases the response time of the device. For non-hysteretic SQUIDs, there is a more convenient operation mode. The device is current-biased just above its critical current and the voltage across it is measured. As the flux going through the loop changes, it modulates the critical current and a change in voltage δV can be measured. The maximum peak-to-peak voltage difference ΔV is obtained between the applied magnetic fluxes $n\,\Phi_0$ and $(n+1/2)\,\Phi_0$. This is shown

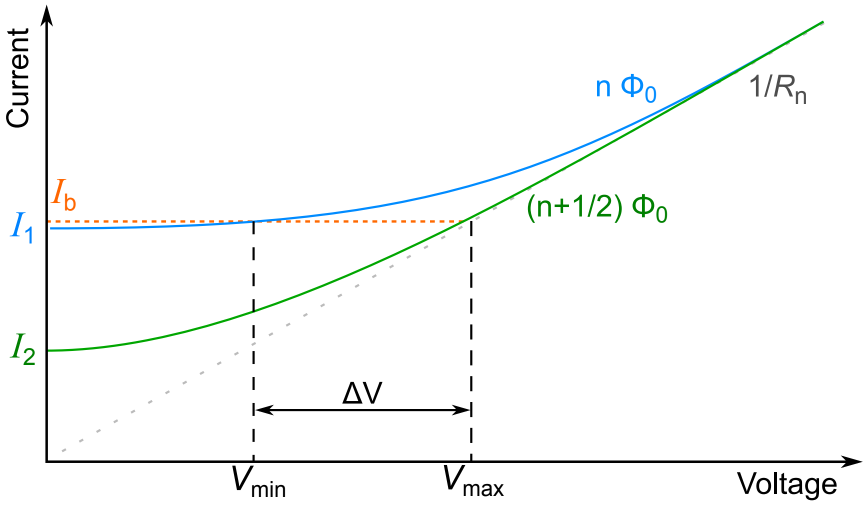

Figure 1.16: I-V characteristics of a non-hysteretic SQUID shown for two different fluxes $n\Phi_0$ and $(n + 1/2)\Phi_0$. The maximum peak-to-peak voltage difference is ΔV.

in Figure 1.16. The maximum response voltage obtained with this operation mode is ideally sinusoidal and is shown in Figure 1.17 for various values of β_L. SQUIDs can be operated in small signal mode. The device is flux-biased at $\sim \Phi_0/4$ where it has the maximum sensitivity $\mathrm{d}V/\mathrm{d}\Phi$. Over a small range of applied flux, the voltage response of the SQUID is approximately linear. Another mode of operation, the flux-locked loop (FLL), relies on a flux-feedback based on the electronics schematised in Figure 1.18 which linearises the response and allows signals with a much larger dynamic range (e.g. $\sim \Phi_0$) to be measured. Its operation is explained in Figure 1.19. The main limitation of this technique for the present work is that it can be impossible to apply the necessary feedback flux to nanoSQUIDs due to their very small effective areas.

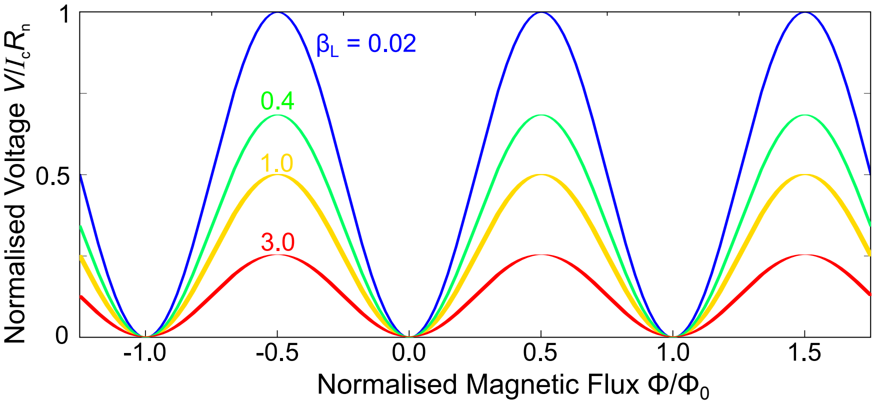

Figure 1.17: Normalised voltage modulation depth ΔV as a function of the applied magnetic flux Φ, characteristic for an ideal SQUID. Adapted from Tesche and Clarke [65].

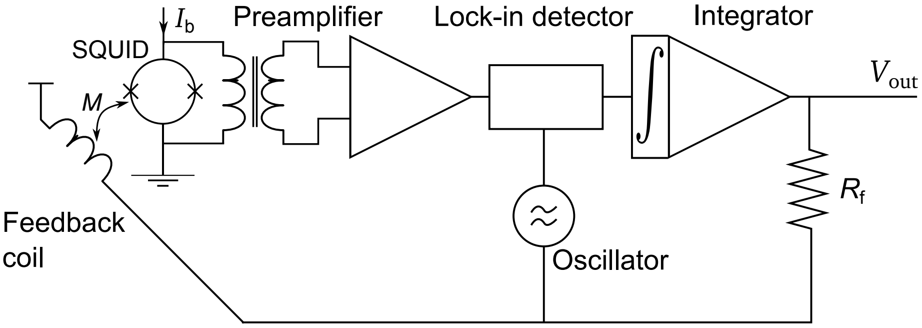

Figure 1.18: Flux-locked loop (FLL) read-out electronics. Adapted from Seeber [67].

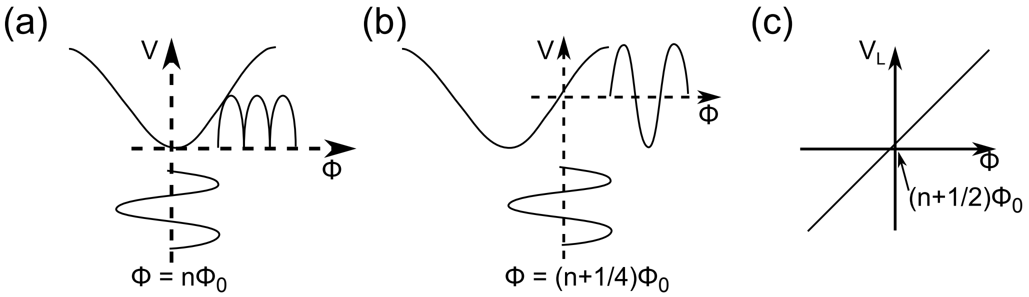

Figure 1.19: Schematic diagram of the operation of a flux-locked loop. An oscillating flux of amplitude $\Phi_0/2$ and frequency f_0, typically 100 kHz, is applied to the SQUID. If the external flux $\Phi_{\text{ext}} = 0$ (case (a)), the output of the SQUID is a rectified ac voltage of frequency $2f_0$. The lock-in detector, referenced to f, will therefore have an output equal to zero. If $\Phi_{\text{ext}} = \Phi_0/4$ (case (b)), the frequency of the SQUID output voltage will be exactly f_0, yielding the maximum output for the lock-in detector. This ensures a linearisation of the SQUID response (c). Picture adapted from Seeber [68].

SQUID Sensitivity

SQUIDs are currently considered to be the most sensitive fluxmeters and have been used for a variety of measurements.

Transfer function The transfer function $\mathrm{d}V/\mathrm{d}\Phi$ of a SQUID depends on a variety of parameters: temperature, flux, critical current, capacitance C and inductance L [69] and thus can only be determined accurately using numerical simulations. For a "typical" nanobridge-based dc SQUID, i.e. strongly damped with $\beta_\mathrm{c} \ll 1$, $\beta_L \sim 1$ and symmetrical bridges, the voltage at the optimum bias current is [69]:

$$V \approx \frac{\Delta V}{2} \sin\left(\frac{2\pi\Phi}{\Phi_0}\right) \tag{1.48}$$

where ΔV is the modulation depth which can itself be approximated [68] by

$$\Delta V \approx \frac{I_\mathrm{c} R_\mathrm{n}}{1+\beta_\mathrm{L}} \tag{1.49}$$

where β_L is the screening parameter $\beta_\mathrm{L} = 2LI_\mathrm{c}/\Phi_0$. The maximum transfer function, referred to as V_Φ, is given by differentiating the previous expression to obtain:

$$V_\Phi \approx \frac{\pi \Delta V}{\Phi_0}. \tag{1.50}$$

The voltage sensitivity The sensitivity of SQUIDs has been studied in several classic textbooks [70, 71, 72] and is based on computer simulations originally developed by Tesche and Clarke [65]. Figure 1.20 shows the results of these calculations for various parameters. In the white noise region, the total voltage noise S_V is composed of the voltage spectral density due to the Johnson–Nyquist noise in the shunt resistances R_n: $S_\mathrm{V,R} = 4k_\mathrm{B}T/(R_\mathrm{n}/2)$ and the circulating current spectral density $S_\mathrm{V,circ} = 4k_\mathrm{B}T/2R_\mathrm{n}$. For a bias current just above I_c, it can be shown that $S_\mathrm{V} = S_{V,R}R_\mathrm{d}^2 + \left(dV/d\Phi_\mathrm{ext}\right)^2 L^2 S_\mathrm{V,circ}$ where R_d is the differential resistance at the point of operation. In the case where $\beta_L \ll 1$, numerical simulations yield the optimum values for $dV/d\Phi_\mathrm{ext} \sim R_\mathrm{n}/L$ and $R_\mathrm{d} = \sqrt{2}R_\mathrm{n}$. We then obtain

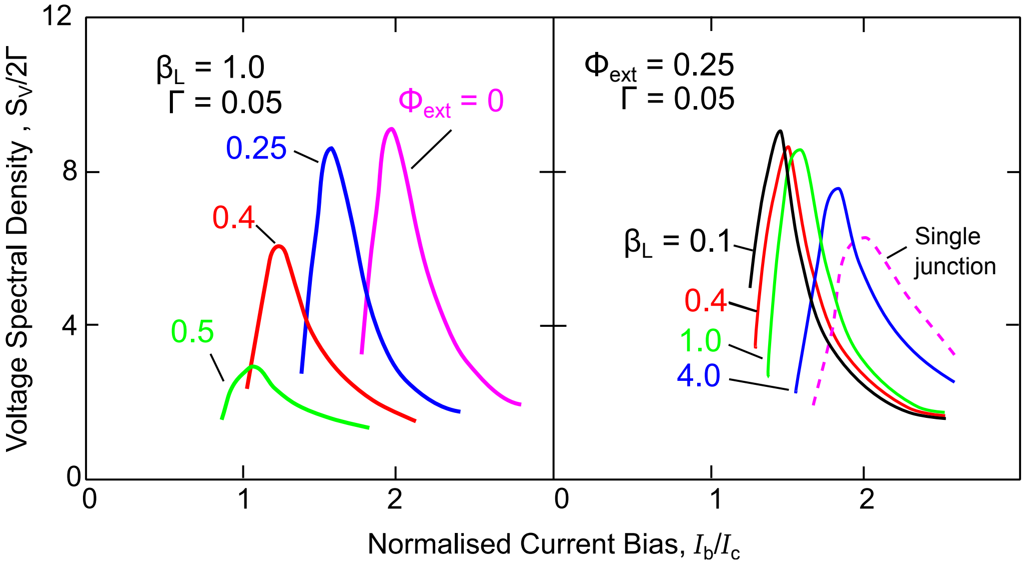

Figure 1.20: Predicted voltage spectral density versus bias current for SQUIDs with various parameters. On the left, the inductance and temperature are fixed so that $\beta_L = 1$ and $\Gamma = 0.05$ and the applied flux Φ_{ext} is variable. On the right, $\Phi_{\text{ext}} = 0.25$ and $\Gamma = 0.05$, the inductance is the variable. Adapted from Tesche and Clarke [65].

$S_V \approx 18\mathrm{k_B}TR_\mathrm{n}$. In the case where $\beta \sim 1$, we have

$$S_V \approx 16\mathrm{k_B}TR_\mathrm{n}. \tag{1.51}$$

The flux noise spectral sensitivity S_Φ of a SQUID is defined by:

$$S_\Phi^{1/2} = \frac{S_V^{1/2}}{\frac{\mathrm{d}V}{\mathrm{d}\Phi}\Big|_{\max}}. \tag{1.52}$$

$S_\Phi^{1/2}$ is commonly referred to as the flux noise Φ_{ns} and is most commonly given in $\mu\Phi_0/\sqrt{\mathrm{Hz}}$. In the negligible screening limit ($\beta_L \ll 1$), $S_\Phi^{1/2} \approx k_\mathrm{B}TL^2/R_\mathrm{n}\beta_L^2$ whereas in the strong screening limit ($\beta_L \gg 1$) it becomes $S_\Phi^{1/2} \approx 4k_\mathrm{B}TL^2/R_\mathrm{n}$. Typical values for good nanoSQUIDs ($\beta_L \sim 1$) at 4.2 K are in the range 0.1 – 1 $\mu\Phi_0/\sqrt{\mathrm{Hz}}$.

The intrinsic noise energy $\epsilon(f)$ of a SQUID per unit bandwidhth is defined by

$$\epsilon_{\mathrm{n}} = \frac{\Phi_{\mathrm{ns}}^2}{2L} \tag{1.53}$$

The noise energy sets the energy resolution of the device. The ultimate limit of resolution for a SQUID is set by the uncertainty principle ($\epsilon > \hbar$) which corresponds to a quantum flux noise $\Phi_{\mathrm{ns,Q}} = \sqrt{2L\hbar}$. The flux noises of real SQUIDs are often compared to how close they are to this limit.

The spin sensitivity of a SQUID can be determined by estimating the flux coupled by a magnetic dipole moment of one Bohr magneton to the SQUID loop, and using this to convert the flux noise into spins/$\sqrt{\mathrm{Hz}}$. It was originally studied by Ketchen *et al.* [1], and later by others, who considered a dipole magnetically coupled to a filamentary circular loop. If the dipole is located in the centre of a loop of radius a as shown in Figure 1.21(a), then the spin sensitivity is found to take the form:

$$S_{\mathrm{n}} = \frac{2a\Phi_{ns}}{\mu_0\mu_B} \tag{1.54}$$

Equation 1.54 has been verified experimentally and gives a good approximation [73]. It provides general guidelines to optimise our devices as it shows that the spin

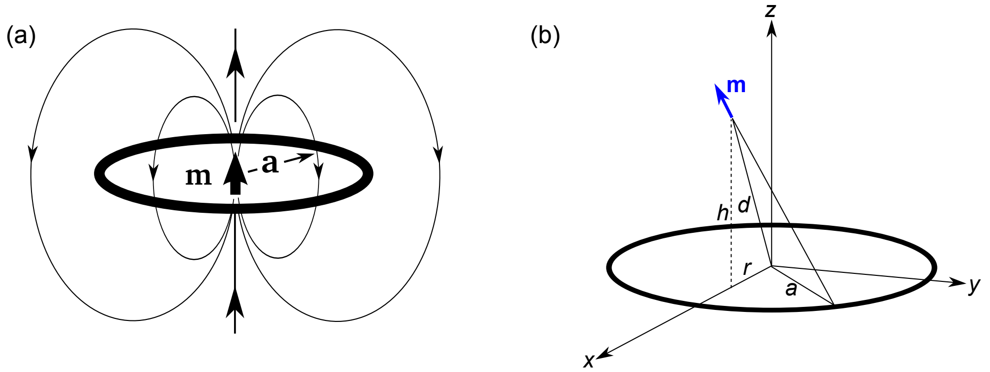

Figure 1.21: Schematic diagrams of (a) the on-axis coupling of a spin of momentum **m** to a SQUID loop of radius a as considered by Ketchen *et al.* [1]. (b) the geometry considered in Tilbrook's model [74]. The moment $\mathbf{m} = (m_x, m_y, m_z)$ is located at a height h and distance r from the axis passing through the centre of a filamentary circular SQUID of radius a in the x-y plane.

sensitivity can be improved by having a smaller loop radius a and a smaller flux noise, which can be achieved by reducing the inductance L and operating the device at a lower temperature.

Going further, by solving Maxwell's equations for any position of the spin, Tilbrook *et al.* [74] were able to estimate to flux coupled by an arbitrary moment of components (m_x,m_y,m_z) to a filamentary SQUID of radius a. As shown in Figure 1.21(b), the moment is located at a height h above the SQUID and at a radius r away from the normal axis going through the centre of the SQUID. The flux coupled is then:

$$\begin{aligned}\Phi = \frac{\mu_0}{\pi}\frac{a}{(h^2+r^2+a^2)^{3/2}}\frac{hm_x - rm_z}{k(1+k)\sqrt{1-k}} \\ \times\left(\left[E\left(\frac{2k}{k-1}\right) - (1+k)K\left(\frac{2k}{k-10}\right)\right] + aE\left(\frac{2k}{k-1}\right)m_z\right) \quad (1.55)\end{aligned}$$

where $k = 2ar/(a^2+r^2+h^2)$ and E and K are complete elliptic integrals of first and second kinds. Using these equations, we used Python and Matplotlib to calculate and plot the flux coupled into different series of SQUID loops as shown in Figure 1.22.

This shows it is possible to increase the coupling by having the spin very close to the edge of the loop. As in reality SQUIDs are not filamentary, spins would have to be located as close to a nanobridge as possible, and the radius of the bridge will be an important factor. For instance, that was the motivation of other groups to fabricate SQUIDs with carbon-nanotubes as weak links as we will describe in Chapter 2.

(a) a = 100 nm

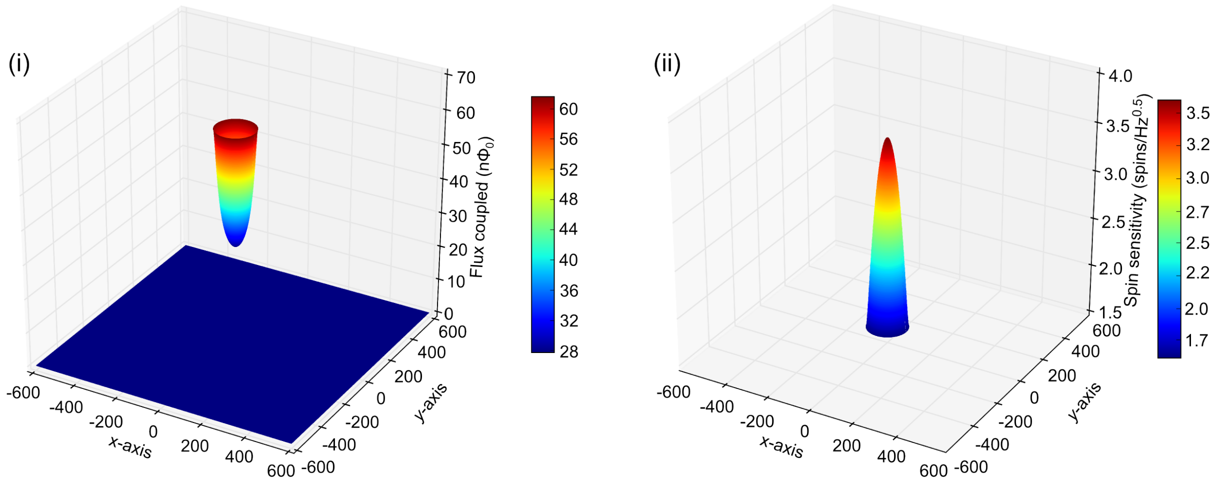

(b) a = 500 nm

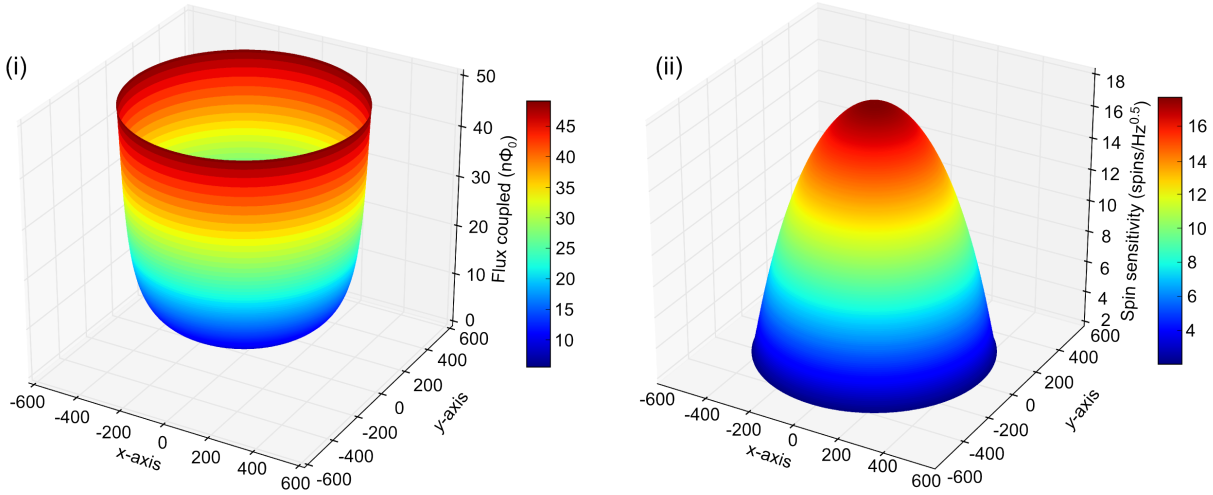

Figure 1.22: Responses plotted for two circular filamentary SQUIDs of radius (a) 100 nm and (b) 500 nm. (i) Flux (in $\mu\Phi_0$) coupled to the SQUID loop by a single spin aligned with the z-axis versus its position x and y. (ii) Spin sensitivity of the SQUID versus the position of the spin inside the loop assuming a flux noise of $0.1\,\mu\Phi_0/\sqrt{\mathrm{Hz}}$ which is typical for good devices at 100 mK (see Chapter 5). Graphs plotted using Python and Matplotlib using Equation 1.55.

Chapter 2

Review of State-of-the-art NanoSQUIDs for Single Spin Detection

Since their invention in the 1960s, SQUIDs have known many improvements regarding their various parameters: flux noise, energy sensitivity, etc. However, as we saw in the previous chapter, the spin sensitivity is a function of the loop diameter and magnetic coupling with the sample. Only recently in the last decade has nanopatterning reached a level of perfection sufficient to envisage actual measurements of nanostructures of interest down to the potential measurement of a single spin flip. As we saw in Chapter 1, an important parameter for nanoSQUIDs optimised for single spin detection is their flux noise. For our applications, we will concentrate on the flux noise in the white noise regime, i.e. at higher frequencies where the $1/f$ noise is negligible, as this corresponds to the range of frequencies used for experiments such as magnetisation reversal in nanoparticles. For these experiments, a magnetic field $B_{\|}$ is applied parallel to the SQUID (in plane to reduce its effect on the SQUID) whilst rf pulses are applied at the Larmor frequency of the spin system to induce spin flips [75]. For an electron, $f_{\text{Larmor}} = \mu_{\text{B}} B/\hbar\pi$

which is approximately 28 GHz for a magnetic field of 1 T. For this reason and to provide a constant way to compare devices, unless otherwise specified all the sensitivities quoted in the following correspond to the white noise regime. Another important criterion to achieve excellent spin sensitivity is the smallness of the SQUID effective area as it enables a better flux coupling of magnetic moments to the SQUID loop. As the spin sensitivity is improved as the temperature is reduced, the range of operation temperature of the SQUID is another crucial parameter. Ideally, they should be working correctly in the millikelvin range as many systems of interest require these temperatures. Finally, the practicality of integration and performing measurement and the ability to operate in large magnetic fields are other parameters to take into account. In the following, after a brief overview of conventional devices we will focus on the most recent devices found in the literature and discuss their performance in terms of the criteria aforementioned.

2.1 Conventional Devices

In the early 1970s, shortly after their invention by Jaklevic *et al.* in 1964 [62], the scientific interest had moved to rf-SQUIDs mainly because creating a single junction was easier and they were showing the best performance at the time [76]. However, in 1976, Clarke *et al.* demonstrated both theoretically and experimentally that dc-SQUIDs could outperform their rf counterparts [69]. By taking advantage of the advances of the niobium-based tunnel junctions, they fabricated a SQUID having two shunted Nb-NbO$_\mathrm{x}$-Pb tunnel junctions operated at 4.2 K and reported an energy sensitivity of $7 \times 10^{-30}\,\mathrm{J.Hz^{-1}} = 10^4\,h$ at 10 kHz, which was on a par with the best rf-SQUIDs at the time: a 10 GHz rf-SQUID operated at 4.2 K showing an energy resolution of 3500 h at a few kHz, fabricated by Pierce *et al.* [77]. In the 1980s, a better control over evaporation conditions and the windowing technique enabled the creation of devices operating with an energy sensitivity of the order of Planck's constant. In 1979 Ketchen *et al.* [78] reported a device with an intrinsic energy sensitivity of 5 h based on Pb-alloy S-I-S junctions. Cromar *et al.* [79]

managed to get a device with a flux noise of $1.7 \times 10^{-2}\,\mu\Phi_0/\sqrt{\text{Hz}}$ and an intrinsic energy sensitivity of $0.9\,h$. The use of Electron Beam Lithography (EBL) enabled the patterning of structures significantly smaller and requiring less manufacturing steps using Dayem bridges as Josephson elements. Voss *et al.* [80] took advantage of this technique to define an all-niobium SQUID with nanobridges as short as 120 nm. This device had an energy sensitivity of $3\,h$ at 100 kHz corresponding to a flux noise of $0.4\,\mu\Phi_0/\sqrt{\text{Hz}}$.

2.2 Modern NanoSQUIDs: Toward Single Spin-Flip Sensitivity

In 2002, Gallop *et al.* [75] fabricated a device based on trilayer junctions with a smaller $3 \times 3\,\mu\text{m}^2$ loop and reported a flux noise of $0.5\,\mu\Phi_0/\sqrt{\text{Hz}}$ in the white noise limit at 4.2 K. This would correspond to an estimated spin sensitivity of $38\,\text{spins}/\sqrt{\text{Hz}}$ (theoretically they expected $2.5\,\text{spins}/\sqrt{\text{Hz}}$). They were the first research group to address the possibility to measure the single spin flip of an electron by reducing the effective area. They suggested that it would be advantageous to replace the trilayer junctions, which had to be excessively wide because of their low supercurrent density, by constrictions as weak links. Most of the present scientific effort is still focussed on miniaturising the nanobridges and loop whilst keeping a standard operation mode. The most important results are presented below.

FIB NanoSQUIDs Hao *et al.* used Focussed Ion Beam (FIB) to create nanoSQUIDs [81] by milling films of sputtered niobium from Strathclyde university. Figure 2.1 shows a SEM micrograph of their best device which features $65\,\text{nm} \times 80\,\text{nm}$ bridges and a $200\,\mu\text{m} \times 200\,\mu\text{m}$ loop. The film was previously covered with a layer of ebeam-deposited tungsten which served the triple purpose of limiting the contamination of the niobium layer by the ion beam, providing a thermal shunt to prevent hot spot formation and an electrical shunt to prevent hysteresis in the I-V characteristics. This SQUID was operated in small signal mode at its optimal bias current and was coupled to a SQUID Series Arrays (SSA), a low-temperature

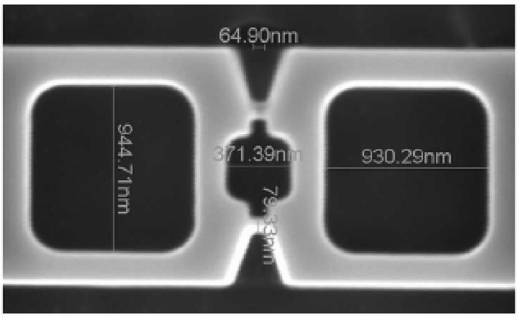

Figure 2.1: SEM micrograph of the FIB SQUID fabricated by Hao *et al.* [81].

pre-amplifier characterised by an extremely low intrinsic noise level. By using this experimental set-up, the noise measured for the nanoSQUID was measured to be as low as $0.2\,\mu\Phi_0/\sqrt{\mathrm{Hz}}$ at 10 kHz [10] and $0.8\,\mu\Phi_0/\sqrt{\mathrm{Hz}}$ at 1 Hz where the $1/f$ noise dominates. It is currently the lowest reported noise for current-biased SQUID operated at helium temperatures. This would translate into an estimated spin sensitivity of $2\,\mathrm{spins}/\sqrt{\mathrm{Hz}}$ at high frequencies. The critical temperature can be effectively tuned from 5 K to 9.1 K by the thickness of the niobium, offering a wider range of operation temperatures. This device was used to measure the magnetic response of a ferromagnetic particle deposited on a bridge [82]. It is unclear if this technique could enable the creation of yet smaller SQUIDs with better results.

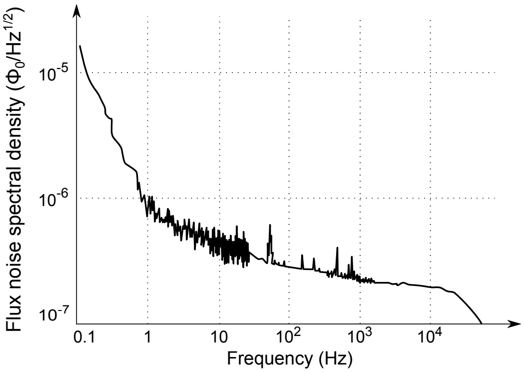

Figure 2.2: Flux noise spectrum as measured for the device by Hao *et al.* at a bias current of $60\,\mu$A and temperature of 6.8 K [10]. The high-frequency roll-off is characteristic of the readout electronics.

Tettamanzi *et al.* [11] focussed on reducing the loop size to create the smallest FIB SQUID possible. The device, made of niobium and shown in Figure 2.3(a), has a

50 nm-radius loop and its noise spectrum, reproduced in Figure 2.3(b), indicates a flux noise of 2.6 $\mu\Phi_0/\sqrt{\mathrm{Hz}}$ at high frequencies. The authors interpreted this as being the result of gallium-ion implantation from the FIB over a lateral distance of $\sim$ 20 nm which generates a non-negligible area with a high density of defects on the periphery of the hole. The advances of helium-based FIB might allow to get around this contamination issue in future (see Chapter 7).

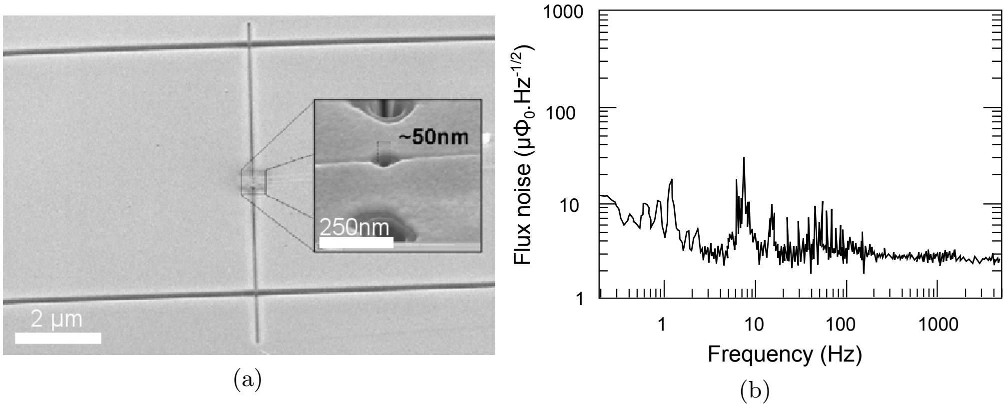

(a)

(b)

Figure 2.3: (a) SEM image of the device fabricated by Tettamanzi *et al.* with the smallest loop. (b) Flux noise spectrum measured for this device at 6 K, saturating at 2.6 $\mu\Phi_0/\sqrt{\mathrm{Hz}}$. Images adapted from Tettamanzi *et al.* [11].

Standard EBL NanoSQUIDs Other groups have investigated niobium nanoSQUIDs based on Dayem bridges patterned using Electron Beam Lithography. Granata *et al.* [9, 83] defined niobium bridges with dimensions 200 nm × 100 nm × 80 nm and reported a theoretical spin sensitivity of 100 spins/$\sqrt{\mathrm{Hz}}$, which could go down to 20 spins/$\sqrt{\mathrm{Hz}}$ depending on the estimated quality of the coupling [74]. To improve the spin sensitivity and reduce the susceptibility to out-of-plane magnetic field, Lam *et al.* reduced to a minimum the loop dimensions and realised the smallest reported EBL patterned nanoSQUID [84] which could be described as a hole in a track (see Figure 2.4). Its diameter was 70 nm, located in the middle of a 250 nm wide Au/Nb track. The measured effective area of the device was 0.040 $\mu\mathrm{m}^2$, three times bigger than the geometrical one. Despite these exceptional dimensions, its estimated flux noise was only $\Phi_{\mathrm{ns}} = 5\,\mu\Phi_0/\sqrt{\mathrm{Hz}}$ corresponding to a

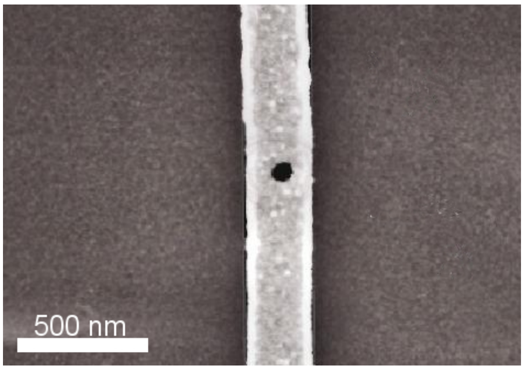

Figure 2.4: SEM micrograph of the hole-in-a-track SQUID fabricated by Lam *et al.* [84]. The strip width is 250 nm and the hole diameter is 70 nm.

predicted spin sensitivity of 70 spins/$\sqrt{\text{Hz}}$.

3D structures In contrast with the above-mentioned devices which are two-dimensional, Vijay *et al.* [14] developed a lift-off technique using electron beam lithography followed by a two-stage metal evaporation to produce more advanced structures in three dimensions as shown in Figure 2.5. They evaporated 8 nm of aluminium normally to the sample and then angled the substrate *in situ* to deposit an additional 80 nm-thick layer of aluminium. This prevents the evaporated metal from being deposited in the smaller features, i.e. the nanobriges, whilst the banks are getting thicker. They state that the presence of thicker banks can be considered "holding" the phase to a greater extent than thinner banks. Therefore, they report achieving a nearly ideal behaviour with deeper modulations and an $I_\text{c}R_\text{n}$ product close to the theoretical value predicted by the KO-1 theory and 70 % better than what is typically reported for more conventional devices (see Figure 2.6).

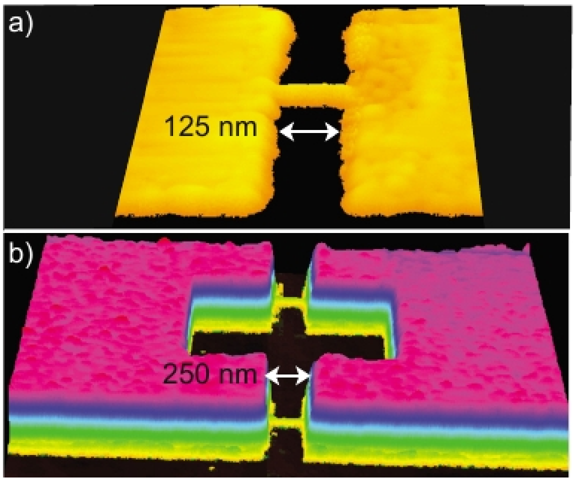

Figure 2.5: AFM images of devices fabricated by Vijay *et al.* [14]. (a) represents a nanobridge after the first stage of metallisation normal to the substrate. (b) represents the completed device after a second step of metallisation with a variable angle giving it a three dimensional profile.

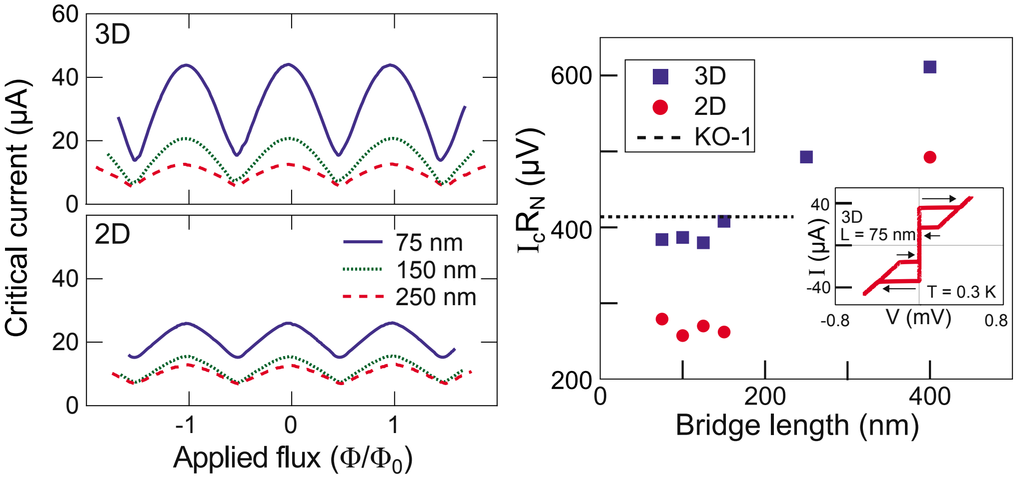

(a)

(b)

Figure 2.6: (a) Critical current as a function of applied magnetic flux for devices with different bridge lengths and 2 D or 3 D metallisation at 30 mK. 3 D devices are characterised by 70% deeper modulations than their 2 D equivalents (b) $I_{\mathrm{c}}R_{\mathrm{n}}$ product as a function of bridge length for 2 D and 3 D devices at 30 mK. The dashed line is the theoretical value according to the KO-1 theory, demonstrating that 3 D SQUIDs follows more closely this model. The inset shows the I-V characteristics for a 3 D device which is hysteretic at these temperatures. Images adapted from Vijay *et al.* [14].

2.3 SQUIDs Optimised for Millikelvin Applications

The aforementioned SQUIDs present excellent characteristics close to their T_c for which they have been optimised. However, much below T_c, heating of the bridge when biasing the SQUID becomes an issue and leads to hysteretic I-V characteristics which make the SQUID virtually impossible to operate in a conventional way. In the following we review recent devices and modes of operation that explicitly try to solve the issue to enable millikelvin magnetic measurements.

Use as flux-to-critical-current transducer The hysteresis in the I-V characteristics is currently generally understood to originate from the fact that as a device is operated far from T_c, the critical current I_c becomes larger than the retrapping current I_r, which is the minimum current that can sustain a hot spot of normal metal in the nanobridge. As fabricating a Dayem bridge unaffected by this issue is very complex, Wernsdorfer *et al.* [85] designed a workaround by using their SQUID as a flux-to-I_c transducer. Their custom electronics ramps the current until triggered by the sudden voltage jump which defines I_c and then restarts the cycle. While enabling the use of hysteretic SQUID at any temperature, this technique comes at the price of a reduced bandwidth (a few kHz) and increased flux noise: $300\,\mu\Phi_0/\sqrt{\mathrm{Hz}}$. The spin sensitivity, estimated to be about $1000\,\mathrm{spins}/\sqrt{\mathrm{Hz}}$, proved to be sensitive enough to measure the magnetisation reversal of a 3 nm cobalt nanoparticle located on one of the two Dayem bridges with a technique dubbed the *cold mode* [86]. Russo *et al.* [87] have subsequently improved this technique by using asymmetrical bridges to boost $I_\Phi = \partial I_\mathrm{c}/\partial\Phi$ up to $60\,\mu\mathrm{A}/\Phi_0$, shown in Figure 2.7(a), giving an improved flux noise of $160\,\mu\Phi_0/\sqrt{\mathrm{Hz}}$. This proved sensitive enough to measure the magnetisation of a $\mathrm{Fe_3O_4}$ nanoparticle as shown in Figure 2.7(b).

Carbon NanoTube (CNT) based nanoSQUID To significantly reduce the cross-section of the nanobridges and ensure they are symmetrical, Cleuziou *et al.* [7] used carbon nanotubes as Josephson elements to fabricate the device shown in

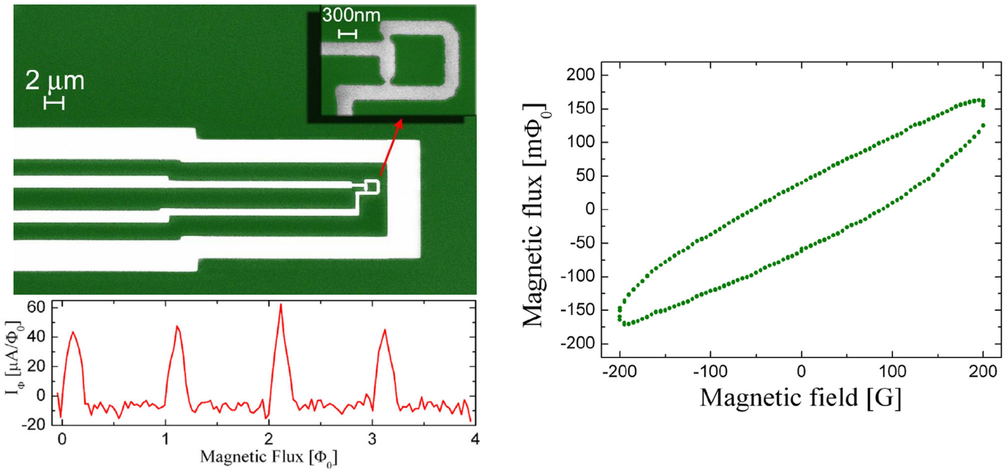

(a)

(b)

Figure 2.7: (a) top: SEM micrograph of the device developed by Russo *et al.* [87]; bottom: $I_\Phi = \partial I_c/\partial\Phi$ measured as a function of applied magnetic flux. (b) Example of a magnetic measurement with their device: magnetisation of a Fe_3O_4 nanoparticle as a function of magnetic field at 4.2 K.

Figure 2.8. Despite a flux noise in the order of $10\,\mu\Phi_0/\sqrt{\mathrm{Hz}}$ at 30 mK in the white noise region, which is quite high in absolute terms, placing the spin system of interest in close contact with the bridge would result to an estimated spin sensitivity of only $2\,\mathrm{spins}/\sqrt{\mathrm{Hz}}$ due to the extremely small radius of the nanotubes leading to a very large coupling as illustrated by Figure 2.8(b).

SQUID on a Tip Other original solutions have been investigated. By evaporating aluminium on an hollow quartz needle with three different angles as shown in Figure 2.9, Finkler *et al.* managed to create a SQUID self-aligned on a tip [88] with a flux sensitivity of $1.8\,\mu\Phi_0/\sqrt{\mathrm{Hz}}$ at 10 kHz. This device has been coupled to an AFM tip to perform extremely precise scanning SQUID magnetometry mapping of serpentine samples [6]. As there is no thermal contact with the sample, the SQUID is not affected by the fact the substrate was kept at 300 mK. As the loop diameter is only 200 nm, the estimated spin sensitivity assuming perfect coupling to an on-axis moment located less than 100 nm below the loop is $65\,\mathrm{spins}/\sqrt{\mathrm{Hz}}$. Very recently, this fabrication technique has been perfected by Vasyukov *et al.* [89]

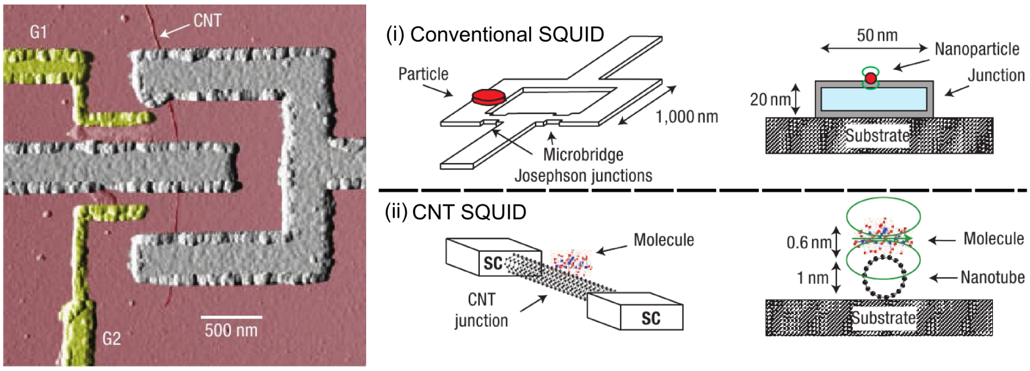

(a) (b)

Figure 2.8: (1) Colourised AFM picture of the carbon nanotube (CNT) SQUID fabricated by Cleuziou *et al.* [7]. The magnetic coupling between a nanoparticle and a regular SQUID is shown in (i) and is much smaller than what it would be to CNT shown in (ii) thanks to its reduced dimensions (radius ∼2 nm).

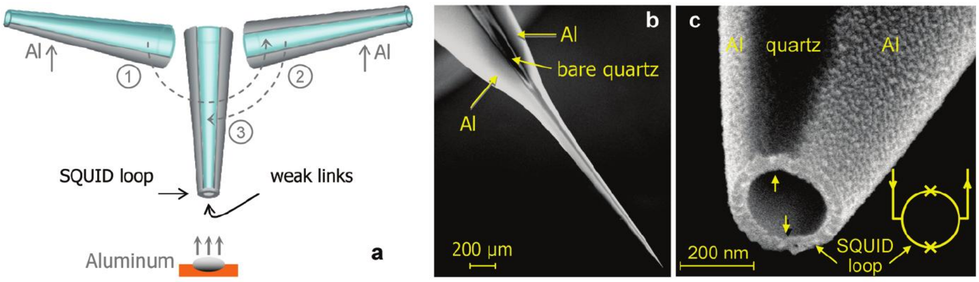

Figure 2.9: (a) Schematic diagram presenting the procedure to fabricate the SQUID on a tip. 25 nm of aluminium are deposited in position 1 and 2 to define the superconducting leads then a subsequent 17 nm in position 3 to define the bridges. (b) SEM images of the quartz tip (c) terminated by the SQUID at its apex with a 200 nm wide loop. Bright regions are aluminium, darker ones are bare quartz. Illustrations taken from Finkler *et al.*. [88].

to fabricate similar SQUIDs based on lead films to get an unprecedented flux noise of $50\,\mathrm{n}\Phi_0/\sqrt{\mathrm{Hz}}$ at 4.2 K which corresponds to a spin sensitivity of $0.38\,\mathrm{spins}/\sqrt{\mathrm{Hz}}$ as the tip can be hovered at only 10 nm above the sample. In an in-plane magnetic field of 1 T, they estimate their spin sensitivity to be $0.6\,\mathrm{spins}/\sqrt{\mathrm{Hz}}$. This work, published after the fabrication and characterisation of the devices presented in the present thesis, enabled us to re-examine some aspects of our work. This will be discussed in Chapter 7.

Non-linear Phase-sensitive Inductance As we saw in Section 1.2.2, a SQUID can be seen as a non-linear phase-sensitive inductor. By shunting with a capacitor a variable-thickness aluminium SQUID as described by Vijay *et al.* [14], Levenson-Falk *et al.* obtained a nonlinear LC oscillator with a flux-dependent resonant frequency from 4 to 8 GHz [90]. This is an improved, nanobridge-based version of a previous Al-AlO$_x$-Al device fabricated by Hatridge *et al.* [91] which was characterised by a flux noise of $0.14\,\mu\Phi_0/\sqrt{\mathrm{Hz}}$ for a 0.6 MHz bandwidth. Levenson-Falk *et al.* report a noise level down to $0.03\,\mu\Phi_0/\sqrt{\mathrm{Hz}}$ for a 20 MHz bandwidth with the device shown in Figure 2.10. This very low noise floor can be explained by the use of a Lumped-element Josephson Parametric Amplifier (LJPA) which acts as a virtually noiseless preamplifier as explained by Schematic 2.11. Without the use of the LJPA the flux noise of the device is only $0.2\,\mu\Phi_0/\sqrt{\mathrm{Hz}}$ over an extended bandwidth.

Return of the Tunnel-Junction SQUID Tunnel junctions are not subject to thermal hysteresis unlike their Dayem bridges counterparts and could therefore be used in a wider range of temperature. However, the technique used traditionally – the “window technique” – does not allow the fabrication of reproducible structures smaller than a few micrometers. The typical current density through S-I-S junctions is also very small resulting in the need of large junctions which affects the device performance. The electrical hysteresis arising because of their typically high capacitance and resistance has to be addressed as well. By using a technique

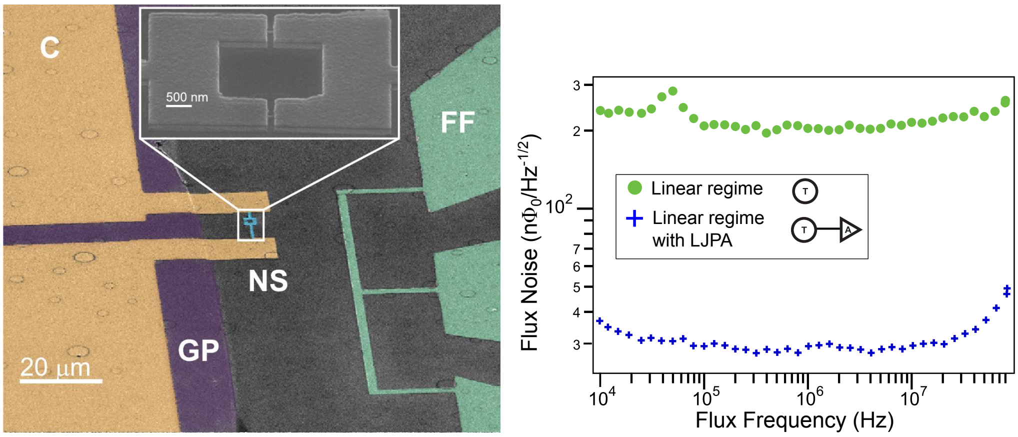

(a) (b)

Figure 2.10: (a) False-coloured SEM image of the device fabricated by Levenson-Falk *et al.* [90]. The nanoSQUID NS is shunted by the capacitor C sitting on a niobium ground plane GP. FF are flux lines used to calibrate the sensitivity of the device. (b) Effective flux noise spectrum of the device if the LJPA is bypassed (green dots) or not (blue +).

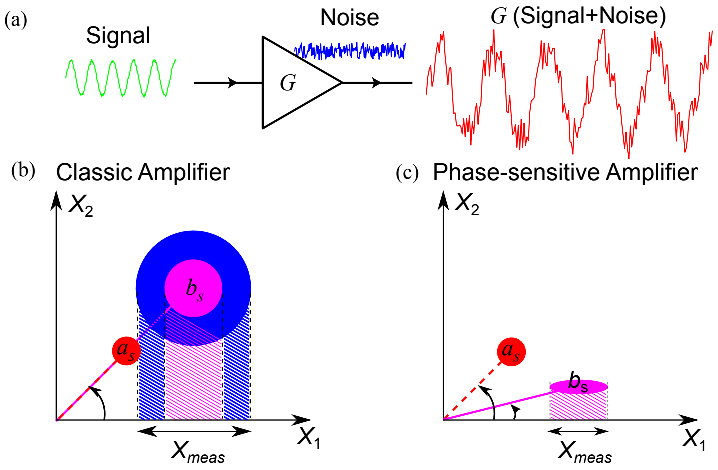

Figure 2.11: Schematic diagram showing the advantage of using a phase sensitive amplifier such as a LJPA. (a) and (b): For a quadratic signal $V(t) = 2V_0\left(X_1(t)\cos\omega_0 t + X_2(t)\sin\omega_0 t\right)$, an amplification of both components will always result in some additional noise, at best limited to the quantum limit. (c) However, amplifying one component while attenuating the other using a phase sensitive amplifier changes the phase φ but allows an ideally noise-free amplification of the measured signal. Adapted from Beltran [92].

making possible the fabrication of $0.6\,\mu\text{m} \times 0.6\,\mu\text{m}$ low capacitance junctions [93], Schmelz *et al.* were able to create the SQUID shown in Figure 2.12(a) that exhibited a flux-noise density of $0.5\,\mu\Phi_0/\sqrt{\text{Hz}}$ [94] in the white noise regime as shown in Figure 2.12(b). They speculated that a miniaturised SQUID of this kind with a loop area of $0.25\,\mu\text{m}^2$ would give a noise of $10\,\text{n}\Phi_0/\sqrt{\text{Hz}}$, in other words reaching a spin sensitivity of $1\,\text{spin}/\sqrt{\text{Hz}}$.

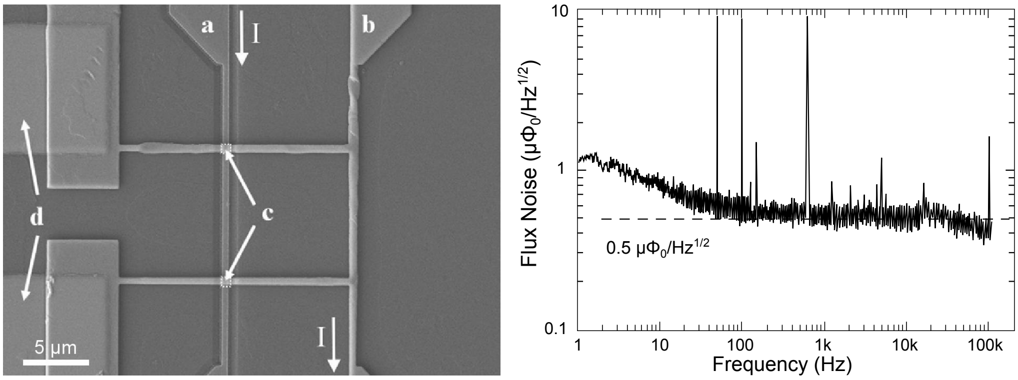

(a) (b)

Figure 2.12: (a) SEM micrograph of the SIS-based microSQUID fabricated by Schmelz *et al.* [94]. On the schematics “a” and “b” are contact pads, “c” are the two tunnel junctions and “d” is the shunting capacitor. (b) The flux noise spectrum measured at 4.2 K using a Series SQUID Array amplifier (SSA), which plateaus at $0.5\,\mu\Phi_0/\sqrt{\text{Hz}}$.

To avoid issues related to S-I-S junctions without sacrificing their advantages, Wölbing *et al.* [95] used S-N-S junctions made from a Nb (200 nm)/HfTi (24 nm)/Nb (160 nm) trilayer. The high current density, of the order of $10^5\,\text{A/cm}^2$, allowed the area of these junctions to be only $200\,\text{nm}\times200\,\text{nm}$ for a critical current of $200\,\mu\text{A}$ at 4.2 K. The SQUID effective area was $1.6\,\mu\text{m}^2$ and the flux noise spectrum they reported, measured with a commercial SQUID amplifier and reproduced in Figure 2.13b, indicated a white noise contribution of $0.2\,\mu\Phi_0/\sqrt{\text{Hz}}$ in the absence of magnetic field, resulting in an estimated spin sensitivity of $23\,\text{spins}/\sqrt{\text{Hz}}$. The noise was only mildly affected by magnetic fields up to 0.5 T in which case the white noise contribution was $0.7\,\mu\Phi_0/\sqrt{\text{Hz}}$.

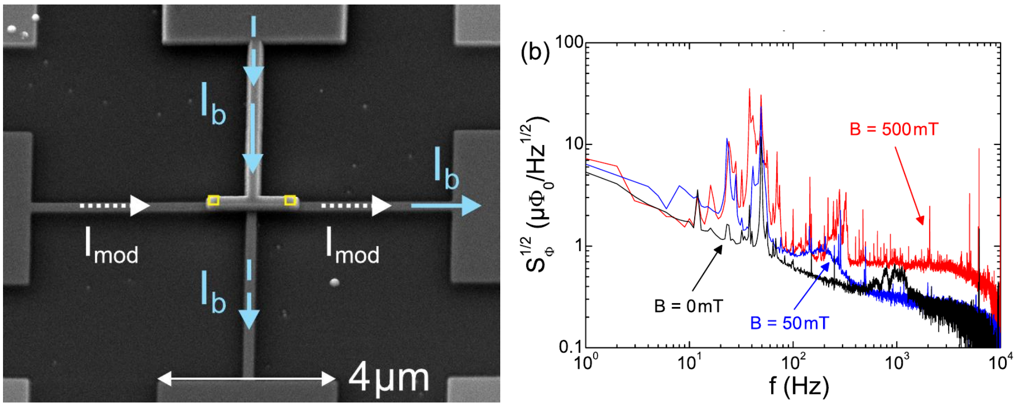

(a) (b)

Figure 2.13: (a) SEM image of the SIS-based microSQUID fabricated by Wölbing *et al.* [95]. (b) Flux noise spectrum at 4.2 K for the device in three applied magnetic fields: 0 T (black), 0.05 T (blue) and 0.5 T (red). The flux noise plateaus at $0.2\,\mu\Phi_0/\sqrt{\mathrm{Hz}}$ for 0 T and 0.05 T, and $0.7\,\mu\Phi_0/\sqrt{\mathrm{Hz}}$ for 0.5 T.

High-T_c SQUID In his publication, Schwarz *et al.* [96] pointed out that most measurements on interesting structures involved a parallel magnetic field much higher than the critical field for niobium or aluminium devices even with a near-perfect angle adjustment. That led them to use Pulsed Laser Deposition (PLD) epitaxially-grown yttrium barium copper oxide ($YBa_2Cu_3O_{7-x}$), a high-T_c superconductor, to fabricate the device shown in Figure 2.14(a). After depositing a gold layer as shunt and protective layer, they patterned the devices by FIB to get 300 nm × 100 nm nanobridges. They reported a noise performance (shown in Figure 2.14(b)) down to $2.3\,\mu\Phi_0/\sqrt{\mathrm{Hz}}$ even in high parallel magnetic fields up to 1 T. They claimed this could be easily optimised up to 3 T with a better amplifier.

2.4 Overview of Other Magnetometry Devices

Several other systems exhibit extreme sensitivity to magnetic fields and might represent a valid alternative to SQUIDs.

2.4.1 Superconducting Cylinders and Rings

The flux going through a superconducting ring is quantised in units of Φ_0 because of the global phase coherence of the Cooper pairs. This leads to what is known as the Little-Parks effect [97]: the half-integer quantum flux periodicity of

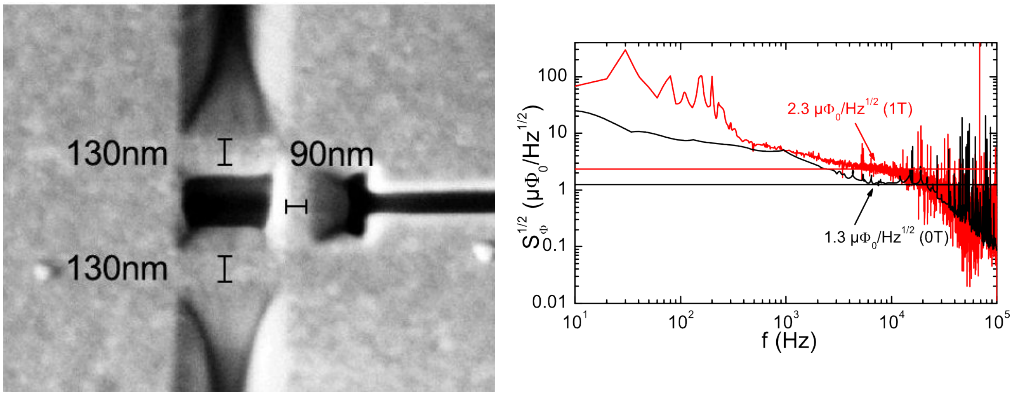

(a) (b)

Figure 2.14: (a) SEM micrograph of the device fabricated by Schwarz *et al.* [96]. (b) Flux noise spectrum at 4.2 K for two different applied magnetic fields: 0 T in black, 1 T in red at the optimum bias currents (respectively 33 µA and 31 µA). It plateaus at $1.3\,\mu\Phi_0/\sqrt{\mathrm{Hz}}$ for 0 T and $2.3\,\mu\Phi_0/\sqrt{\mathrm{Hz}}$ for 1 T.

the critical temperature of a superconducting ring/cylinder. For ultrasmall loops, de Gennes predicted that the variation of T_c will be so large that superconductivity itself would be destroyed at any temperature for $\Phi = \Phi_0/2+n$. Work on this subject includes the contribution of Staley and Liu [98] presented below in Figure 2.15(a). Although this was never used for an actual magnetic measurement, this effect could permit very precise magnetic characterisations in future. Assuming an increase of $50\,\Omega$ over $0.25\,\Phi_0$ with a measurement current of 100 nA as estimated from their publication, we can calculate that the voltage response would be about $20\,\mu\mathrm{V}/\Phi_0$ which would translate into a flux sensitivity at 50 mK equal to $1.6\,\mu\Phi_0/\sqrt{\mathrm{Hz}}$ and an estimated spin sensitivity of about $35\,\mathrm{spins}/\sqrt{\mathrm{Hz}}$ considering the radius ~ 50 nm of the loop. An alternative method to create nano-rings with extremely small radius is described by Sternfeld *et al.* [99] whose device, shown in Figure 2.15(c), is obtained by coating a nanowire with superconducting material. They report $R(\Phi)$ characteristics (Figure 2.15(d)) quite similar to those of Staley and Liu (Figure 2.15b).

A limit to this type of device is that the diameter d of the ring must be larger than the coherence length $\xi(0)$ of the material. Another issue is the very small

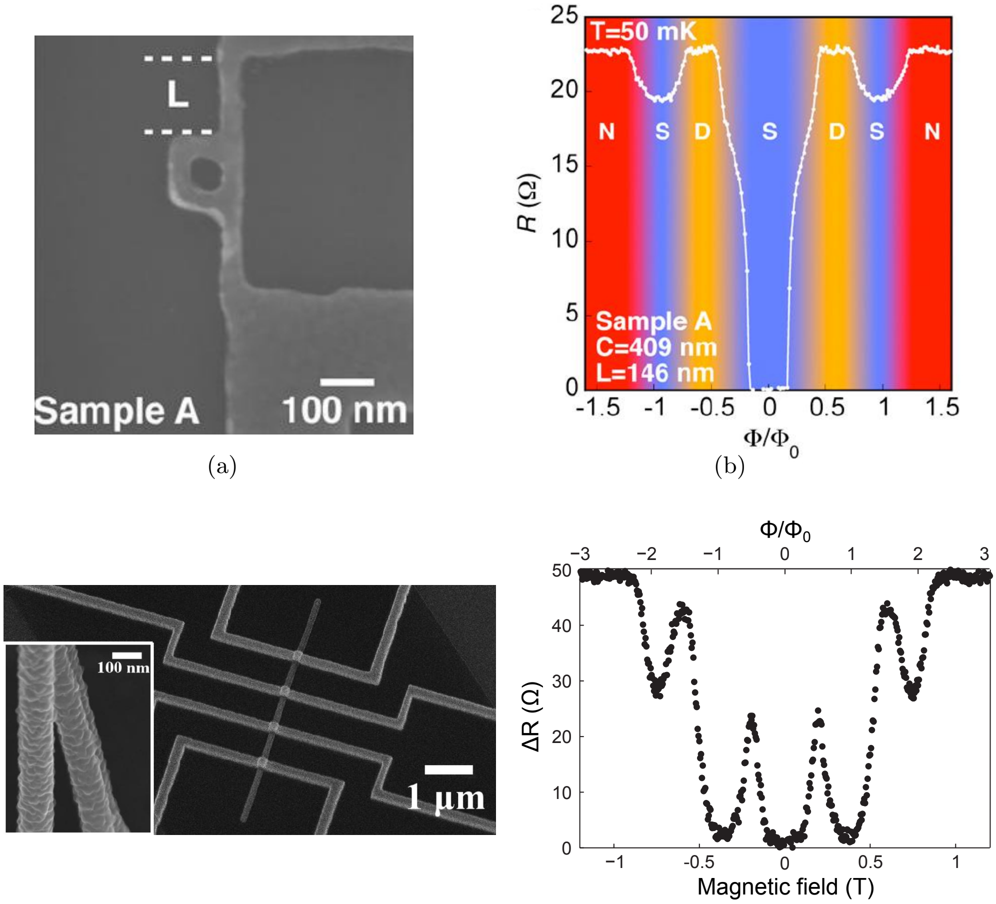

(a) (b)

(c) (d)

Figure 2.15: (a) SEM micrograph of a integrated superconducting loop created by Stanley and Liu [98]. (b) The typical $R(\Phi)$ they report with a measurement current of 100 nA at a temperature of 50 mK. (c) SEM micrograph of the superconducting cylinder made by coating a nanowire by Sternfeld *et al.* [99] with its ohmic contacts. The inset gives a detailed view of the coated nanowire. (d) Residual resistance of a typical sample of Sternfeld *et al.* as a function of magnetic field (bottom axis) and flux (top axis) at 70 mK for a measurement current of 100 nA.

range of magnetic flux for which the device has a linear response.

2.4.2 Josephson Junctions

As we saw in Section 1.2.4, a magnetic field applied perpendicularly to the junction modulates I_c following the Fraunhofer pattern given by Equation 1.32. The $I_\mathrm{c}(B)$ bahaviour is similar to that of a SQUID having the same effective area. A major restriction however is that the modulation depth quickly decreases as Φ increases, limiting the range of operation of the device. This technique has been successfully used for scanning SQUID microscopy [100, 101]. Current research is mainly focusing on the $1/f$ noise of Josephson junctions as read-out for qubits.

2.4.3 Non-Superconducting Devices

There exists alternative devices extremely sensitive to magnetic field that rely on a different branch of physics than superconductivity. For instance, Taylor *et al.* reported a sensitivity of $3\,\mathrm{fT}/\sqrt{\mathrm{Hz}}$ with a $(3\,\mathrm{mm})^2 \times 1\,\mathrm{mm}$ crystal using isolated spins in solids [102]. Spin-Exchange Relaxation-Free (SERF) atomic magnetometers are also known to have ultrahigh magnetic field resolution. The best performance to date was achieved by Kominis *et al.* [103] with a magnetic field sensitivity of $0.54\,\mathrm{fT}/\sqrt{\mathrm{Hz}}$ for a volume of $0.3\,\mathrm{cm}^3$. However, the size of these two types of magnetic sensors do not allow an easy coupling with magnetic samples.

A scanning microscope relying on a Bose-Einstein spinor was demonstrated by Vengalattore *et al.* [104] to have a sensitivity of $0.9\,\mathrm{pT}/\sqrt{\mathrm{Hz}}$ over a $120\,\mu\mathrm{m}^2$ area, corresponding to a flux noise of $0.05\,\mu\Phi_0/\sqrt{\mathrm{Hz}}$ and an estimated spin sensitivity of $109\,\mathrm{spins}/\sqrt{\mathrm{Hz}}$. However, they still lack the flexibility of SQUIDs as they are currently limited to $60\,\mathrm{pT}$. For instance, magnetic measurements of a cobalt particle were performed with a spinor device by Maser *et al.* [105]. The radius of the particle was $2\,\mu\mathrm{m}$ with an estimated limit for detection of $0.17\,\mu\mathrm{m}^3$. This result can be compared with a similar experiment using a nanoSQUID [86] where Jamet *et al.* were able to measure the magnetisation of a $3\,\mathrm{nm}$ nanoparticle.

Group	Year	Technique	Area (μm^2)	$T_{op}(K)$	Material	Φ_{ns} ($\mu\Phi_0/\sqrt{Hz}$)	S_{spin} ($\mu_B/\sqrt{Hz}$)
Lam *et al.* [2]	2002	EBL	0.04	4.2	Nb	7	250
Cleuziou *et al.* [7]	2006	CNT SQUID	0.3	0.04	CNT / Al	10	2
Hao *et al.* [10]	2008	FIB	0.3 (eff)	6.8	Nb	0.2	20
Granata *et al.* [9]	2009	EBL	0.025	4.2	Nb	1.5	20-60
Schwarz *et al.* [96]	2012	FIB	0.04	4.2	YBCO	1.5	62
Tettamanzi *et al.* [11]	2009	FIB	0.08 (eff)	6.8	Nb	2.6	~ 75
Wernsdorfer *et al.* [66]	2009	EBL	1	4.2	Nb	300	1000
Finkler *et al.* [88]	2010	SQUID on tip	0.034	4.2	Al	1.8	33-65
Lam *et al.* [84]	2011	EBL	0.04	5	Nb	5	70
Russo *et al.* [87]	2012	EBL	1	4.2	Nb	160	500
Schmelz *et al.* [94]	2012	S-I-S junctions	120	4.2	Nb/AlOx/Nb	0.5	55
Levenson-Falk *et al.* [90]	2013	Dispersive SQUID	15	0.025	Al	0.03	< 1
Vasyukov *et al.* [89]	2013	SQUID on tip	0.045 (eff)	4.2	Pb	0.05	0.38
Wolbing *et al.* [95]	2013	S-N-S junctions	$\sim$2	4.2	Nb/HfTi/Nb	0.25	23

Table 2.1: Review of the most advanced reported nanoSQUIDs.

Conclusion

The recent years have seen the development of many interesting ideas, summarised in Table 2.1, to stretch the limits of nanoSQUIDs in terms of flux noise and expected spin sensitivity, mainly by reducing the effective area of the device. Even though trilayer junctions, which have been generally avoided for some time due to their low current density and complexity are slowly being developed again as technology matures, most of the current effort to reduce the loop dimensions involves the use of nanobridges as Josephson elements. The majority of them are based on niobium and could not be operated in a standard way by current-biasing in the millikelvin range due to hysteretic I-V characteristics. Alternative methods of measurements with this type of SQUID such as flux-to-I_c transducer, imply a sacrifice in terms of simplicity, bandwidth and sensitivity.

More unconventional solutions have been reported and would provide near single-spin-flip sensitivity in the millikelvin range. However, they are all extremely complex and come with many limitations compared to conventional devices. The dispersive SQUID by Levenson-Falk *et al.* requires highly complex electronics and a large capacitor to create the resonator. The device by Schwarz *et al.* uses YBCO which is not an ideal superconductor for processing and can only be grown successfully on certain types of substrates. Scanning SQUID microscopy such as reported by Finkler *et al.* comes at the price of a lower coupling. There is therefore still the need for a SQUID that can be operated with standard electronics in the millikelvin range but this would involve solving the issue of the hysteresis that plagues all nanobridge-based SQUIDs at these temperatures. This is the subject of the rest of this thesis.

Chapter 3

Apparatus and Methods

NanoSQUIDs operating at millikelvin temperatures are highly sensitive yet fragile devices that require a carefully controlled fabrication and measurement process to ensure their correct operation and reproducibility. This requires many fabrication steps and technical choices to be made. The first part of this chapter describes the different patterning techniques that can be used. This includes standard lithography, used for coarse features such as tracks and contact pads, and a review of two ultrahigh resolution techniques: Focussed Ion Beam (FIB) lithography and Electron Beam Lithography (EBL). In this project, we chose to fabricate our nanoSQUIDs using EBL and lift-off using the e-beam resist Poly(MethylMethAcrylate) (PMMA). We will explain the reasons that led to this choice including a short review of the other resists available, a comparison of lift-off and etching, and a description of how we optimised our process to achieve ultrahigh resolution. From this analysis, we determined the general design for the devices by considering both the physics and the technical constraints. This discussion forms the second part of this chapter. Finally, we outline the set-up for our measurements down to 60 mK using an Adiabatic Demagnetisation Refrigerator (ADR) at NPL and the different aspects that need to be considered to reduce the system noise.

3.1 Chip Preparation

Ideally the nanoSQUIDs should be easily deposited on any system of interest. For prototyping, we used oxidised silicon substrates as they are quite similar to many substrates of interest, e.g. perovskites or topological insulators, in terms of chemical resistance and surface flatness whilst being inexpensive. We used single-side polished silicon wafers supplied by Compart Technology Ltd[1] which were thermally oxidised in an HighTech furnace at 1100 °C for eleven hours leading to the formation of a 200 nm thick layer of SiO_2. We then patterned and deposited macroscopic contact pads, tracks and alignment markers on the substrate using optical photolithography. This provides a template on which thinner, more precise structures can be added, saving a lot of process time and bridging the gap between nanodevices and the macroscopic world. The pattern of the chip is shown in Figure 3.1. All fabrication processes were realised in the class 100 cleanroom at the London Centre for Nanotechnology. The standard lift-off technique encompasses

---

[1] now part of PI-KEM Ltd., Tamworth, U.K.

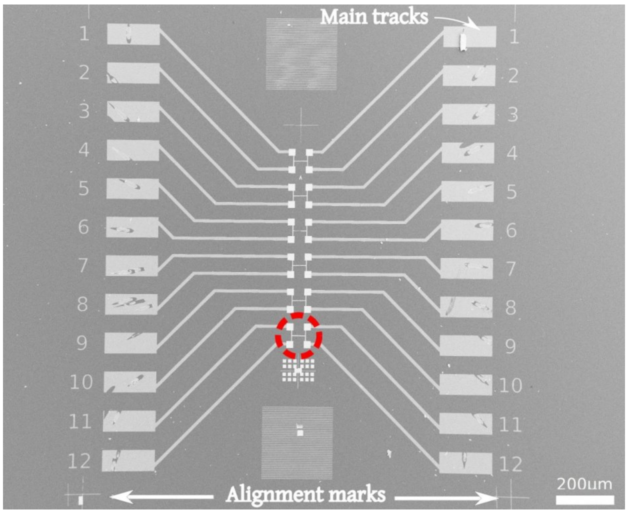

Figure 3.1: SEM micrograph of the sample chip. The patterns are created by standard lithography and lift-off of a sputtered niobium/gold bilayer or an electron-beam evaporated titanium/gold bilayer. 24 main tracks provide the link between a nanoscale device and microscale bonding. Alignment marks are used to calibrate the subsequent Electron Beam Lithography (EBL) step. Circled in red is a device region with its EBL patterned structures (not visible).

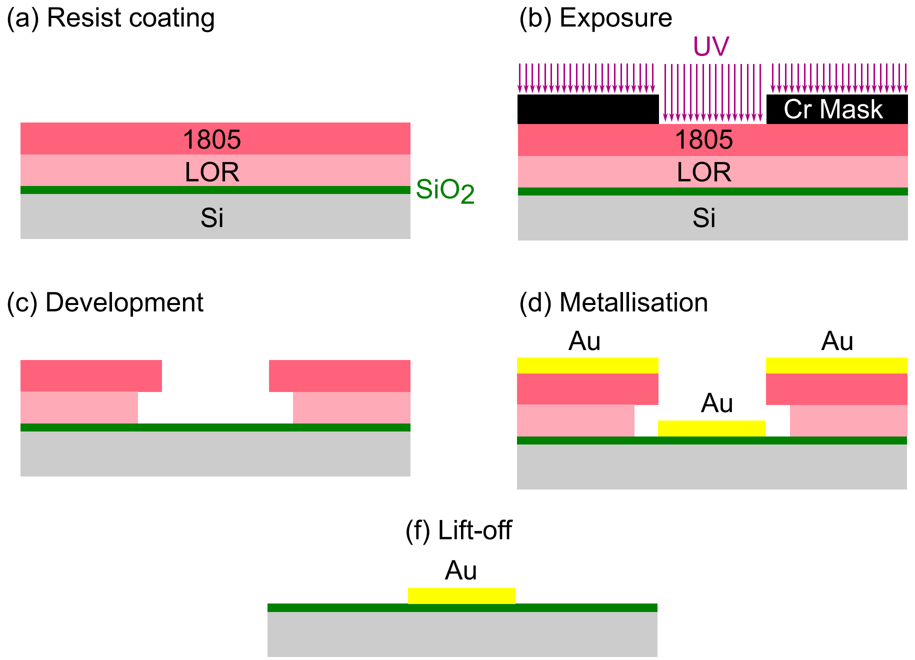

Figure 3.2: Not-to-scale schematics showing the different steps of the fabrication of the large scale features on a chip using UV patterning and lift-off.

several steps that are schematised in Figure 3.2 and described in greater detail below.

Step 1: Cleaning & Resist coating The wafer is cleaned in a sonicated bath of acetone to remove any organic trace, then rinsed with isopropanol and subsequently de-ionised water. The wafer is then left to dry on a hot plate before being treated in an oxygen-plasma for three minutes. This removes any remaining impurities or moisture and promotes the adhesion of the photoresist to the sample. Lift-Off Resist (LOR) 3A from MicroTech[2] is spun on the wafer at 3000 revolutions per minute (RPM), giving a 500 nm thick layer which is hard-baked at 180°C for 5 minutes. The LOR is a pre-exposed resist that is used to provide an undercut profile below another layer of resist in order to facilitate the lift-off. The positive photoresist 1805 from Microtech is then spun on top at 3000 RPM for 45 s and baked at 115°C for one minute. This gives a 2 μm thick layer of 1805 resist that allows lateral resolution during exposure of 2 μm.

---

[2] MT Systems Inc., California

Step 2: Exposure The coated resist is then exposed with ultraviolet light through a chromium mask manufactured by JD Photo[3]. It is exposed for three seconds using a Quintel Q4000-6 Mask Aligner which has an exposure power of 10 mW/cm^2. The energy dose required is specific to the resist and depends on its composition, viscosity and light absorbance. The UV light breaks chemical bonds in the resist molecules making them soluble in developer. In our case, the 1805 resist is positive, i.e. the exposed area will be cleared, and the dose it requires is 30 mJ/cm^2, hence the 3 s of exposure with the Quintel mask aligner.

Step 3: Development The wafer is then dipped in MF-26, a TMAH-based (tetramethylammonium hydroxide) developer. After 75 s of mild agitation, the exposed areas are removed and there is an appreciable undercut as the LOR has a higher etching rate by the developer than the 1805. Even though most metals and substrates are compatible with TMAH, it should be noted that this is not the case for aluminium.

Step 4: Metallisation Depending on the materials desired for the tracks, a titanium/gold bilayer is then deposited using an Edwards-500 electron-beam evaporator or a niobium/gold bilayer is sputtered using a SVS 600 sputter machine, described in Section 3.5. Titanium is used as a non-magnetic adhesion layer (approximately 1 nm thick) and gold provides a stable, highly conductive layer. For a 300 nm layer, the resistance of the tracks was approximately 6 Ω at 100 mK. For measurements with the Series SQUID Array amplifier (SSA), described later, it was desirable to reduce to a minimum the track resistance and so superconducting niobium was used. A layer of gold was still deposited in this case to provide a protective layer with a better thermal conductivity and improved bondability.

Step 5: Lift-off The chip is then left to soak in acetone heated to 40°C for at least 15 minutes. The resist is dissolved and the overlying metal layer is therefore removed. 20 seconds of sonication gently remove the remaining resist and overlying

---

[3] JD Photo-Tools, Oldham, UK

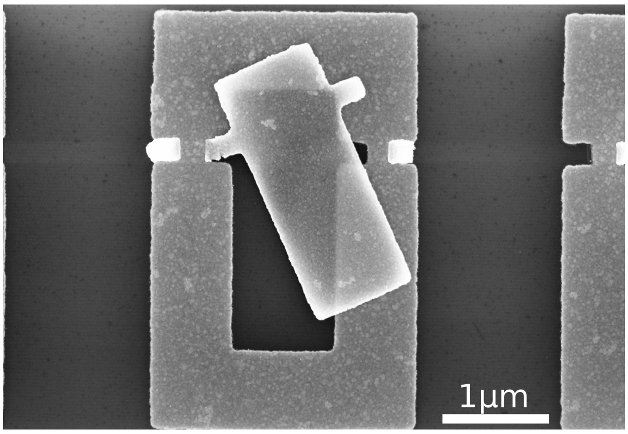

Figure 3.3: SEM micrograph of a partially lifted-off feature of a dummy SQUID, made of 150 nm thick Ti film. It was obtained by imaging after a gentle agitation by hand instead of sonication.

film as shown in Figure 3.3. The wafer is then diced to 10 mm × 10 mm samples using an automatic DAD3230 dicing saw.

3.2 Nanolithography: Overview of the Different Techniques

In order to pattern the SQUIDs with nanobridges as thin and narrow as possible, we cannot use standard lithography as the smallest feature size is limited by the wavelength used (365 nm for UV). A better resolution requires higher incident energy. Apart from extreme UV lithography and nanoimprint lithography which are very complex to implement and more suitable for mass production, there are only two options to pattern features down to the nanometre scale: Focussed Ion Beam (FIB) lithography and Electron Beam Lithography (EBL).

3.2.1 Focussed-Ion Beam Lithography

FIB is a very versatile tool combining an SEM and a gallium ion source. The ions are energetic enough – typically 10 keV – to mill metal films with an excellent resolution of approximately 40 nm. They can also be used to crack molecules thus enabling *in situ* deposition of metals suspended in a volatile carbonised form. The main drawback of this technique is that ions are scattered inside the substrate and can contaminate the underlying structure, or create defects in the film over a great length, up to 50 nm [106]. This is larger than the diameter of the standard nanobridge used in the present work and therefore FIB does not seem to be suitable. Recently introduced neon or helium-ion FIBs are not subject to this limitation and in future may be the tool of choice. Unfortunately, they were not available when we carried out the present project. We will discuss their potential application in Chapter 7 of this thesis.

3.2.2 Electron Beam Lithography

This technique relies on a controlled beam of electrons to expose the resist. The range of incident energy available goes from a few hundred electronvolts to 100 keV. Generated by field electron emission, the beam goes through a series of electrostatic and magnetic lenses whose general set-up is shown in Figure 3.4. Among them, one set controls the aperture and therefore the current of the beam. A bigger aperture leads generally to better images and a better signal-to-noise ratio but comes at the cost of a smaller depth of focus, a lower patterning resolution and more damage to the sample. Another set of lenses blanks the beam to protect the sample from unwanted exposure during idle time or when the stage is moving. Finally, some demagnifying lenses and deflectors steer the beam precisely to the required position. The pattern has to be represented by a vector-based file, the industry standard being the GDSII format. The software first fragments the pattern into several areas, called write-fields, whose dimensions are set by the operator. The stage is fixed during exposure of a write-field and is then moved to the next one sequentially. The larger they are, the quicker the exposure, but the beam would have to be steered over greater distance which can result in aberrations. Typical write-field sizes are 40 µm for high resolution and 200 µm for regular work. The error in alignment between write-fields and stage repositioning is known as the stitching error. Each write-field is further fragmented into simple elements by the software converter that provides machine-readable instructions to scan the beam.

The patterning was achieved using a Raith 150$^{\mathrm{TWO}}$ Direct Write. It features an

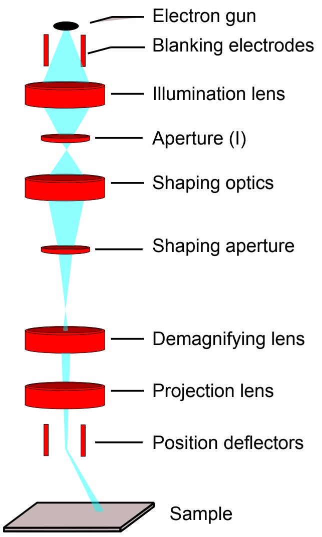

Figure 3.4: Schematic diagram of the different electronic lenses in an EBL machine. Figure adapted from Kasper *et al.* [107].

airlock for quick automatic loading/unloading, a precise laser-controlled stage with a stitching error guaranteed below 40 nm, and a 2 nm Gaussian beam which follows a vector-based routine.

3.2.3 Etching or Lift-off

As it is less damaging and contaminating than the FIB, EBL was the most suitable technique in order to make our nanobridges. Another crucial technical choice was to determine whether to use lift-off or etching. There has been much debate in the literature about which of these techniques is superior to the other. Both are based on diametrically opposed principles. In the etching process, the metal film is deposited first on the wafer and is then patterned by applying a protective mask – most often resist patterned by standard or e-beam lithography – followed by an etching of the unprotected area. The etching can be performed by immersion into a chemical solution, in which case it is referred to as a "wet etching" technique, as opposed to "dry etching" techniques. The latter includes plasma etching, where an etching gas mixture is turned into a plasma and pulsed toward the sample, and ion milling, described in Section 3.5, where ions are accelerated toward the sample and mill both the sacrificial layer of resist and the film at different rates.

The lift-off process relies on depositing the film on an already-patterned sacrificial layer of resist. After lift-off in solvent, only the film deposited on the substrate through the opening of the resist will adhere. The metal deposited on the resist will be removed at the same time as its underlying layer. The differences between these processes are schematised in Figure 3.5. Wet etching is not used for very fine patterning due to its isotropy which limits the resolution to the thickness of the film, and due to the difficulty in precisely controlling the etching rate. This technique is mostly used for the making of relatively large structures over large areas, such as patterning tracks on a wafer, where its selectivity, simplicity and fast etching rate give it an advantage. Plasma etching, though more anisotropic, interacts with the side-wall and is unable to provide sharp edges [108]. However, ion milling and lift-off have both demonstrated the ability to pattern sub-30 nm structures and there are strong arguments supporting the use of either one of these techniques for ultrahigh resolution.

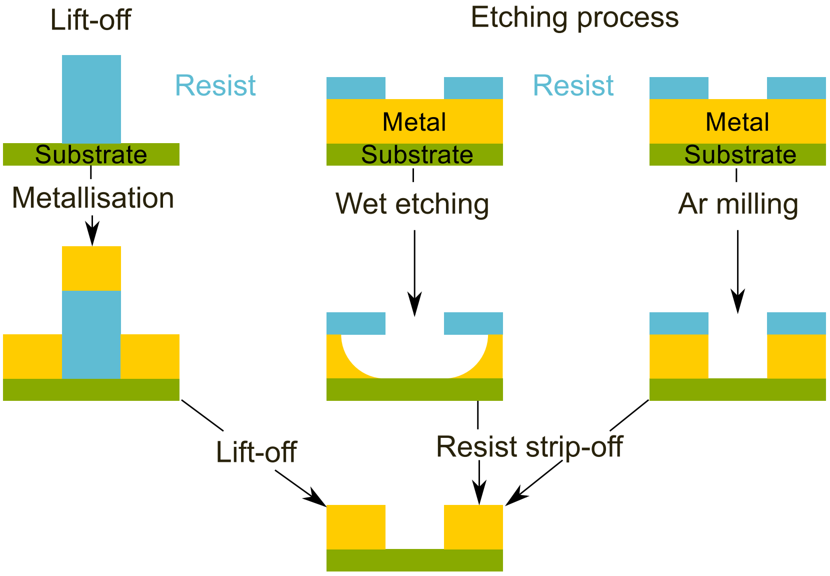

Figure 3.5: Schematic diagram presenting the lift-off process, the dry etching of a metal film, isotropic (plasma or wet etching) and anisotropic (ion milling).

The lift-off technique has two main advantages over the etching technique. The first one is its relative innocuity to the substrate as the resist is typically removed using only a mild solvent such as acetone. Such reprocessing proved invaluable for magnetic measurements as we will see in Chapter 6. It also permits the use of pre-existing large features that would be otherwise buried under the deposited metal, such as macroscopic tracks and pads made by faster UV lithography which saves a lot of machine time as electron-beam lithography tends to require a long exposure. The second advantage is the ability to use variable-angle deposition techniques [14]. However, having the resist already in place during the evaporation can be restrictive as heat can cause the resist to outgas, causing contamination [109, 110] or even destruction of the resist. Many materials, especially refractory metals such as niobium or molybdenum, typically require a very high evaporation temperature and/or a heated substrate for optimal performance. There are also reports that low-temperature metals could see their crystal structures affected when deposited in a narrow trench of the resist whereas a uniform film would show less stress [111, 112]. Ion milling uses a relatively small energy beam – about 500 eV – which limits the penetration of ions to only a few nanometres [113]. Even though this is much smaller than the 50 nm reported for FIB techniques [106], this might not be negligible when dealing with 40 nm wide nanobridges.

Due to its higher flexibility, and the absence of pre-established methods to grow high-purity low-T_c films in the cleanroom, we believed that the lift-off process was more suitable for this project and we exclusively focussed our research on this technique.

3.3 Optimisation of the EBL process towards nanoSQUID patterning

3.3.1 Electron-Beam Resist

Whilst the size of the beam may suggest sub-5 nm features can be easily achieved, the main factor limiting the resolution of e-beam lithography is in fact the resist. There is a wide range of e-beam resist available: organic or inorganic, chemically-amplified or not, each having distinct properties and uses. The criteria to consider when choosing a resist are listed in the following.

Tone A resist is said to have a positive tone if an exposed area is cleared by the developer and negative if only exposed areas stay after development. Some resists can be positive in a certain range of doses and negative in another. That is the case for PMMA as two reactions compete in the resist: the scission of long molecular chains into smaller units that become soluble in solvents such as isopropanol and Methyl Isobutyl Ketone (MIBK); and the molecules cross-linking, making PMMA less and less soluble. At lower doses, the former is dominant and the PMMA is a positive-tone resist but at higher doses (typically ten times higher) it turns into a negative resist [114]. In the following, we only consider positive-tone PMMA.

Contrast This is defined by $1/\log_{10}(D_2/D_1)$ where D_1 is the maximum dose applicable to the resist that does not affect it at all and D_2 the minimum dose that would clear entirely the resist, shown in Figure 3.6. Ideally, D_1 and D_2 should be equal to get the sharpest features. The contrast is also affected by the nature of the developer used and its temperature.

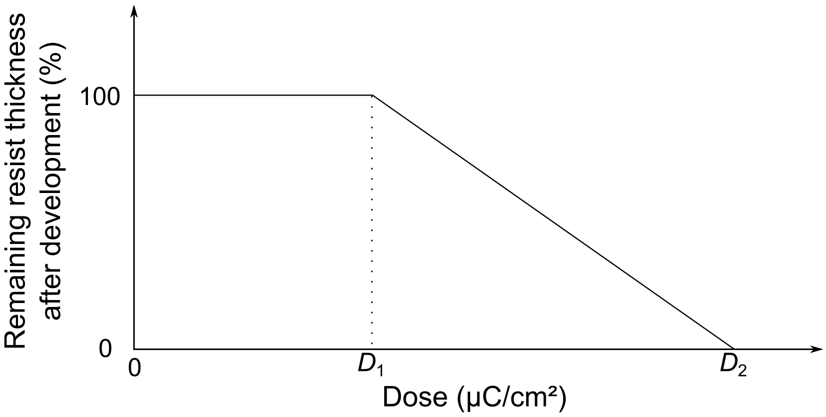

Figure 3.6: Remaining thickness of resist after development as a function of the applied dose. The doses D_1 and D_2 are used for the definition of the contrast of a resist. Adapted from Grigorescu *et al.* [115].

Sensitivity The sensitivity (D_2 in the above) is another important factor as ultrafine features require a small beam current (a few pA) which can lead to unrealistically long exposure time. Ideally, an e-beam resist should have both a high contrast and a high sensitivity but in practice they are conflicting parameters. For instance some resists are chemically-amplified and are several orders of magnitude more sensitive than conventional resists but at the cost of a reduced contrast and linewidth as the chemical reactant can migrate. The sensitivity is a function of the beam energy. For instance, it varies linearly for PMMA from $100\,\mu\mathrm{C/cm^2}$ at $10\,\mathrm{kV}$ to $300\,\mu\mathrm{C/cm^2}$ at $30\,\mathrm{kV}$.

Resolution and Minimum Linewidth These are respectively the minimum pitch achievable between two lines and the narrowest line achievable. If both are an indication of the quality of the process, their origins are different: forward scattering of the electrons is the main factor affecting the linewidth while backward scattering – electrons bouncing back from the substrate – affects the resolution.

Edge Roughness This depends on the size and the nature of the molecule of the resist. Short molecules give better results as these reduce the occurrence of clusters and inhomogeneities.

Etch & Thermal resistance Organic resists tend to be more sensitive to attacks by strong acids, argon milling or exposure to heat than their inorganic counterparts. Table 3.1 summarises the properties of the main resists available for ultrahigh-resolution patterning.

With our use of prepatterned chips carrying the broader features, the overall area we need to expose is fairly small. At a dose of $300\,\mu\mathrm{C/cm^2}$, exposing the area of four SQUIDs with their contacts takes approximately one hour and a half. We do not need highly sensitive resist but very low sensitivity resists such as polystyrene would require too much machine time and cannot be used. As we chose to use lift-off, a positive tone resist is more convenient as we only have to expose the area we want to clear. Poly(MethylMethAcrylate) (PMMA) is therefore the resist of choice as it is positive and can achieve sub-10 nm features whilst being inexpensive, safe to process and very versatile.

Resist	Tone	Contrast	Sensitivity ($\mu C/cm^2$)	Line width	Etch Resistance	Notes
ZEP-520[1]	+	2.7	10 [116]	30 nm [117]	Medium	Stable, inexpensive
PMMA	+	4.2 [118]	300	$<$ 10 nm [119]	Low	Stable, inexpensive
Polystyrene	-	4.4	4000	15 nm	High	
SU-8[2]	-	0.99	0.5	30 nm	High	Hard to strip
HSQ	-	7 [120]	210 [121]	7 nm [115]	Very high	Unstable

Table 3.1: Overview of the properties for the most common EBL resists available. The contrast is given at room temperature for the usual developer of the resist[3] and the sensitivity corresponds to a beam of 30 kV. The linewidth is a typical value found in the literature for standard films (better values can be achieved by having 2–3 nm of metal with 10 nm thick resist but that is not relevant to our work.).

[1] Manufactured by Nippon Zeon Co.

[2] Manufactured by MicroChem Corp., Newton, MA

[3] n-Amyl acetate for ZEP-520, MIBK:IPA for PMMA, xylene for polysterene, 1-Methoxy-2-propyl acetate for SU-8, TmAH for HSQ.

3.3.2 Initial Experimental Study of PMMA

In a preliminary stage, we concentrated on optimising the lift-off process using PMMA patterned by EBL in order to determine the best linewidth realistically achievable for our films. Most papers focussing on trying to get the best linewidth/resolution are using a very thin layer of PMMA ($<$ 10 nm) to lift-off a few nanometres of metal as a proof of concept. To manufacture actual devices, we require at least 200 nm of PMMA which changes some aspects of the processing. For instance, sonication in developer has been reported to improve the resolution [119] but is not suitable for our application because the fluid would exert too much drag on a thick but narrow slab of PMMA – e.g. a nanobridge – and would tear it apart. Instead we used exclusively MIBK:IPA 1:3 at room temperature as a developer with gentle agitation by hand for 75 seconds.

Linewidth

The main factor affecting the linewidth is the incident energy of electrons. When electrons enter the resist, their interactions with its molecules lead to forward scattering which can be studied by Monte-Carlo simulations as shown in Figure 3.7a.

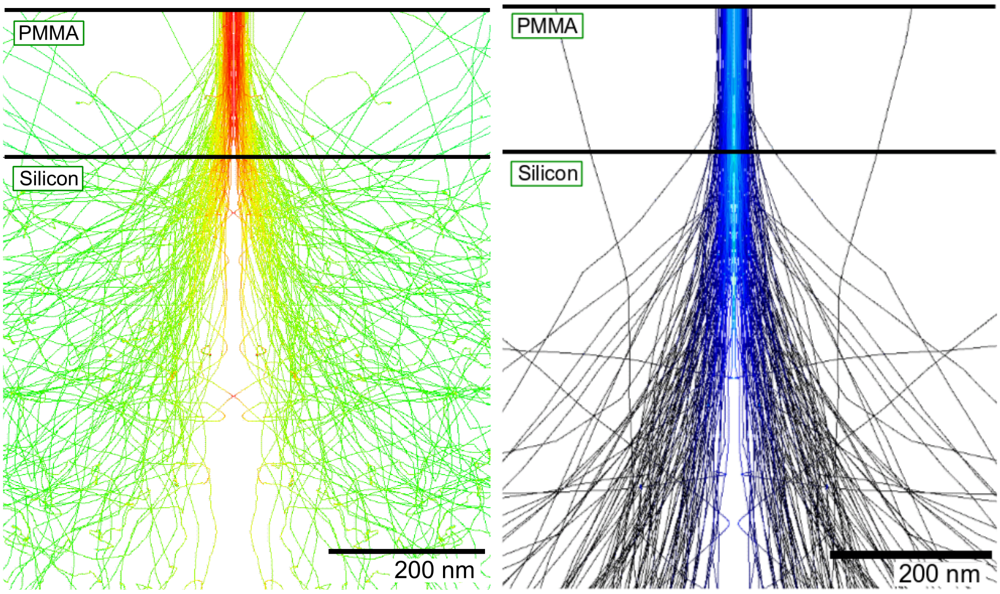

(a) 20 kV (b) 30 kV

Figure 3.7: Monte-Carlo simulations of the trajectories of electrons in a 200 nm thick PMMA layer using the Raith simulation software included with the EBL. The simulations are shown for one hundred electrons and for two different acceleration voltages (a) 20 kV and (b) 30 kV.

Though each interaction only deviates electrons by a small angle, they are very frequent which can lead to a wide diffraction angle, especially at lower beam voltages, and broaden the features. A higher beam energy results in less scattering and enables the patterning of thicker resist with finer features. However this can potentially cause more damage to the substrate or lead to more backward scattering, electrons bouncing back on the substrate and exposing resist away from the features. Figure 3.8 shows the best linewidth we obtained with our equipment for two different beam voltages.

We obtained on average a diameter of 65 nm at 20 kV whereas we obtained 20 nm or better with 30 kV due to the reduced forward scattering. The PMMA layer used and the film we deposited were respectively 240 nm and 150 nm thick which gave the excellent aspect ratio (film thickness:feature width) of 12:1.

A thinner resist results in less scattering but limits the thickness of the film that can be lifted-off, the rule of thumb being that it is possible to lift-off successfully about

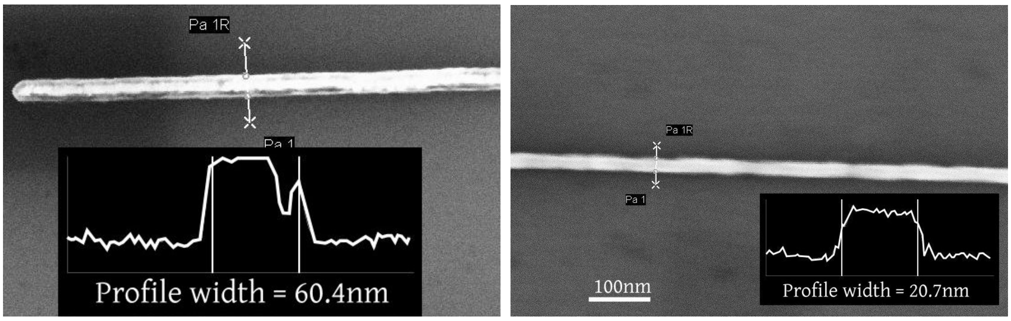

(a) 20 kV (b) 30 kV

Figure 3.8: SEM micrographs showing the typical linewidths we achieved with EBL lithography and lift-off using a 240 nm layer of PMMA 950k patterned with two different beam voltages: 20 kV (a) and 30 kV (b) at an aperture of 20 µm and a working distance of 5 mm. The lines were made of a 150 nm thick titanium film.

half the thickness of the resist. More material can result in side-walling (coating of the vertical part of the developed resist) that traps the resist. The thickness of the PMMA can be adjusted based on the nature of the solvent (anisole or chlorobenzene), its concentration and the rotation speed during coating. Unless otherwise specified, we used PMMA A4-950k from MicroTech spun at 3000 Revolutions Per Minute (RPM) and baked at 180°C for seven minutes which consistently gave a uniform 240 nm-thick layer. Other standard PMMA resists available were the A2-950k, which is A4 twice diluted in anisole and results in a 120 nm-thick layer when spun at 3000 RPM, and the A4-495k which is 240 nm thick as well but whose molecular weight is twice smaller. This makes it more sensitive which can be useful to create an undercut profile. Several layers can be very easily combined to achieve an overall thicker resist without noticeable adverse effects.

Dose Adjustment

To successfully pattern structures that are very close one to another, such as the banks of a 100 nm nanobridge, it is necessary to adjust the dose. If it is too low, some remaining resist can compromise the quality of the deposited metal; if too high the two structures would be merged together as the resist separating them would be sensitised as well. This is commonly referred to as the proximity effect (which has to be distinguished from the superconducting proximity effect described in Chapter 1). This dose adjustment is done by repeating a series of some identical test pattern with increasing doses and selecting the minimal dose yielding the optimal result. Possible test structures include dots, whole dummy devices (see Figure 3.9) and striped structures as shown in Figure 3.10. They can be deposited during the same exposure step as the working devices at an unobtrusive location on the chip. This ensures the settings are consistent and helps the debugging process, as well as optimising subsequent patterning of structures.

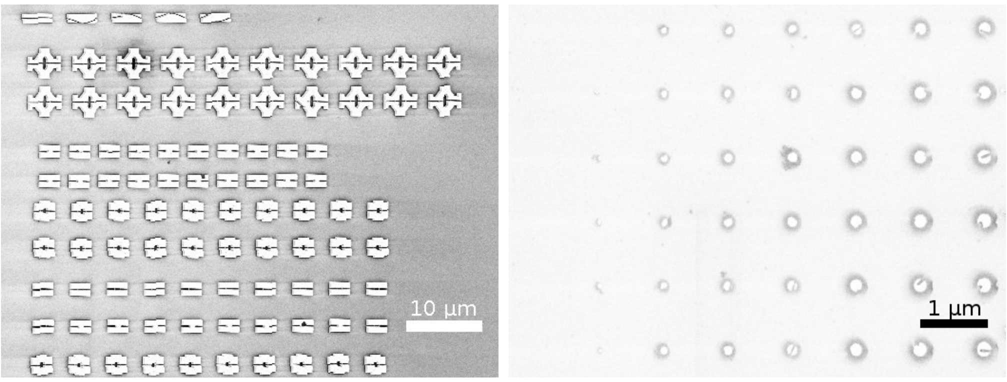

(a) (b)

Figure 3.9: SEM micrographs of test regions for typical geometries using a 240 nm layer of PMMA A4-950k patterned with a 30 kV beam and a 20 µm aperture at a working distance of 5 mm. The metal film is 150 nm of titanium. (a) Different geometries for SQUIDs with the dose increasing from left to right by 10 µC/cm^2, starting from 280 µC/cm^2. (b) Spots obtained for different doses increasing by 10 µC/cm^2 from left to right and top to bottom, starting at 250 µC/cm^2. It illustrates the broadening of the beam due to electron scattering.

3.4 NanoSQUIDs General Design

During the present work, the design of the nanoSQUIDs evolved by iterations to tackle issues and optimise the performance suggested by previous experiments. However, there were several general considerations that provided guidelines for the initial design of the devices.

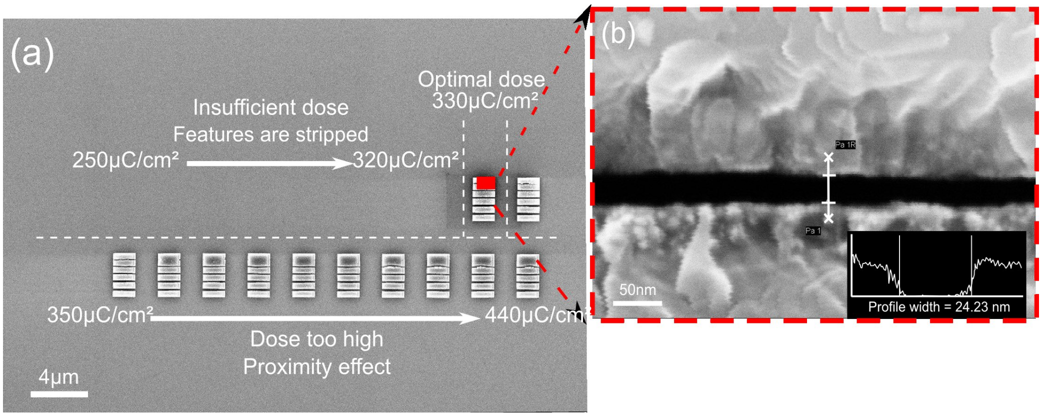

Figure 3.10: (a) SEM images of one of the separation tests that we realised by lift-off of a 150 nm thick titanium film, using an EBL patterned 240 nm-thick PMMA layer using a 30 kV beam and a 20 µm aperture. The dose increases from left to right in each row by 10 µC/cm^2. At the optimal dose of 330 µC/cm^2, we achieved separations between stripes ranging from 25 nm to 100 nm without compromising the film quality. Below this dose, the PMMA did not develop and the features could not be realised. Above this dose, the smallest gap is exposed by the proximity effect and the two rectangles are merged. The red region is shown at higher magnification in (b).

3.4.1 Dimensions of the Bridges

As mentioned in Chapter 1, if the length of the bridge L is short compared to the Ginzburg-Landau coherence length ξ_{GL} of the film, the current-phase relationship (CPR) of the SQUID is sinusoidal. As the ratio L/ξ_{GL} increases, the CPR becomes increasingly distorted until it becomes multivalued for a ratio of 3.5 [122]. At this point, the bridges can no longer be approximated as Josephson junctions and the device cannot work properly. As we saw in the first chapter, $\xi_{\mathrm{GL}}(T) \sim \sqrt{\xi_0 l/(1-T/T_{\mathrm{c}})}$ where ξ_0 is the BCS coherence length and l is the mean free path. As $\xi_0 = \hbar v_{\mathrm{F}}/k_{\mathrm{B}}T_{\mathrm{c}}$ where v_{F} is the Fermi velocity, we have for most metals $\xi_0 T_{\mathrm{c}} \approx 1.5\,\mu\mathrm{m\,K}$. Superconductors having their transition temperatures in the millikelvin range have a BCS coherence length of several micrometers. However, as we are considering thin films, the mean free path is likely to be of the order of the thickness of the film which is approximately 100 nm so we can expect $\xi_{\mathrm{GL}} \sim 200\,\mathrm{nm}$. We should therefore limit the length of the bridges to 700 nm.

3.4.2 Film thickness

As we saw, the inductance of the loop is an important factor that has to be minimised as it affects the sensitivity of nanoSQUIDs. The total inductance is the sum of a geometrical component related to the size of the loop and a kinetic component L_k due to the kinetic energy of the Cooper pairs. For a track of width w and thickness t, L_k is equal to $4\mu_0\lambda(T)^2/wt$ per unit length [154]. The thickness of the film should ideally be much larger than the penetration depth $\lambda(T)$ of the material to keep the kinetic inductance negligible. Unfortunately, a lower T_c is synonymous with an increased penetration depth that can be 0.8 µm for titanium. The thickness is therefore a compromise between the penetration depth and the limitations of the lift-off technique. If we consider the standard aspect ratio of 4:1 for e-beam structures [123], to have a reasonable 50 nm resolution over the bridge width we can only use a 200 nm-thick resist layer, limiting the thickness we can lift-off to less than 150 nm. Using the optimisation of the EBL patterning mentioned above, as we improved our process we gradually increased the aspect ratio up to 12:1 which enabled us to lift-off up to 450 nm. However, only the later devices in this thesis took advantage of this advanced process. These will be described in Chapter 5.

3.4.3 Loop Area

While theoretically a SQUID with smaller loop area has a better spin sensitivity, we chose to use bigger areas for practicality of measurements during the initial stage of the development. In order to see several $V(\Phi)$ modulations, we need to apply several Φ_0. The critical field of potential materials (titanium, aluminium) is of the order of 0.1 T and is reduced as T approaches T_c following roughly $B_\mathrm{c}(T) = B_\mathrm{c}(0)(1 - T/T_\mathrm{c})^2$. At $T/T_\mathrm{c} = 2/3$, B_c is therefore reduced by one order of magnitude and so to be able to measure up to about $10\,\Phi_0$, the SQUID area A must be bigger than $10 \times \Phi_0/B = 2.5\,\mu\mathrm{m}^2$. The geometrical inductance of the SQUID is a function of the loop perimeter, being very approximately 1 pH per 100 nm of the loop perimeter. Such an area would have a perimeter of about 6 μm contributing a geometric inductance of approximately 6 pH. This is likely to be much smaller than the kinetic inductance that can reach several hundred picohenrys. We will discuss ways to reduce this contribution in Chapter 5 but in practice we have fabricated devices with loop areas ranging from 1 to 10 μm^2.

3.4.4 Leads

In order to reduce the noise level, the sample can be cooled in a niobium shielding. As this prevents us from applying an external magnetic field with the sample magnet, we chose in some designs to use the inductance of part of the loop to couple some magnetic flux into the loop by passing a current through one side of the SQUID. In these devices there are two additional leads for this purpose as shown in Figure 3.11. To reduce the probability of superconductivity suppression that might arise at e.g. defects in long and thin superconducting connecting tracks [124], and to reduce the track resistance for coupling the SSA as we will discuss later, the current leads for I-V measurements were made broad, symmetric and straight whilst the voltage across the device was measured by narrower tracks that joined the current connections close to the device. Four terminal measurements were used for all the I-V curves. Figure 3.11 shows Device J-1 fabricated following all the general guidelines stated earlier.

3.5 Film Deposition

All metal evaporations took place in the cleanroom of the London Centre for Nanotechnology. Depending on the materials and their properties (e.g. evaporation temperature and reactivity), they were deposited by electron beam or thermal evaporation, or by sputtering.

3.5.1 Electron-beam Evaporation

For materials with a relatively low evaporation temperature such as aluminium, germanium, silver, gold and titanium, we used an Edwards A500 electron-beam evaporator with a base pressure of 10^{-7} mbar. Figure 3.12 shows a schematic

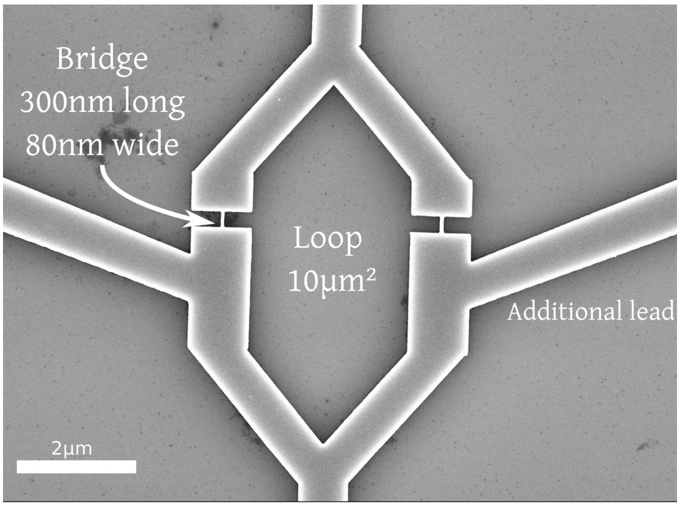

Figure 3.11: SEM micrograph of SQUID J-1, described in detail in Chapter 5, made of Ti(100 nm)/Au(22 nm). The loop area is 10 μm^2. This device is connected to the bonding pads using thick Nb(200 nm)/Au(200 nm) tracks (not visible).

drawing of the machine. The metal is kept in a crucible sitting tightly on a water-cooled copper carousel allowing us to change the source *in situ* among four different materials. The crucible has to be chosen according to the metal to be evaporated. The most common crucible is graphite, giving good results for most noble metals. Aluminium however has the tendency to creep along the walls and overflow. It is therefore recommended to use a boron-nitride crucible which can contain this metal more efficiently in the centre. Titanium forms a ball that does not adhere to copper and therefore does not require a crucible for high quality evaporation. An electron beam with an accelerating voltage of 10 kV and a current up to 600 mA is then steered onto the crucible and heats the metal by the Joule effect. With the sample shutter closed, we ramp up the beam current while monitoring the deposition rate with a crystal monitor (#1 on Figure 3.12) until we reach a stable reading of about 1 nm/s. This requires a current of approximately 50 mA for gold, aluminium and silver and 150 mA for titanium. We then open the shutter to start the deposition. This is monitored by a second crystal monitor (#2 on the schematic) which is closer to the sample and more accurate. Once the thickness is right, the shutter is closed again, the power ramped down and the sample left to cool to ambient temperature.

Evaporation at these power levels did not seem to affect the PMMA layer and the features were always sharp. However, when trying to evaporate niobium or molybdenum, whose evaporation temperatures are respectively 5017 K and 4912 K, we had to use the maximum beam power of 6 kW to get a rate of 0.2 nm/s. The PMMA could not withstand the heat and was obliterated.

3.5.2 Sputter Machine

Sputtering constitutes a common alternative to electron-beam evaporation as it enables the deposition of materials hard to evaporate otherwise such as refractory metals or complex alloys. We used a SVS 600[4] system to sputter niobium/gold bilayers and silicon nitride and a PVD-75[5] system for rf sputtering of molybdenum/copper.

---

[4] Manufactured by Scientific Vacuum Systems Ltd., Finchampstead, UK

[5] Manufactured by Kurt J. Lesker Company Ltd., Hastings, UK

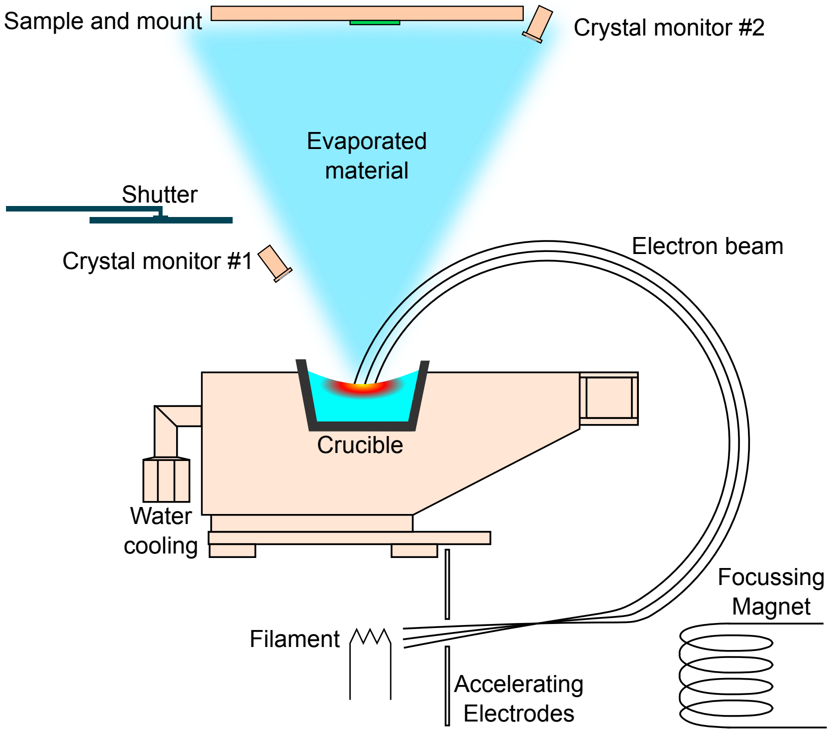

Figure 3.12: Schematic diagram depicting the Edwards A500 electron-beam evaporator that we used to evaporate non-refractory metals.

For conductive targets, we used dc sputtering as illustrated in Figure 3.13. Argon gas is introduced into the target compartment and is then ionised by thermionic emission. Positive ions are accelerated towards the target whose atoms are ejected upon impact and land on the substrate. The SVS-600 is fitted with magnetrons which magnetically contain the plasma close to the target, enabling higher yield and sustained operation at lower pressures.

RF sputtering is used for insulating targets or to operate with much lower argon pressure which can produce films of higher quality, e.g. for molybdenum [46]. In that case, the sign of the voltage between anode and cathode is changed at high frequencies to limit charge accumulation. Depending on its pressure, the background gas interacts with the ejected particles and tends to lead to a diffused, isotropic coating that is not compatible with the process we developed in Chapter 5. As this anisotropy also leads to broader features, sputtering was mostly used for the metallisation of wide tracks or a few devices based on Nb or Mo.

3.5.3 Ion Milling

To create a good contact between an already-existing film and a newly evaporated metal, it is desirable to remove the few nanometres of native oxide that have formed during its exposure to the atmosphere. In our process, it was especially useful to etch the oxide layer covering the small contacting tracks leading to the SQUIDs before depositing the material for the bigger tracks, thus enabling electrically transparent contacts. This was possible thanks to the presence of an argon miller in the chamber of the SVS 600 sputter machine. As shown in Figure 3.13, the sample mount can be rotated to face the argon miller without breaking the vacuum. Argon milling is a gentle highly anisotropic etching technique that relies on a non-focussed beam of neutral argon atoms to mill the film. The gas is introduced at the back on the discharge chamber where it is ionised by a hot cathode. The ions are accelerated towards the sample by the electric field generated by the acceleration grid, protected of the incoming ions by the screen grid. The accelerated ions finally pass through another electron-emitting grid,

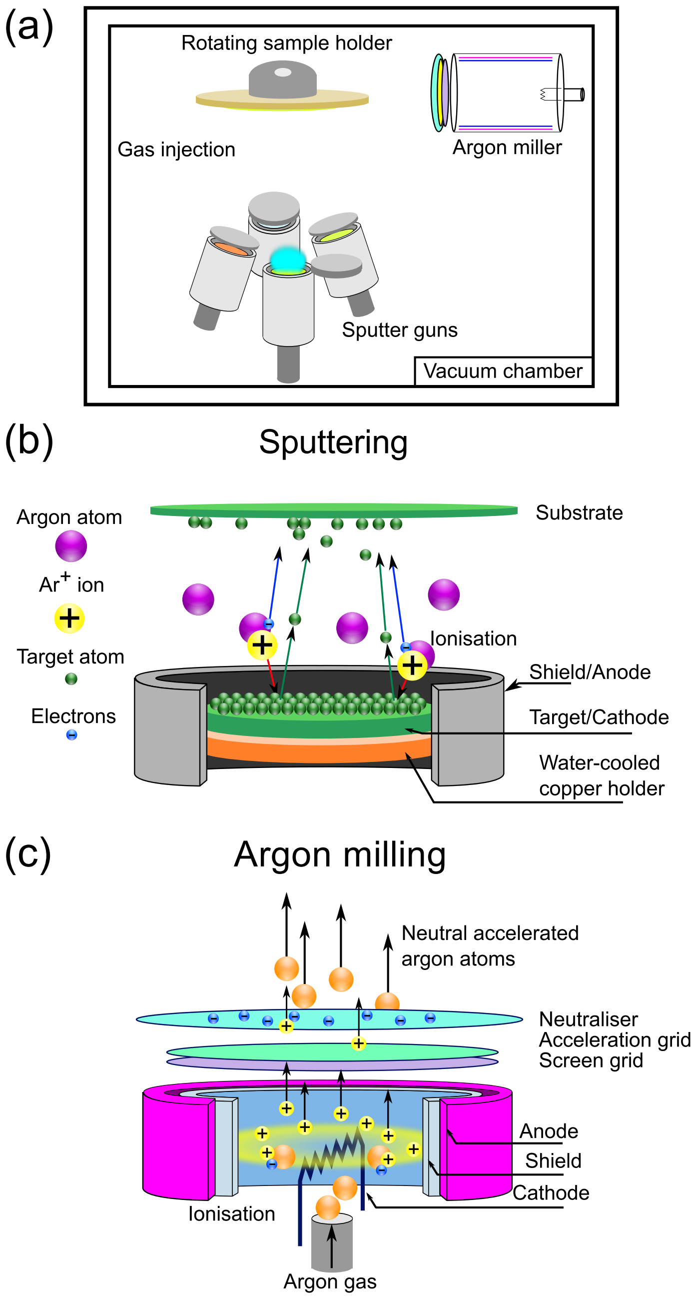

Figure 3.13: (a) Schematic diagram of the inside of the SVS 600 sputter machine combining four sputter guns with magnetrons in a high vacuum chamber. The machine includes an argon miller. The sample holder can rotate continuously on its axis to ensure uniform coating but can also rotate perpendicularly to face either the argon miller or the guns. (b) Schematic diagram illustrating the sputtering process, argon atoms are ionised by the hot cathode and Ar^+ ions are then accelerated towards the target and eject atoms that are deposited onto the sample. (c) Schematic diagram illustrating the creation of the accelerated Ar beam of the argon milling, relying on the ionisation and acceleration of ions followed by neutralisation with electrons to produce a neutral Ar beam.

called the neutraliser, to produce a neutral Ar beam.

3.6 Adiabatic Demagnetisation Refrigerator

All samples in this thesis were measured with the kind assistance and collaboration of Dr Sergiy Roshko using an Adiabatic Demagnetisation Refrigerator (ADR) manufactured by Cambridge Magnetic Refrigeration (CMR) and installed at the National Physical Laboratory (NPL), Teddington.

3.6.1 Principles of Adiabatic Demagnetisation

ADRs rely on the magnetocaloric effect that was discovered by Warburg in 1881 who noticed that iron temperature increases when exposed to a magnetic field [125]. Giauque [126] and Debye [127] demonstrated that these properties are due to the presence of magnetic ions that have a non-zero spin due to incomplete electronic shells in the crystalline structures. These atoms are in such a small proportion that the different interactions are not enough to order the spins, that are therefore randomly oriented. In 1933, Giauque built the first ADR using a gadolinium alloy and reached 250 mK [128]. Since then, many other paramagnetic materials have been discovered such as potassium chromate alum or ferric ammonium alum (FAA). ADRs are now a mature technology. Even though dilution refrigerators outperform them in many ways (e.g. continuous operation, magnetic noise), they are still used for their reliability, cost-efficiency and autonomy, especially for space applications. State-of-the-art ADRs have several magnetic pills with complementary cycles to operate continuously and to have a broader operating range of temperatures. Whatever their build and features, ADRs are based on the same cooling cycle. Without loss of generality, we can explain the operation of our ADR based on the entropy-temperature cycle of FAA shown in Figure 3.14.

(i) Transition from 1 to 2 The sample is magnetised at constant temperature. In our system, this is ensured by a 1 K pot continuously pumping liquid helium which keeps the temperature around 1.5 K. The magnetic field is ramped up slowly to 1.6 T, aligning the spins of the FAA, i.e. the paramagnetic salt used in the pill,

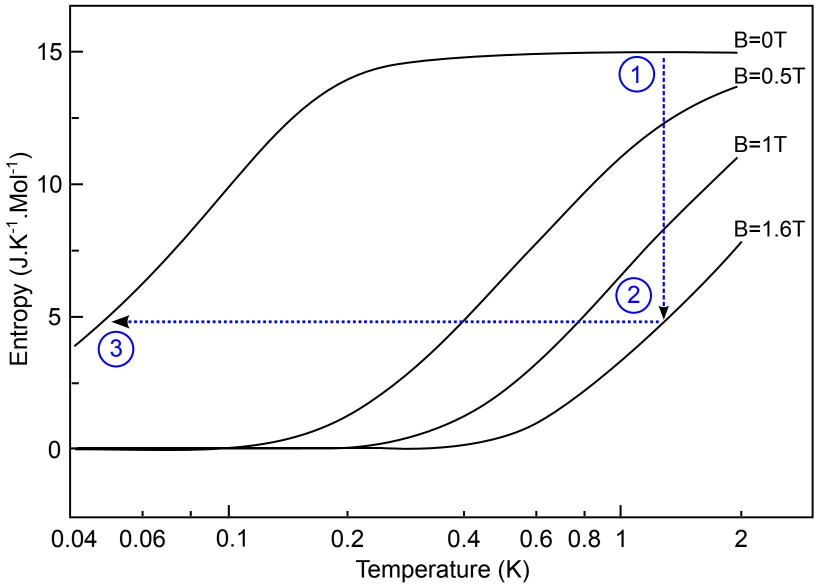

Figure 3.14: The entropy-temperature cycle of Ferric Ammonium Alum used by the ADR at NPL. The meaning of the numbers is given in the text below. Adapted from Wikus *et al.* [129].

which is the part of the system providing the cooling. The small component of the disorder due to lattice vibration S_{thermal} stays constant while the dominant part representing the spin disorder S_{spin} decreases as the spins become aligned, reducing the total entropy for the salt. This change in entropy removes some heat Q, that is transferred to the 1 K pot and the process is isothermal.

(ii) Transition from 2 to 3 Once the pill has been fully magnetised, the thermal link with the rest of the system is opened via an heat switch. The system $\{\text{sample} + \text{pill}\}$ is therefore completely isolated, i.e. adiabatic. The second law of thermodynamics states that in that case $\delta Q = T\mathrm{d}S = 0$. This implies that $\mathrm{d}S = 0$ and $S_{\text{spin}} = S_{\text{spin}}(B/T)$ is then constant along (2) to (3). If B changes, the temperature must change. By tuning the magnetisation of the pill, it is possible to precisely sit at a given temperature between (2) and (3). If the system was truly adiabatic, it could be possible to adjust the temperature via the magnetic field indefinitely. Due to heat leakage (vibrations, radiations, joule effect of the wires) the ADR cannot hold its base temperature infinitely and the pill has to undergo another magnetisation to restore its cooling power.

3.6.2 Experimental Set-up

The ADR we used is composed of two parts: a fibreglass insert, shown in Figure 3.16, including the sample and the pill, sitting in a Dewar filled with liquid helium. It contains two sets of superconducting magnets: one used for the pill magnetisation and the other as a sample magnet. It should be noted that the field generated to magnetise the pill is designed to be compensated by a third coil to prevent stray field from interfering with the sample. The insert is fitted with a custom-made pill that contains the FAA salt crystallised around a matrix of gold-plated copper wires to maximise the thermal link with the sample stage as described by Wilson *et al.* [130]. The pill is sealed using epoxy and is completely hermetic. To further limit the risk of corrosion and the dangerous build-up of gas in the pill, it has to be kept in a refrigerator when not in use. We designed and fabricated a chip holder and its thermal link to the pill in order to suit our requirements (see Figure 3.15). The chip holder is made of a Glass-APPE epoxy substrate, specifically designed for high-frequency applications, clad with 35 μm of high-purity electrodeposited copper. Compared to the standard PCB, it has a much denser structure and therefore does not outgas in the ADR vacuum. A first generation of holders had the tracks patterned by standard lithography and etching in hydrochloric acid diluted in hydrogen peroxide. A second generation was gold-plated and machined-made from a Gerber file (the standard file type used in industry) using an automatic mill. To maximise the thermal link, the 10 mm×10 mm sample sits on a copper piece in contact with the pill through a M-8 copper screw. The sample mounted on its chip carrier in the ADR is shown in Figure 3.16.

As the noise of the device is smaller than the input noise of a room-temperature preamplifier, the signal preferably needs to be amplified at low temperature. For several of the measurements in this thesis we used a Series SQUID Array (SSA)

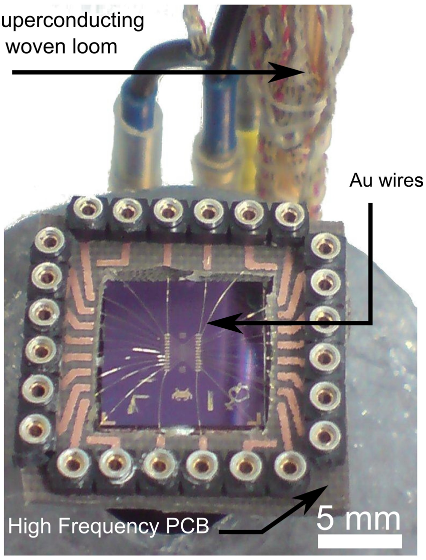

Figure 3.15: The sample and its ADR mount.

amplifier manufactured by Magnicon[6] which acts as a low-noise preamplifier. It sits inside a superconducting niobium shield, shown in Figure 3.17, to keep its input noise level as small as possible: $< 10\,\mathrm{pA}/\sqrt{\mathrm{Hz}}$. The SSA is designed to operate at 4.2 K but in our system was thermally connected to the 1 K-pot because of structural constraints without any observed adverse effects on its performance. More details regarding its operation will be given in Section 5.4.5 when discussing the noise measurement of samples.

3.7 Breakout Box

Twenty-four contacts can be used with the sample. The chip holder shown in Figure 3.15 has to be connected to an adapter which ends with a male LEMA-24 connector specially designed to provide reliable contacts at low temperature. A woven-loom cable of niobium-titanium twisted pairs clad with cupro-nickel then goes up to the top of the sample space. From there, a series of cables brings the signal up to the top of the insert ending with a female Fisher connector. To prevent high-frequency noise from entering the box, each line is fitted with a passive LC filter, whose electric circuit is shown in Figure 3.18b. This filter is a

---

[6] Magnicon GmbH, Hamburg, Germany

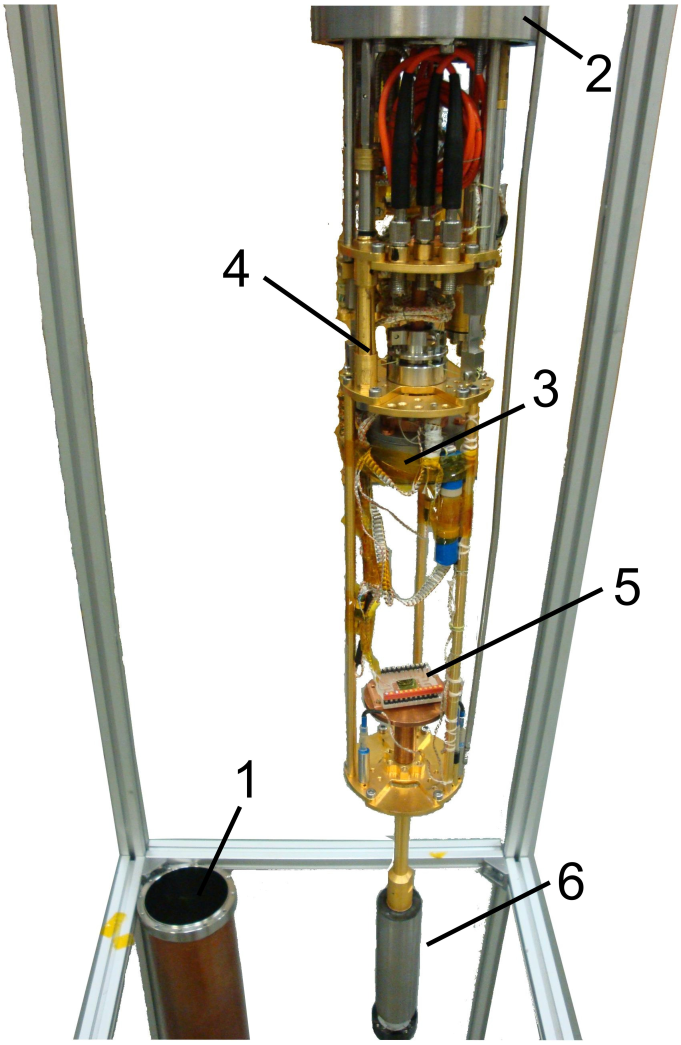

Figure 3.16: The ADR insert showing the different parts: (1) Copper enclosure protecting the insert. For operation, it is sealed with indium and pumped to a very high vacuum to minimise the heat exchange between the environment and the sample space. (2) 1 K pot. This part is a small chamber connected to the main helium bath and that is pumped by an external pump. Due to the lower pressure generated, some helium is evaporated which effectively cools it down to $\sim 1.5\,K$. (3) SSA in its Nb enclosure. (4) Kevlar threads and heat switch. The heat switch is closed to allow the cooling down to 1.5 K and then is opened during the operation.The sample holder is thermally insulated from the upper part by being held by kevlar threads. (5) Sample space. In order to reduce its exposure to noise, it can be encased in a superconducting lead shield but in this case we lose the option of applying an external magnetic field to the sample. (6) FAA pill.

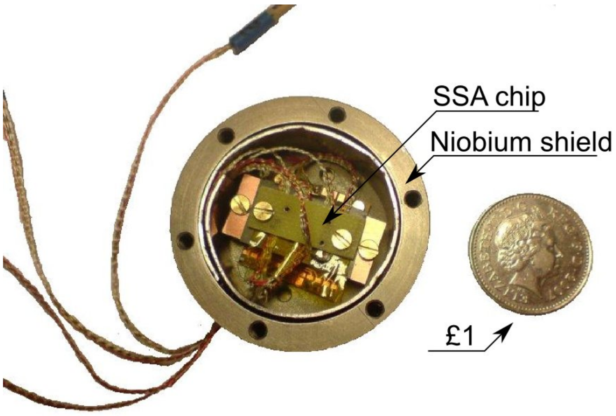

Figure 3.17: The SSA amplifier in its opened Nb shield.

second-order low-pass filter, its main advantage over a RC filter being the steeper attenuation for the same number of components. Considering the angular frequency $\omega = 2\pi f$ and the imaginary unit j, the capacitor and inductor have respective impedances $Z_{\mathrm{C}} = 1/jC\omega$ and $Z_{\mathrm{L}} = jL\omega$. The LC filter is a voltage divider and therefore $V_{\mathrm{out}}/V_{\mathrm{in}} = Z_{\mathrm{C}}/(Z_{\mathrm{C}} + Z_{\mathrm{L}})$. By introducing the angular cut-off frequency $\omega_c = 1/\sqrt{LC}$, the transfer function can be rewritten

$$H(j\omega) = \frac{1}{1 + LC\omega^2} = \frac{1}{1 + (\omega/\omega_c)^2}. \tag{3.1}$$

We chose to set the cut-off frequency at about 1 MHz, or 6.38×10^6 rad/s, as we believed all the experiments of interest (magnetic response, $1/f$ noise and white noise measurements) can be carried out below this. We then selected a combination of standard commercially available values for C and L approaching the desired frequency: $L = 10\,\mu\mathrm{H}$ and $C = 4.7\,\mathrm{nF}$, which gave a cut-off frequency of 0.73 MHz. The gain for the filter $G = -20 \log |H|$, represented on the Bode diagram in Figure 3.18b, shows an attenuation of 40 dB per decade.

3.8 Cool-Down and Typical Measurements

Once the chip has been mounted to the copper block connected to the pill and wired, we close the insert with the copper shield sealed with indium. It is

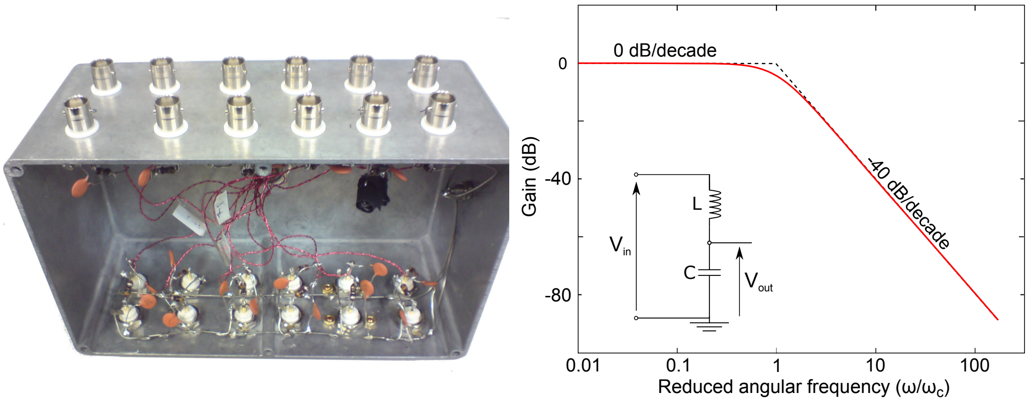

(a) (b)

Figure 3.18: (a) Photograph of the actual break-out box, opened to show its internal electronics. (b) Diagram of the filter and Bode diagram of the expected noise filtering, the cut-off frequency ω_c is set to be 4.4×10^6 rad/s . The inset is a schematic diagram of the electronics filtering the pins of each BNC connector. Only the inner core of the BNC is used as the outer parts are connected with the box.

then pumped down to 10^{-6} mbar and flushed with helium gas twice. This replaces atmospheric gases with helium which is much faster to pump. Then some more helium is introduced via a needle valve up to 10^{-3} mbar to ensure heat transport during the initial stage. The insert is then slowly dipped into a Dewar filled with 150 litres of liquid helium. Once its temperature has reached 4.2 K, we start pumping helium through the 1 K pot to lower the temperature to 1.5 K while slowly magnetising the pill up to 1.6 T. We also heat a sorb which is a charcoal absorption pump close to the sample stage.

Once the thermal equilibrium is reached, the heat switch is opened, we remove the transfer helium and let the sorb cool down. This traps the residual gas atoms and creates a very high vacuum ($< 10^{-9}$ mbar) inside the insert. Subsequent changes to the system {pill and sample} will therefore be adiabatic. The base temperature of the system is about 60 mK but we typically stop at 100 mK to be able to work at this stable temperature for an extended period of time, up to several hours, before the pill needs to be remagnetised.

The I-V characteristics of the devices are then assessed at various temperatures from 100 mK to their T_c. The current is sourced using a Universal Source HP3245A current source while the voltage across it is recorded using a FLUKE 8842A multimeter after an initial preamplification by a factor ×1000 using a Low Noise Preamplifier SR560. Typically, the response of non-hysteretic devices to applied magnetic field is then assessed by current-biasing above I_c and sweeping the magnetic field. This is achieved using a SMR-MPS power supply to source a dc current through the sample magnet built into the system which is designed to create 21.3 mT/A in the sample space. We measured the noise of the most successful devices using the SSA. The procedure to do so is described in its respective section in Section 5.4.5.

Chapter 4

Non-Hysteretic NanoSQUIDs at Millikelvin Temperatures: New Thermal Models and Device Fabrication

As we will discuss in the first part of this chapter, an inherent issue generally reported for many nanobridge-based nanoSQUIDs is hysteretic I-V characteristics when the device is operated far below its critical temperature T_{c}. In this chapter, we propose to solve this issue by using a superconductor with a lower T_{c} in conjunction with a noble metal layer. This layer will not only serve as a thermal shunt to evacuate heat as already done by several groups, but will also be used in a novel way to partially suppress the superconductivity and tune T_{c}.

As this hysteresis has thermal origins, we first developed a new thermal model to accurately model the heat flow in nanobridges at millikelvin temperatures. We then used this model to study several superconductor/noble metal bilayers that were good candidates for the fabrication of non-hysteretic SQUIDs, and finally selected the combination yielding the best results. We confirmed our prediction by creating a nanoSQUID that was not hysteretic down to 60 mK.

4.1 Introduction: Issue of Hysteresis for nanoSQUIDs at Millikelvin Temperatures

4.1.1 Preliminary Measurements of Niobium Devices

As discussed earlier, if nanoSQUIDs can be operated at millikelvin temperatures, this will present a lower level of thermal noise than operation at 4.2 K. This would also enable the measurement of many quantum systems that require this range of temperature. As we saw in Chapter 2, the most common route to get high quality SQUIDs is to use niobium: very pure films can be obtained either by electron-beam evaporation or sputtering, and its relatively high T_c of 9.2 K makes it convenient to measure in liquid helium or a cryocooler. To have a first-hand understanding of this material, we fabricated four Nb SQUIDs, A-1 to A-4, with different bridge lengths ranging from 200 nm to 500 nm. They were based on the design shown in Figure 3.11 in Chapter 3 and fabricated using lift-off of a 150 nm-thick sputtered niobium film. SQUID A-1 is shown in Figure 4.1.

To allow for quick preliminary measurements, we measured the devices using a dip probe in a helium dewar. This technique is very convenient for quick characterisation but in our system only offers a limited choice of stable temperatures: 4.2 K when the insert is fully dipped into the liquid helium and 5.6 K just over the level of the helium. The I-V characteristics for these two temperatures are shown in Figure 4.2. As the operating temperature is reduced, the hysteresis of the I-V curve increases as the critical current increases, whilst the retrapping current I_r – the current for which the device returns into superconducting state – increases slightly. At millikelvin temperatures, we can expect I_c to be much larger than the retrapping current. To be non-hysteretic, such a device has to be operated close to its T_c.

4.1.2 Determination of the Origin of the Hysteresis

For devices based on SIS junctions, hysteretic I-V characteristics are usually the result of the junctions being underdamped as the capacitance and resistance are

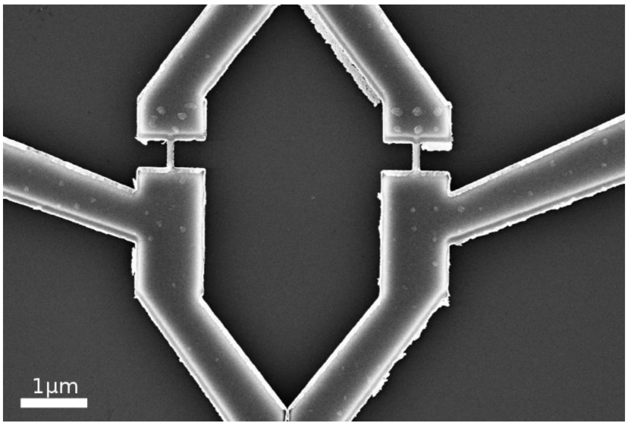

Figure 4.1: SEM micrograph of the Nb device A-1, fabricated using EBL patterning and lift-off of a sputtered niobium (150 nm). The irregularities on the edges, dubbed “lillypadding”, are typical of the lift-off of sputtered film as the deposition is quite isotropic and covers the walls of the resist as well. It does not affect the device.

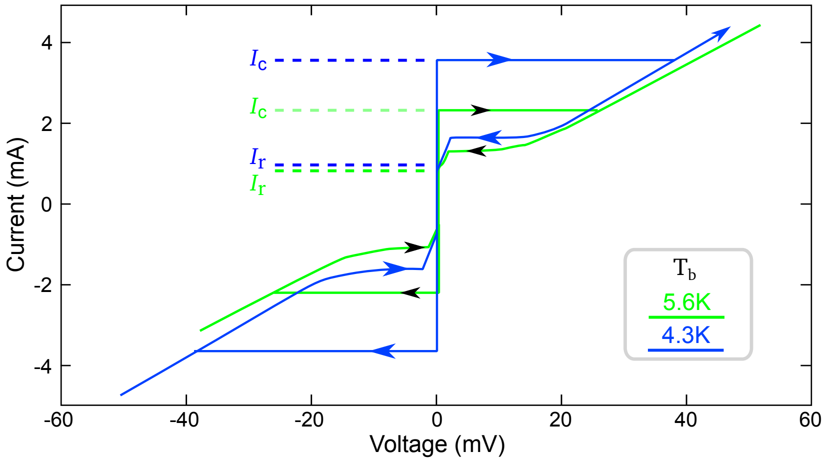

Figure 4.2: I-V characteristics for a niobium device: SQUID A-1 at two temperatures 4.2 K (blue) and 5.6 K (green), showing hysteresis.

both high and so $\beta_c > 1$. For a device based on Dayem bridges, we can roughly estimate what β_c can be. This requires an estimate of the capacitance between the two banks, which can be considered as two semi-infinite coplanar strips. The electrical field is not uniform and is very complex to model, being solvable only using such techniques as conformal mapping. However, the capacitance per unit width will be of the form [131]

$$C = \epsilon_0 \epsilon_\mathrm{r} \frac{K(k')}{K(k)} \tag{4.1}$$

where ϵ_0 is the vacuum permittivity ($\epsilon_0 = 8.854 \times 10^{-12}\,\mathrm{F/m}$), K is the elliptic integral of the first kind, k is the modulus which depends on the gap dimensions, k' is its complementary modulus and ϵ_r is the average relative permittivity of the region between the banks. Since half this region is air ($\epsilon_{\mathrm{r,\ air}} \approx 1$) while the other half is SiO$_2$ ($\epsilon_{\mathrm{r,SiO2}} = 3.9$ [132]) a reasonable value is $\epsilon_\mathrm{r} \approx 2.45$. Typically $K(k')/K(k) \approx 1$ so for a bank width of $2\,\mathrm{\mu m}$, we can estimate that the capacitance between the two banks will be of the order of $5 \times 10^{-17}\,\mathrm{F}$. As we saw earlier in Section 1.2.2 in the RCSJ model the McCumber parameter for a SQUID is given by

$$\beta_\mathrm{c} = \frac{2\pi}{\Phi_0} I_\mathrm{c} R^2 C$$

From the I-V characteristics in Figure 4.2, $R = 25\,\Omega, I_\mathrm{c} = 1.85\,\mathrm{mA}$, we estimate that $\beta_c \approx 10^{-4} \ll 1$. This means that the hysteresis is not related to the capacitance, unlike the common situation for tunnel junctions. A widely accepted alternative explanation for the hysteresis was introduced by Skocpol *et al.* in 1974 [12]. When the current increases above the critical current of the nanobridge, the bridge turns normal and a hot spot due to Joule heating is created in this region. The hot spot can then self-sustain the normal region and, depending on the thermal conductivity of the film, it may be necessary to reduce the current well below the critical current to get back to the superconducting state. This current is called the retrapping current I_r and is function of the geometry, materials and operating temperature of the bridge. Despite the hysteresis, measurements are still possible, for instance by sweeping the current until I_c is detected [66] and then iterating this process. However, the electronics required is more complicated and slower than the conventional one, thus limiting the bandwidth and response time of the device. The maximum repetition rate obtained by Wernsdorfer *et al.* [66] was 10 kHz, limited by the time it took to settle the current.

The relatively high T_c of niobium, although for many applications being an advantage, is for millikelvin operation of nanobridge devices a major drawback as it leads to a very high critical current density. For this reason, this type of device can only be used non-hysteretically close to T_c where I_c is still small.

4.2 Solving the Hysteretic Issue: Choice of Superconducting Materials with a Lower T_c

An option to get rid of the hysteresis at millikelvin temperatures is to employ a superconducting material with a lower T_c and operate the SQUID close to this temperature. In this section, we discuss how this can be achieved using proximity bilayers. We first determine which elemental superconductors could be used as the base layer by considering their T_c and chemical stability with noble metals. We then investigate how the T_c of the bilayers can be tuned using the proximity effect by varying the thickness ratio of normal metal to superconductor.

4.2.1 Pure Metals with Sub-kelvin T_c

Among the 29 superconducting elemental metals [133], 13 have a superconducting transition between 100 mK and 1.2 K. A narrowing in choice can be guided by recent research on bolometers and Transition Edge Sensors (TES) which also require the use of millikelvin T_c superconductors with sharp transitions. These devices usually take advantage of the proximity effect where an overlayer of noble metal is used to partially suppress the superconductivity and precisely tune T_c. In our devices it would also act as a thermal shunt which can help extract heat from the hotspot. Literature reviews such as Irwin and Hilton's [134] distinguish four materials that can be used in the millikelvin range thanks to their T_c and the existence of a compatible noble metal with which they can be coupled: aluminium, titanium, molybdenum and iridium. However the latter is not suitable as its T_c (140 mK) is too low to be used for many millikelvin measurements of interesting systems, e.g. the superconducting transition of several topological insulators or some heterointerfaces such as lanthanium aluminate - strontium titanate. In addition, its deposition requires very controlled conditions with the substrate heated to 600°C in an ultrahigh vacuum system to have reproducible results [135].

Therefore, only three materials would *a priori* be acceptable as the basis for the fabrication of our devices: aluminium, molybdenum and titanium. If we are to exploit the proximity effect as for bolometers, then the noble metal overlayer has to be chosen to be very stable with, and minimise intermixing with the superconductor. Titanium gives the best results when combined with gold [136], whereas copper is optimal for molybdenum [137]. Aluminium is known for its high reactivity, readily alloying with gold and copper, but is stable with silver [138].

4.2.2 Proximity Effect & Reduction of T_c for Bilayers

Although adding a shunt layer of noble metal increases the heat transfer efficiency and hinders the hot spot formation, it also alters the critical temperature of the superconductor through the proximity effect. There is an optimum thickness as there should be enough normal metal to extract all the heat but not too much lest the critical temperature is depressed below our requirements. In addition, too much normal metal would electrically shunt the weak links, significantly reducing R_n and the modulation depth ΔV. We aim to have the device operating correctly in the $50\,\mathrm{mK} - 400\,\mathrm{mK}$ range which means T_c should be about $400 - 500\,\mathrm{mK}$.

Since the original work of de Gennes *et al.* in 1964 [44], there are been several theories studying the critical temperature of proximity bilayers [139]. In the following, we used results from Martinis *et al.* [140] based on Usadel's theory [141] to determine the critical temperature of the bilayers as it seems to provide a good compromise between the quality of prediction and the complexity of the model.

According to Martinis *et al.*'s theory, if the film is thinner than the coherence length so its superconducting order parameter is constant across it, then the critical temperature of a bilayer is given by:

$$T_{\mathrm{c}} = T_{\mathrm{c}0}\,\frac{d_s}{d_0}\,\frac{\alpha}{\alpha+1}\,\frac{1}{1.13t} \tag{4.2}$$

$$\text{where } \frac{1}{d_0} = 0.5\pi\, k_B\, T_{\mathrm{c}0}\, \lambda_f^2\, n_s \tag{4.3}$$

$$\text{and } \alpha = \frac{d_n n_n}{d_s n_s}. \tag{4.4}$$

In the equations above, n is the electronic density of the material (subscript s for superconductor, n for the normal metal), k_{B} is the Boltzmann constant (expressed in eV.K^{-1}: $k_{\mathrm{B}} = 8.61733 \times 10^{-5}\,\mathrm{eV.K^{-1}}$), λ_{f} is the Fermi wavelength of the normal metal and $T_{\mathrm{c}0}$ is the nominal T_{c} of the superconductor. The fitting parameter t is called the transmission factor and accounts for the various unknown experimental factors such as the interface quality, etc. The Fermi wavelength is the de-Broglie wavelength of the electrons carrying the conduction current (electrons located near the Fermi surface) and is of the order of several angstroms for most metals. The noble metals we use in our devices can be considered in good approximation to be Fermi metals and so λ_f can be calculated from the electronic density n_{e} [142]: $\lambda_{\mathrm{f}} = 2^{3/2}(\pi/3n_{\mathrm{e}})^{1/3}$. As electrons occupy all the available energy levels up to the Fermi energy E_{F} according to Pauli's exclusion principle, n_{e} can itself be deduced from E_{F} which has been tabulated for many materials [143, 144]: $n_{\mathrm{e}} = 8\sqrt{2}\,\pi\, m^{1.5}/h^3 \left(2/3E_{\mathrm{F}}^{3/2}\right)$. Values for reported compatible superconductor/normal metal bilayers, i.e. Mo/Cu, Ag/Al and Ti/Au are given in Table 4.1.

To determine the transmission factor, we measured the critical temperature for different thickness ratios of superconductor/normal metal (see Figure 4.3) and performed a best fit. The transmission factor takes into account the different transmission processes at the interface that are very sensitive to the metallisation conditions. For our aluminium/silver bilayers (see Figure 4.3), the estimated

Material	E_F (eV)	n_e (10^{28}states/eVm^3)	λ_f (Å)
Nb	9.26	12.80	5.70
Au	7.25	8.86	6.44
Mo	11.36	17.39	5.15
Cu	9.03	12.32	5.77
Al	11.3	17.25	5.16
Ag	7.43	9.19	6.36
Ti	8.84	11.93	5.83

Table 4.1: Fermi energy E_F, electronic density n_e and Fermi wavelength λ_f for the main superconductor/normal metal bilayer materials of interest.

transmission factor was 0.295 having a determination coefficient $R^2 = 0.9976$. For comparison, Martinis *et al.* report a transmission parameter of 0.21 between molybdenum and copper so our estimate seems reasonable. The critical temperature of our aluminium was also smaller than 1.2 K. This is due to the fact the film is very thin, as thicker films (> 250 nm) that we evaporated in the same conditions had the usual T_c of 1.2 K. We performed the same sort of regression for titanium/gold bilayers: the estimated transmission parameter was 0.17 with $R^2 = 0.9841$. Using this model, we can fabricate a SQUID with any T_c from 200 mK to 700 mK and can estimate the T_c of any bilayer. This is a crucial factor for building up an accurate heat model of the bridges which is the subject of the following section.

4.3 Heat Models - Determination of I_r

4.3.1 General Approach

For SIS based SQUIDs, the hysteresis usually arises due to electrical effects related to the McCumber parameter β_c of the junctions. However, as we showed for niobium, this cannot be the case for nanobridges as β_c is very small. The widely-accepted origin for the hysteresis is thermal. In the following, we will first briefly describe the two models existing in the literature. The first one that laid the foundations of this sort of analysis was written by Skocpol, Beasley and Tinkham and will be referred to in the following as the SBT model [12]. It was further refined by another model published by Hazra, Pascal, Courtois and Gupta, referred to as the HPCG model [13]. However, these were originally designed to model niobium SQUIDs operated at 4.2 K. At this temperature, the heat transfer coefficient to the substrate is about $\alpha = 20\,\mathrm{kW/m^2K}$ but this typically decreases significantly at lower temperatures following $\sim T^n$ where $n = 3$ [145]. We then detail two new thermal models we developed, referred to as Models M-1 and M-2 in the following, to take into account the much reduced α at millikelvin temperatures. In Section 4.4, these models will be used to study several bilayers systems and discuss whether a non-hysteretic SQUID can be achieved.

4.3.2 Original Thermal Model: the SBT Model

Two cases are considered in the original paper by SBT depending on how the length of the nanobridge compares with the typical length over which the heat spreads in the film, called the thermal healing length $\eta = \sqrt{\kappa d/\alpha}$ where κ is the thermal conductivity of the film, which in this model is assumed to be similar for superconducting and normal state (this approximation will be addressed in the HPCG model), d its thickness and α the heat transfer coefficient per unit

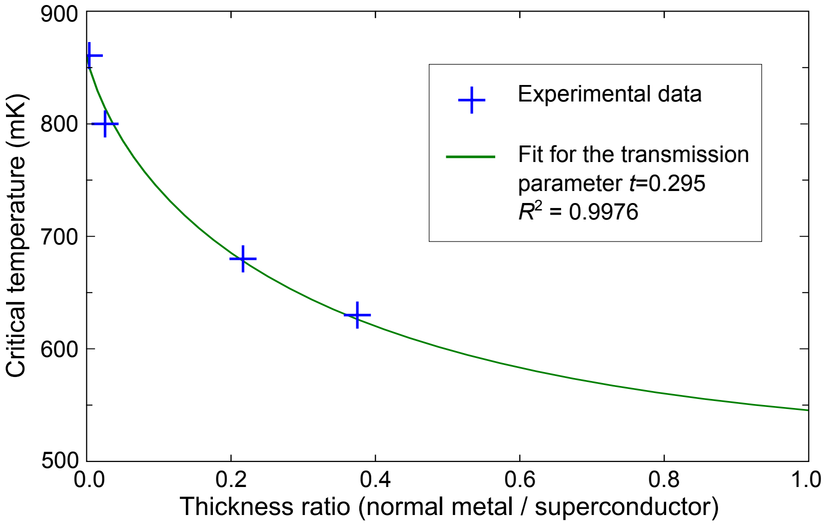

Figure 4.3: Bilayer critical temperature as a function of the silver to aluminium thickness ratio with the aluminium thickness set to 120 nm. The curve is a fit of Martinis *et al.*'s theory to the experimental data for a transmission factor of $t = 0.295$.

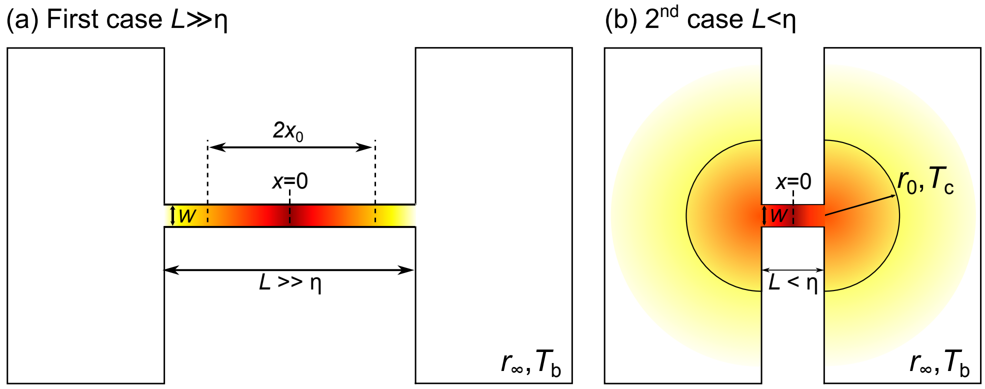

Figure 4.4: Schematic diagram showing the dimensions used for the SBT model in the two cases they considered depending on how L compares to the thermal healing length η. (a) If $L \gg \eta$, the hotspot appears at the middle of the bridge and spreads linearly. The temperature at both ends of the bridge is T_b. (b) If $L < \eta$, the heat starts spreading radially into the banks up to a radius r_0 at which $T = T_\mathrm{c}$.

area to the substrate. Typical values at 4 K for niobium are $\kappa = 5\,\mathrm{W/m\,K}$ and $\alpha = 20\,\mathrm{kW/m^2K}$. SBT assume that κ stays constant over the considered range of temperature and is determined using the Wiedemann-Franz law considering the resistivity of the material just above T_c. The thermal healing length is typically of the order of a few micrometres for niobium. The first case they consider is for a bridge of width W and length L such that $L \gg \eta$ as shown in Figure 4.4(a). In that case, the hotspot is assumed to arise in the middle of the bridge and the heat flow is contained in one dimension along it. The temperature is a function of x, the position along the x-axis. The temperature at both ends of the bridge is assumed to be the bath temperature T_b, i.e. $T(L/2) = T_\mathrm{b}$. Due to the heat generated, the normal region extends over $-x_0 < x < x_0$ where x_0 is the position along the bridge where $T(x_0) = T_c$ (necessarily, we have $x_0 < L/2$). The entire normal region contributes to the overall Joule effect which means the problem has to be solved self-consistently. The heat flows for that case are

$$-\kappa\frac{\mathrm{d}^2T}{\mathrm{d}x^2} + \frac{\alpha}{d}(T - T_\mathrm{b}) = \begin{cases} \left(\dfrac{I}{Wd}\right)^2 \rho & \text{in the normal region, } x < x_0 \\ 0 & \text{in the superconducting region, } x > x_0. \end{cases} \tag{4.5}$$

The first term on the left represents the heat spreading along the film that depends on its thermal conductivity κ and the second term is the heat transmitted to the substrate that depends on the area of contact and α. By solving these equations, SBT obtain an expression linking the current applied to the bridges I to the extent of the normal region x_0:

$$I^2(x_0) = \left(\frac{\alpha W^2 d(T_\mathrm{c} - T_\mathrm{b})}{\rho}\right)\left(1 + \coth\frac{x_0}{\eta}\coth\left(\frac{L}{2\eta} - \frac{x_0}{\eta}\right)\right) \tag{4.6}$$

The retrapping current is defined as the minimum current that can sustain a hotspot and can be found graphically from the plot shown in Figure 4.5 or by numerical methods.

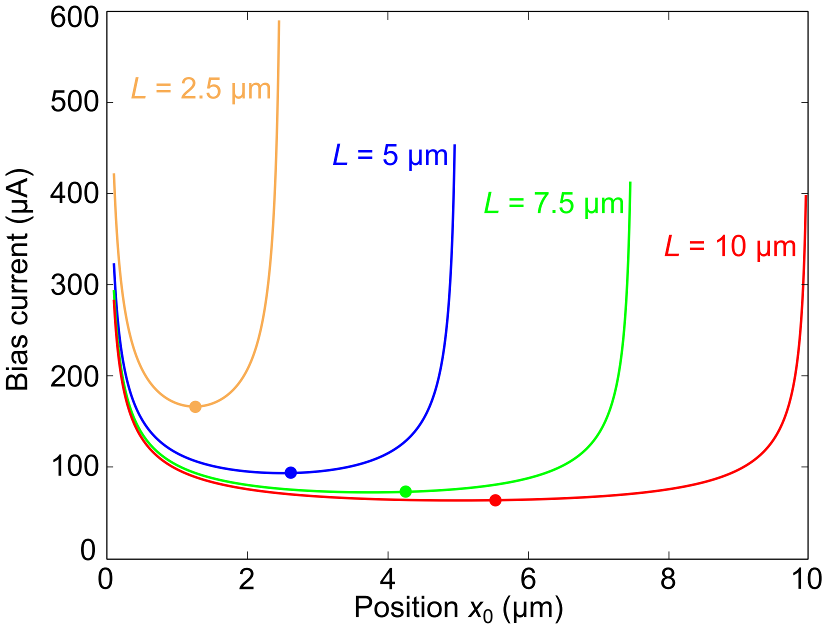

Figure 4.5: Current versus x_0 for long niobium bridges of various lengths and fixed width of 70 nm at 4.2 K calculated from the SBT model using Python and Matplotlib to plot Equation 4.6. The dots indicate the minimum of the current sustaining a normal hotspot, i.e. I_r.

The second case SBT considered is if the bridge is short compared to η, so the hotspot enters the banks where it can be considered to spread radially over a radius

r_0. This is shown in Figure 4.4(b). The equations for the second case are given by:

$$-\kappa\left(r^2\frac{\mathrm{d}^2T}{\mathrm{d}r^2}+r\frac{\mathrm{d}T}{\mathrm{d}r}\right)+\frac{\alpha}{d}r^2(T-T_\mathrm{b})=\begin{cases}\left(\dfrac{I}{\pi d}\right)^2\rho & \text{if normal,}\\ 0 & \text{if superconducting.}\end{cases} \tag{4.7}$$

SBT solved Equation 4.7 analytically using the Bessel functions $\mathcal{I}_0$ [1], $\mathcal{K}_0$ and $\mathcal{K}_1$ and found

$$I^2(x_0)=\left(\frac{\kappa W^2 d(T_\mathrm{c}-T_\mathrm{b})}{\rho}\right)\mathcal{K}_0\left(\frac{r_0}{\eta}\right)^{-1}$$
$$\times\left[\left(\frac{\eta}{W}\right)^2\left[\mathcal{K}_0\left(\frac{W}{2\eta}\right)+\frac{\pi}{2}\mathcal{K}_1\left(\frac{W}{2\eta}\right)\coth\left(\frac{L}{2\eta}+\frac{W}{4\eta}\right)\right]^{-1}+\pi^{-2}\int_{W/2\eta}^{r_0/\eta}\frac{\mathcal{I}_0(x)}{x}dx\right]^{-1} \tag{4.8}$$

Again finding the minimum of this function, which can be performed graphically or numerically, gives the retrapping current. According to SBT's analysis of Equations 4.6 and 4.8, the retrapping currents are approximately:

$$I_\mathrm{r}\approx\sqrt{\frac{\alpha w^2 T_\mathrm{c} t}{\rho}}\sqrt{1-\frac{T}{T_\mathrm{c}}}\ \text{for long bridges and} \tag{4.9}$$

$$I_\mathrm{r}\approx\sqrt{\frac{\kappa t^2 T_\mathrm{c}}{\rho}}\sqrt{1-\frac{T}{T_\mathrm{c}}}\ \text{for short bridges.} \tag{4.10}$$

4.3.3 Refined Thermal Model: the HPCG Model

Hazra, Pascal, Courtois and Gupta (HPCG) [13] carried the SBT model further by considering how the thermal conductivity of a superconductor decreases as the temperature is reduced. A lower temperature means the number of free electrons is reduced as an increasing number of electrons form Cooper pairs which cannot carry heat. In this model, this effect is linearised so that $\kappa_\mathrm{s}/\kappa_\mathrm{n}=T/T_\mathrm{c}$. When solving the heat equation with this assumption, the length scale of the effect becomes $\eta=\sqrt{2L_0T_\mathrm{c}/\pi\alpha R_\mathrm{c}}$ where L_0 is the Lorentz parameter, and $R_\mathrm{c}=2\rho_\mathrm{N}/d\pi$. In

---

[1] NB: This is not to be confused with I_0 which is the current scale in the following.

addition, the current scale becomes $I_0 = \pi\alpha\eta^2/\sqrt{L_0}$. There are subtle differences with the SBT model regarding the hypothesis and dimensions used (see Figure 4.6). In the HPCG model, the bridge is always considered to be short enough so that

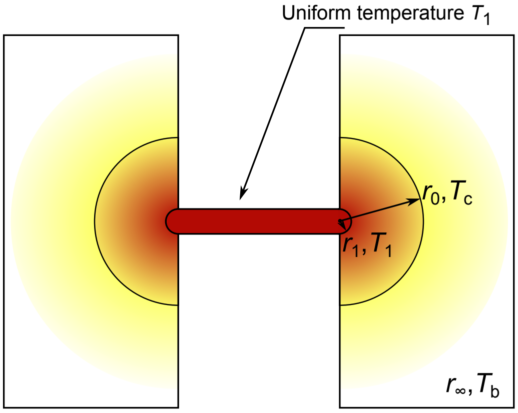

Figure 4.6: Schematic diagram showing the dimensions used in the HPCG model. The temperature of the bridge and a small semicircular area of radius r_1 at each extremity is assumed to be uniform. In the banks the temperature decreases radially to reach T_c at $r = r_0$.

its temperature T_1 is uniform. To avoid mathematical divergence issues, the half-circular region of radius r_1 is included as part of the bridge, its resistance being $R_0 = (l + 2r_1)\rho_\mathrm{N}/wd$. The normal region in the banks extends over a radius r_0 larger than the radius of the bridge. Its resistance is then $R = R_\mathrm{c} \ln(r_0/r_1)$. By introducing the reduced variables $x = r/\eta$, $x_0 = r_0/\eta$ and $t_\mathrm{b} = T_\mathrm{b}/T_\mathrm{c}$, where T_b is the temperature of the helium bath, and solving the heat equations, HPCG demonstrated that the retrapping current is defined by $i_\mathrm{r} \times I_0$ where i_r is the minimum of

$$i^2(x_0) = \frac{\lambda x_0(1 - t_\mathrm{b}^3)\mathcal{K}_1(\lambda x_0)}{3(\ln(x_0/x1) + \beta)\mathcal{K}_0(\lambda x_0)} \tag{4.11}$$

where $\mathcal{K}_0$ and $\mathcal{K}_1$ are modified Bessel functions of the second kind of zeroth and first order respectively. This minimum is determined similarly to the SBT model: either graphically or numerically as shown in Figure 4.7. Figure 4.8 gives I_c estimated from the KO-1 theory and I_r from the two heat models for a niobium bridge of typical dimensions 150 nm × 50 nm. HPCG's correction changes the overall shape

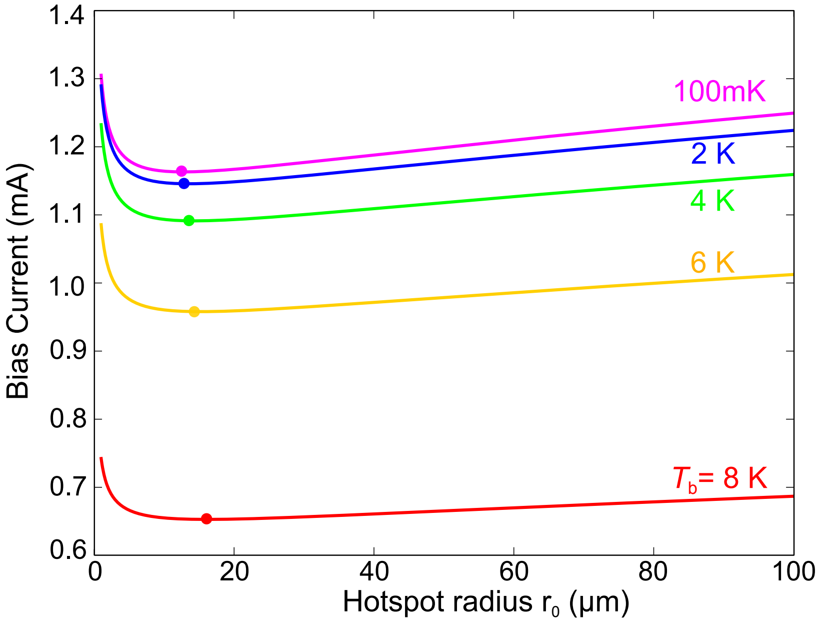

Figure 4.7: Current versus the hotspot radius r_0 for a 150 nm × 50 nm × 100 nm nanobridge of niobium in the HPCG model. This is plotted at several bath temperatures. Here α is not temperature dependent and is set to $20\,\mathrm{kW/m^2K}$. Dots correspond to the retrapping current I_r.

of the retrapping current curve as the thermal conductivity is impaired by the formation of Cooper pairs at lower temperatures. The retrapping current saturates whereas it keeps on increasing in the SBT model.

4.3.4 Issues with SBT and HPCG Models in the Millikelvin Range

Introduction

The previous models laid the foundations to understand the origin of the hysteresis for nanobridges and usually give satisfying results for planar microSQUIDs at 4.2 K. However they are ill-fitted for nanoSQUIDs at millikelvin temperatures. A hypothesis not stated but implied in these models by the radial propagation of heat is that there is always a solution for r_0 and that there is an equilibration between the heat generated by Joule effect and that transferred to the substrate, regardless of the geometrical dimensions of the actual device. Indeed, the authors of the previous studies consider that the heat transfer coefficient to the substrate α is always such that the temperature of the film reaches the bath temperature T_b

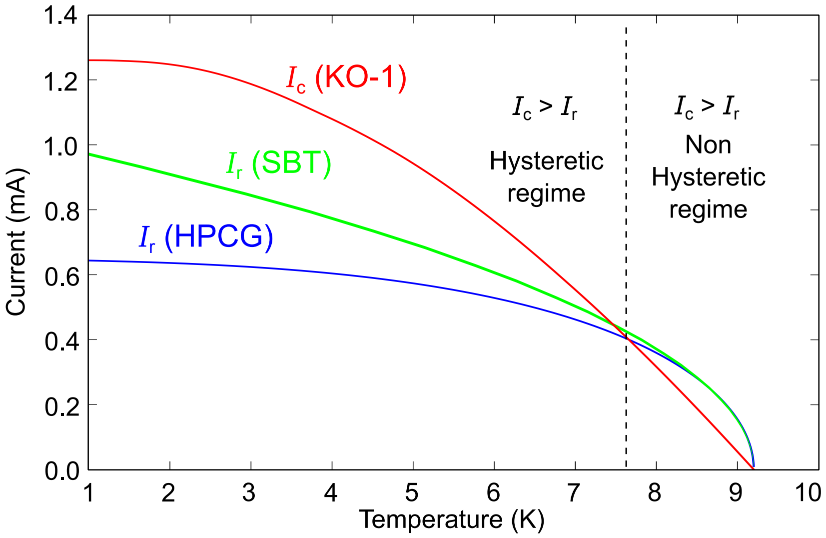

Figure 4.8: Estimation of the critical current I_c following the KO-1 theory using $R_\mathrm{n} = 2.3\,\Omega$ and of the retrapping currents according to the SBT and HPCG models versus bath temperature T_b for a Nb nanobridge of dimensions $150\,\mathrm{nm} \times 50\,\mathrm{nm} \times 100\,\mathrm{nm}$.

well before the edges of the real devices. The authors did not consider the cases where r_0 or η would be larger than the physical width of the banks. As mentioned earlier α scales as $\sim T^3$ so assuming it is $20\,\mathrm{kW/m^2K}$ at $4.2\,\mathrm{K}$ as assumed by SBT, it would be typically three to four orders of magnitude lower at millikelvin temperatures. In that case, we can estimate $\eta \sim 10\,\mu\mathrm{m}$ for niobium and $\eta \sim 100\,\mu\mathrm{m}$ for a bridge of titanium, which is much larger than any realistic device. This leads to a large overestimation of the retrapping current. This point will be discussed in further detail in a later section when comparing these models to real systems.

Study with COMSOL

COMSOL is a powerful finite-element solver incorporating a variety of physical models including heat propagation in materials. However, superconductivity and many other aspects of low-temperature physics have not been implemented at present. Due to this, our COMSOL analysis has only a limited predicting power as it relies on the parameters obtained from the thermal models. However, we can check the validity of our hypotheses and determine if the heat is spreading radially or linearly. We modelled a strip of width W with a bridge of width w_b and length l_b

in the middle. In this model, we set ρ and κ of the device to be $\rho = 200\,\mathrm{n\Omega.m}$ and $\kappa = 0.122\,\mathrm{W/m\,K}$ which are typical values for titanium. The model accounts for the linear decrease of κ below T_c. We set the underside of the device to have a heat transfer $Q = \alpha(T - T_\mathrm{b})$ where $T_\mathrm{b} = 100\,\mathrm{mK}$ and α is a variable. The other surfaces are thermally insulating except each extremity of the strip that we constrain to T_b. We set the bridge to generate the heat $Q = \rho I_\mathrm{bias}^2 l_\mathrm{b}/(w_\mathrm{b} t_\mathrm{b})$ where $I_\mathrm{bias} = 2.75\,\mathrm{\mu A}$. To simplify the COMSOL model, we consider the banks do not contribute to the Joule heating.

We then check the heat profiles for several values of α. For $\alpha = 20\,\mathrm{kW/m^2K}$, the heat spreads radially as described by the SBT and HPCG models. The temperature reaches T_b well before the hotspot reaches the edge of the bank. The inset of Figure 4.10(b) clearly shows that the hotspot extends only over $\sim 150\,\mathrm{nm}$. For $\alpha = 20\,\mathrm{W/m^2K}$, the isothermal contours are straight and the heat is mostly travelling along the axis of the strip. The length to reach thermal equilibrium is also much larger. In the following, we discuss two thermal models M-1 and M-2 that we developed assuming a linear heat flow.

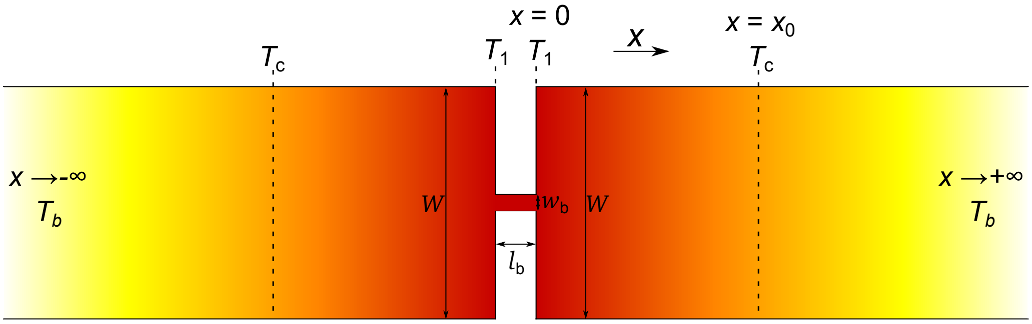

Figure 4.9: Schematic diagram showing the dimensions used in our models M-1 and M-2. The bridge is l_b long and w_b wide. We consider that the banks are infinitely long and $T(x \to \infty) = T_\mathrm{b}$. The heat flows linearly along the x-axis.

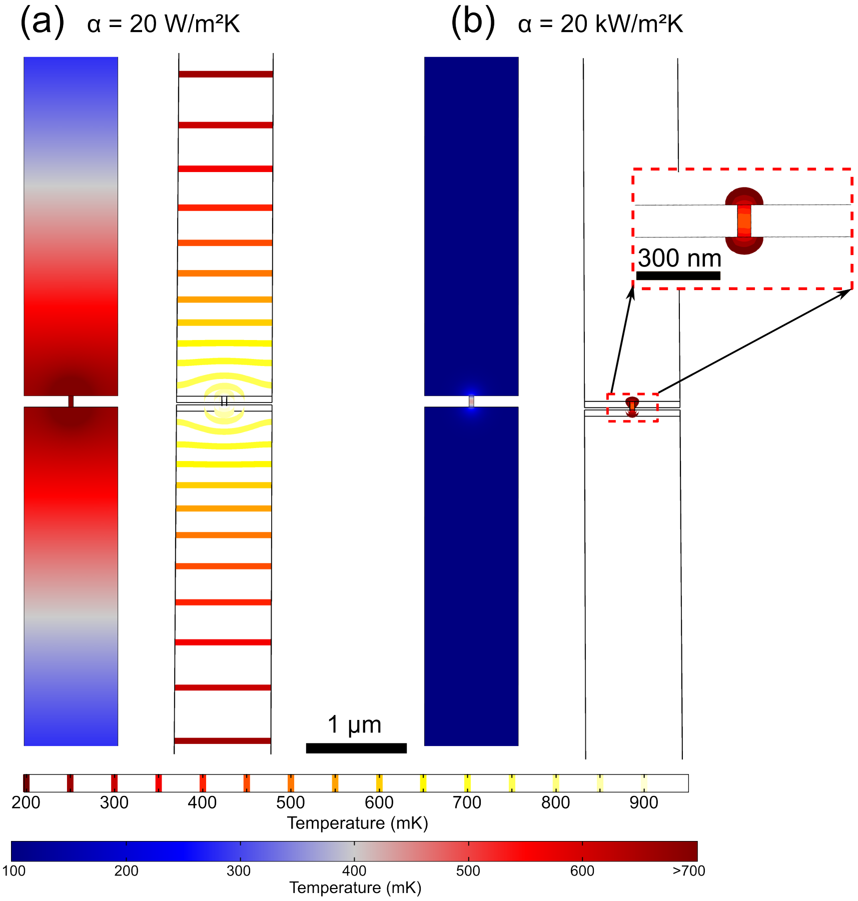

Figure 4.10: COMSOL simulations showing the isothermal contours and temperature for a nanobridge made of titanium ($\rho = 200\,\mathrm{n\Omega.m}$, $\kappa = 0.122\,\mathrm{W/mK}$) for $I_{\mathrm{bias}} = 2.75\,\mu\mathrm{A}$ on a substrate at a constant temperature $T_{\mathrm{b}} = 100\,\mathrm{mK}$ for (a) $\alpha = 20\,\mathrm{W/m^2K}$ and (b) $\alpha = 20\,\mathrm{kW/m^2K}$.

4.3.5 New Thermal Models for Millikelvin Temperatures

Power Equation for Linear Heat Propagation

In the following we explain in detail how we solved the heat equation with this hypothesis of a linear heat propagation to build a model that corresponds more closely to the physics in the millikelvin range. As shown in Figure 4.9, we consider a nanobridge of dimensions $l_\mathrm{b} \times w_\mathrm{b} \times t_\mathrm{b}$, of resistivity ρ_b connected to infinitely long banks of width W, thickness d and resistivity ρ. We assume that the bridge is small enough to have a uniform temperature T_1. The system is completely symmetrical with respect to the centre of the nanobridge and the problem is then exactly equivalent to half a bridge transmitting heat to one single bank. We also assume the power generated by the Joule effect in the bridge is uniformly spread over the whole width of the bank. This approximation is accurate if $W/\eta \ll 1$, which is most likely to be the case at millikelvin temperatures as $\eta \sim 20\,\mu\mathrm{m}$ and $W \sim 2\,\mu\mathrm{m}$. In the opposite case ($W/\eta \gg 1$), the SBT and HPCG models are more physically accurate.

At any position x along the x-axis, the power equation of the system is

$$\underbrace{-\kappa(T)\,\mathrm{d}T/\mathrm{d}x\,Wd}_{①} + \underbrace{\int_0^x \alpha(T-T_\mathrm{b})W\mathrm{d}x}_{②} + \underbrace{\alpha(T_1-T_\mathrm{b})A_\mathrm{bridge}}_{③} = \underbrace{I^2R(x)}_{④} + \underbrace{P_\mathrm{bridge}}_{⑤} \tag{4.12}$$

where

① Heat flow per second along the film

② Heat flow per second transferred by the banks to the substrate

③ Heat flow per second transferred by the bridge to the substrate

④ Power generated in the banks by the Joule effect where $R(x) = \rho x/Wd$

⑤ Power generated in the bridge by the Joule effect $P_\mathrm{bridge} = 0.5(\rho_\mathrm{b} l_\mathrm{b} I^2/w_\mathrm{b} t_\mathrm{b})$

As the heat transfer to the substrate is much reduced at low temperatures, we will neglect ③ to simplify the equations.

Model M-1: Solution with Constant κ

As a check of the validity at millikelvin temperatures of HPCG's hypothesis that κ is a function of temperature, we start by solving the heat equation with SBT's assumption that it stays constant over the whole range of temperature. This new model will be referred to in the following as Model M-1. Taking the derivative of Equation 4.12 with respect to x and dividing on both sides by Wd, we obtain the system

$$-\kappa_{\mathrm{N}}\frac{\mathrm{d}^2T}{\mathrm{d}x^2}+\frac{\alpha}{d}(T-T_{\mathrm{b}})=\left(\frac{I}{Wd}\right)^2\rho_{\mathrm{b}} \qquad \text{if } x<x_0\text{, i.e. normal state} \tag{4.13}$$

$$-\kappa_{\mathrm{S}}\frac{\mathrm{d}^2T}{\mathrm{d}x^2}+\frac{\alpha}{d}(T-T_{\mathrm{b}})=0 \qquad \text{if } x>x_0\text{, i.e. superconducting state.} \tag{4.14}$$

where κ_{S} and κ_{N} are respectively the thermal conductivity of the superconductor and the normal metal. Similarly to SBT's analysis, we will assume that $\kappa_{\mathrm{N}}=\kappa_{\mathrm{S}}$. These two heat equations have the same homogeneous equation which admits the characteristic equation $-\kappa r^2+\alpha/d=0$. Noting $\eta=\sqrt{\kappa d/\alpha}$, its two roots are $r_1=-1/\eta$ and $r_2=1/\eta$. Solutions are therefore of the form $T_h(x)=\mathrm{Constant}_1\times\cosh x/\eta+\mathrm{Constant}_2\times\sinh x/\eta$.

$$T_{\mathrm{p}}=\frac{d}{\alpha}\left[\left(\frac{I}{Wd}\right)^2\rho_{\mathrm{b}}\right]+T_{\mathrm{b}} \tag{4.15}$$

is a particular solution of Equation 4.13 and T_{b} is a particular solution of Equation 4.14. The solutions in the two domains are therefore

$$T(x)=A\cosh x/\eta+B\sinh x/\eta+T_{\mathrm{p}} \qquad \text{if } x<x_0 \tag{4.16}$$

$$T(x)=C\cosh x/\eta+D\sinh x/\eta+T_{\mathrm{b}} \qquad \text{if } x>x_0 \tag{4.17}$$

where A, B, C and D are constants. Their determination requires the use of six conditions presented below:

$$\begin{array}{lll}
(c1) & T(x \to +\infty) = T_\mathrm{b} & \Rightarrow \quad C = -D \\
(c2) & T(x = x_0^-) = T_\mathrm{c} & \Rightarrow \quad A\cosh x_0/\eta + B\sinh x_0/\eta + T_\mathrm{p} = T_\mathrm{c} \\
(c3) & T(x = x_0^+) = T_\mathrm{c} & \Rightarrow \quad C = (T_\mathrm{c} - T_\mathrm{b})e^{x_0/\eta} \\
(c4) & T(x = 0) = T_1 & \Rightarrow \quad A = T_1 - T_\mathrm{p} \\
(c5) & \mathrm{d}T/\mathrm{d}x \text{ continuous in } x_0 & \Rightarrow \quad \kappa_\mathrm{s}\left(A\sinh x_0/\eta + B\cosh x_0/\eta\right) = -\kappa_\mathrm{n} C e^{-x_0/\eta} \\
(c6) & \text{Using Eq. 4.12 at } x = 0 & \Rightarrow \quad B = \dfrac{-P_\mathrm{in}\eta}{W d\kappa_\mathrm{s}}
\end{array}$$

In the following we write $X = x_0/\eta$. To clarify the notation by factorising out I^2, we introduce the constants Z and Y_2:

$$Z = -\frac{0.5\,\eta\, l_\mathrm{b}\,\rho_\mathrm{b}}{w_\mathrm{b}\,t_\mathrm{b}\,W\,d\,\kappa} \quad \text{and} \tag{4.18}$$

$$Y_2 = \frac{d}{\alpha}\left[\left(\frac{1}{Wd}\right)^2 \rho_\mathrm{b}\right]. \tag{4.19}$$

We can then write $T_p = Y_2 I^2 + T_\mathrm{b}$ and $B = ZI^2$ using (c6). Using (c2), we express A as a function of X and I to get

$$A = \frac{T_\mathrm{c} - T_\mathrm{b}}{\cosh X} - I^2\frac{Y_2 + Z\sinh X}{\cosh X}. \tag{4.20}$$

We substitute A into (c5) and obtain after rearrangement and refactorisation by I^2:

$$(T_\mathrm{c} - T_\mathrm{b})(\tanh X + 1) = I^2\left[(Y_2 + Z\sinh X)\tanh X - Z\cosh X\right]. \tag{4.21}$$

The bias current and the position of the normal/superconducting interface are linked by:

$$I^2 = \frac{(T_\mathrm{c} - T_\mathrm{b})(\tanh X + 1)}{(Y_2 + Z \sinh X)\tanh X - Z \cosh X}. \tag{4.22}$$

By definition, the retrapping current I_r corresponds to the minimum current that can sustain a hotspot. In a similar fashion to the SBT and HPCG models, this can be found by numerical methods or graphically as shown in Figure 4.11 for a 150 nm × 50 nm × 100 nm bridge of superconductor of resistivity $\rho = 100\,\mathrm{n\Omega.m}$ for various α. As can be seen on this plot, I_r is quite close to the value for $x_0 \to 0$ which we can refer to as the scaling current I_0:

$$I_0 = \sqrt{\frac{T_\mathrm{c} - T_\mathrm{b}}{-Z}} = \sqrt{\frac{2(T_\mathrm{c} - T_\mathrm{b})\; w_\mathrm{b}\; t_\mathrm{b}\; W\; d\; \kappa}{\eta\; l_\mathrm{b}\; \rho_\mathrm{b}}}. \tag{4.23}$$

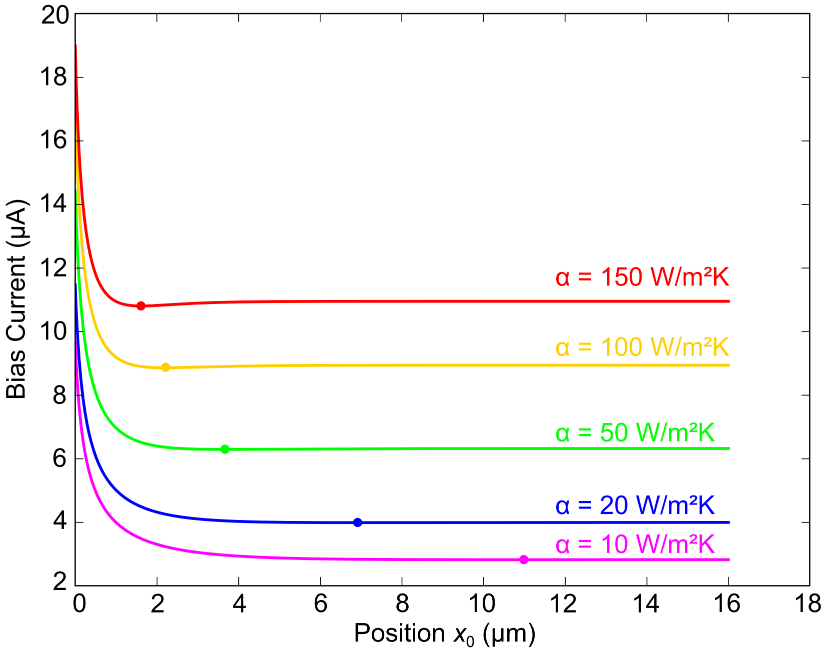

Figure 4.11: Current predicted by Model M-1 versus the position of x_0 along the x-axis for various α. The parameters correspond to a 150 nm × 50 nm × 100 nm nanobridge of a superconductor with resistivity $\rho = 200\,\mathrm{n\Omega.m}$ and $T_\mathrm{c} = 500\,\mathrm{mK}$ at a bath temperature of 100 mK. The bank width is set to 1 μm. The dots show the minimum of current to sustain the normal hotspot, i.e. the retrapping current I_r.

Model M-2: κ as a function of T in the Superconducting State

Similarly to Hazra *et al.*, we now look at the case where κ decreases linearly with the temperature below T_c. Noting κ the thermal conductivity at T_c, we have $\kappa(T) = \kappa T/T_\mathrm{c}$. Replacing $\kappa(T)$ in Equation 4.12 and considering its derivative with respect to x as we did above, we obtain the system of equations:

$$-\kappa\frac{\mathrm{d}^2T}{\mathrm{d}x^2} + \frac{\alpha}{d}(T - T_\mathrm{b}) = \left(\frac{I}{Wd}\right)^2 \rho_\mathrm{b} \qquad \text{if } x < x_0 \tag{4.24}$$

$$\frac{\mathrm{d}}{\mathrm{d}x}\left(T\frac{\mathrm{d}T}{\mathrm{d}x}\right) - \frac{\alpha T_\mathrm{c}}{d\kappa}(T - T_\mathrm{b}) = 0 \qquad \text{if } x > x_0. \tag{4.25}$$

The differential equation for the normal region ($x < x_0$) is the same as before and admits a solution $T(x) = A\cosh x/\eta + B\sinh x/\eta + T_p$ where η and T_p are defined above. To solve the differential equation of the superconducting part, we apply the change of variable $y = T^2$. This gives $y' = 2T'T$ and we can rewrite Equation 4.25 in the form $y'' = 2\alpha T_\mathrm{c}/d\kappa(\sqrt{y} - T_\mathrm{b})$. At this point, this equation can only be solved numerically but we want to go further and offer an analytical solution. We use the approximation $\sqrt{y} - T_\mathrm{b} \approx (y - T_\mathrm{b}^2)/(1 + T_\mathrm{b})$. This approximation is more precise as y approaches T_b^2 but stays fairly accurate down to zero. Equation 4.25 can be rewritten

$$y'' = \frac{1}{\gamma^2}(y - T_\mathrm{b}^2) \text{ where } \gamma = \sqrt{\frac{d\kappa(1 + T_\mathrm{b})}{2\alpha T_\mathrm{c}}} \tag{4.26}$$

which admits a solution $y(x) = C\sinh x/\gamma + D\cosh x/\gamma + T_\mathrm{b}^2$. We then have for the superconducting part $T(x) = \sqrt{C\sinh x/\gamma + D\cosh x/\gamma + T_\mathrm{b}^2}$.

To determine the constants A, B, C, D, we use the six boundaries conditions as we did previously. (c1) and (c6) are unchanged and respectively give $B = ZI^2$ and $C = -D$. Using (c2) we can express A as a function of B and get

$$A = \frac{T_c - T_\mathrm{b}}{\cosh x_0/\eta} - I^2\frac{Y_2 + Z\sinh x_0/\eta}{\cosh x_0/\eta}. \tag{4.27}$$

Similarly, we express D as a function of C using (c3) and as function of x_0 alone by using (c1),

$$D = \frac{(T_\mathrm{c} - T_\mathrm{b})(T_\mathrm{c} + T_\mathrm{b})}{\sinh x_0/\gamma - \cosh x_0/\gamma}. \tag{4.28}$$

Finally, using the continuity of $\mathrm{d}T/\frac{d}{x}$ (c5) we have

$$\begin{aligned} \frac{1}{\eta}\left(A \sinh x_0/\eta + B \cosh x_0/\eta\right) = \frac{1}{2\gamma}&\left(C \sinh x_0/\gamma + D \cosh x_0/\gamma\right) \\ &\times \underbrace{\left(C \cosh x_0/\gamma + D \sinh x_0/\gamma\right)^{-1/2}}_{T_\mathrm{c}} \end{aligned} \tag{4.29}$$

Inserting the expressions for the constants, it can be found that

$$I^2(x_0) = \frac{(T_\mathrm{c} - T_\mathrm{b})\left[\tanh x_0/\eta + \frac{\eta}{2\gamma} T_\mathrm{c}(T_\mathrm{c} + T_\mathrm{b})\right]}{(Y_2 + Z \sinh x_0/\eta) \tanh x_0/\eta - Z \cosh x_0/\eta}. \tag{4.30}$$

Again, the retrapping current is obtained by finding the minimum of the function either graphically as shown in Figure 4.12 or numerically using Python and NumPy. In practice, this value tends to be relatively close to $I(x_0 = 0)$ in most cases.

$$I_\mathrm{r} \approx \sqrt{\frac{T_\mathrm{c} - T_\mathrm{b}}{-Z} \frac{\eta}{2\gamma} T_\mathrm{c}(T_\mathrm{c} + T_\mathrm{b})}. \tag{4.31}$$

Figure 4.12 shows the position of x_0 along the x-axis for a typical nanobridge made of titanium. As expected, a higher bath temperature means a smaller I_r and a hotspot extending further along the film. This is confirmed by the temperature profile in the bridge plotted for several values of T_b in Figure 4.13. Contrarily to the HPCG model, the width of the bank is taken into account and strongly affects the value of I_r. We can finally plot the retrapping current as a function of temperature for a typical bridge as shown in Figure 4.14. As expected, I_r is well over-estimated by the previous models. The overall shape of M-2 when compared to M-1 is similar to that between HPCG and SBT, as the heat conductivity is reduced at lower temperatures below T_c.

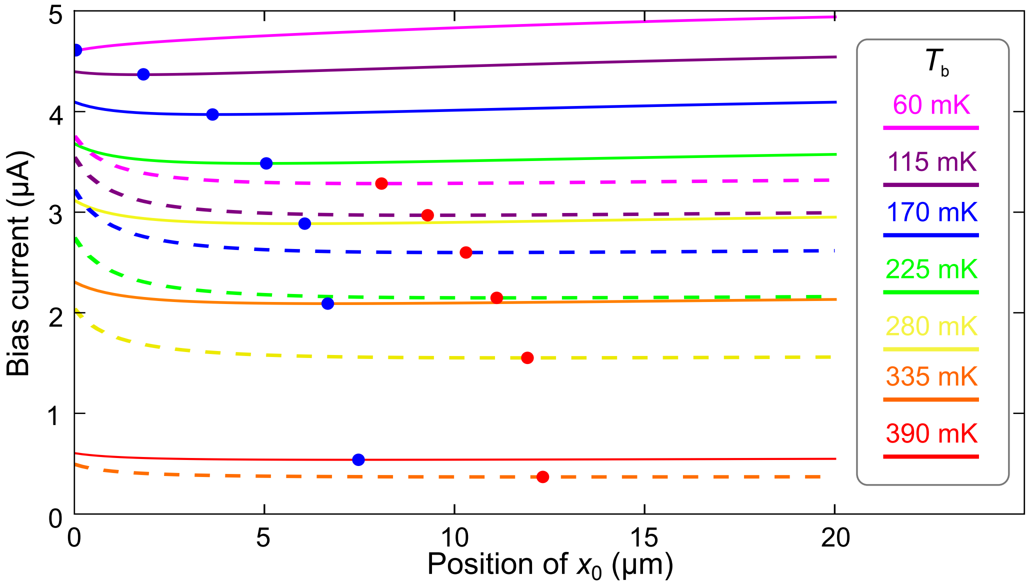

Figure 4.12: Bias current following Equation 4.30 versus the position of x_0 along the x-axis. Both sets of curves correspond to a 100 nm × 50 nm × 90 nm bridge of titanium ($\rho_{\mathrm{mK}} \approx 200\,\mathrm{n\Omega.m}$, $T_c = 400\,\mathrm{mK}$) at bath temperatures ranging from 60 mK to 390 mK. The heat transfer coefficient α is set to 20 $\mathrm{W/m^2K}$. Solid lines are for a bank width of 1.5 μm whilst dashed lines are for a bank width of 1 μm. The dots show the minimum of current to sustain the hotspot, i.e. the retrapping current I_r, in blue for $W = 1.5\,\mu\mathrm{m}$, red for $W = 1\,\mu\mathrm{m}$.

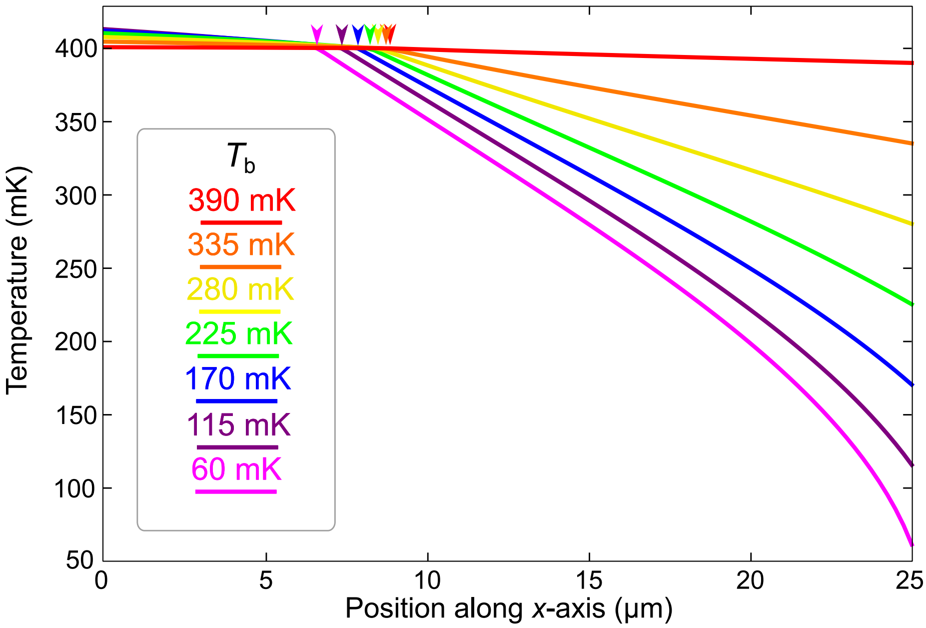

Figure 4.13: Temperature profile in the M-2 model of a 100 nm × 50 nm × 90 nm bridge of titanium ($\rho_{\mathrm{mK}} \approx 200\,\mathrm{n\Omega.m}$, $T_c = 400\,\mathrm{mK}$) at bath temperatures ranging from 60 mK to 390 mK. The banks are 1 µm wide. The heat transfer coefficient α is set to $20\,\mathrm{W/m^2K}$. The arrowheads correspond to the x_0 at the temperature matching their colours.

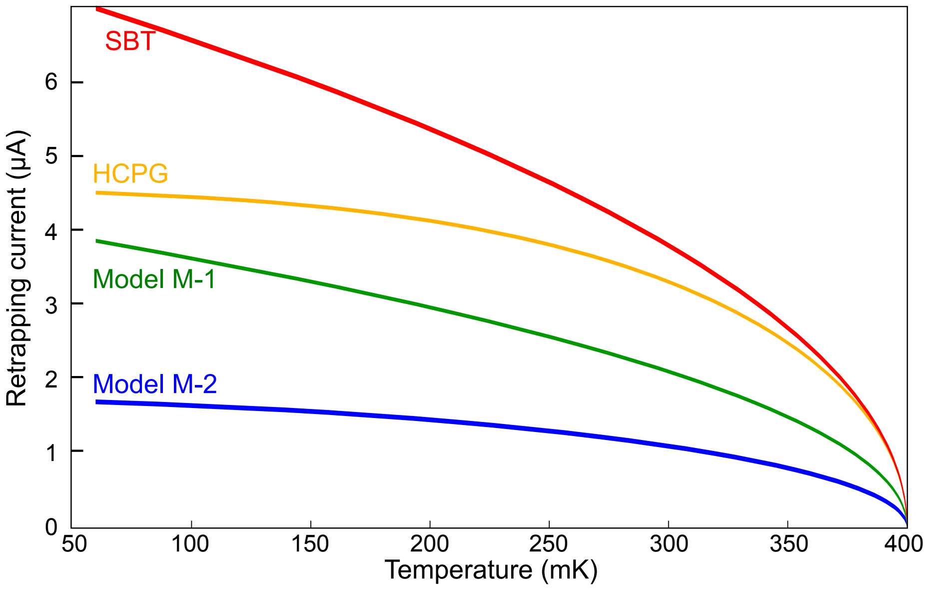

Figure 4.14: Retrapping current versus bath temperature for a 100 nm × 50 nm × 90 nm bridge of titanium ($\rho \approx 200\,\mathrm{n\Omega.m}$, $T_c = 400\,\mathrm{mK}$) for the four models SBT, HPCG, M-1 and M-2. The banks are 1 µm wide. The heat transfer coefficient α is set to $20\,\mathrm{W/m^2K}$.

4.3.6 Hypotheses for Bilayers

α for Bilayers The heat flow from the bilayer to the substrate is very complex to model due to the presence of a thermal boundary resistance between the normal metal and the superconductor. The thermal boundary resistances $R_B = 1/\alpha$ between dissimilar materials are set by parameters such as their acoustic mismatch. Assuming we are dealing with good quality interfaces, we can assume the order of magnitude will be similar for most metals and semi-conductors. In the following we simply treat α as a fitting parameter to account for the thermal boundary resistances of both interfaces substrate/superconductor and superconductor/normal metal. The additional surface heat extraction from the contact pads is also included in this value.

κ for Bilayers To adapt these thermal models to the case of a proximity bilayer, we make the assumption that the two layers act as a single material from a thermal conductivity point of view. The resistivity of this average material corresponds to the parallel combination of the two layers:

$$\rho = \frac{\rho_S \rho_N (d_N + d_S)}{d_S \rho_N + d_N \rho_S} \tag{4.32}$$

where ρ_N, d_N and ρ_S, d_S are the resistivity and thickness of respectively the normal metal and the superconductor. As the metal films are very thin, scattering due to surface effects dominates and the temperature dependence of the resistivity is greatly reduced [146]. In the following, we will consider the limiting case where the resistivity is completely temperature-independent over the range of temperatures of interest. The thermal conductivity of the bilayer just above T_c, κ_c, is determined by the Wiedemann-Franz law and we assume that below T_c it follows the $1/T$ dependency discussed in the HPCG's paper. Our assumptions should be valid as long as the contact between layers is good and the thickness of the normal metal is smaller than the normal state coherence length ξ_N, the decay length of the order parameter due to the proximity effect.

Critical Current Determination for Bilayers It is worth noting that the retrapping current I_r and the critical current I_c are determined by two completely independent branches of physics. As we saw, I_r relies on a purely thermal model whilst I_c is related to quantum physics and depends on the properties of the superconductor such as its gap energy. If I_c is lower than I_r, there is no self-sustaining hotspot possible and therefore no hysteresis. As we saw in Section 1.2.5 we can use the KO-1 theory described to calculate the $I_\mathrm{c}R_\mathrm{n}$ product from which we can extract I_c. Here we should stress the fact that in in this theory the normal state resistance that appears is the normal state resistance of the superconducting bridge without an additional metal shunt. It is therefore a "virtual" value and not the actual resistance that would be measured from the I-V curve. We will note it $R_\mathrm{n,0}$ in the following to distinguish it from the actual measurable junction resistance R_n. The explanation is that apart from depressing T_c via the proximity effect, the normal metal has no other effect on the superconducting properties of the bridge. For example, publications on shunted SQUIDs [65] do not report a change in critical current as the junction is shunted. The $I_\mathrm{c}R_\mathrm{n,0}$ product depends on the gap energy which is a function of the bath temperature and T_c of the material. As the critical temperature is reduced by the proximity effect, adding normal metal reduces the gap and $I_\mathrm{c}R_\mathrm{n,0}$. After determination of the $I_\mathrm{c}R_\mathrm{n,0}$ product from the KO-1 theory, we then fit it to I_c using $R_\mathrm{n,0}$ as a fitting parameter.

In the following, we use theoretical fits to experimental data to check the validity of our models and to refine our estimates of parameters such as $R_\mathrm{n,0}$, T_c, κ and α. From these values, we can then predict the critical current and the retrapping current at any temperature and arbitrary thickness ratios and determine the range of non-hysteretic operation for any given bilayer bridge.

4.4 Determination of the Best Bilayer for NanoSQUID Fabrication

As we saw earlier from our initial analysis in Section 4.2.2, molybdenum/copper, aluminium/silver and titanium/gold are good candidates to create nanoSQUIDs with no hysteresis at millikelvin temperatures. In this section, we perform the theoretical study of several samples made of these various bilayers using the models and hypotheses discussed above. This allows a fine prediction of the retrapping current and critical current for arbitrary nanobridges from which we can select the most appropriate material. Before doing so, we first use our models to confirm whether or not niobium can be used to fabricate our devices.

4.4.1 Case of Niobium

Niobium is currently the most studied material for nanoSQUIDs and several techniques have been used to increase their range of operation: tuning T_c down to approximately 5 K by adjusting the film thickness and adding normal metal as a thermal shunt [10]. However the critical current of niobium increases dramatically as the temperature is reduced and always seems to dominate the retrapping current. By analysing the I-V characteristics of the SQUIDs of chip A described earlier and fitting the KO-1 theory and the thermal models to the data, we can estimate the parameters $R_{n,0}$ and κ which are given in Table 4.2:

The fitted resistivity is also very close to the values reported for thin niobium films $\approx 152\,\mathrm{n\Omega.m}$[147]. According to Wiedemann-Franz's law, it implies $\kappa \approx 1.4\,\mathrm{W/m\,K}$ that in turn implies a thermal length scale of $\eta \approx 2.7\,\mu\mathrm{m}$ which is comparable to the device dimensions in this range of temperature. The heat would then flow radially and the HPCG description is more appropriate, yielding more realistic values for α and the resistivity. Models M-1 and M-2 tend to under-estimate α as in their hypotheses the heat is considered spreading over the whole width of the banks whereas it does not extend that much in reality. The $R_{n,0}$ extracted are in accordance with the resistivity and dimensions of the Nb bridges – about

SQUID	KO-1 T_c K	 $R_{n,0}$ Ω	 R^2	HPCG model ρ nΩ.m	 α kW/m^{2}K	 R^2	Model M1 ρ nΩ.m	 α kW/m^{2}K	 R^2	Model M2 ρ nΩ.m	 α kW/m^{2}K	 R^2
A-1	7.37	1.75	0.91	139	25.8	0.87	37.7	10.8	0.04	562	5.8	0.05
A-2	7.37	1.63	0.78	157	15.8	0.76	40.0	6.9	0.93	710	5.5	0.94
A-3	7.37	2.16	0.80	152	17.1	0.73	41.0	5.9	0.90	774	5.4	0.91
A-4	7.37	2.86	0.75	160	19.8	0.61	48.6	5.5	0.79	964	5.7	0.80

Table 4.2: Fitted parameters of the KO-1 model for I_c and of the thermal models HPCG, M-1 and M-2 for I_r. The data points were taken from the I-V characteristics of samples A-1 to A-4 at 4.2 K and 5.6 K. The samples are made of a 150 nm thick niobium film and the bridges were all 120 nm wide and respectively 250, 300, 400 and 500 nm long.

120 nm wide – allowing for the small additional resistance on both ends due to phase relaxation as stated by Likharev [56].

By using the averaged values $\alpha = 19.64\,\text{kW/m}^2\text{K}$ and $\rho = 152\,\text{n}\Omega\text{.m}$ given by the HPCG model as this is the most accurate thermal model at helium temperatures, we can predict the non-hysteretic temperature range for any bilayer-based Nb nanobridge. As an example, Figure 4.15 shows I_c and I_r for a fixed 100 nm base layer of Nb at 100 mK as a function of the thickness of gold added on top. The critical current I_c is reduced as the critical temperature T_c is lowered by the proximity effect. As the coherence length of gold is approximately 30 nm, adding more gold does not suppress T_c any further whilst the heat transfer keeps increasing. This naively suggests that it would be possible to reach the non-hysteretic regime by adding a very thick layer of gold on top. However, the M-2 model which correctly takes into account the finite device size shows that this layer would have to be prohibitively thick at millikelvin temperatures. To conclude, niobium is indeed not suitable for nanoSQUIDs operated in the millikelvin range and a material with a lower T_c is therefore a requirement. In the following, we will assess the operability of devices based on the three potential materials molybdenum, aluminium and titanium.

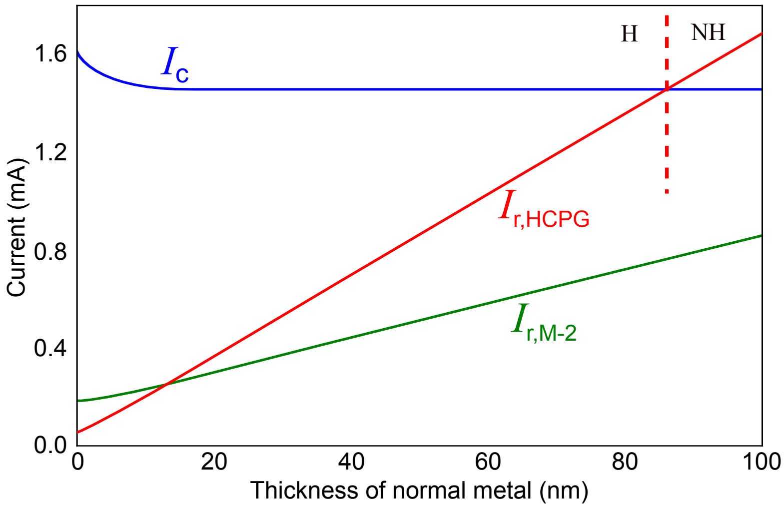

Figure 4.15: Predicted I_c and I_r at 100 mK for different models (in red, HPCG; in green M-2) as a function of the thickness of gold deposited on top of a 100 nm layer of niobium for a 150 nm × 50 nm nanobridge. At this temperature, we assume $\alpha = 20\,\mathrm{W/m^2K}$. The dashed line marks the threshold between the hysteretic regime (H) and the non-hysteretic regime (NH) predicted (incorrectly) by the HPCG model.

4.4.2 Material 1 - Molybdenum

Pure molybdenum goes into superconducting state at 920 mK and is of growing interest in the TES field for its very stable interfaces with gold and copper [137], which both give reproducible and sharp superconducting transitions; and also for its durability for devices that have to endure extreme conditions in space applications. With a boiling point at atmospheric pressure of 4912 K and a low vapour pressure, molybdenum is a good candidate for sputtering. Most papers report a strong increase of conductivity when sputtered at higher energy and when the substrate is heated [148]. However, there are also successful reports of RF-sputtering at very low argon pressure without heating the substrate [46]. We followed the latter using a PVD-75 sputter machine (described in Section 3.5).

We fabricated SQUID B-1 made of a Mo (70 nm)/Cu (70 nm) bilayer with similar dimensions to the niobium SQUID discussed in Section 4.4.1 with a bridge length of 400 nm. We extracted I_c and I_r from the I-V characteristics measured at several temperatures and then fitted the KO-1 and thermal models to this data. The

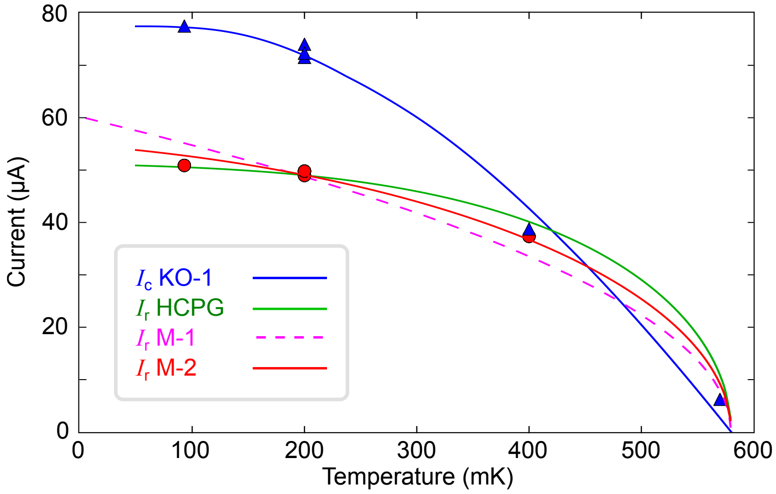

Figure 4.16: Experimental values for I_c (blue triangles) and I_r (red circles) for sample B_1 (Mo (70 nm)/Cu (70 nm)). The lines show the fits to the various thermal models.

results are shown in Table 4.3.

SQUID	KO-1			HPCG model			Model M1			Model M2		
	T_c mK	$R_{\mathrm{n},0}$ Ω	R^2	ρ nΩ.m	α W/m^{2}K	R^2	ρ nΩ.m	α W/m^{2}K	R^2	ρ nΩ.m	α W/m^{2}K	R^2
B-1	580	4.725	0.99	91.5	43.8	0.91	14.4	148.2	0.63	6.72	101.6	0.86

Table 4.3: Table showing the fitted parameters of the KO-1 model for I_c and of the thermal models HPCG, M-1 and M-2 for I_r. The data points were taken from the I-V characteristics of SQUID B-1 at several temperatures ranging from 100 mK to 600 mK. B-1 was made of a Mo (70 nm)/Cu (70 nm) bilayer, with bridges that were 400 nm long and 175 nm wide.

Only M-1 and M-2 appear to predict a reasonable resistivity for the Mo/Cu bilayer, given the expected value at room temperature is 11.25 nΩ.m. The HPCG model leads to an over-estimation of the contact area for thermal exchange with the substrate, giving an over-estimated I_r. For this reason the best fit yields a much higher than expected resistivity to counteract this over-estimation. Using the fitted experimental values for α, ρ and $R_{\mathrm{n},0}$ found using the M-2 model, we can plot the predicted I_c and I_r at 100 mK for a typical small nanobridge (150 nm × 50 nm) as a function of the Cu thickness added on top of a 100 nm Mo base layer. This

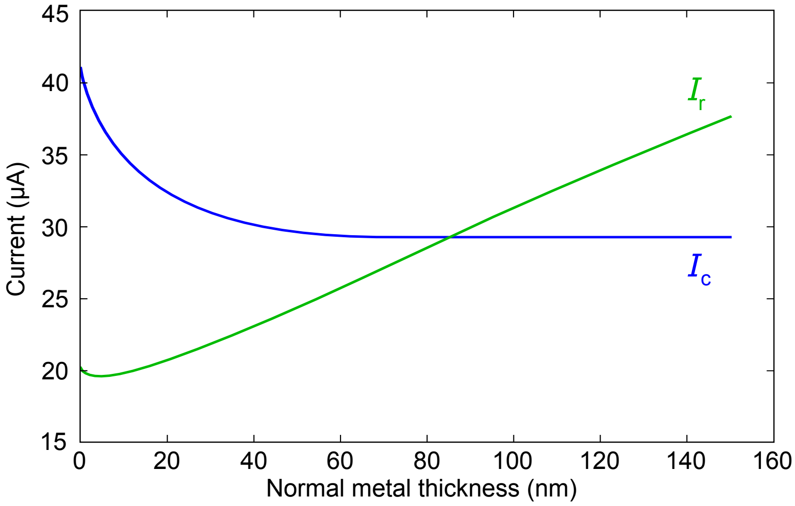

Figure 4.17: Predicted I_c and I_r for a 150 nm × 50 nm bridge with a fixed 100 nm Mo base layer as a function of the thickness of the copper overlayer. The temperature of the substrate is 100 mK.

is shown in Figure 4.17. It shows that the Cu layer must be very thick to obtain non-hysteretic I-V characteristics. Depositing fine lateral features with this sort of thickness is practically impossible to achieve by sputtering and lift-off. For this reason, we decided to favour aluminium and titanium devices and did not investigate Mo/Cu further.

4.4.3 Material 2 – Aluminium

Aluminium is often used to make tunnel junctions thanks to its stable oxide layer [149, 150], and since it is highly conductive and easy to evaporate. A foreseeable difficulty with this material is that its critical temperature is a bit high ($T_c = 1.2\,\mathrm{K}$) and would have to be suppressed by a factor 2. This can be difficult as it is reactive with many compounds, including most noble metals, leading to poor transmission at the interface. For instance, the aluminium/gold interface is not stable at temperatures above 200°C as the two materials form an alloy that is brittle and insulating, dubbed “the purple plague”. Fortunately, there are reports of successful aluminium/silver TES sensors with reproducible properties and a stable interface [138]. Three chips with devices of various bridge lengths were fabricated to study aluminium. Chip C was metallised with 40 nm of bare aluminium, Chip

D with Al (25 nm)/Ag (10 nm) and Chip E with Al (80 nm)/Ag (30 nm). As we did previously, we fit the KO-1 and thermal models to the I_c and I_r taken from the I-V characteristics at several temperature. Figures 4.18 and 4.19 show the experimental values and their best fit for SQUIDs C-2 and D-3 respectively. The fitted parameters for these devices have been tabulated in Table 4.5.

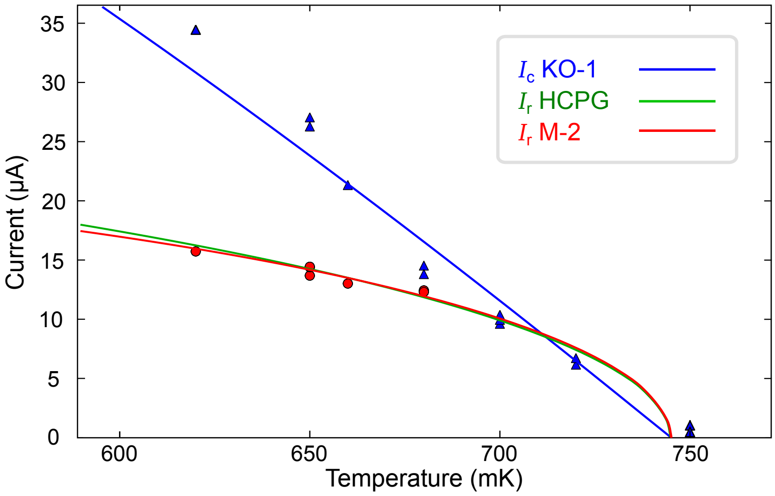

Figure 4.18: Experimental values for I_c (blue triangles) and I_r (red circles) for SQUID C-2 made of a 40 nm thick layer with bridges 200 nm long and 85 nm wide. The lines show the fits to the various models. (Model M-1 is nearly identical to M-2 in this range of temperature and is not shown for clarity.)

SQUID	Material	Bridges dimension (length × width)
C-1	Al (40 nm)	200 nm × 85 nm
C-2	Al (40 nm)	200 nm × 85 nm
D-1	Al (25 nm)/Ag (10 nm)	100 nm × 100 nm
D-2	Al (25 nm)/Ag (10 nm)	250 nm × 100 nm
D-3	Al (25 nm)/Ag (10 nm)	650 nm × 100 nm
E-1	Al (80 nm)/Ag (30 nm)	300 nm × 80 nm

Table 4.4: Dimensions and materials for the various Al/Ag bilayer SQUIDs we fabricated.

As for molybdenum, the M-1 and M-2 models give more physically believable results. The fitted resistivity at low temperature is about one third of that measured

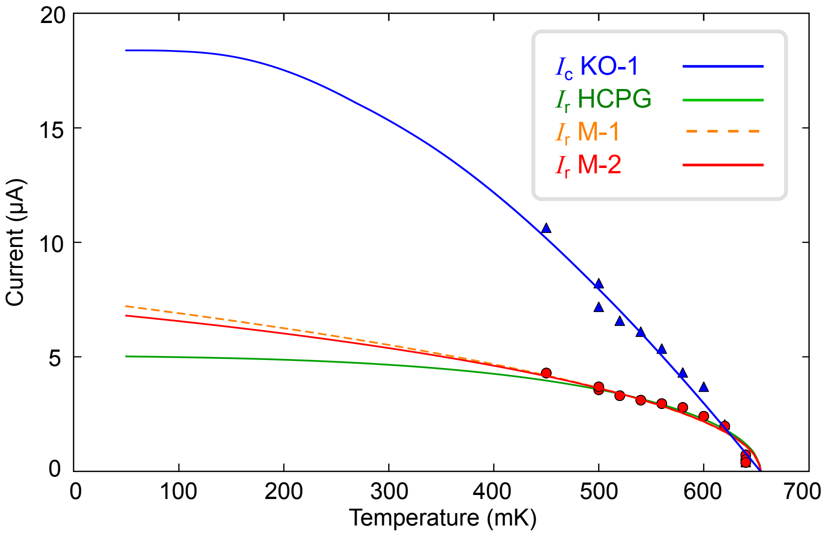

Figure 4.19: Experimental values for I_c (blue triangles) and I_r (red circles) for SQUID D-3 made of an Al (25 nm)/Ag (10 nm) bilayer with bridges 100 nm wide and 650 nm long. The lines show the fit to the various models.

SQUID	KO-1			HPCG model			Model M1			Model M2		
	T_c	$R_{n,0}$	R^2	ρ	α	R^2	ρ	α	R^2	ρ	α	R^2
	mK	Ω		nΩ.m	W/m^{2}K		nΩ.m	W/m^{2}K		nΩ.m	W/m^{2}K	
C-1	755	6.3	0.97	77.6	40.6	0.91	8.8	107	0.92	9.32	192	0.92
C-2	745	4.8	0.94	47.0	12.5	0.89	6.3	105	0.82	7.42	252	0.84
D-1	645	23.7	0.87	287.1	6.3	0.97	122	169	0.97	123	257	0.96
D-2	673	26.7	0.98	264.4	31.3	0.94	120	151	0.97	104	201	0.97
D-3	654	22.5	0.98	181.3	23.0	0.92	107	174	0.93	60.1	175	0.93
E-1	353	2.4	0.93	61.1	31.0	0.72	6.0	49.5	0.83	5.63	273	0.82

Table 4.5: Table presenting the different results fitted for the various Al/Ag bilayer SQUIDs described in Table 4.4.

at room temperature which is consistent with our measurements. The heat transfer coefficient α is one order higher than for Mo. We believe this is the result of the very high film quality generally achieved with electron-beam evaporation of aluminium in a very high vacuum $\sim 10^{-7}$ mbar. For deposition of silver, we developed a technique to enhance the thermal contact. We first added a 1 nm wetting layer of germanium before depositing silver, then aluminium. The germanium allows an ultra-smooth silver layer, following a recipe used in optics [151], and gives a contact between the layers that is close to ideal. Using the experimental values we obtained from the M-2 model to get the averaged $\alpha = 225\,\mathrm{W/m^2K}$, we can predict I_c and I_r for any Al/Ag nanobridge. The curve for a typical 150 nm × 50 nm nanobridge with various silver thicknesses deposited on top of a base layer of 80 nm is shown in Figure 4.20. Both metals are highly conductive and therefore the retrapping current is high, but as aluminium has a fairly large gap, I_c tends to be very high as well. It would require about 85 nm of silver to have non-hysteretic Al bridges down to 100 mK.

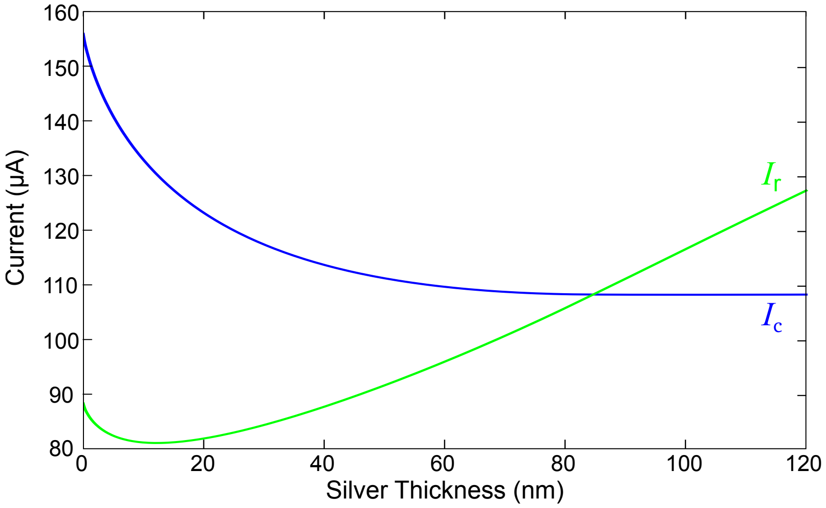

Figure 4.20: Predicted I_c and I_r using Model M-2 as a function of the thickness of Ag added on a 80 nm thick, 150 nm × 50 nm Al bridge for $T_\mathrm{b} = 100\,\mathrm{mK}$.

4.4.4 Material 3 – Titanium

Titanium has often been used for TES sensors thanks to its T_{c} of 390 mK and its good interface with gold (though some intermixing has been reported [152, 136]). It is most commonly deposited by electron beam evaporation and is often used to provide a good non-magnetic adhesion layer with noble metals. It is also very sensitive to the evaporation conditions, especially the presence of oxygen and magnetic contaminants, which can have a significant effect on its T_{c} [153]. In order to determine more accurately the heat transfer coefficient, we measured the retrapping current and the critical current for four bare Ti SQUIDs of Chip F, all made of a 150 nm thick titanium film with various bridge lengths and a width of 100 nm. We also fabricated two SQUIDs G-1 and G-2, made of Ti (105 nm)/Au (15 nm), with gold evaporated first, as a check of the thermal properties of devices deposited in that way. Experimental results and fitted theories are presented for SQUID F-1 (bridges 200 nm × 100 nm) in Figure 4.21(a) and the fitted parameters of the different models are tabulated in Table 4.6.

SQUID	KO-1			HPCG model			Model M1			Model M2		
	T_{c}	$R_{\mathrm{n},0}$	R^2	ρ	α	R^2	ρ	α	R^2	ρ	α	R^2
	mK	Ω		nΩ.m	W/m^{2}K		nΩ.m	W/m^{2}K		nΩ.m	W/m^{2}K	
F-1	712	47.6	0.86	1711	27.5	0.76	225	7.2	0.73	166	11.1	0.86
F-2	71	49.1	0.67	1711	6.9	0.93	254	19.8	0.51	116	8.6	0.81
F-3	725	47.8	0.68	1470	3.0	0.75	225	18.3	0.69	126	13.4	0.81
F-4	65	18.8	0.94	1749	37.5	0.89	197	7.2	0.52	130	10.7	0.78
G-1	445	22.5	0.92	1250	16.3	0.95	52	4.2	0.71	36	14.6	0.95
G-2	375	28.7	0.97	1185	20.6	0.85	61	5.6	0.97	38	17.8	0.99

Table 4.6: Table presenting the different results fitted for various Ti/Au bilayer SQUIDs. SQUIDs F-1, F-2, F-3 and F-4 are made of bare Ti (150 nm) with bridges that are 215 nm wide and respectively 300 nm, 500 nm, 600 nm and 700 nm long. SQUIDs G-1 and G-2 are made of Ti (105 nm)/Au (15 nm) and both have 300 nm × 110 nm bridges.

Although bare titanium is hysteretic at all temperatures in the millikelvin range like the other superconductors we studied, it should be noted that its I_{c} is but

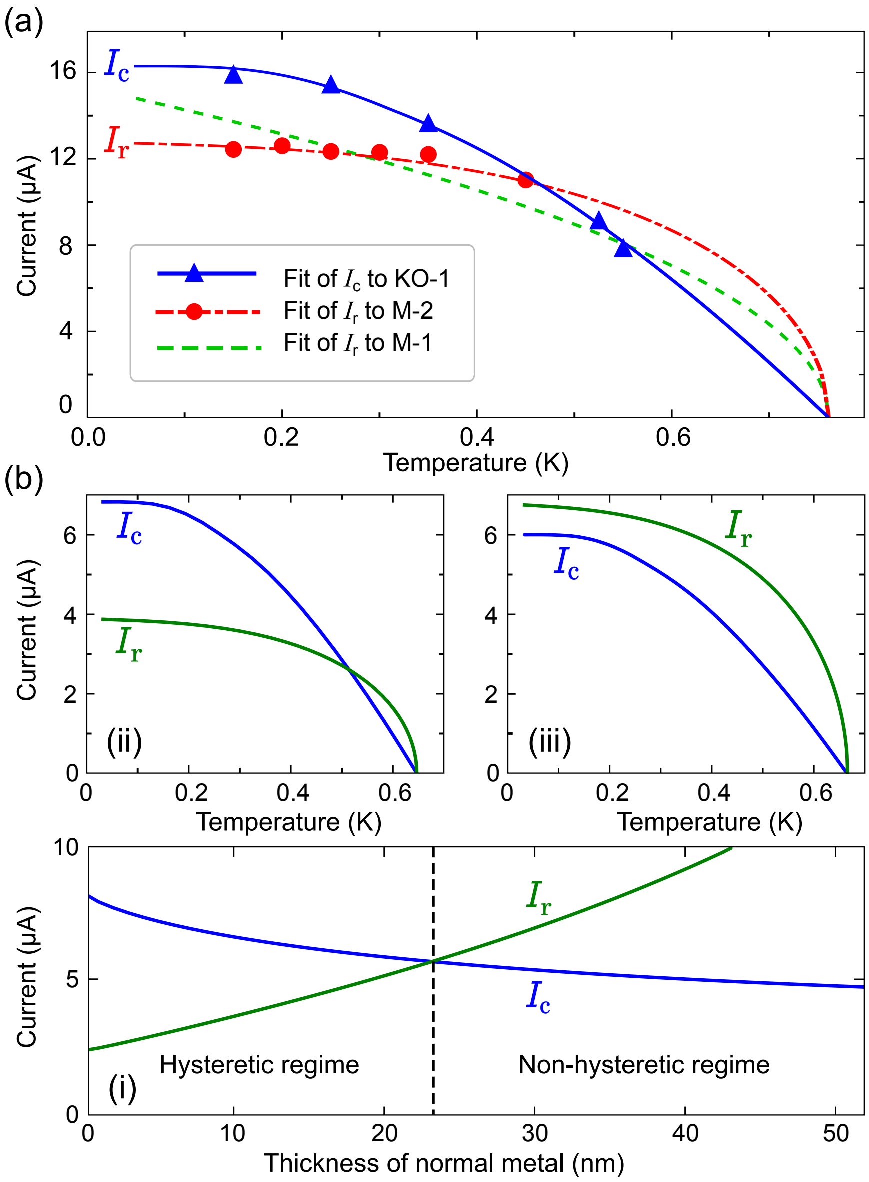

Figure 4.21: (a) Fits to the measured I_c and I_r for the pure Ti SQUID F-1. (b)(i) The predicted I_r and I_c for a Ti/Au nanobridge at a fixed temperature of 60 mK as a function of the normal metal thickness d_N on a superconducting layer of thickness $d_S = 100$ nm. The device will be non-hysteretic down to 60 mK if $d_N > 23$ nm. Examples of the predicted temperature dependencies of I_c and I_r on either side of this threshold are shown in (ii) for $d_N = 10$ nm and in (iii) for $d_N = 25$ nm. The device with $d_N = 10$ nm shows hysteresis in the region where $I_r < I_c$. The device with $d_N = 25$ nm shows no hysteresis at any temperature.

a fraction of that of niobium and aluminium, being the order of a few μA for a 150 nm × 50 nm bridge. This low critical current is due to the reduced T_c and a smaller carrier concentration. Whilst this is an advantage in terms of Joule heating, it is double-edged as it means titanium has a relatively high resistivity as well: 420 nΩ.m at room temperature which is large compared to aluminium (28.2 nΩ.m) or niobium (152 nΩ·m). Due to this, the retrapping current tends to be small as well.

The T_c of our titanium films is a bit higher than the bulk value which is likely due to traces of oxygen during evaporation affecting the film. Figure 4.21(b) clearly shows that having a non-hysteretic behaviour at any temperature is achievable by adding more than 23 nm of gold on a 150 nm × 50 nm bridge with a 100 nm Ti layer. This thin layer provides a heat conduction sufficient to tackle the reduced Joule heating due to the smaller critical current.

4.4.5 Outcome of the Material Study

In conclusion, only aluminium and titanium appear to be suitable superconducting materials for the development of bilayer nanoSQUIDs that would be non-hysteretic at 100 mK. To choose between these we can consider the fact that the power dissipated by the Joule effect once the bridge turns normal is RI^2. As resistance and critical current are roughly inversely proportional, titanium will transfer less heat to the substrate than aluminium due to its lower critical current and higher resistance. This would also limit detrimental heating effects on the systems of interest to study as these can be very temperature sensitive. In the following, we will therefore mainly focus our study on titanium/gold devices.

4.5 Demonstration of Non-hysteretic Devices Based on Titanium

Figure 4.22 shows the I-V characteristics of SQUID F-1 mentioned previously made of 150 nm thick titanium with bridges that were 300 nm × 120 nm, operated at 200 mK. The hysteresis is quite large and remains so up to $T = 575$ mK. As

$T_c = 745\,\mathrm{mK}$, it means the hysteretic behaviour starts below $0.8\,T_c$ which is in good agreement with the prediction shown in Figure 4.21.

To test the prediction of Figure 4.21, we made another device: SQUID H-1, made in the same conditions and with the same geometry but with 25 nm of gold layer deposited under the titanium. This device proved to be completely hysteresis-free at this temperature as shown by its I-V characteristics in the inset of Figure 4.23. I-V measurements down to the base temperature of the ADR (60 mK) showed no hysteresis at all. The fit of the KO-1 theory to the experimental data shown in Figure 4.23 indicates the critical temperature is 446 mK and the fitted value for $R_{n,0}$ is $49.04\,\Omega$ with a R^2 coefficient of 0.93.

4.6 Conclusion

In this chapter, we have first developed a thermal model (M-2) describing the hot spot formation at millikelvin temperatures much more accurately than the two existing models developed for He temperatures. Using our thermal model in combination with the KO-1 model to analyse experimental data, we then predicted the minimal amount of normal metal to add on any bridge to make it non-hysteretic at a given temperature. A candidate of choice appeared to be titanium due to its reduced critical current and good contact with gold. We succeeded in making titanium/gold devices that proved to be non-hysteretic down to 60 mK. However, solving the issue of hysteresis was only the first step toward the fabrication of nanoSQUIDs operating in the millikelvin range. In Chapter 5, we will build upon this progress to solve two further issues affecting non-hysteretic devices in the millikelvin range, a large kinetic inductance and some excess heat, to achieve the best performance.

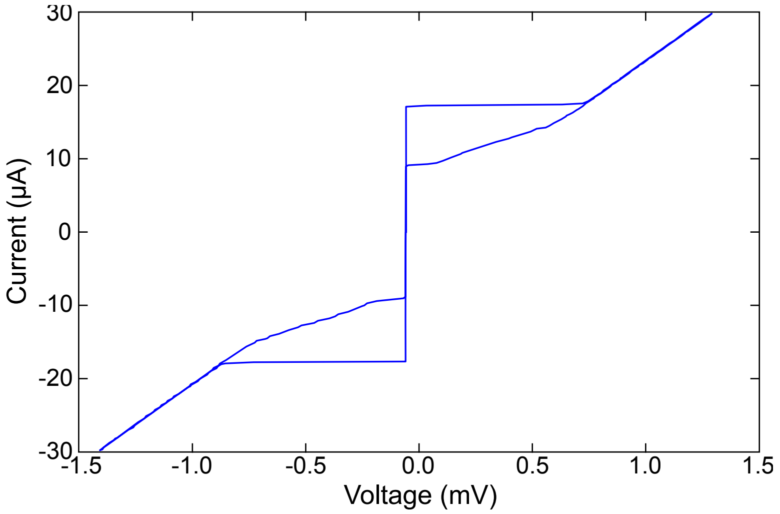

Figure 4.22: I-V characteristic for SQUID F-1 made of bare Ti (150 nm thick) at 100 mK, showing a pronounced hysteresis.

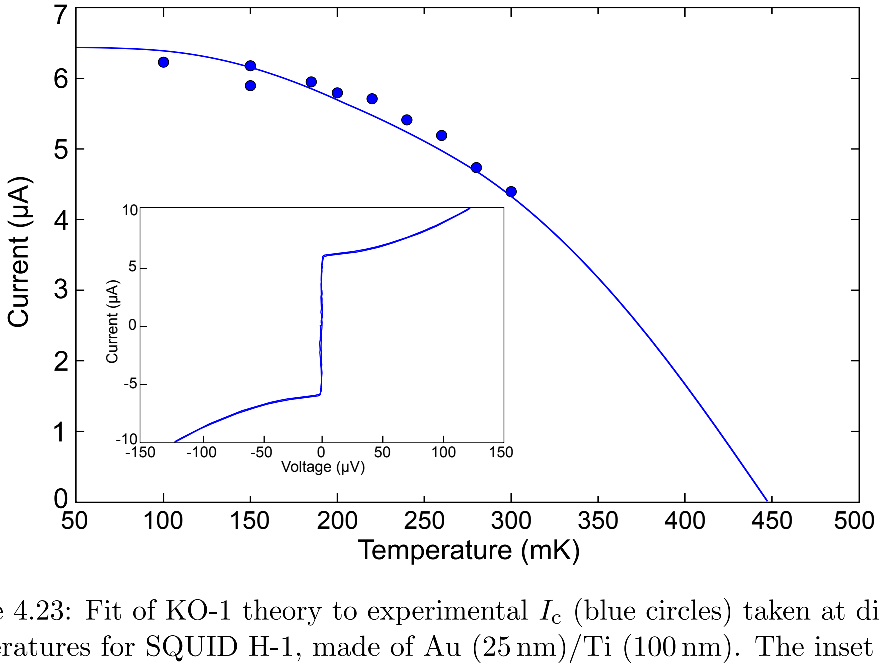

Figure 4.23: Fit of KO-1 theory to experimental I_c (blue circles) taken at different temperatures for SQUID H-1, made of Au (25 nm)/Ti (100 nm). The inset shows the I-V characteristic at 60 mK for the device, without any hysteresis.

Chapter 5

3D NanoSQUIDs for Improved Thermal & Flux Sensing Performance

5.1 Problems with Existing Devices

5.1.1 Outline of Issues

To the untrained eye the I-V characteristics for the non-hysteretic SQUID H-1 we obtained in Chapter 4, shown again in Figure 5.1, would seem perfect and could be a textbook example. However, when we attempted to measure voltage modulations in an applied magnetic field, we could only see them in a very narrow bias current region just above what appeared to be the critical current. A close-up of this region, shown in the inset of Figure 5.1, reveals in fact the existence of two critical features in superconductivity: the bridges[1] have a first jump to the voltage state at I_c followed by a second to a higher resistance at a larger current that we will call I_sat. For device H-1, the usable bias current was very narrow as

---

[1] In the following, to keep a consistent notation throughout and with the literature, I_c, I_b, I_sat and R_n are parameters for a single junction. They can be deduced from the I-V characteristics of the SQUIDs as the junctions are symmetrical (see Section 5.4.1 for a discussion on the symmetry of the bridges).

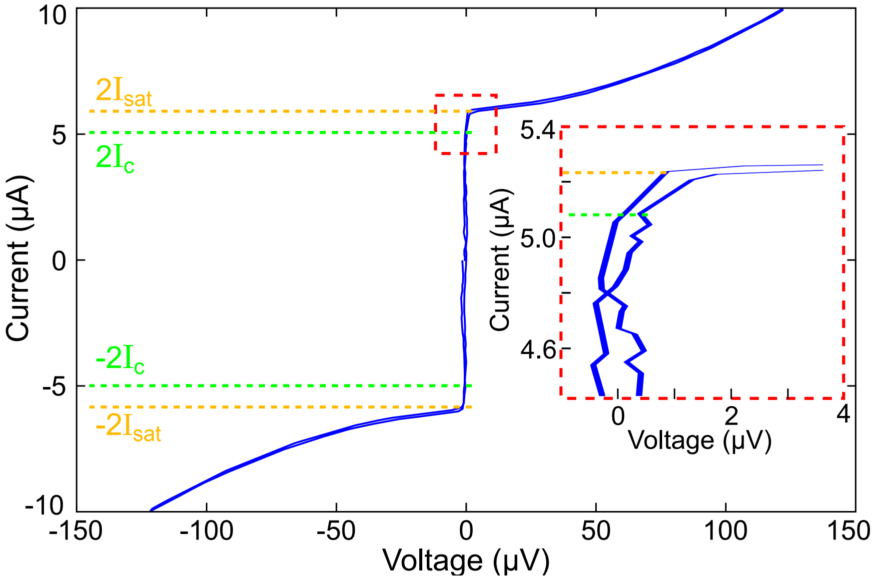

Figure 5.1: I-V characteristics at 150 mK of SQUID H-1, made of Au 25 nm/Ti 100 nm bilayer. The inset is a magnified view of the dashed region on the graph which shows the two breakdowns in superconductivity at $2I_{\rm c}$ and $2I_{\rm sat}$.

$I_{\rm sat} \approx 1.025\, I_{\rm c}$. The optimum bias current is typically found at $\sim 1.2\, I_{\rm c}$. Above $I_{\rm sat}$, the measured resistance corresponds to that of the whole device in normal state which indicates the superconductivity is entirely destroyed. As we will see in detail in Section 5.1.2, this is due to excess heat generated by the Joule effect.

Also, the best voltage-flux response $V(\Phi)$ for SQUID H-1 we could obtain given our limited bias range, shown in Figure 5.2, had a poor peak-to-peak modulation depth ΔV of only 5 μV at 150 mK. This is small compared to the $I_{\rm c}R_{\rm n}$ product $\sim$ 17 μV, and limits the device sensitivity. As we will discuss in Section 5.1.3, this is due to a large kinetic inductance component of the SQUID inductance. We thus have identified two issues that need to be solved to achieve the full potential of the device: excess heat and large kinetic inductance. We will analyse these in the following.

5.1.2 Full analysis: Excess Heat

As we saw above, the entire SQUID goes into the normal state and cannot be operated when the bridges are current-biased above $I_{\rm sat}$. As the heat transfer coefficient α is very small in the millikelvin range ($\sim$ 20W/m^{2}K), this behaviour is

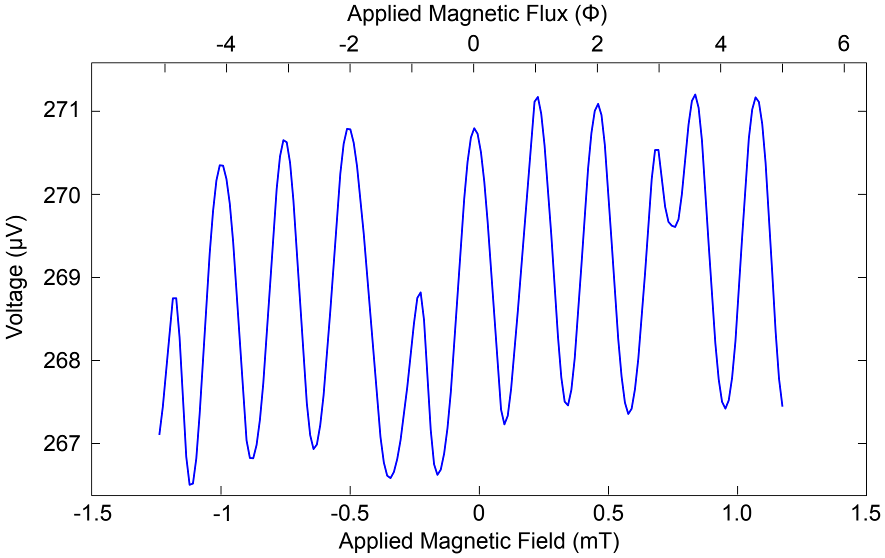

Figure 5.2: Voltage as a function of applied magnetic field at 150 mK for SQUID H-1 and bias current of 2.6 μA, smoothed by a running average.

likely to have thermal origins. In this section, we will describe how the thermal model M-2 [2] we developed in Chapter 4 can be used to account for this excess heat issue.

If we consider the curves showing the relationship between the bias current I and the hotspot radius r_0 for the SBT and HPCG models (see Figure 5.3 for an example for unrealistically large bias currents), we can see that I diverges when r_0 tends to infinity. In other words, these models suggest that there is always a mathematical solution for r_0 satisfying the heat flow equations for any arbitrary current flowing through the nanobridge, regardless of any limitation due the physical dimensions of the device. Unlike these models, the M-2 model successfully accounts for the existence of the maximum current I_{sat} for which thermal equilibration can be achieved. As shown in Figure 5.4, I tends to an horizontal asymptote I_{sat} when x_0 tends to infinity.

The equation for this asymptote can be very easily determined by considering

---

[2] The model M-1 can of course be used as well for the I_{sat} analysis. However, M-2 was proven more accurate to describe the physics in Chapter 4. For clarity, we will therefore only discuss M-2 in this section.

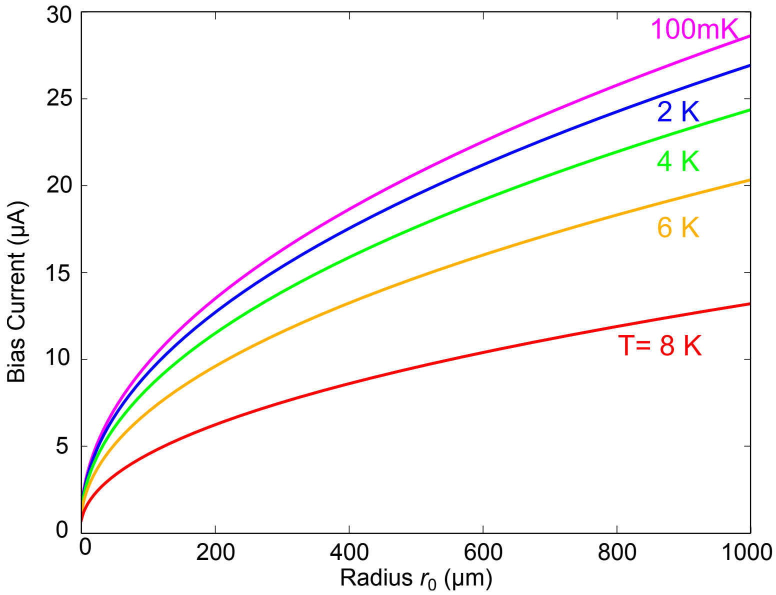

Figure 5.3: Bias current versus r_0 for a 150 nm × 50 nm × 100 nm Nb nanobridge according to the HPCG model at various bath temperatures ranging from 100 mK to 8 K. The reduction of α with temperature is not taken into account and is set to 20 kW/m^{2}K. The bank width is 2 μm.

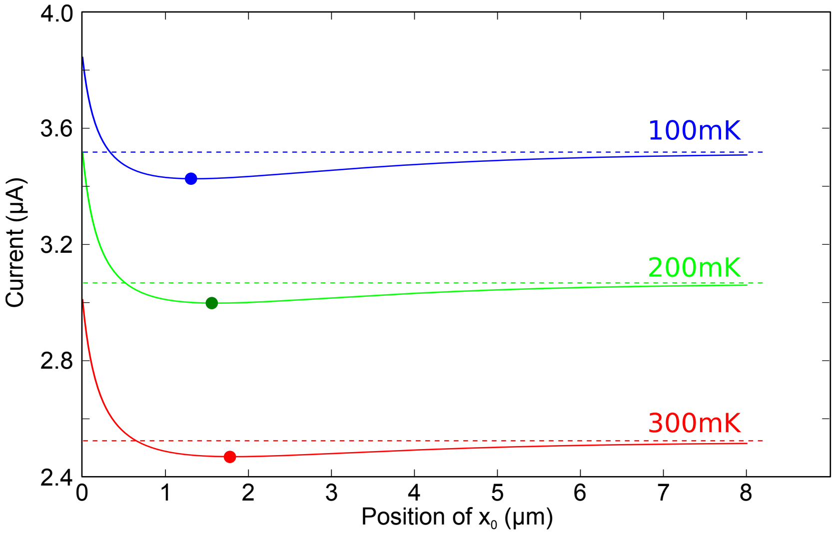

Figure 5.4: Bias current versus the position of x_0 along the x-axis using the M-2 model. The solid lines correspond to a 150 nm × 50 nm × 100 nm bridge of titanium ($\rho_{\mathrm{mK}} \approx 200\,\mathrm{n\Omega.m}$, $T_{\mathrm{c}} = 445\,\mathrm{mK}$) at bath temperatures ranging from 100 mK to 300 mK. The heat transfer coefficient α is set to 20 W/m^{2}K. The bank width is 2 μm. The dots show the minimum of current to sustain the hotspot, i.e. the retrapping current I_{r}. The dashed lines correspond to the asymptotes I_{sat}.

the limit $x_0 \to +\infty$ in Equation 4.30 giving:

$$I_{\text{sat}} \approx \sqrt{\frac{\alpha W^2 d}{\rho} \frac{\eta}{2\gamma} T_{\text{c}}(T_{\text{c}} + T_{\text{b}})(T_{\text{c}} - T_{\text{b}})} \tag{5.1}$$

where l_{b}, w_{b} and t_{b} are the dimensions of the bridges, L_{strip}, W and d the dimensions of the banks, $\eta = \sqrt{\kappa d/\alpha}$ and $\gamma = \sqrt{d\kappa(1 + T_{\text{b}})/2\alpha T_{\text{c}}}$. κ is the thermal conductivity of the banks and ρ the electrical resistivity of the bridges. The bridges can only be current-biased between I_{c} to I_{sat}. Should $I_{\text{c}} > I_{\text{sat}}$, the heat generated by the bridges on entering the normal state leads instantly to a breakdown of superconductivity for the whole device.

From Equation 5.1, we can see that in order to maximise I_{sat} we have to get α as large as possible. As discussed in Section 4.3.6, α includes the heat flow going to the substrate and the heat flow going to the contact tracks. To increase the latter, we developed a new process to connect the SQUIDs to the contact pads with larger, thicker, more conductive tracks during a subsequent fabrication step. The first device to benefit from this technical improvement was SQUID J-1 made from a Au (25,nm)/Ti (100 nm) bilayer, with a 5 µm^2 loop and 150 nm × 75 nm bridges. The chip was re-coated with PMMA and the fine tracks leading from the macroscopic contact pads to the devices were patterned by EBL using fine alignment marks deposited in the same step as the SQUID. As we were no longer limited by the requirement in this step to pattern ultrafine features of a certain material, i.e. the nanobridges, we could use a thicker resist, higher exposure current and deposit different materials such as sputtered niobium or thick thermally evaporated gold for the tracks. We used 400 nm-thick gold contact tracks to connect SQUID J-1 as shown in Figure 5.5 before and after deposition of the contacts. Its I-V characteristics were then measured down to 120 mK and the KO-1 theory and the M-2 model were fitted to the experimental data for I_{c} and I_{sat} as shown in Figure 5.6. The fits are very good and give a value for α that is 50 % larger than we obtained in Chapter 4 for SQUIDs without these thicker contact tracks. Thanks to

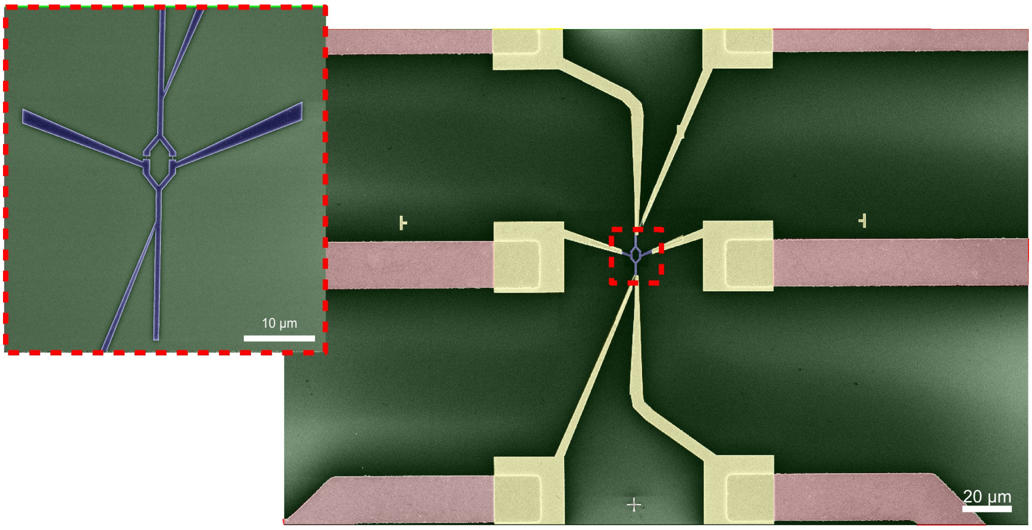

Figure 5.5: False-coloured SEM micrographs of SQUID J-1. In red: pretemplated Nb (200 nm)/Au (200 nm) contact tracks. In a first step, small alignment marks (yellow crosshairs) were deposited in the same fabrication step as the SQUID (in blue). The inset shows the SQUID magnified and before the deposition of the contact tracks. Thick gold (400 nm) contact tracks (in yellow) were deposited on the SQUID during the final fabrication step.

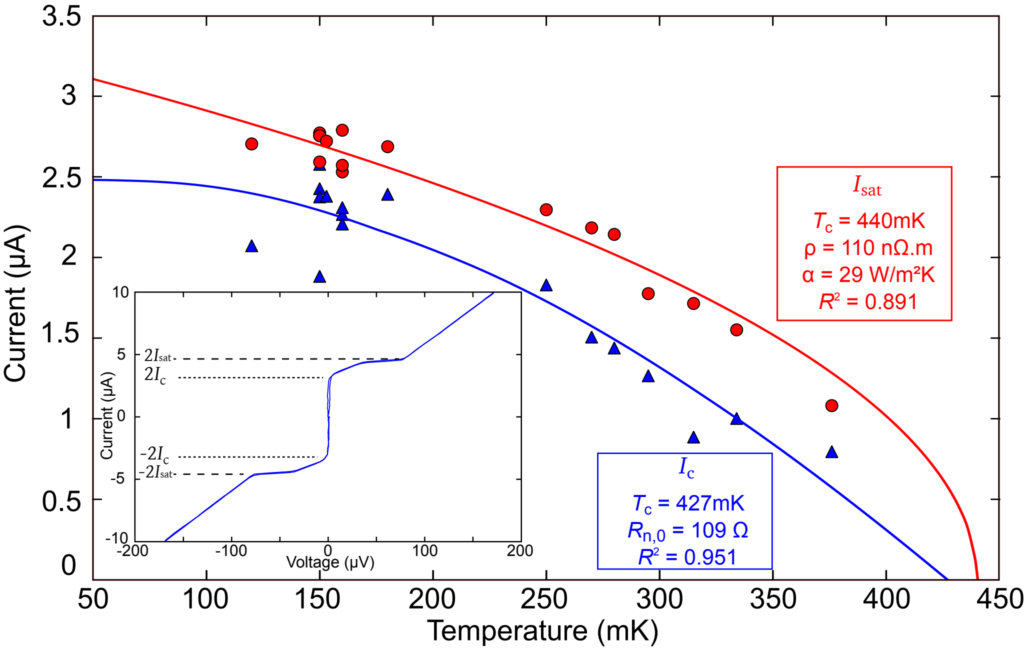

Figure 5.6: Experimental I_c (blue triangles) and I_{sat} (red circles) at different temperatures for SQUID J-1. The red line is a fit of the M-2 model for I_{sat} and the blue line a fit of the KO-1 theory. In inset: the I-V characteristics for this device showing the two distinctive critical features in superconductivity I_c and I_{sat} at 120 mK.

this we were able to increase I_{sat} to $\sim 2.75\,\mu\mathrm{A}$ at 120 mK, which is $\sim 1.17\,I_{\mathrm{c}}$. This is already a larger usable bias range, closer to the typical optimum bias current. As a check on the M-2 model, we used the COMSOL finite-element model we described earlier to estimate the temperature distribution of SQUID J-1. The results are shown in Figure 5.7 for $T_{\mathrm{b}} = 100\,\mathrm{mK}$ at two bias currents. At $1.1\,I_{\mathrm{c}}$, the bridge temperature exceeds 700 mK and the normal region extends over about 3 μm. At a bias current of $1.3\,I_{\mathrm{c}}$, i.e. above I_{sat}, the heat has spread over $\sim 10\,\mu\mathrm{m}$ so that the two arms of the SQUID loop are entirely in the normal state which prevents any $V(\Phi)$ modulation. According to Equation 5.1, the wider and thicker the banks, the higher I_{sat} will be. Evidence of this is clearly shown by the COMSOL model as the temperature is about 50% lower in the region where the side tracks are located. Though initially intended to couple flux to the device by passing current through part of the SQUID loop, these tracks also behaved as cooling fins. Such features were then intentionally added to all subsequent devices. However, making the banks globally wider would increase the effective area of the devices and lower their spin sensitivities. Also, making the whole film thicker would be counter-productive as the resistance would be lowered but the critical current increased, yielding an overall larger Joule effect. The only solution would be to increase the bank thickness whilst not increasing the thickness of the bridges. The technical solution to this problem will be described in a later section.

5.1.3 Further Analysis: Kinetic Inductance

Another concern that arose when measuring SQUID H-1 was the low modulation depth. As we saw, the modulation depth ΔV for an ideal SQUID of negligible inductance should be of the order of the $I_{\mathrm{c}}R_{\mathrm{n}}$ product [80]:

$$\Delta V = \frac{I_{\mathrm{c}}R_{\mathrm{n}}}{1+\beta_L} \tag{5.2}$$

The $\Delta V = 5\,\mu\mathrm{V}$ we measured for SQUID H-1 is somewhat lower than the $I_{\mathrm{c}}R_{\mathrm{n}}$ product $\sim 17\,\mu\mathrm{V}$. This poor modulation depth could be due to asymmetrical

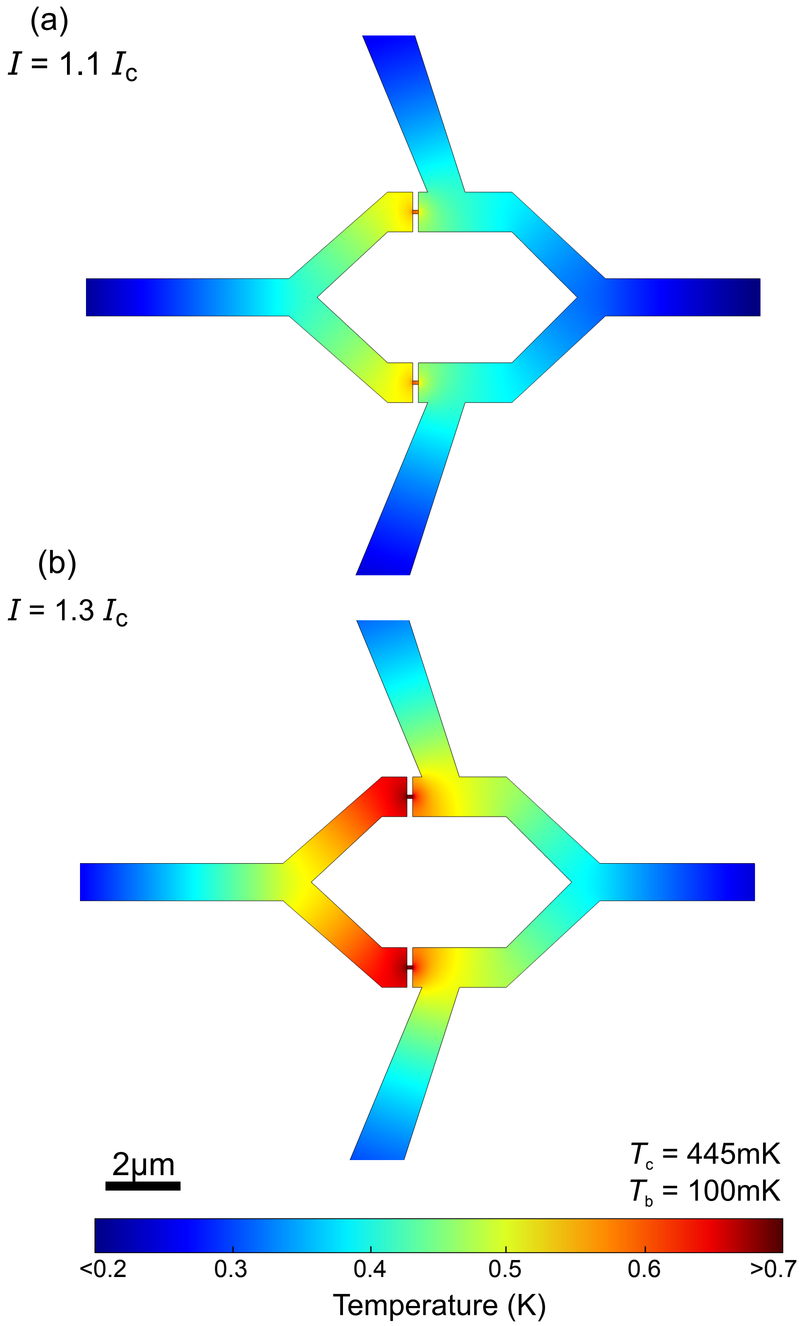

Figure 5.7: Finite element model of the temperature distribution at bias currents of (a) 1.1 I_c and (b) 1.3 I_c showing the reason for the limited bias range at a base temperature of 100 mK. In (b) the hotspots extend so far that the two arms of the SQUID loop are fully normal (> 445 mK) thus preventing any SQUID modulation.

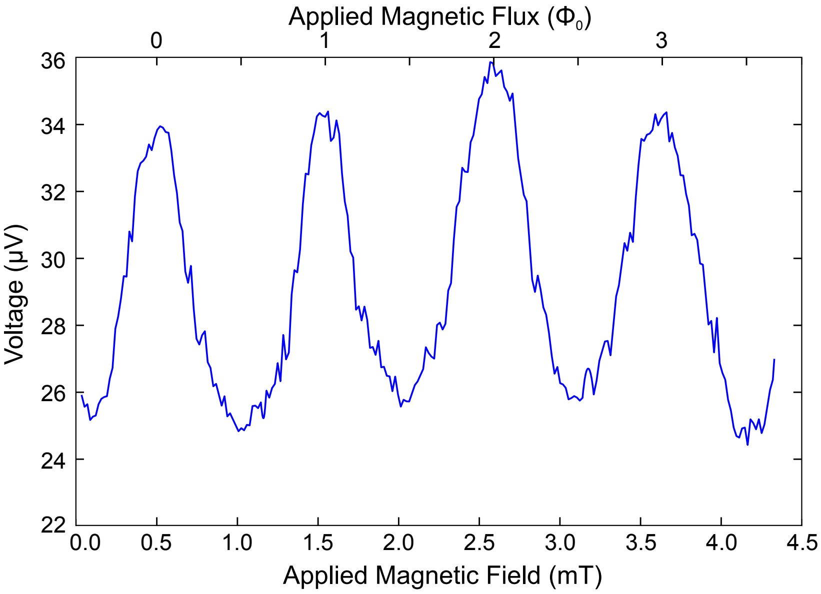

Figure 5.8: $V(\Phi)$ characteristics for J-1 at 160 mK for the bias current $I_b = 4.8\,\mu\text{A}$ giving the best modulation we could achieve because of the limited bias range due to excess heat.

bridges but as we will discuss in detail in Section 5.4.1 later in this chapter, this is not the case for our nanoSQUIDs. We can therefore postulate that the low ΔV is due to a high inductance. Assuming at the optimum bias that the modulation depth for SQUID H-1 is not considerably larger than the value we measured, and assuming that the bridges are symmetrical, this would imply $\beta_L \approx 2.5$ which would suggest a very large inductance for the device of $\sim 1\,\text{nH}$. SQUID J-1 thanks to its improved α could be biased closer to the optimal bias current. The best $V(\Phi)$ curve we could obtain, shown in Figure 5.8, presents a modulation depth $\Delta V = 10.8\,\mu V$ which according to the above means that $\beta_L \sim 1.05$ which yields an estimate for the inductance of about $L \sim 495\,\text{pH}$. A large inductance for a SQUID is an issue as this reduces the flux sensitivity of the device and affects its ultimate flux noise as $T \to 0$ limited by the Heisenberg uncertainty principle: $\Phi_{\text{ns,Q}} = \sqrt{2L\hbar}$. Such a high inductance cannot be explained by only considering the geometrical inductance L_{geo}. As we are considering devices made of superconducting films with dimensions comparable to the London penetration depth λ, we have to account for the kinetic inductance L_k, due to the kinetic energy of the Cooper pairs. For a superconducting wire of diameter d, $L_\mathrm{k} = 4\,\mu_0\lambda^2/\pi d^2$ per unit length [154]. The penetration depth in the dirty limit can be estimated using [155, 25]:

$$\lambda(T) = \lambda(0)\sqrt{\frac{\Delta(0)}{\Delta(T)}\coth\left(\frac{\Delta(T)}{2k_B T}\right)} \tag{5.3}$$

$$\text{where } \lambda(0) = \sqrt{\frac{\hbar\rho_0}{\pi\mu_0\Delta(0)}}. \tag{5.4}$$

Figure 5.9 shows the estimated penetration depth as a function of temperature for the three superconducting materials of our study where the resistivities used are the measured values. As expected, superconductors with a higher T_c or a lower resistivity tend to have a smaller penetration depth. This is due to a larger concentration of Cooper pairs allowing the existence of stronger screening currents. Aluminium, thanks to its high conductivity, and niobium, thanks to its relatively high T_c, have both very short penetration depths, respectively $\lambda_0 \sim 120\,\mathrm{nm}$ and

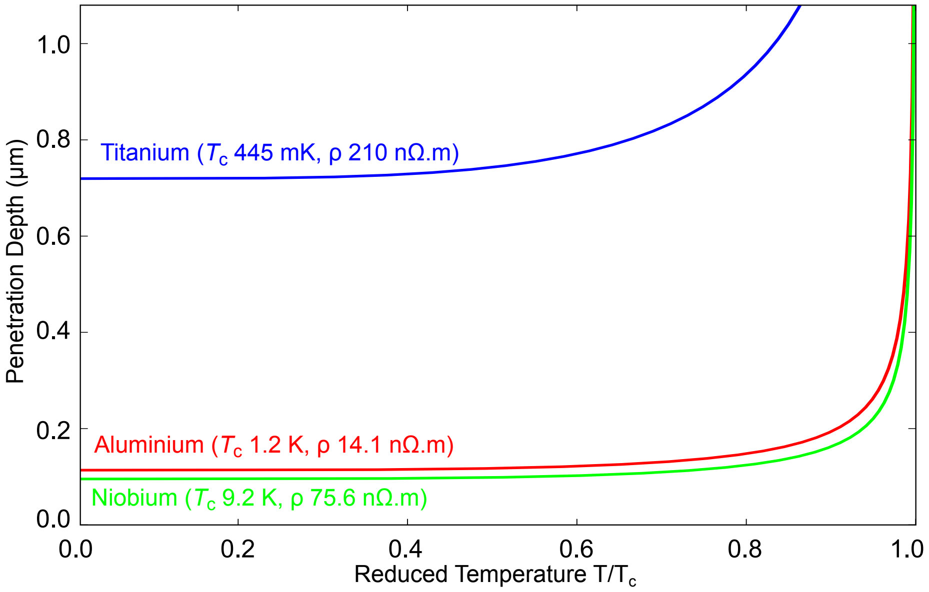

Figure 5.9: Penetration depth as a function of temperature for the three materials of our study: niobium, aluminium and titanium, estimated using Equation 5.3 and film resistivities in the millikelvin range equal to 1/3 the bulk resistivities at room temperature, which are approximately the typical values we noticed in our experiments.

$\lambda_0 \sim 90\,\mathrm{nm}$. However, titanium has both a poor conductivity and a low T_c which translates into a longer $\lambda_0 \sim 740\,\mathrm{nm}$. This is the cause of the high L_k.

To estimate the total inductance $L = L_\mathrm{geo} + L_\mathrm{k}$ for our nanoSQUIDs, we used the package 3D-MLSI [156] to model the inductance of the devices using finite-element analysis. The device geometry is represented in the form of a text file with the vertex coordinates. A typical code to generate this is given in Appendix B. The images rendered after meshing of the finite elements and after simulation are shown in Figure 5.10.

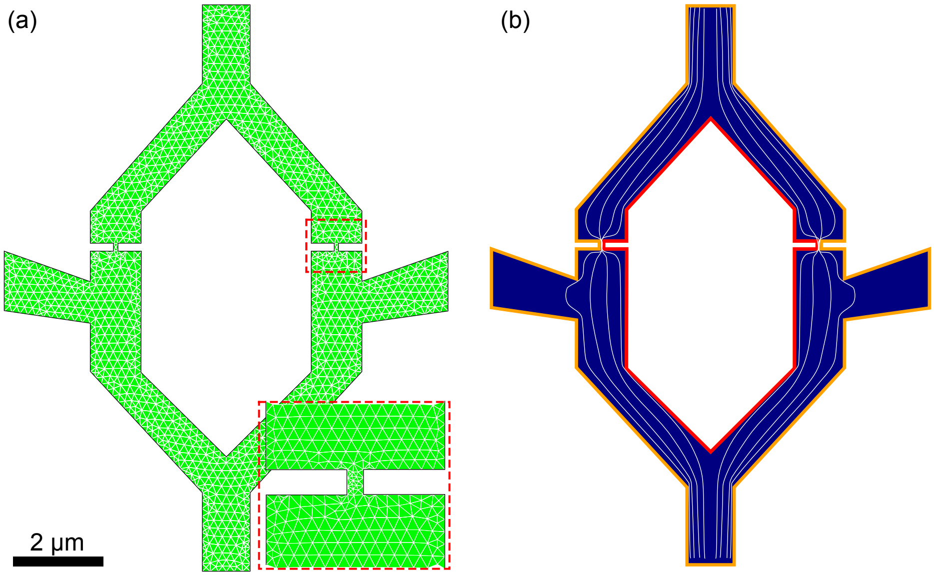

Figure 5.10: (a) 3D-MLSI model for J-1 (a) after meshing of the triangular finite elements. The size can be adjusted to fit some features as seen in the inset for a bridge. (b) The 3D-MLSI output after the finite element analysis showing the current lines.

3D-MLSI is limited to modelling a device with given parameters. To allow batch calculations and automatic data processing with varying parameters, we wrote a custom interface in Python. An important input parameter is the penetration depth λ of the SQUID material. Using our model, we were able to plot the predicted inductance of our device versus the penetration depth we input. This is shown in Figure 5.11 for SQUID J-1 for two film thicknesses: 100 nm which corresponds to the actual thickness of the real device, and 300 nm for comparison to illustrate the

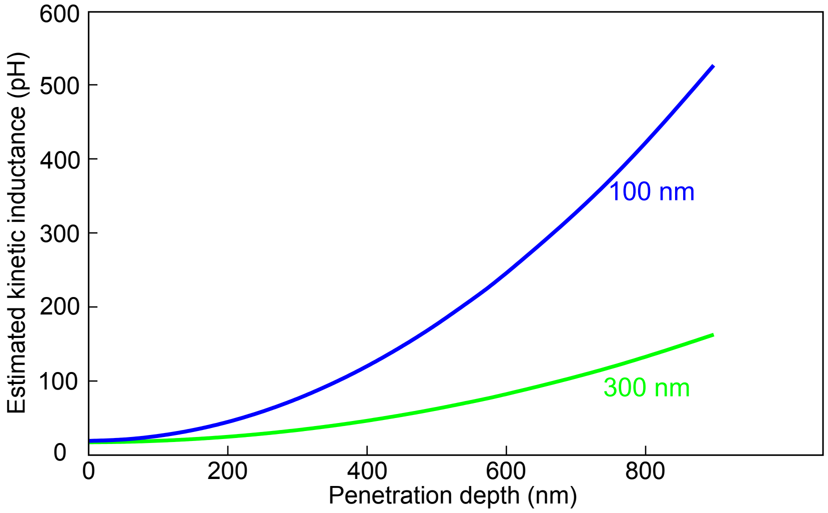

Figure 5.11: Estimated inductance of SQUID J-1 as a function of the λ input in the 3D-MLSI model for two film thicknesses 100 nm and 300 nm.

effect of a thicker film. As λ increases, L_{k} increases quadratically and completely dominates the geometrical component which we assume to be the residual value for $\lambda \to 0$: $L_{\mathrm{geo}} = 18\,\mathrm{pH}$. Using the plot, we can determine that the penetration depth corresponding to a total inductance of 415 pH is $\lambda \sim 760\,\mathrm{nm}$. This is in good agreement with the estimate from the conductivity. In contrast with this, if SQUID J-1 was made of aluminium ($\lambda \approx 120\,\mathrm{nm}$) its total inductance would be close to the geometrical value $\sim 25\,\mathrm{pH}$. However, as the better penetration depth of aluminium is a result of its higher carrier concentration, the critical current across the bridges would be larger as well by approximately the same order of magnitude, theoretically reaching more than 100 µA for a 100 nm film of bare aluminium, so β_L might not be smaller for this material. Similarly, increasing the thickness of the whole superconductor would lower the inductance but would increase I_{c} as well, which is counter-productive in terms of β_L. As the bridges account for approximately 20 % of the inductance whilst the rest is due to the loop body, it clearly appears that thickening the banks selectively would tend to lower the overall inductance without affecting I_{c}.

To conclude, we have identified two issues affecting planar devices: some excess heat generated by the Joule effect which limits the usable current bias range of the devices, and a high kinetic inductance due to the thickness of the film being comparable with the penetration depth. Both these issues can be addressed by thickening the banks selectively.

5.2 Fabrication of 3D NanoSQUIDs

To solve the issues we described above, we adapted a shadow evaporation technique introduced by Vijay *et al.* [14] to our proximity bilayers nanoSQUIDs. In the following we describe the modified fabrication process to obtain nanoSQUIDs whose banks are much thicker than the bridges, that we will call “3D devices” in contrast with “planar devices”. The technique involves angling the sample *in situ* during the evaporation. The edge of the PMMA then acts as a shadow mask and the metal can no longer enter fine features in the resist such as the nanobridges but can still be deposited in the broader parts such as the tracks and the loop. The patterning process is similar to that of planar SQUIDs and is achieved using EBL. The beginning of the metallisation process is also similar: to metallise the nanobridges the sample directly faces the evaporation source allowing the evaporated metal to reach all the features independently of their sizes. It should be noted that the noble metal needs to be evaporated first in order to use this technique. As titanium is commonly used as an adhesion layer for gold, this does not affect the bilayer quality. An initial evaporation of 0.5 nm of titanium efficiently ensures the adhesion of the gold to the substrate. After the initial nanobridge metallisation, the device cross-section appears as shown in Figure 5.12. In our initial devices, the PMMA layer was 240 nm thick (a single layer of PMMA 950 k A4 spun at 3000 RPM) which limited the overall metal thickness that could be deposited to ~ 170 nm. We later succeeded in patterning several PMMA layers up to 800 nm thick using a highly focussed 30 kV electron-beam whilst still keeping a linewidth below 50 nm. A lift-off at that point would give a conventional planar SQUID. When the crystal monitors indicate that the desired

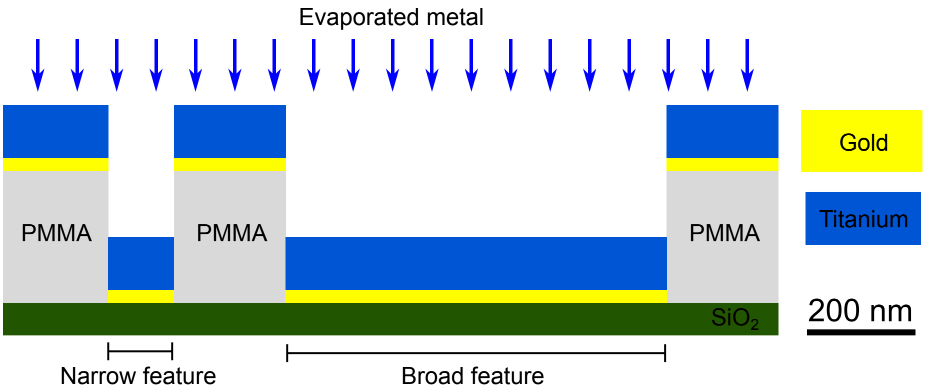

Figure 5.12: Schematic diagram showing a cross-section of the different layers of the planar metallisation, just before tilting the sample.

thickness of perpendicularly-evaporated titanium has been deposited (typically 100 nm), the sample is tilted *in situ*. This is done by having the sample sitting on a custom-made table that is attached flat at the beginning of the evaporation and is released to an angle when we activate the sample rotator. The angle has to be optimised before loading the evaporator according to the thickness of PMMA. It has to be large enough to ensure there is no deposition in the fine features but small enough to minimise the shadow on the banks. Typical angles are approximately 35° for 240 nm, 25° for 500 nm and 15° for 750 nm of PMMA. Figure 5.13 illustrates how the edges of the PMMA shadow-mask the smaller features as the evaporated metal is no longer deposited perpendicular to the surface.

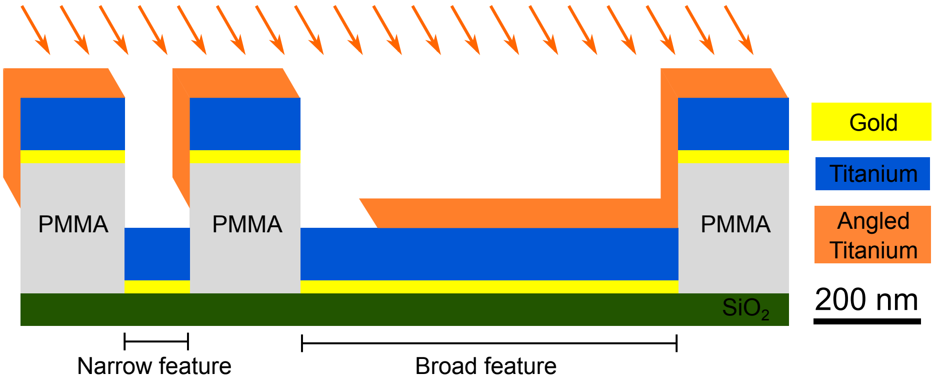

Figure 5.13: Schematic diagram showing a cross-section of the different layers during the angled metallisation.

After lift-off in acetone, features of different widths will present different thickness profiles as shown in Figure 5.14: the fine features are left unchanged while the broader features have been selectively thickened. The thickness of extra material that can be added is proportional to the thickness of PMMA, we were able to deposit up to 450 nm of additional metal using a 800 nm thick PMMA layer that was the maximum thickness we could pattern whilst keeping a linewidth below 50 nm.

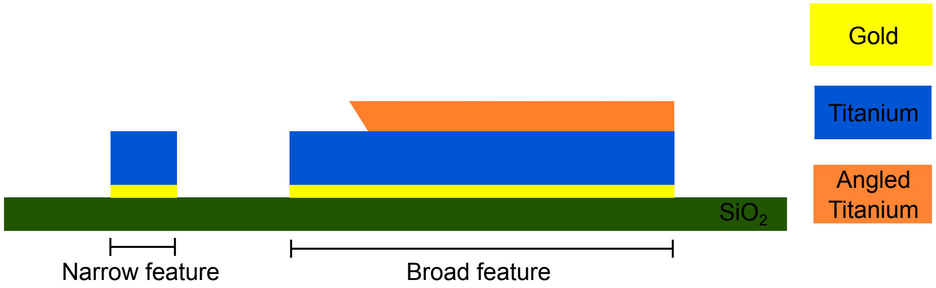

Figure 5.14: Schematic diagram showing a cross-section of the different layers after lift-off. The broad features have been selectively thickened.

5.3 3D Devices & Excess Heat

By using the angle deposition technique, we fabricated four SQUIDs: L-1, L-2, P-1 and Y-1 with increasing titanium thickness. All were based on a Au (25 nm)/Ti (100 nm) bilayer for the bridges upon which were added 45 nm of extra titanium for SQUID L-1, 65 nm for SQUID P-1 (shown in Figure 5.15) and 250 nm for SQUID Y-1 (shown in Figure 5.16). L-2 was made identical to L-1 as a check of the reproducibility of our fabrication process. The other devices shared the same overall shape, but with some slight differences that were taken into account in the modelling.

The I-V characteristics for these devices are shown in Figure 5.17. As expected, the ratio of I_{sat} to I_{c} increases as more titanium is added on the banks. The usable bias range was up to $1.6\,I_{\mathrm{c}}$ for SQUID P-1, $1.8\,I_{\mathrm{c}}$ for SQUID X-1 and $4.6\,I_{\mathrm{c}}$ for SQUID Y-1 before I_{sat} was reached. As we did earlier for SQUID J-1, we can fit the KO-1 model to the experimental I_{c}, and the M-2 model to the experimental I_{sat}, to determine the heat conduction parameters. As there is no hysteresis, the

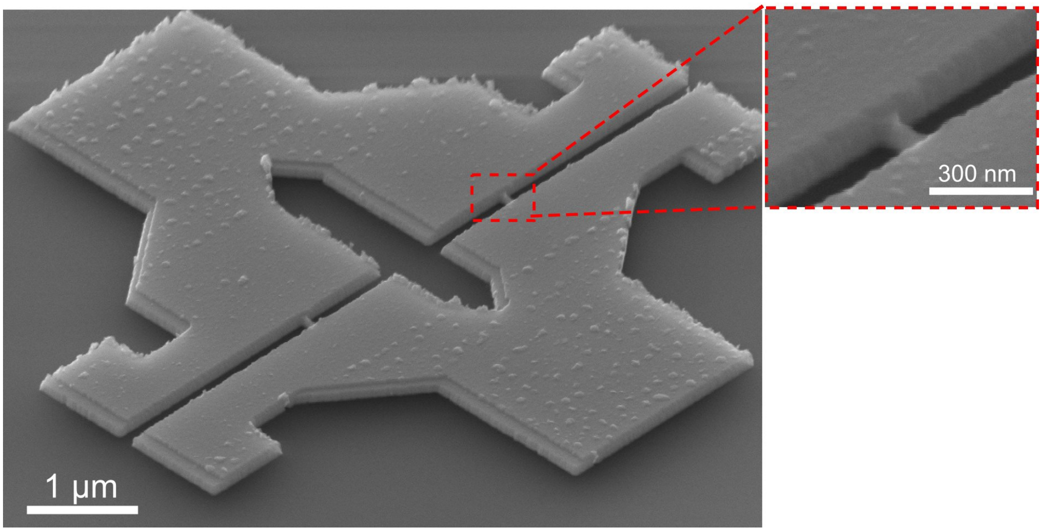

Figure 5.15: SEM micrographs of SQUID P-1 Au (25 nm)/Ti (100 nm)/angled Ti (65 nm) seen with a 34° viewing angle. The inset is a magnified view of the bridge region.

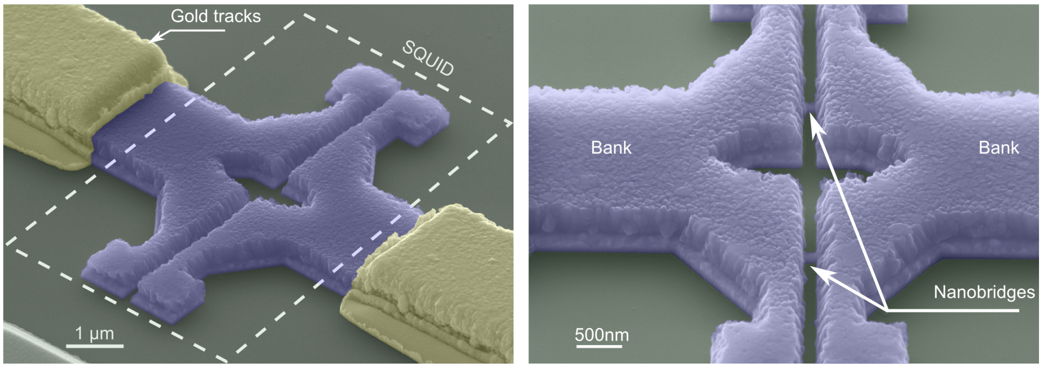

Figure 5.16: False-coloured SEM micrographs of SQUID Y-1 Au (25 nm)/Ti (100 nm)/angled Ti (300 nm) seen with a 34° viewing angle under two different orientations.

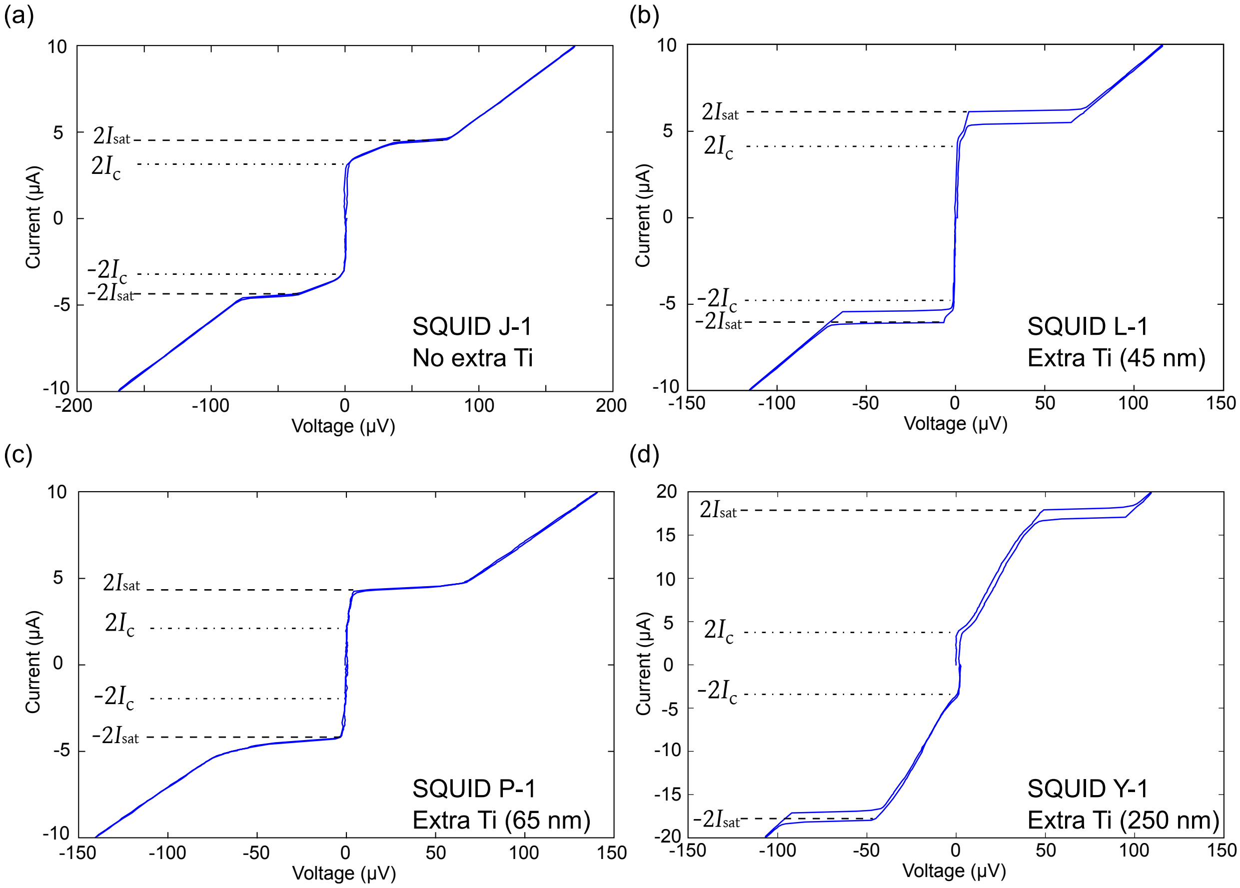

Figure 5.17: I-V characteristics at 100 mK for SQUIDs (a) J-1, (b) L-1, (c) P-1, and (d) Y-1, showing I_{c} and I_{sat}.

value of the retrapping current cannot be measured so this is the only way to access thermal parameters such as α. The analyses for SQUIDs L-1, P-1 and Y-1 are shown in Figures 5.18, 5.19 and 5.20 respectively.

The critical current is not affected by the presence of more titanium, its slight decrease being due to narrower bridges as we improved the patterning by EBL. The fitted value $R_{\mathrm{n},0}$ is larger than the measured resistance at large bias. As we mentioned earlier, this is due to the fact that the shunt resistance of the gold is depressing the measured resistance whilst not affecting the superconducting properties of the titanium other than by depressing T_{c}. The critical temperature of the banks is higher than that of the bridges as the proximity effect is weaker on a thicker layer of titanium. This is an advantage as it renders the SQUID loop

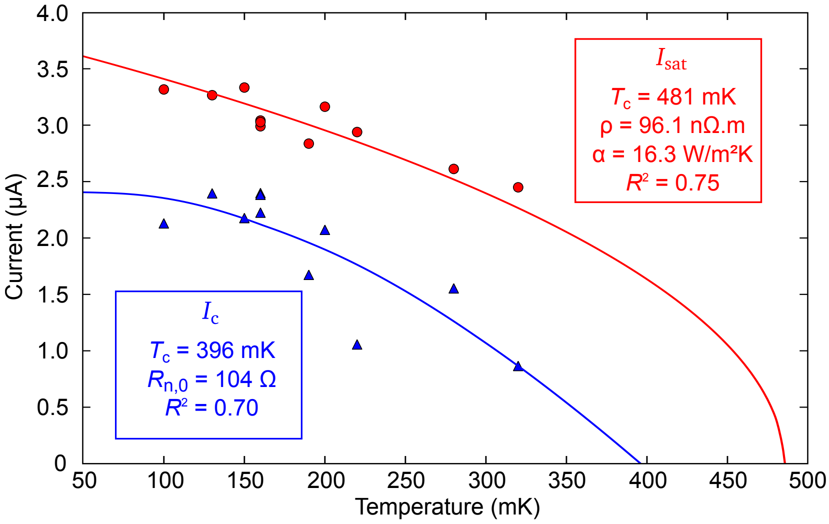

Figure 5.18: Fit of KO-1 theory to the experimental I_c (blue triangles) and the M-2 model to the experimental I_{sat} (red circles) at different temperatures for SQUID L-1.

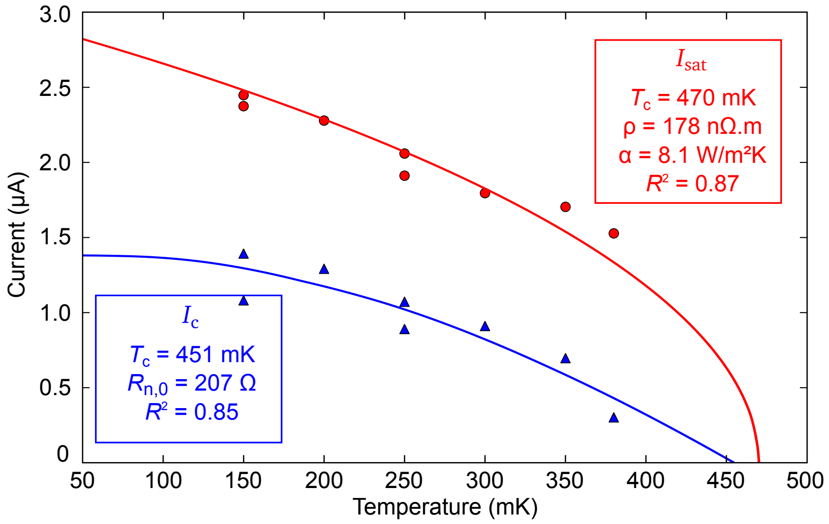

Figure 5.19: Fit of the KO-1 theory to the experimental I_c (blue triangles) and the M-2 model to the experimental I_{sat} (red circles) at different temperatures for SQUID P-1.

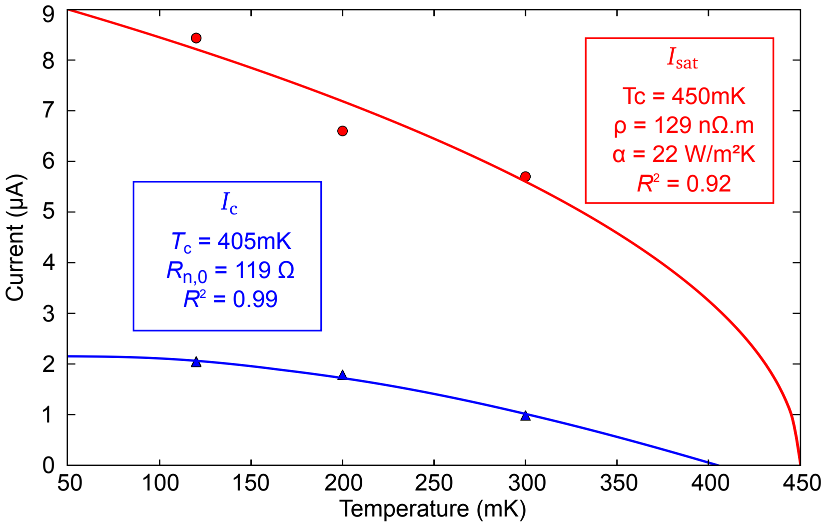

Figure 5.20: Fits of the KO-1 theory to the experimental I_c (blue triangles) and of the M-2 model to the experimental I_sat (red circles) taken at different temperatures for SQUID Y-1.

less sensitive to the excess heat. The values of α obtained from the fits to I_sat, $\alpha \sim 8 - 22\,\text{W/m}^2\text{K}$, are consistent with the magnitude we obtained in Chapter 4 from the study of I_r which confirms the validity of the M-2 model.

To further validate our model, we modelled SQUID Y-1 using COMSOL with the parameters obtained from the fit. The results, shown in Figure 5.21, confirm that both arms of the SQUID loop go into normal state at bias current $I_\text{b} = 4.6\,I_\text{c}$. The normal region at $I_\text{b} = 1.3\,I_\text{c}$ is contained in the nanobridges only and their temperatures are below T_c. This means that the bridges will go into superconducting state as soon as I_b is reduced below I_c, which confirms the fact they are not hysteretic in the millikelvin range.

We can conclude that 3D nanoSQUIDs offer a complete solution to the excess heat issue, allowing a much wider bias range to optimally operate the devices. As the optimal I_b is typically found around $1.2\,I_\text{c}$, only a small amount of additional titanium is actually needed. However adding more superconductor further helps containing the hotspot, and lowers the SQUID inductance. This is discussed in the next section.

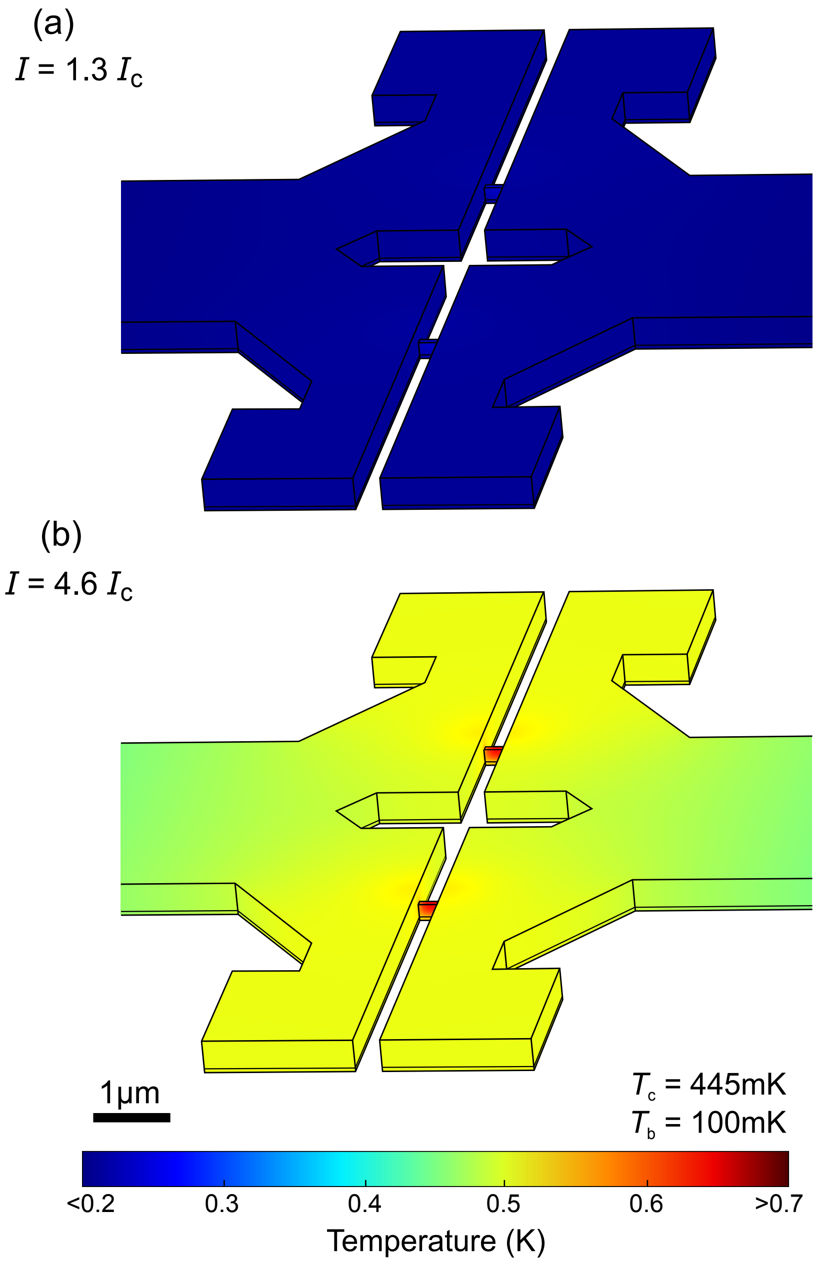

Figure 5.21: (a) The modelled temperature distributions at bias currents of (i) $1.3\,I_\mathrm{c}$ and (ii) $4.6\,I_\mathrm{c}$. In (i) the self-heating is negligible, whereas in (ii) the two arms of the SQUID loop have become normal.

5.4 Performances of 3D NanoSQUIDs with Reduced Inductance

In the previous section, we showed that the 3D profile efficiently alleviates the issue of excess heat. In this section, we first investigate the effect of thicker banks on the other issue mentioned: the large kinetic inductance of the devices. This study will be performed using the $V(\Phi)$ characteristics in applied magnetic field of the 3D nanoSQUIDs introduced in the previous section plus some new devices taking advantage of an aluminium overlayer described later. In the present section, we first assess how symmetric the nanobridges are and from then discuss the effect of the lower inductance on the modulation depth ΔV. We then estimate the noise performance of the devices, and conclude with the predicted spin sensitivity since this is the primary goal of our nanoSQUIDs.

5.4.1 Symmetry of the Bridges and Optimisation of Current Bias

A first step before any measurement using a dc-biased SQUID is to find the optimal bias current I_b, i.e. the bias giving the largest voltage modulation ΔV in an applied magnetic field. This optimisation, done systematically on all devices, is shown in Figure 5.22 for SQUID J-1. This ensures we find the optimal transfer

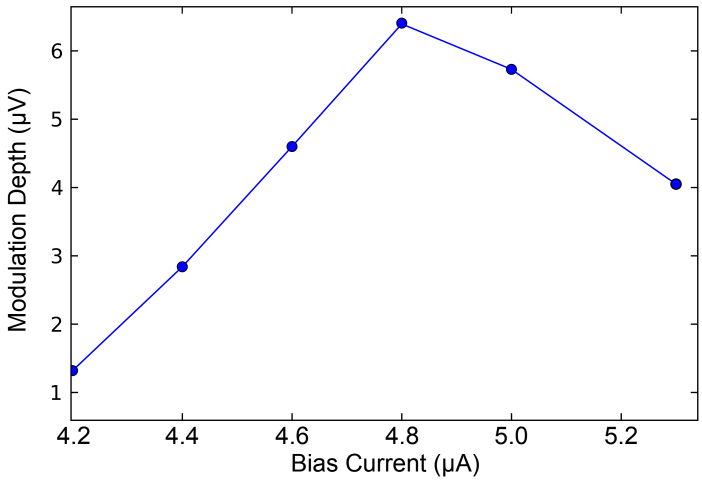

Figure 5.22: Modulation depth ΔV measured for SQUID J-1 at 150 mK as a function of bias current. The bias current maximising the voltage response is $I_\mathrm{b} = 4.8\,\mu\mathrm{A}$.

function $V_\Phi = (\delta V/\delta \Phi)_{\max}$, which will be $V_\Phi = \pi \Delta V/\Phi_0$ for a perfectly sinusoidal device. It is also possible to use the V_Φ at different I_b to assess the symmetry of the bridges, which is an indication of how good the fabrication process is. As we saw in Figure 1.15, there are two main factors leading to a reduced peak-to-peak modulation ΔV which in turn is detrimental to the SQUID performance: the asymmetry between the two nanobridges and the screening parameter β_L. To exclude the former, we analysed the $V(\Phi)$ curves at various bias currents for several SQUIDs. Figures 5.23 and 5.24 show this for SQUIDs J-1 and Y-1 respectively. If there was an asymmetry α_sym between the two junctions, the currents flowing through junctions 1 and 2 would be $I_\mathrm{j1} = (1 + \alpha_\mathrm{sym})I_\mathrm{b}$ and $I_\mathrm{j2} = (1 - \alpha_\mathrm{sym})I_\mathrm{b}$. This would lead to a circulating current $\delta I = 2\alpha_\mathrm{sym} I_0$ which would couple a magnetic flux of $\delta\Phi = L\delta I = 2L\alpha_\mathrm{sym} I_\mathrm{b}$ to the SQUID. From the Figures 5.23 and 5.24, there is no detectable shift to the limit of our resolution. As the distance between two data points is 6 µT, which for a SQUID of effective area $A_\mathrm{eff} = 10\,\mu\mathrm{m}^2$ corresponds to a magnetic flux of $0.03\,\Phi_0$, we can therefore conclude that $\delta\Phi < 0.03\,\Phi_0$. Taking

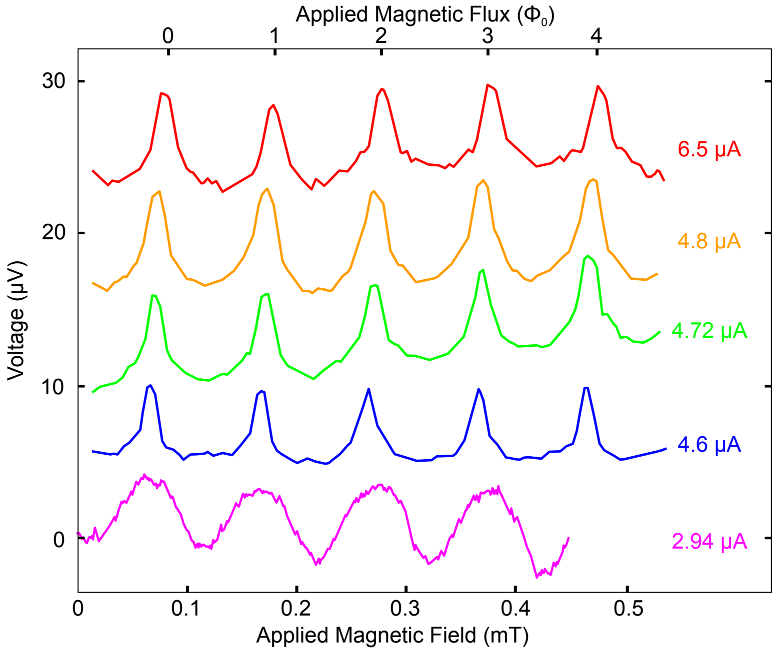

Figure 5.23: $V(\Phi)$ characteristics of SQUID J-1 at 150 mK at various bias currents ranging from 2.94 µA to 6.5 µA.

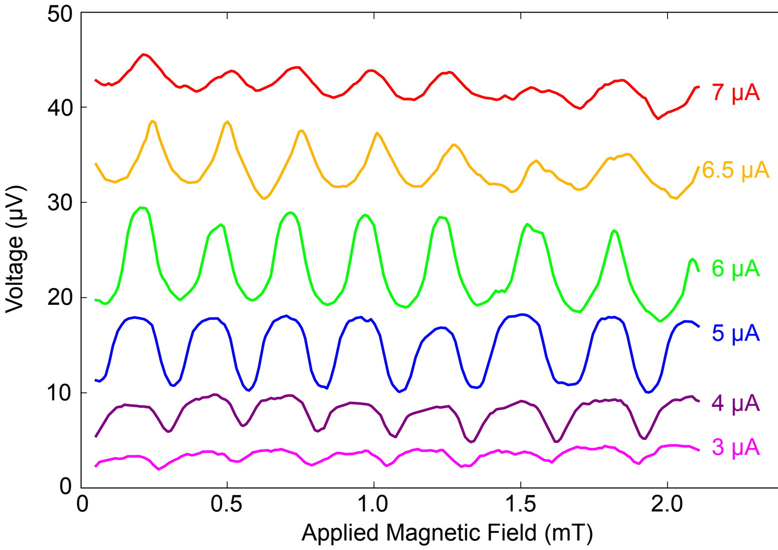

Figure 5.24: $V(\Phi)$ characteristics of SQUID Y-1 at 100 mK at various bias currents ranging from 3 μA to 7 μA.

$L \approx 100\,\mathrm{pH}$ we have $\alpha_{\mathrm{sym}} < 0.08$. According to the simulations by Tesche and Clarke [65] shown in Figure 1.15, this asymmetry is negligible and would result in a drop of ΔV of less than 2 %. The bridge can therefore be considered symmetrical which is also confirmed by the very high yield of our fabrication process.

5.4.2 Modulation Depth & Inductance

In the following, all values given for ΔV are assumed to be at the optimal bias current. Figure 5.25 shows the best $V(\Phi)$ characteristics we obtained for the SQUIDs described above. The $V(\Phi)$ curves are mostly sinusoidal which given the fact the bridges are symmetric confirms the validity of the equation $\Delta V \approx I_\mathrm{c}R_\mathrm{n}/(1+\beta_L)$. There are only some slight deviations from the sine in the vicinity of $\Phi_0/4 + n\Phi_0/2$ where the curve appears to be slightly steeper than a perfect sine. This means the maximum of the transfer function V_Φ will be slightly higher than the estimate $\pi\Delta V/\Phi_0$ which assumes a perfectly sinusoidal response. This is in fact an advantage as it improves the flux noise. From the $V(\Phi)$ curves and the parameters I_c and R_n of the SQUIDs, we estimated β_L and L for the 3D Ti nanoSQUIDs, with the values tabulated in Table 5.1.

To check the reliability of the inductance estimated using ΔV, we compare it

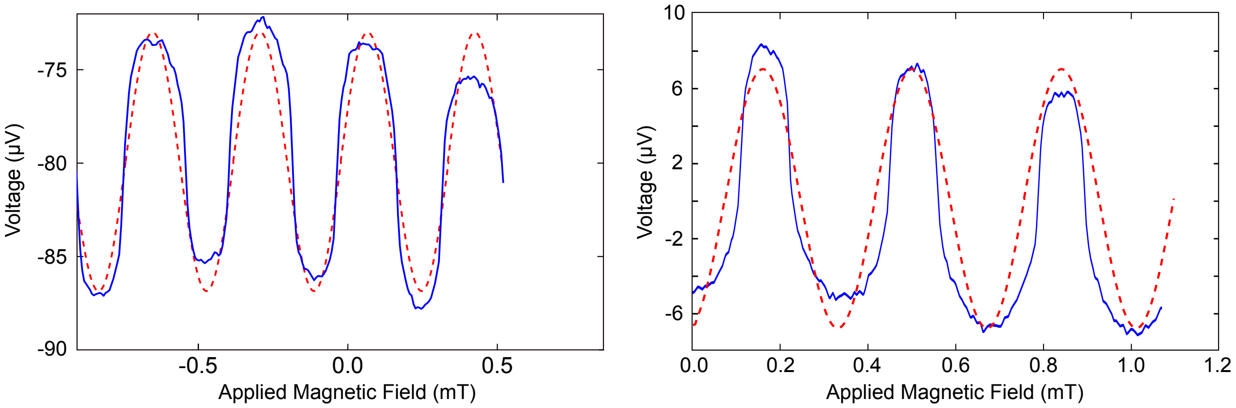

(a) SQUID L-1 (45 nm extra Ti)

(b) SQUID L-2 (45 nm extra Ti)

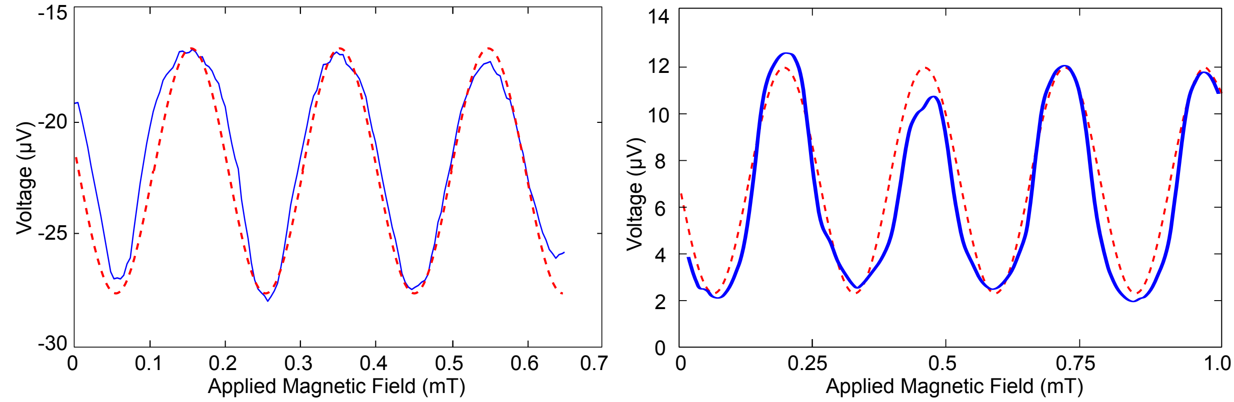

(c) SQUID P-1 (65 nm extra Ti)

(d) SQUID Y-1 (250 nm extra Ti)

Figure 5.25: In blue: $V(\Phi)$ characteristics showing the largest ΔV for the 3D nanoSQUIDs with extra titanium at 100 mK (a) L-1, (b) L-2, (c) P-1, and (d) Y-1. The red dotted curves are a guide to the eye showing a sine of corresponding amplitude and period.

SQUID	Extra Ti nm	T mK	I_b µA	I_c µA	R_n Ω	$I_\mathrm{c}R_\mathrm{n}$ µV	ΔV µV	β_L	L pH	$\lambda_{\mathrm{3DMLSI}}$ nm
J-1	0	100	2.95	2.6	8.6	21.9	10.82	1.03	415	720
L-1	45	100	2.90	2.73	6.2	16.9	12.25	0.38	145	670
L-2	45	100	2.95	2.72	6.2	16.9	11.82	0.43	162	712
P-1	65	150	1.75	1.29	6.4	8.27	7.29	0.14	108	679
Y-1	250	100	3	2.12	4.9	10.4	9.14	0.14	68	770

Table 5.1: Different parameters taken from the best $V(\Phi)$ characteristics of several 3D nanoSQUIDs. All devices have a Au (25 nm)/ Ti (100 nm) base bilayer. SQUID J-1 does not have extra material, L-1 has 45 nm extra Ti, 65 nm for P-1, 250 nm for Y-1. The value for $\lambda_{\mathrm{3DMLSI}}$ is the value required to get the inductance found from Equation 5.4 using 3D-MLSI models and is intended as a check of the consistency.

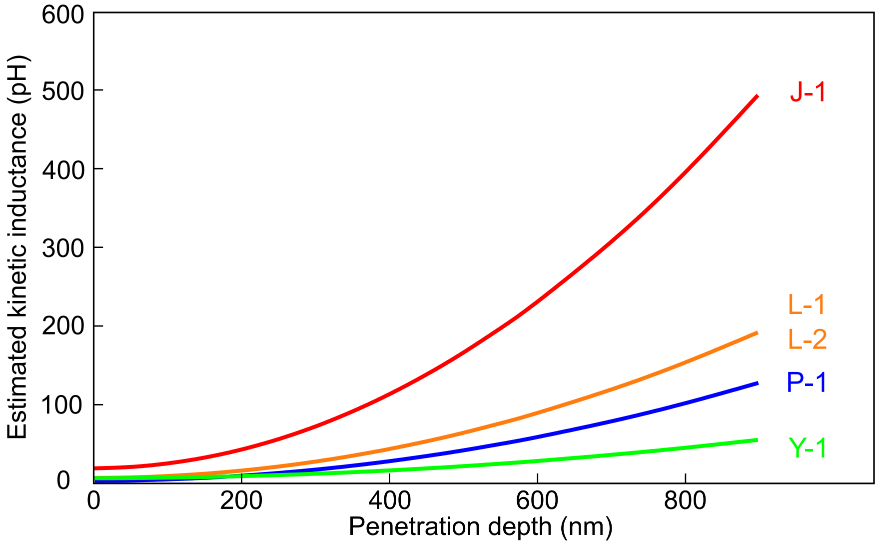

Figure 5.26: Inductance estimated by 3D-MLSI versus the penetration depth λ we input in the model. The different colours represent the 3D-MLSI models of the devices mentioned in the text with their differing shapes and dimensions.

to another estimate using 3D-MLSI. This was achieved as we did previously for SQUID J-1 by plotting the predicted inductance of the SQUIDs as a function of the input penetration depth. This is shown in Figure 5.26 for the different devices geometries. As we increased the additional thickness of titanium, we were able to lower the screening parameter from $\beta_L = 1.03$ to $\beta_L = 0.14$. This corresponds to a decrease of the inductance from 415 pH to 68 pH which is consistent with the 3D-MLSI model and the estimate for $\lambda_{\mathrm{Ti}} \sim 740\,\mathrm{nm}$ based on its resistivity. Even the inductance of SQUID Y-1 is mostly dominated by the kinetic inductance despite having the thickest loop body. This is due to the residual kinetic inductance contributions of the nanobridges which cannot be reduced by the angled deposition technique. However, a further reduction of β_L is not necessary in terms of ΔV as shown in Figure 1.15.

5.4.3 Estimated Noise Performance for 3D Ti NanoSQUIDs

As we saw in Chapter 1, the voltage sensitivity is $S_V \approx 18 \mathrm{k_B} T R_{\mathrm{n}}$ and the flux noise is $\Phi_{\mathrm{ns}} = S_V^{1/2}/V_\Phi$. We obtained V_Φ by taking the maximum derivative of $V(\Phi)$ calculated with Python and NumPy. We tabulated all these values in Table

SQUID	Extra Ti (nm)	T (mK)	V_Φ (µV/Φ_0)	S_V ($10^{-22}\,\mathrm{V}^2/\mathrm{Hz}$)	Φ_ns (n$\Phi_0/\sqrt{\mathrm{Hz}}$)	$\Phi_\mathrm{ns,Q}$ (n$\Phi_0/\sqrt{\mathrm{Hz}}$)
J-1	0	100	100	2.14	146.2	101.6
L-1	45	100	190	1.54	65.3	59.8
L-2	45	100	157	1.54	79.6	64.3
P-1	65	150	109	2.39	141.7	51.7
Y-1	250	100	59.1	1.22	187.1	41.0

Table 5.2: Table showing the transfer function, voltage spectral density, flux noise and quantum flux noise for the 3D Ti nanoSQUIDs we fabricated.

5.2. The best device in terms of flux noise was SQUID L-1 with an estimated flux noise of $65\,\mathrm{n}\Phi_0/\sqrt{\mathrm{Hz}}$. Interestingly this is not the device with the thickest layer of extra titanium. The explanation for this comes from the fact that 45 nm of extra Ti are sufficient to reduce the kinetic inductance by a fairly large proportion. Adding more material further reduces the inductance but to a lesser extent. In the meantime the thickened banks will hold the phase more efficiently as suggested by Likharev [56] (see Section 1.2.6). Due to this, the nanobridges behave more closely to Josephson junctions and the $V(\Phi)$ characteristics are closer to being sinusoidal, which makes the transfer function smaller. However, very sinusoidal devices have a transfer function that tends to be more constant over a wider flux range around $\sim \Phi_0/4$ whereas non-sinusoidal SQUIDs have only a very narrow region with an optimal $\mathrm{d}V/\mathrm{d}\Phi$. This means that although they might be less sensitive in absolute terms, thicker SQUIDs can actually perform better for actual measurements. Sinusoidal responses are also desirable for some experiments such as monitoring the change of A_eff induced by a superconducting plane as we will discuss in Section 6.1.2.

On average, we obtained $\Phi_\mathrm{ns} \sim 100\,\mathrm{n}\Phi_0/\sqrt{\mathrm{Hz}}$ but it can be as low as $\sim 50\,\mathrm{n}\Phi_0/\sqrt{\mathrm{Hz}}$ for the best devices. Thanks to their ability to be operated in the millikelvin regime where they benefit from a lower noise floor, we predict our nanoSQUIDs outperform the best Nb devices operated at 4.2 K [10]. They are also two orders of magnitude more sensitive (in terms of flux noise) than the carbon-nanotube devices [7] that can be operated in the millikelvin range.

5.4.4 Further Improvement: Aluminium Overlayer

In this section to further improve the inductance we developed a new type of 3D nanoSQUID based on an aluminium overlayer. As we saw, the penetration depth of aluminium is about three times lower than that of titanium because of its better conductivity and higher T_c. We decided to take advantage of this fact by selectively depositing Al instead of Ti during the angled evaporation. This process is schematised in Figure 5.27. We fabricated a series of devices made of Au (25 nm)/Ti (100 nm)/Al (65 nm). SQUIDs X-3 and X-4 have relatively large loop areas, similar to that of SQUIDs L-1 and P-1. However we also fabricated two SQUIDs, X-1 and X-2, with much reduced inner holes, respectively 0.2 $\mu\mathrm{m}^2$ and 0.3 $\mu\mathrm{m}^2$ as shown in Figure 5.28. The $V(\Phi)$ characteristics for the devices, shown in Figure 5.29, show larger peak-to-peak modulations than the previous Ti/Au devices. This is mostly due to an increase of I_c as aluminium boasts a higher Cooper pair density which are coupled to the titanium layer via the proximity effect. This led to a small degree of hysteresis that affected the response of the SQUIDs and limited the devices operation to temperatures above $\sim 150\,\mathrm{mK}$. This issue especially affected the smallest SQUIDs X-1 and X-2 with their shorter bridges. This could be easily solved for future devices by either adding slightly more gold

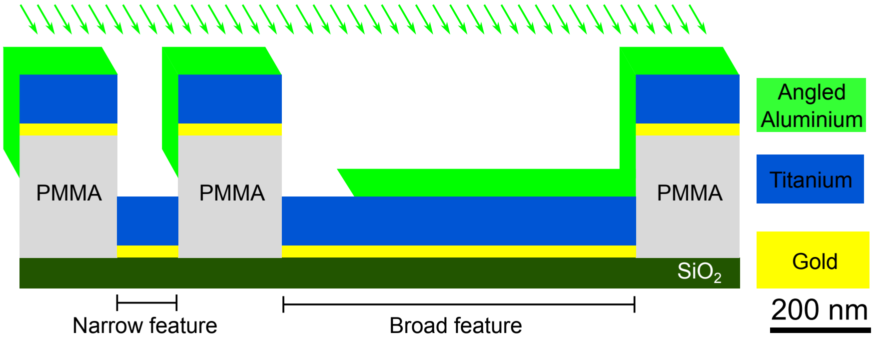

Figure 5.27: Schematic diagram showing the last step to get nanoSQUIDs with an aluminium overlayer (the X series).

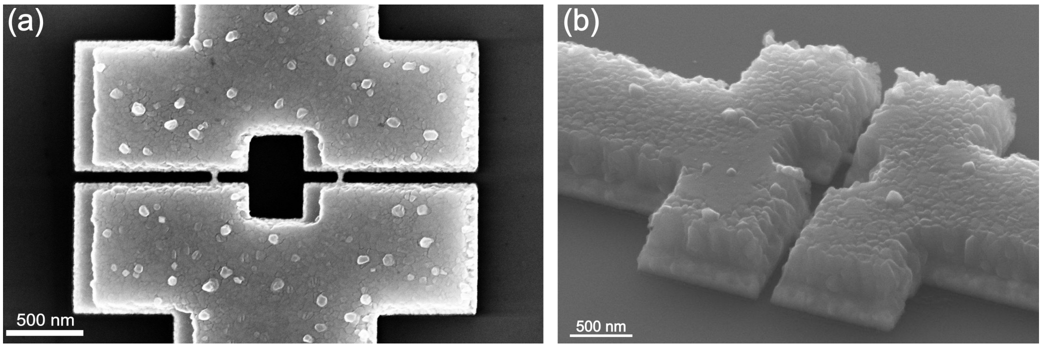

Figure 5.28: (a) SEM micrograph of SQUID X-2 with a 0.3 µm^2 inner loop and a 65 nm Al overlayer. (b) SEM micrograph at a 34° viewing angle of a device similar to SQUID X-2 but thicker with a 200 nm Al overlayer (device not measured).

to account for this effect or by depositing some angled titanium before aluminium to reduce the coupling.

As shown in Table 5.3, the $I_\mathrm{c}R_\mathrm{n}$ product for this type of device is higher yielding a larger ΔV. The penetration depth from the 3D-MLSI model is very consistent with the estimate using the resistivity of a parallel combination of Ti and Al: 30 nΩ.m for a T_c of 550 mK giving $\lambda = 254$ nm. As expected, devices with an aluminium overlayer have the smallest inductance ~ 20 pH which tend toward the value of the geometric inductance $\sim 3 - 6$ pH. The kinetic inductance remains the dominant

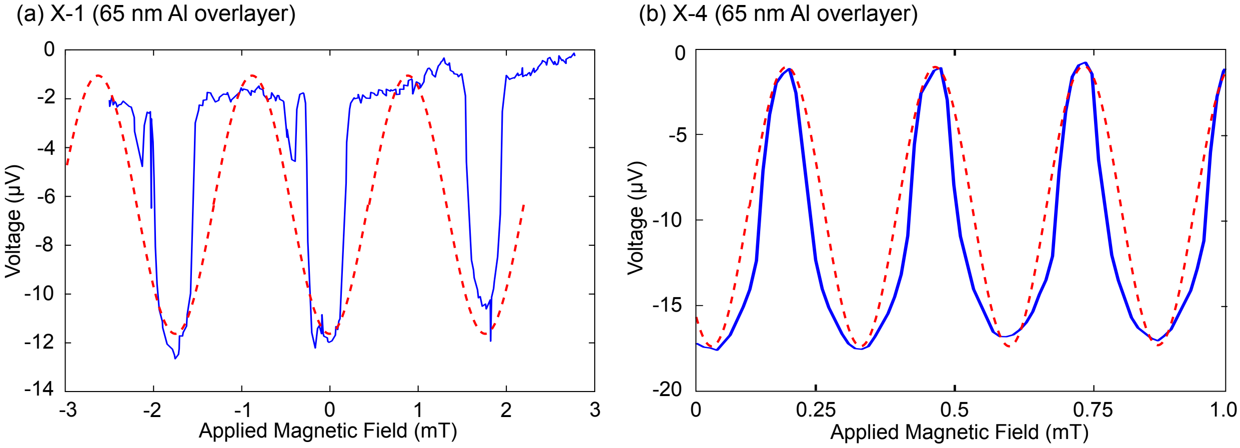

Figure 5.29: In blue: $V(\Phi)$ characteristics showing the largest ΔV for two SQUIDs with a 65 nm thick Al overlayer on top of a (25 nm)/Ti (100 nm) base layer. (a) X-1 at 160 mK and (b) X-4 at 200 mK. The red dotted curves are a guide to the eye showing sines of corresponding amplitude and period.

SQUID	T (mK)	I_b (μA)	I_c (μA)	R_n (Ω)	$I_\mathrm{c}R_\mathrm{n}$ (μV)	ΔV (μV)	β_L	L (pH)	$\lambda_{\mathrm{3DMLSI}}$ (nm)
X-1	200	3.3	3.21	3.9	12.4	10.49	0.18	18.5	275
X-3	160	2.6	2.34	6.2	14.6	12.74	0.14	20.0	255
X-4	200	4.25	2.98	6.2	18.5	15.78	0.17	19.2	240

Table 5.3: Different parameters extracted from the best $V(\Phi)$ characteristics of several 3D nanoSQUIDs with a 65 nm aluminium overlayer. All devices have a Au (25 nm)/Ti (100 nm) base bilayer. The estimated penetration depth $\lambda_{\mathrm{3DMLSI}}$ is obtained by matching the inductance obtained with the appropriate 3D-MLSI model (see Figure 5.30).

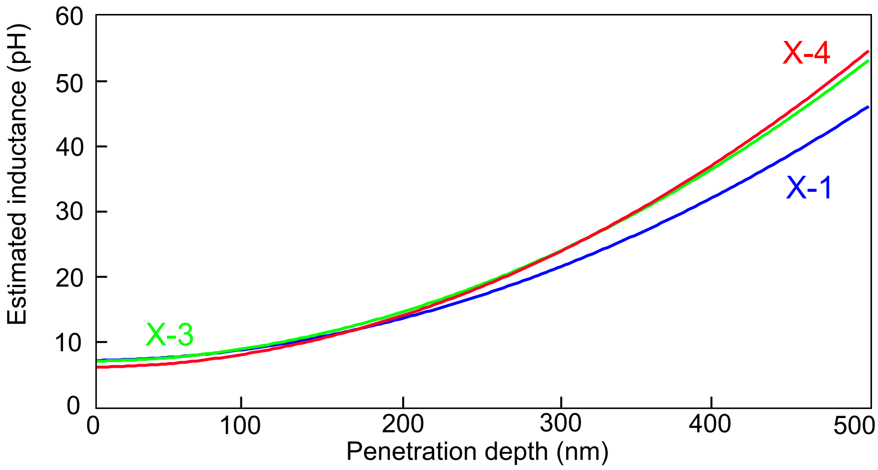

Figure 5.30: Inductance estimated by 3D-MLSI versus the penetration depth λ we input in the models of the different SQUIDs with an Al overlayer.

SQUID	T (mK)	V_Φ (μV/Φ_0)	S_V (10^{-22} V^2/Hz)	$\Phi_{\rm ns}$ (n$\Phi_0/\sqrt{\rm Hz}$)	$\Phi_{\rm ns,Q}$ (n$\Phi_0/\sqrt{\rm Hz}$)
X-1	200	252	1.92	55.0	38.0
X-3	160	72.65	2.47	207.5	38.5
X-4	200	127.91	3.09	137.4	39.7

Table 5.4: Table showing the transfer function, voltage spectral density, flux noise and quantum flux noise for the nanoSQUIDs with an Al overlayer we fabricated.

factor due to the contribution of the bridges.

Despite the slightly higher temperature range of operation due to the slight hysteresis, the smallest device X-1 shows the best estimated flux noise of our nanoSQUIDs. This would be only $38\,{\rm n}\Phi_0/\sqrt{\rm Hz}$ assuming we could remove the hysteresis and operate the device down to 100 mK. The larger Al-based SQUID X-4 has a flux sensitivity that is 60 % better than that of its Ti-based analogue SQUID Y-1 which has a similar geometry. This fact, combined with the smaller inductance and penetration depth we discussed above, is very beneficial in terms of spin sensitivity as we will see in Section 5.5.

5.4.5 Noise Measurements with a Series SQUID Array Amplifier

The noise floor we estimated for our SQUIDs above is lower than the input noise of any room-temperature pre-amplifier. In order to measure the noise level of our devices and to use them at their full sensitivity for actual magnetic measurements, we have to use a low-temperature pre-amplifier. Such amplifiers are fairly expensive and have to be carefully chosen to match the characteristics of the devices. The only low-temperature pre-amplifier available to us in the course of this project was a 16-SQUID Series SQUID Array (SSA) amplifier manufactured by Magnicon GmbH. The SSA is coupled to the nanoSQUID following the simplified schematic in Figure 5.31. A controllable current-source included in the SSA electronics is used to drive bias currents up to 500 μA. The nanoSQUID is biased in parallel with an internal resistor $R_{\rm SSA} = 0.1\ \Omega$. As $R_{\rm SSA}$ is much lower than the nanoSQUID resistance, the nanoSQUID is essentially voltage biased. In this configuration the SSA acts as a current sensor with an input current noise guaranteed below $< 10\,\mathrm{pA}/\sqrt{\mathrm{Hz}}$ at 4.2 K. In normal operation, the current source is adjusted so that the current component going through the SQUID matches the optimal bias current. When the SQUID responds to an applied magnetic flux, the change of voltage across it leads to a change in the current going through the inductance. As it is magnetically coupled to the SSA, this change is detected and amplified. The transfer function of the SSA has to be calibrated for each device by looking at the $V(\Phi)$ of the SQUID measured after amplification by the SSA to translate the spectral voltage density into flux sensitivity. A typical conversion factor we found was that $1\,\mu\mathrm{V}/\sqrt{\mathrm{Hz}}$ corresponds to approximately $0.8\,\mu\Phi_0/\sqrt{\mathrm{Hz}}$ in terms of flux noise.

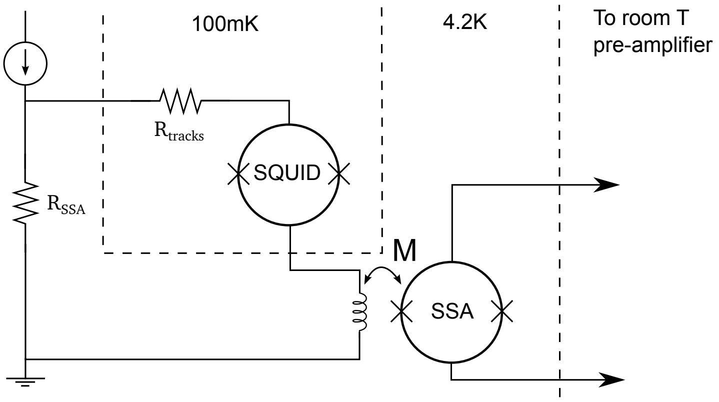

Figure 5.31: Simplified schematics of the SSA electronics. The SSA chip is designed to operate at 4.2 K, though in our case it was sitting at 1.5 K next to the 1 K pot due to technical constraints. No adverse effects were observed.

If the flux going in the nanoSQUID changes by $\Delta\Phi$, the difference in input current ΔI in the SSA is

$$\Delta I = \left(\frac{\partial I}{\partial V}\right)\left(\frac{\partial V}{\partial \Phi}\right)\Delta\Phi. \tag{5.5}$$

Considering the input current sensitivity of the SSA, the minimum detectable flux is

$$\Delta\Phi_{\text{min}} = \left(\frac{\partial V}{\partial I}\right)\left(\frac{\partial \Phi}{\partial V}\right) \times 10\,\text{pA}/\sqrt{\text{Hz}}. \tag{5.6}$$

The typical values for our nanoSQUIDs are $\partial V/\partial I \sim 3\,\Omega$ and $\partial V/\partial\Phi \sim 50\,\mu\text{V}/\Phi_0$, from which we can estimate that $\Delta\Phi_{\text{min}} \sim 1.4\,\mu\Phi_0/\sqrt{\text{Hz}}$. This is one order of magnitude higher than the theoretical limit we estimated for our nanoSQUIDs, and so the SSA is the limiting factor. This SSA was originally intended as a relatively versatile pre-amplifier which can be connected with various cryogenic detectors that may be operated dynamically with fast signals; for this reason its input inductance is relatively low (3 nH). This allows shorter time constants for some specific uses, but it comes at the price of a relatively low input sensitivity of 23 $\mu\text{A}/\Phi_0$ as a given change in current leads to a fairly small amount of flux being coupled to the SSA.

Typical flux noise characteristics that we measured for devices J-1 and P-1 using the SSA are shown in Figure 5.32.

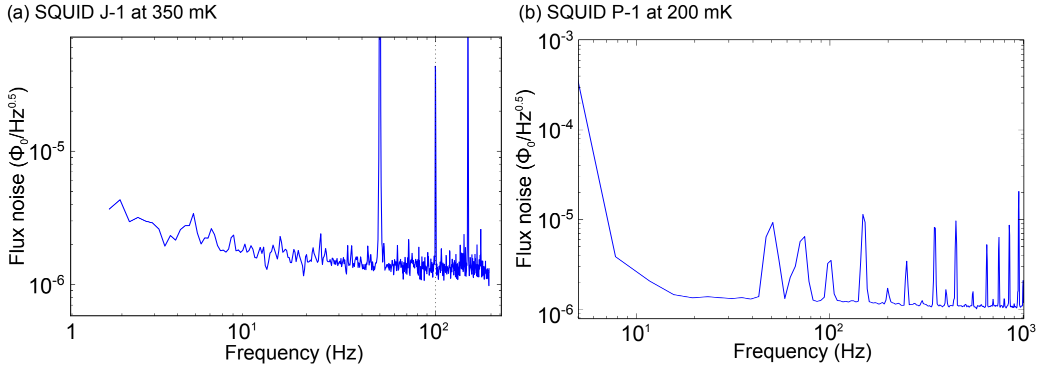
(a) SQUID J-1 at 350 mK

(b) SQUID P-1 at 200 mK

Figure 5.32: Flux noise measurement using the SSA of (a) SQUID J-1 at 350 mK, and (b) SQUID P-1 (65 nm extra Ti) at 200 mK.

As expected, the noise level appeared to be the same for both devices: $1.8\,\mu\Phi_0/\sqrt{\text{Hz}}$ at 100 Hz without significant excess noise down to 5 Hz. Another indication that the SSA was the limiting factor is that the measured noise was not sensitive to the temperature of the device nor to its bias flux. However, even though the SSA was the limiting factor, this overall level of noise already constitutes reasonable performance. The overall flux noise is superior to other devices reported operating in the millikelvin range, such as the carbon nanotube SQUIDs fabricated by Cleuziou *et al.* [7]. An estimate of the corresponding spin sensitivity of our devices will be given in Section 5.5.

For our application, we do not require a low input inductance and so we could use a current sensor matching more closely the characteristics of our devices. Under consideration at the end of the project was the purchase of a SQUID current sensor 6L116 from Magnicon GmbH which is a double transformer, integrated two-stage current sensor. This involves a first stage single sensor SQUID that is then read out by a 16-SQUID SSA. Thanks to its high input inductance of the order of $1\,\mu\mathrm{H}$, the input current sensitivity is only $0.5\,\mu\mathrm{A}/\Phi_0$, nearly fifty times more sensitive than the SSA. The flux noise of this SQUID current sensor is $0.8\,\mu\Phi_0/\sqrt{\mathrm{Hz}}$ at 4.2 K and $0.25\,\mu\Phi_0/\sqrt{\mathrm{Hz}}$ which translates into an input current sensitivity of $0.4\,\mathrm{pA}/\sqrt{\mathrm{Hz}}$ at 4.2 K and $0.125\,\mathrm{pA}/\sqrt{\mathrm{Hz}}$ at 0.3 K. If this were used to readout the above nanoSQUID, we would obtain $\Delta\Phi_{\mathrm{min}} = 30\,\mathrm{n}\Phi_0/\sqrt{\mathrm{Hz}}$ at 4.2 K and $\Phi_{\mathrm{min}} = 8\,\mathrm{n}\Phi_0/\sqrt{\mathrm{Hz}}$ at 300 mK. In that case, we would no longer be limited by the intrinsic noise of the amplifier and could realistically access the noise level of our nanoSQUIDs.

5.5 Spin Sensitivity

One of the current trends and remaining goals for nanoSQUIDs is to reduce their sizes to improve their spin sensitivities and make them useful tools to characterise nanoscale magnetic systems, ideally able to measure the flip of a single spin. As the spin sensitivity is highly dependent on the dimensions of the SQUID, we begin with a study of the effective area A_{eff} of our devices which is a function of the penetration depth and geometry. Using a model developed by Granata *et al.* [9], we give in this section an estimate of the spin sensitivities of our 3D nanoSQUIDs for various locations of a magnetic dipole moment inside the SQUID loop.

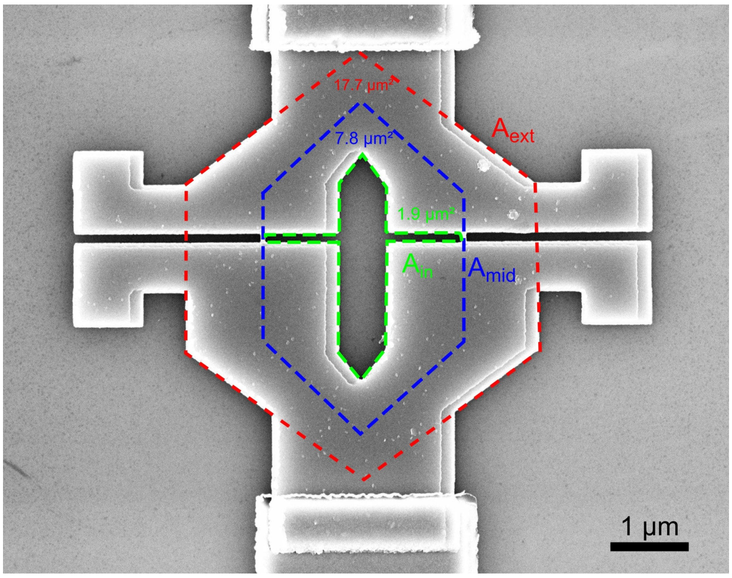

Figure 5.33: SEM micrograph of SQUID P-1 showing the three areas discussed in this section: the inner area corresponding to the SQUID hole A_{in} in green, the area corresponding to the middle of the SQUID loop A_{mid} in blue, and the outer area of the SQUID A_{ext} in red.

5.5.1 Study of Flux Focussing

A precise determination of the effective area A_{eff} is crucial when estimating the spin sensitivity of a SQUID, and also for a variety of measurements that will be described in Chapter 6. The main parameter affecting A_{eff} when dealing with films thinner than the penetration depth λ is Λ, the Pearl penetration depth, which is the length scale characterising the magnetic field distribution. We have $\Lambda = \lambda^2/t$ where t is the thickness of the film. For a circular SQUID of inner diameter a and outer diameter b, we can estimate A_{eff} using $A_{\mathrm{eff}} \approx \pi b(a + \Lambda)$ [81]. However, the geometries of our SQUIDs are not as simple and this formula would not accurately model the actual flux focussing effect. We developed a more realistic model based on 3D-MLSI. The hypotheses are as follows: if the superconducting film had the same diamagnetic properties as the bulk ($\lambda \to 0$), all the magnetic flux incident on A_{mid} (in blue in Figure 5.33) would be focussed into the SQUID hole whilst all the flux outside A_{mid} would be pushed out past the closest outside edge of the SQUID. The effective area would therefore be exactly defined by the middle of the

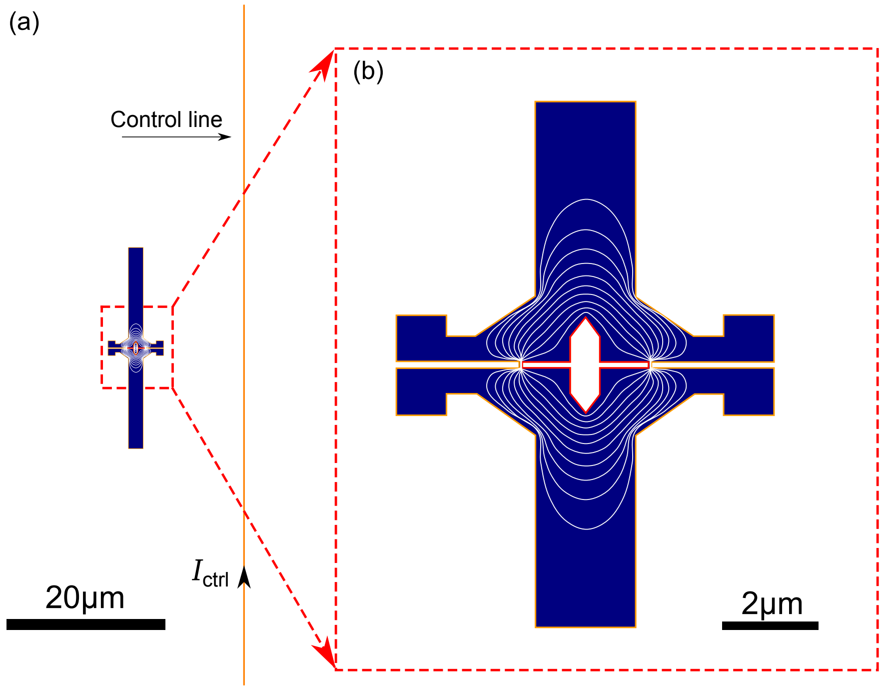

Figure 5.34: Image rendered by 3D-MLSI after modelling the SQUID P-1 showing in white the current lines. (a) 3D-MLSI calculates the mutual inductance between the control line and the SQUID. The dashed red region corresponds to the device which is shown magnified on the right in (b).

loop track, i.e. the area A_{mid}. As the penetration depth increases (or the thickness is decreased which is equivalent), there is less screening current and the magnetic flux can start going through the film instead of being focussed into the hole. This effect is complex to model for an arbitrary SQUID and requires finite-element techniques. In our 3D-MLSI model, we consider a control line and estimate its mutual inductance with the SQUID, as shown in Figure 5.34.

The 3D-MLSI software can only output the mutual inductance between elements and not the effective area of a SQUID, however we can show that these two parameters are linearly proportional. By definition of the mutual inductance M between the control line and the SQUID, we have $\mathrm{d}\Phi_{\text{SQUID}}/\mathrm{d}I_{\text{line}} = M$. Assuming the control line is set to be sufficiently long and far away from the SQUID (distance SQUID-line, $R \gg$ radius of the SQUID, a), we can consider that the magnetic field B is constant over the area of the SQUID and equal to $B = \mu_0 I_{\text{ctrl}}/2\pi R$. As

$\Phi_{\mathrm{SQUID}} = BA_{\mathrm{eff}}$, it means that M and A_{eff} in this limit are linearly proportional, related by the equation $A_{\mathrm{eff}} = 2\pi RM/\mu_0$. Therefore, a change of mutual inductance ΔM directly corresponds to a change of ΔA_{eff}. Using a Python script controlling 3D-MLSI to enable batch calculation of the mutual inductance, we were able to generate a precise estimation of the change in the effective area $\Delta A_{\mathrm{eff}} = (A_{\mathrm{eff}} - A_{\mathrm{mid}})/A_{\mathrm{mid}}$ versus the penetration depth λ set for the SQUID as shown in Figure 5.35.

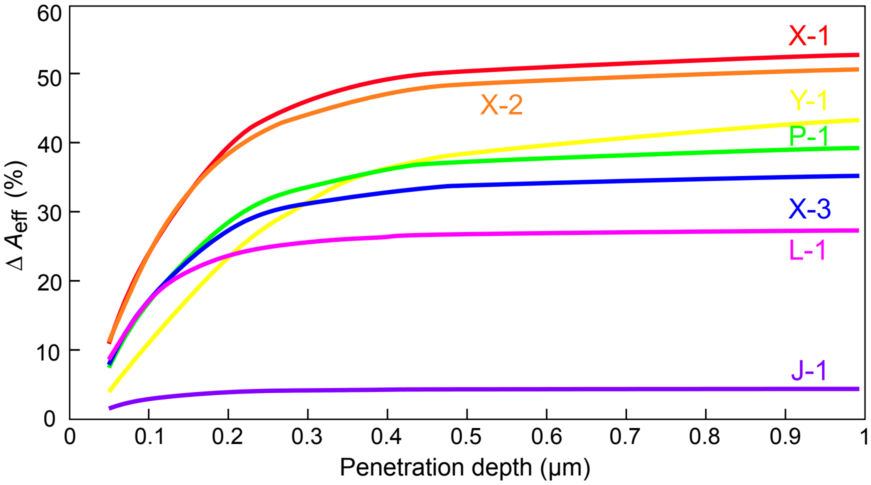

Figure 5.35: Increase of effective area ΔA_{eff} estimated by 3D-MLSI as a function of the penetration depth λ we input in the model. The different colours represents the 3D-MLSI of the different 3D devices we fabricated with their differing shapes and dimensions.

In other words, using this graph we can match any increase in the effective area ΔA_{eff} into a corresponding theoretical value for λ. As titanium has a penetration depth $\sim 750\,\mu\mathrm{m}$, the increase in A_{eff} is expected to be about 5 % for SQUID J-1 which has a smaller loop width and to range from 25 % to 38 % for devices with a broader loop. It is interesting to note that above $\lambda \sim 250\,\mathrm{nm}$, the effective area of the SQUID becomes increasingly insensitive to the penetration depth. This fact is useful for some measurements of superconducting samples as a function of temperature as we will see in Chapter 6.

For devices with the aluminium overlayer, $\lambda \sim 250\,\mathrm{nm}$, we can expect the increase to be limited to 20 – 25 % for SQUIDs with a broad loop and 37 % for the SQUIDs with a very small hole like the one shown in Figure 5.28. This is due to the large ratio $A_{\text{ext}}/A_{\text{in}}$ which illustrates the difficulties in achieving devices with very small effective areas despite the creation of a small inner hole [11, 84]. To double-check our estimates, we measured A_{eff} of our devices using the period of their $V(B)$ characteristics and compared these values with A_{mid} estimated from SEM images. The data are given in Table 5.5.

For the 3D titanium nanoSQUIDs, as the penetration depth is long and A_{eff} is nearly insensitive to λ, the model is not sensitive enough to precisely confirm our estimate of $\lambda \sim 740\,\text{nm}$. For the devices with the aluminium overlayer, we could estimate that according to the 3D-MLSI model: $\lambda_{\text{X-1}} \approx 222\,\text{nm}$, $\lambda_{\text{X-2}} \approx 241\,\text{nm}$, $\lambda_{\text{X-3}} \approx 198\,\text{nm}$ and $\lambda_{\text{X-4}} \approx 240\,\text{nm}$. This is in good agreement to the estimate using the resistivity $\rho = 30\,\Omega.\text{m}$ of a Ti (100 nm)/Al (65 nm) bilayer and $\lambda = 254\,\mu\text{m}$. As expected, nanoSQUIDs with an aluminium overlayer with its shorter penetration depth, or SQUIDs with more material have an effective area closer to A_{mid}. This reduced A_{eff}, combined with the lower inductance of such devices, is advantageous in terms of spin sensitivity as we will now discuss.

SQUID	Extra material (nm)	A_{eff} (μm^2)	A_{int} (μm^2)	A_{mid} (μm^2)	A_{ext} (μm^2)	ΔA_{eff} (%)
J-1	0	18.09	10.8	17.3	25.1	4.3
L-1	45 (Ti)	6.02	1.6	4.8	10.9	25.4
L-2	45 (Ti)	6.09	1.6	4.8	10.9	26.8
P-1	65 (Ti)	10.65	1.89	7.8	17.7	36.5
Y-1	250 (Ti)	8.07	1.21	5.9	9.4	30.1
X-1	65 (Al)	1.54	0.14	1.1	5.6	41.0
X-2	65 (Al)	1.75	0.29	1.1	5.6	41.0
X-3	65 (Al)	3.69	0.76	2.9	5.6	27.2
X-4	65 (Al)	7.49	1.21	5.9	9.4	26.9

Table 5.5: Table showing the different areas as defined in the text for the 3D nanoSQUIDs we fabricated.

5.5.2 Estimated Spin Sensitivity for the 3D NanoSQUIDs

To estimate the spin sensitivity of our devices, we used Granata *et al.*'s model [9] which is based on a solution of Maxwell's equations to calculate the flux coupled to a square coil of edge length $2a$ by a Bohr magneton located at a point P(x',y',z'). The equations for this are:

$$\Phi = \frac{\mu_0\mu_B}{4\pi}(A+B+C+D) \text{ where} \tag{5.7}$$

$$A = \int_{-a}^{a} \frac{a-y'}{((x-x')^2+(a-y')^2+z'^2)^{3/2}}dx \tag{5.8}$$

$$B = \int_{-a}^{a} \frac{a+x'}{((a+x')^2+(y-y')^2+z'^2)^{3/2}}dy \tag{5.9}$$

$$C = \int_{-a}^{a} \frac{a+y'}{((x-x')^2+(a+y')^2+z'^2)^{3/2}}dx \tag{5.10}$$

$$D = \int_{-a}^{a} \frac{a-x'}{((a-x')^2+(y-y')^2+z'^2)^{3/2}}dy. \tag{5.11}$$

Using Python and Matplotlib, we can numerically evaluate these integrals and plot the flux coupled to the loop as a function of the localisation of the Bohr magneton (see Figure 5.36 for the results for SQUIDs with loop dimensions of 3 µm × 3 µm similar to most of the SQUIDs studied in this project).

The coupling is much stronger as the spin is located closer to the inner edge of the SQUID which leads to a higher spin sensitivity. Considering for simplicity that our SQUIDs are filamentary square loops of edge length a so that $a = \sqrt{A_{\text{eff}}}$, we can calculate the amount of flux a spin at a certain location would couple to the SQUID and then translate the flux sensitivity into spin sensitivity. The results are given in Table 5.6. We write $S_{\text{spin,C}}$ as the spin sensitivity for a magnetic dipole moment located at the centre of the SQUID loop, $S_{\text{spin,MAX}}$ if it is located 10 nm from a bridge, and $S_{\text{spin,50 nm}}$ if it is 50 nm from a bridge inside the SQUID hole.

With the existing set-up with our SSA, we estimate that the best spin sensitivity reaches 439 spins/$\sqrt{\text{Hz}}$ assuming the magnetic moments are located in the centre of the loop, which could be already used for some measurements, especially considering

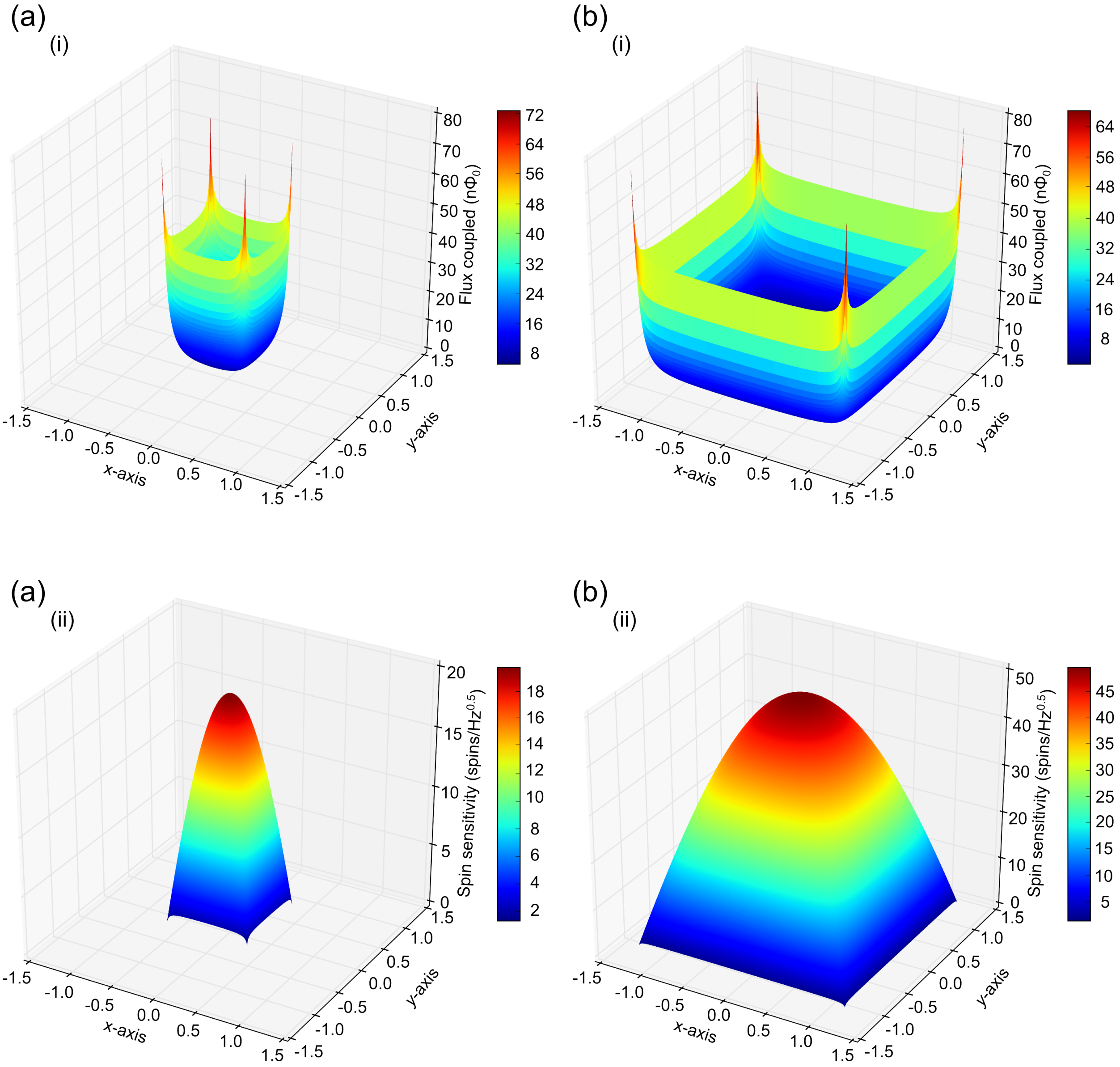

Figure 5.36: For a filamentary square SQUID of edge lengths (a) $a = 1000\,\mu\text{m}$ and (b) $a = 3000\,\mu\text{m}$: (i) magnetic flux coupled by a single spin as a function of its location inside the loop; (ii) estimated spin sensitivity assuming a flux noise of $100\,\text{n}\Phi_0/\text{Hz}^{0.5}$.

			If SSA is limiting factor			If nanoSQUID is limiting factor (6L116)		
SQUID	T mK	Extra Material (nm)	$S_{\mathrm{spin,C}}$ spin/$\sqrt{\mathrm{Hz}}$	$S_{\mathrm{spin,MAX}}$ spin/$\sqrt{\mathrm{Hz}}$	$S_{\mathrm{spin,50\,nm}}$ spin/$\sqrt{\mathrm{Hz}}$	$S_{\mathrm{spin,C}}$ spin/$\sqrt{\mathrm{Hz}}$	$S_{\mathrm{spin,MAX}}$ spin/$\sqrt{\mathrm{Hz}}$	$S_{\mathrm{spin,50\,nm}}$ spin/$\sqrt{\mathrm{Hz}}$
J-1	100	none	1506	19.6	102.4	115.3	1.50	7.94
L-1	100	45 (Ti)	880	19.6	101.8	30.1	0.67	3.48
L-2	100	45 (Ti)	880	19.6	102.4	36.4	0.81	4.21
P-1	150	65 (Ti)	1158	19.6	102.4	85.9	1.46	7.63
Y-1	100	250 (Ti)	439	19.6	102.4	98.4	1.92	10.03
X-1	200	65 (Al)	682	19.6	91.4	13.4	0.6	2.80
X-3	160	65 (Al)	970	19.6	94.2	82.0	2.36	11.35
X-4	200	65 (Al)	1004	19.6	96.0	74.2	1.50	7.35

Table 5.6: Table giving the estimated spin sensitivities for three locations of the magnetic moment: in the centre of the loop, in the centre with a properly matched pre-amplifier, 10 nm and 50 nm from a nanobridge inside the loop. This is given for two set-ups: one using the present SSA (flux noise limited to $1.8\,\mu\Phi_0/\sqrt{\mathrm{Hz}}$) and one that would use a properly matched current sensor such as the two-stage 6L116 sensor (flux noise limited by the nanoSQUID).

the relative ease of fabrication. This goes down to about $100\,\mathrm{spins}/\sqrt{\mathrm{Hz}}$ if the moments are 50 nm away from a bridge. However, with a properly matched pre-amplifier and a very careful set-up as we discussed previously, we would reach the noise floor of the nanoSQUID and the spin sensitivity could be as low as $10\,\mathrm{spins}/\sqrt{\mathrm{Hz}}$ at the centre for the smallest device. Assuming the dipoles could be located 10 nm from the bridge, the spin sensitivity would then be $< 1\,\mathrm{spin}/\sqrt{\mathrm{Hz}}$, or $2.8\,\mathrm{spins}/\sqrt{\mathrm{Hz}}$ at 50 nm which is a more realistic hypothesis. These characteristics could be relatively easily improved at least two-fold simply by reshaping the cooling fins and SQUID body to have A_{eff} closer to A_{int} and by adding more gold to operate the Al overlayer devices at lower temperatures.

5.6 Conclusion

3D nanoSQUIDs are not sensitive to excess heat and have a reasonably low kinetic inductance despite the use of titanium which has a poor λ. Even though we were unable to confirm experimentally that the noise floor was this low for our devices, the predicted flux noise is on average $\Phi_{\mathrm{ns}} \sim 100\,\mathrm{n}\Phi_0/\sqrt{\mathrm{Hz}}$ and could be as low as $50\,\mathrm{n}\Phi_0/\sqrt{\mathrm{Hz}}$. This translates into an estimated spin sensitivity in the order of $10\,\mathrm{spins}/\sqrt{\mathrm{Hz}}$ for moments located in the centre of the hole, and better than $1\,\mathrm{spin}/\sqrt{\mathrm{Hz}}$ assuming they can be located 10 nm from the nanobridge. These devices could therefore be successfully used for millikelvin magnetic characterisation. In the next chapter, we will assess the feasibility of a variety of such measurements.

Chapter 6

Feasibility of Measurements of Systems with Weak Magnetic Responses

In the previous chapters we demonstrated that by tuning the thickness ratio of a normal metal - superconductor bilayer, we can fabricate nanoSQUIDs that are non-hysteretic down to millikelvin temperatures and can be operated with standard electronics by current-biasing them. By thickening their banks selectively, we reduced the adverse effects related to heat dissipation, lowered their inductance and achieved more sinusoidal voltage responses to applied magnetic fields. Our devices could be integrated in future directly onto a magnetic system surface, yielding a spin sensitivity far superior to scanning SQUID systems. This would enable the study of ultrathin systems with weak magnetic responses, such as topological insulators or heterointerfaces between perovskites, for instance $LaAlO_3/SrTiO_3$. In this chapter, we discuss the measured response of our devices to fabricated magnetic test systems including a control line, superconducting islands and superconducting planes. Using these data we can then estimate the sensitivity of our nanoSQUIDs. In the second part of this chapter we use this information to investigate the feasibility of measurements on ultrathin systems of interest. We consider the practical aspects to adapt our fabrication process to very insulating substrates which are needed for some systems. Finally, without loss of generality, we take as an example the heterointerface between $LaAlO_3/SrTiO_3$ as it is currently the subject of intensive research. We use finite element simulations to estimate the response we could expect depending on parameters of this heterointerface such as the penetration depth, carrier concentration, and the extent and location of the 2D electron-gas (2DEG) that is found there.

6.1 Fabricated Test Systems with Large Magnetic Signatures

6.1.1 Control line

As a first test to assess nanoSQUID measurements on a real system, we deposited a control line next to SQUID Y-1 which was studied earlier in Chapter 5. This was deposited at the same time as the contacts to the SQUID, for simplicity and to minimise the number of fabrication steps. The finalised connected system is shown in Figure 6.1. The design was chosen by considering the limitations of the fabrication process. To be certain not to affect the already deposited SQUID, a separation of 2 µm was kept between the control line and the closest edge of the SQUID body. Using a highly-focussed 30 kV beam, it was possible to pattern by EBL up to 800 nm of PMMA whilst still keeping a linewidth below 50 nm. This allowed the deposition of a control line track made of a gold (200 nm)/niobium (300 nm)/gold (20 nm) trilayer.

A simulation using 3D-MLSI, shown in Figure 6.2, predicts a mutual inductance of 0.15 pH corresponding to 70.8 Φ_0/A. As an additional check to verify this estimate, we can apply the Biot-Savart law to determine the magnetic field generated by a current in the control line, and thus estimate the flux going through the loop of the device. The relevant dimensions used in this calculation are shown in Figure 6.3. We only consider the straight section of the wire as the curved parts are sufficiently far away from the device that their contributions tend to cancel each other out. The line is superconducting and therefore the current distribution is not uniform, being slightly larger at the edges. For simplicity, we neglect this effect. The effective area of the SQUID was measured to be 7.9 µm^2. Considering its geometry, we estimate that the effective area is equivalent to a rectangle of width:height ratio $\sim$ 1:3, or 1.62 µm × 4.87 µm, located at about 8 µm from the closest edge of the line. The Biot-Savart law states that the field d$\mathbf{B}$ at a point P generated by a current I flowing in a segment of wire d$\mathbf{l}$ is

$$\mathrm{d}\mathbf{B} = \frac{\mu_0 I}{4\pi} \frac{d\mathbf{l} \times \mathbf{r}}{r^3}. \tag{6.1}$$

The point P is located at $\mathbf{r}$ from the wire. Integrating over the whole length of the

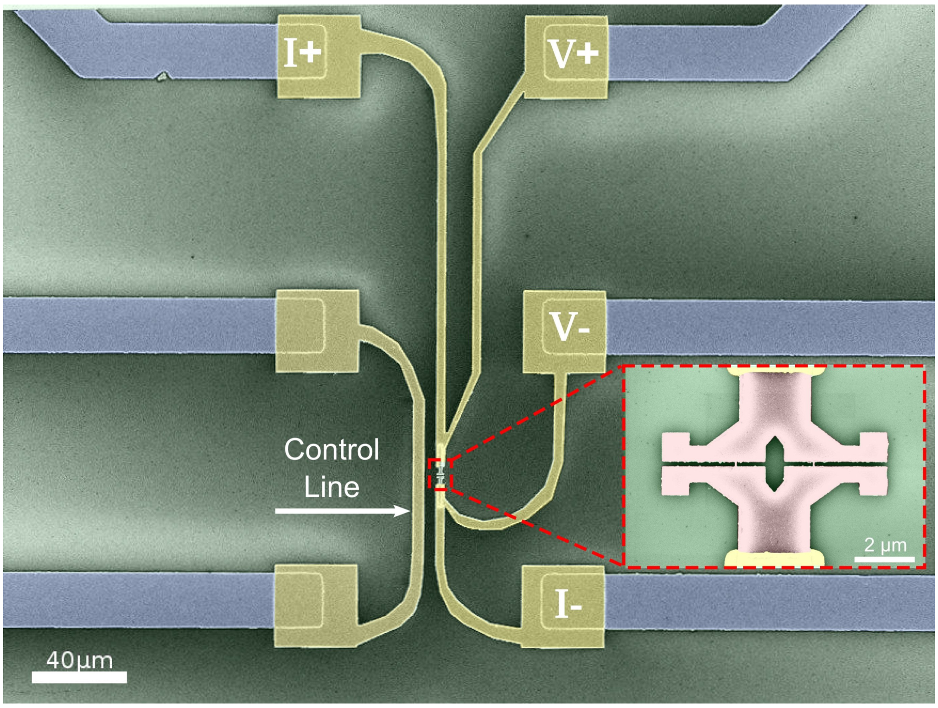

Figure 6.1: False-coloured SEM micrograph of SQUID Y-1, deposited with *in situ* tilting to fabricate nanobridges made of gold (33 nm)/titanium (95 nm) and a loop made of gold (33 nm)/titanium (545 nm). The tracks, in yellow, were EBL patterned and made of sputtered gold (200 nm)/niobium (300 nm)/gold (20 nm) trilayer. The chip tracks are in blue and the substrate (SiO$_2$) in green. The inset shows the zoomed-in SQUID region.

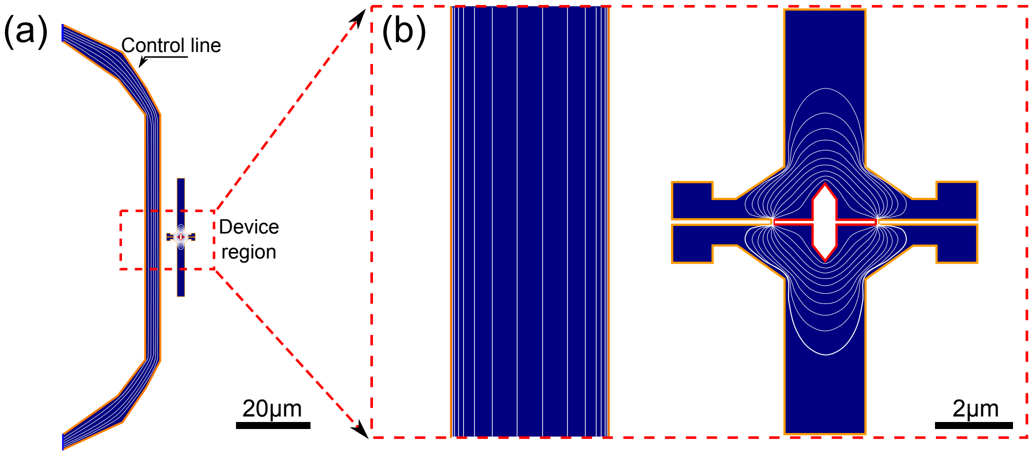

Figure 6.2: Diagram showing the output of the 3D-MLSI model used to estimate the mutual inductance between the SQUID and the control line. (a) The complete model showing the control line is on the left and the device on the right. The region inside the dashed red rectangle is magnified in (b) showing the current streamlines calculated by the mutual inductance determination algorithm.

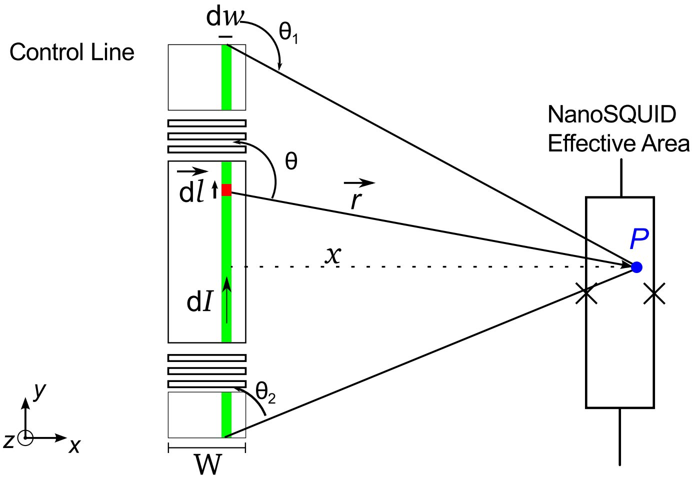

Figure 6.3: Schematic diagram of a simple model used to estimate the flux going through a device using the Biot-Savart law. Only the straight part of the control line is considered. For the analysis, it is decomposed into filamentary elements (in green) of width $\mathrm{d}w$ each carrying a current $\mathrm{d}I = I\mathrm{d}w/W$. Each element is itself split into elementary pieces (in red) $\mathrm{d}\mathbf{l}$ to which we can apply the Biot-Savart law.

wire, it can be found that

$$\mathbf{B}(\mathrm{P}) = \frac{\mu_0 I}{2\pi x}\frac{\cos(\theta_2) - \cos(\theta_1)}{2}\hat{\mathbf{z}} \tag{6.2}$$

where x is the x component of $\mathbf{r}$, and θ_2 and θ_1 are defined in Figure 6.3. As the wire is long (65 µm), the factor $(\cos(\theta_2) - \cos(\theta_1))/2$ is larger than 0.98. We can therefore assume to a good approximation that the wire is infinite and neglect this term. The control line of total width W can be considered as the juxtaposition of filamentary wires of width $\mathrm{d}w$ each carrying a current of $I\mathrm{d}w/W$. Integrating over W, we obtain

$$B(x) = \frac{\mu_0 I}{2\pi W}\ln(1 + W/x). \tag{6.3}$$

The total flux coupled to the loop is therefore given by

$$\Phi = \iint B\mathrm{d}S = \frac{\mu_0 I}{2\pi W}\int_{y=0}^{4.87\times10^{-6}}\mathrm{d}\,y\int_{x=8\times10^{-6}}^{9.62\times10^{-6}}\ln(1 + W/x)\mathrm{d}x \tag{6.4}$$

This integral over x does not admit an analytical solution and requires numerical estimation. This was performed using Python and SciPy. We find that the mutual inductance $M = \Phi/I$ is 0.148 pH, or 71.55 Φ_0/A, which is in good agreement with the estimate provided by the 3D-MLSI model. Considering the critical current density of a high-quality niobium film, $J_\mathrm{c} = 4\times10^{10}\,\mathrm{A/m^2}$ [157], the maximum flux we can couple to the SQUID while keeping the control line in a superconducting state is 3.4 Φ_0 which is a very large signal.

At this point, it should have been possible to flux-bias the SQUID in the ADR at the optimum flux bias point ($\Phi \approx \Phi_0/4$) using the external sample magnet and operate it in small signal mode to measure the magnetic field generated by the control line. However, as the outer rf shielding of the ADR did not shield the device from 50 Hz noise and its harmonics, we instead used the set-up shown in Figure 6.4 to alleviate this issue. Once the system was stable at the chosen temperature, the SQUID bias current was first adjusted to maximise the $V(\Phi)$ response, then

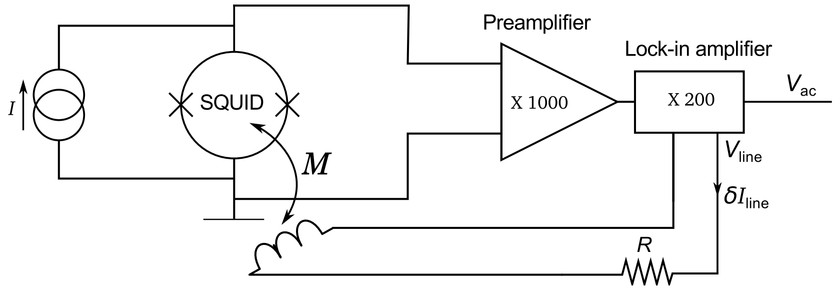

Figure 6.4: Schematic diagram of the set-up used to measure the response of the device to the magnetic field generated by the control line. The SQUID is biased using a dc current source. An ac generator is connected to the control line, applying the current δI_{line} at a given frequency. The response of the device is then recorded by the lock-in amplifier referenced to this frequency.

maintained at this optimal value using a battery-operated current source. An ac current $\delta I_{\text{line}} = 50\,\mu\text{A}$ at 11.139 Hz was then applied through the control line. We chose this frequency to clearly distinguish the signal from the harmonics of the 50 Hz noise. The ac voltage response δV_{AC} of the device was measured using a lock-in amplifier referenced to this frequency. Assuming the signal is small enough (which is valid as 50 µA would correspond to about $\delta\Phi = 3.5 \times 10^{-3}\,\Phi_0 \ll \Phi_0$ according to our estimate of M) the voltage response is linearly proportional to $\mathrm{d}V/\mathrm{d}\Phi$ at any given flux-bias. In this case, the response δV_{ac} and δI_{line} are linked by the equation

$$\delta V_{\text{ac}} = \frac{\mathrm{d}V}{\mathrm{d}\Phi}\frac{\mathrm{d}\Phi}{\mathrm{d}I}\delta I_{\text{line}} = M\frac{\mathrm{d}V}{\mathrm{d}\Phi}\delta I_{\text{line}}. \tag{6.5}$$

Using the external sample magnet, the magnetic flux was then swept over several periods yielding the voltage response shown in Figure 6.5. As the mutual inductance M is a constant, we know from Equation 6.5 that the maximum of δV_{ac}, written as $(\delta V_{\text{ac}})_{\text{max}}$, is reached at the flux-bias that corresponds to the maximum transfer function $V_\Phi = (\mathrm{d}V/\mathrm{d}\Phi)_{\text{max}}$. The knowledge of these two values enables us to estimate M. $(\delta V_{\text{ac}})_{\text{max}}$ can be read directly from Figure 6.5 and equals 130 nV. V_Φ is found using Figure 6.6 which shows the numerical derivative of the $V(\Phi)$ characteristics of the SQUID at the optimal bias current: $V_\Phi = 35\,\mu\text{V}/\Phi_0$. Using these two values in Equation 6.5 gives $M = 74.28\,\Phi_0/\text{A}$ which is in excellent

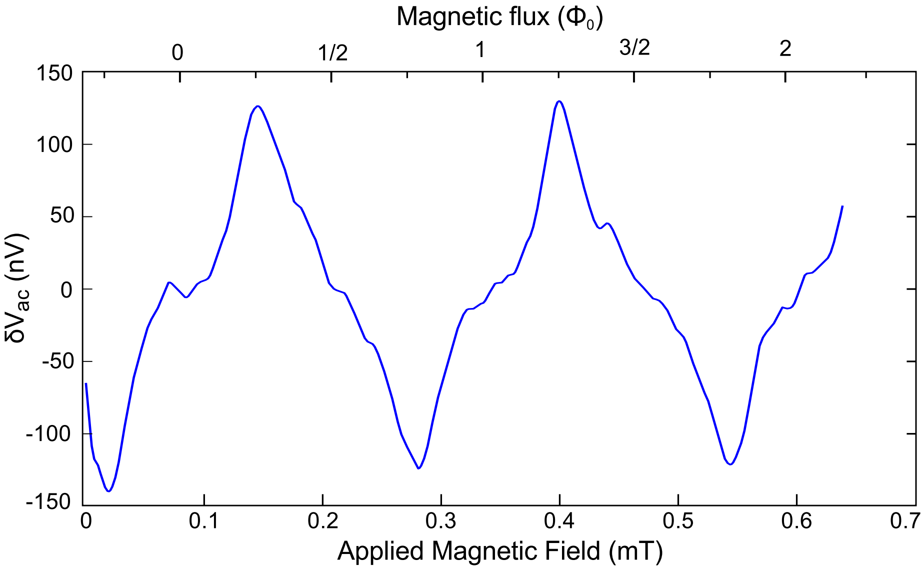

Figure 6.5: Voltage δV_{ac} measured across the SQUID in the setup shown in Figure 6.4 as a function of applied magnetic field for $T = 200\,\mathrm{mK}$, $I_{\mathrm{bias}} = 5\,\mu\mathrm{A}$ and $\delta I_{\mathrm{line}} = 50\,\mu\mathrm{A}$ at 11.139 Hz.

agreement with the theoretical value estimated above.

This experiment with the control line was reproduced at several temperatures and $(\delta V_{\mathrm{ac}})_{\mathrm{max}}$ measured as shown in Figure 6.7. From this, we can estimate the corresponding V_Φ as a function of temperature. As the temperature increases, the sensitivity is reduced due to the decrease of I_{c} and the increase of the kinetic inductance. For a SQUID with a sinusoidal response, symmetric bridges and β_L close to 1, which is the case for SQUID Y-1, theory gives $V_\Phi \approx \pi I_{\mathrm{c}} R_{\mathrm{n}}/(1+\beta_L)$ where $\beta_L = 2LI_{\mathrm{c}}/\Phi_0$ as we saw in Chapter 1. The kinetic component of the inductance is a function of the penetration depth so that $L_{\mathrm{k}} = \mu_0 l \lambda(T)^2/wt$ [154] where l, w and t are the length, width and thickness of the structure. For the loop body of SQUID Y-1, $l = 8.8\,\mu\mathrm{m}$, $w = 1.5\,\mu\mathrm{m}$ and $t = 450\,\mathrm{nm}$ and for the bridges $l_{\mathrm{b}} = 150\,\mathrm{nm}$, $w_{\mathrm{b}} = 50\,\mathrm{nm}$ and $t_{\mathrm{b}} = 100\,\mathrm{nm}$. The penetration depth $\lambda(T)$ is a function of temperature assumed to follow $\lambda(T) = \lambda_0\sqrt{(1-T/T_{\mathrm{c}})^4}$. V_Φ is thus a function of temperature. A best fit of this theory to the data of Figure 6.5 with λ_0 as a fitting parameter yields $\lambda_0 = 623\,\mathrm{nm} \pm 70\,\mathrm{nm}$ ($R^2 = 0.811$). This is consistent with the results obtained in Chapter 5 that suggested $\lambda_0 \approx 750\,\mathrm{nm}$ for titanium.

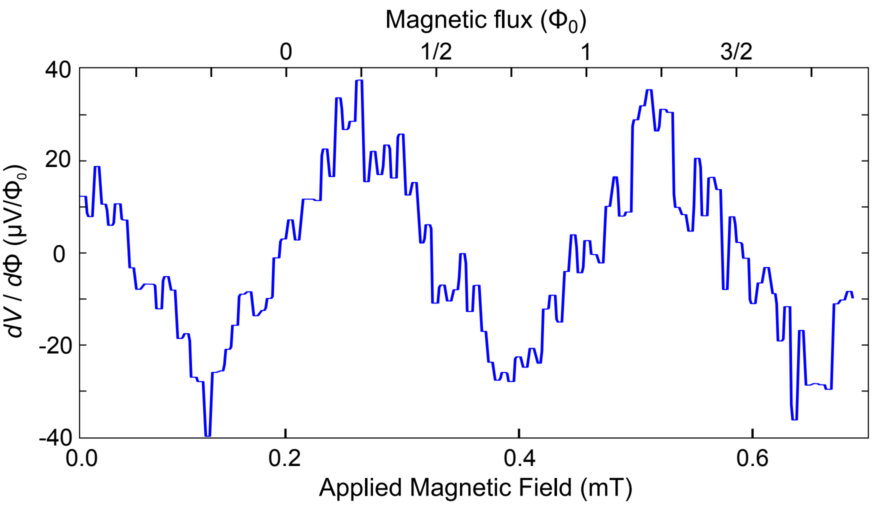

Figure 6.6: Derivative $\mathrm{d}V/\mathrm{d}\Phi$ of the voltage measured across Device Y-1 as a function of applied magnetic field for $T = 200\,\mathrm{mK}$ and $I_{\mathrm{bias}} = 5\,\mu\mathrm{A}$. The effective area, determined from the measured periodicity of $\Delta B = 0.2637\,\mathrm{mT}$, is $7.93\,\mu\mathrm{m}^2$. The apparent quantisation noise is due to the numerical derivation of a fairly low number of points.

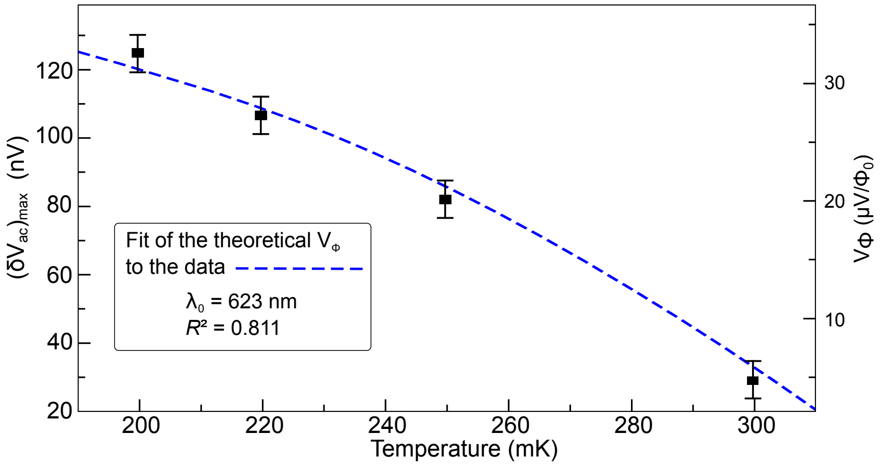

Figure 6.7: $(\delta V_{\mathrm{ac}})_{\mathrm{max}}$ and matching V_Φ as a function of temperature. The blue dashed curve is a fit of the theoretical V_Φ for this SQUID assuming a perfectly sinusoidal response, symmetric bridges and $\beta_L \approx 1$ to the data using λ_0 as a fitting parameter. The fit gives $\lambda_0 = 623\,\mathrm{nm}$ with $R^2 = 0.811$.

With this technique, assuming a typical SQUID flux noise of $0.1\,\mu\Phi_0/\sqrt{\mathrm{Hz}}$, the control current corresponding to the minimum detectable flux with a 1 Hz bandwidth is 1.4 nA. This would be detectable only by using a very low noise low-temperature preamplifier such as a perfectly matched SSA. The noise from a typical room-temperature preamplifier is $1\,\mathrm{nV}/\sqrt{\mathrm{Hz}}$ [158] which is about 30 times higher than the voltage noise of our nanoSQUID. This noise would be the limiting factor of the measurement and the minimum current detectable in this situation would be $\sim 45\,\mathrm{nA}$ with a 1 Hz bandwidth.

6.1.2 Determination of the Penetration Depth of a Superconducting Plane

In this section, we try to replicate the response of a SQUID to a thin underlying superconducting layer as may be seen for some superconducting systems of interest, e.g. $SrTiO_3/LaAlO_3$ heterointerface, but with a larger, easier-to-see, response for preliminary measurements and proof of concept. As the penetration depth of the superconducting plane decreases with temperature, it would more effectively screen flux which translates into a reduced effective area A_{eff} for the SQUID above. The details of this effect would be a function of the parameters of the plane such as its resistivity, critical temperature, etc. To test the feasibility of actual measurements on such systems, we fabricated a sample that mimics the actual integration on a layer of interest, but with the geometry inverted with the layer above the nanoSQUID. After initial characterisation of the bare SQUID X-3 described in Chapter 5, this device was then reprocessed and covered with a $2\,\mu\mathrm{m} \times 2\,\mu\mathrm{m}$ superconducting layer isolated from the SQUID by an insulating layer of silicon nitride Si_3N_4. This was chosen instead of silicon dioxide because of its better properties as a diffusion barrier and also because its deposition does not require the presence of oxygen that might compromise the nanobridges made of titanium. First the chip was coated with a 700 nm-thick PMMA layer and then openings in the resist were created over the device using EBL followed by development in MIBK:IPA. We then deposited a 200 nm thick insulating layer of sputtered Si_3N_4. This layer was thick enough to completely cover the SQUID and prevent any electrical connection with the overlying superconducting layer. To grow Si_3N_4 the plasma was striking a 99.999 % pure silicon target with a constant flow of 20 standard cubic centimetres per minute (SCCM) of nitrogen, corresponding to a partial pressure of 6.6×10^{-3} mbar. At a sputtering power of 150 W, the growth rate was 0.5 Å/s, so it took 65 min to achieve a thickness of 200 nm. After deposition, the resistivity was checked with a four-point probe and was measured to be $> 10^8\,\Omega$.cm.

To choose an appropriate material for the superconducting plane, we had to make sure that its critical temperature was within the operating range of the SQUID ($< T_\mathrm{c} \sim 650\,\mathrm{mK}$). As the temperature is reduced, $\lambda(T)$ becomes shorter and the superconducting overlayer more efficiently screens flux from the SQUID, decreasing its effective area A_eff. We also require the thickness of the superconducting layer to be comparable to λ to obtain a significant effect. Assuming $V(B)$ is sinusoidal, we can fairly accurately estimate its periodicity and thus A_eff, by dividing the difference in field between two peaks by the number of periods separating them. As the true maxima could fall between experimental points, the error in this estimation is of the order of $1/f_\mathrm{s}N_{\Delta B}$ where f_s is the sampling "frequency"[1] (in mT^{-1}) and $N_{\Delta B}$ is the number of periods measured. Typically, we used $f_\mathrm{s} \approx 150\,\mathrm{mT}^{-1}$ and $N_{\Delta B} = 4$ for a period $\Delta B \approx 1.4\,\mathrm{mT}$. The error in reading for a typical measurement is therefore $\sim 1\,\%$, although obviously this could have been improved if necessary by taking a longer sample with a higher sampling frequency.

We used a proximity bilayer of Al/Ag to achieve a superconducting plane with $T_\mathrm{c} \sim 600\,\mathrm{mK}$. We chose to use a 150 nm thick aluminium base layer for its short penetration depth $\lambda_0 \sim 200\,\mathrm{nm}$ which would give an easily measurable shift, and incidentally because the study of its bilayer would give us a better knowledge of the potential characteristics of an aluminium-silver based nanoSQUIDs. To determine

---

[1] Such periodicity analysis and especially FFTs are typically performed on signals that are a function of time and therefore the associated vocabulary refers to time. For simplicity, we use the terms "frequency", "temporal domain", "duration" in the following to refer to a signal which is a function of applied magnetic field. A "frequency" is therefore in mT^{-1}, a "duration" in mT, etc.

the thickness of silver to add to depress T_c, we used the fit to the model of Martinis *et al.* [140] described in Section 4.2.2 for aluminium-silver bilayers that gave a transmission coefficient $t = 0.28$. From this we predicted that adding 80 nm of Ag on 150 nm of Al would bring T_c down to ~ 630 mK which would lead to a significant change of penetration depth within our SQUID operating range. This deposition of the Al (150 nm)/Ag (80 nm) superconducting plane was performed by e-beam evaporation at a pressure $< 10^{-6}$ mbar and a rate of ~ 1 nm/s for both metals. The resulting device is shown in Figure 6.8.

The effective area without the plane was measured to be 7.76 µm^2 and was temperature independent as the penetration depth of the SQUID is sufficiently large ($\sim$ 750 nm) that its increase with temperature does not lead to a measurable change in flux focussing. From this, we expect that any change in effective area at a given temperature is exclusively due to the effect of the superconducting plane. After adding the plane, the device was then cooled down again in the ADR and its effective area re-measured at different temperatures. The data collected is shown in Table 6.1 and shows a change in A_{eff} of up to 35 % at the lowest temperature.

T (mK)	ΔB (µT)	A_{eff} (µm^2)	$A_{\text{eff}}/A_{\text{eff,0}}$ (%)	Reference #
150	407	5.09	65.5	♯1
250	390	5.31	68.3	♯2
350	368	5.62	72.4	♯3
450	286	7.23	93.0	♯4
500	266	7.77	100	
550	265	7.82	100	
600	267	7.75	100	
650	268	7.73	100	

Table 6.1: Table presenting the effective area measured for Device X-3 after deposition of the Al-Ag layer at different temperatures. The reference numbers (#) are used to interpret Figure 6.10. $A_{\text{eff,0}}$ is the effective area of the bare SQUID before the superconducting plane deposition.

We developed a 3D-MLSI model to link the measured change of A_{eff} to the predicted

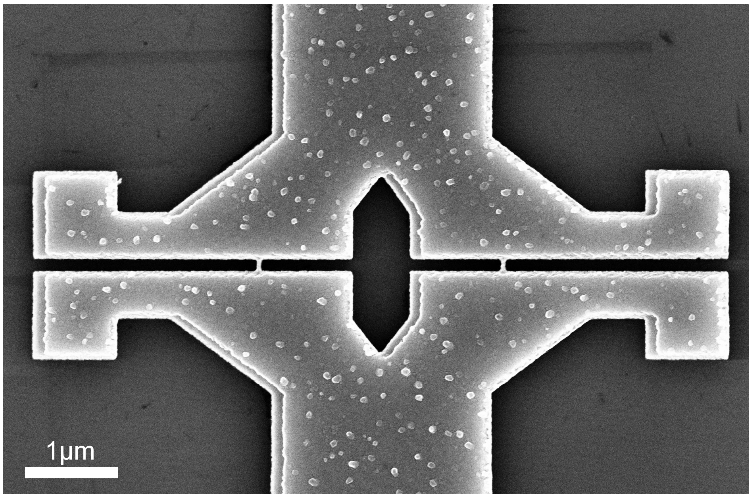

(a) Before deposition of the superconducting plane

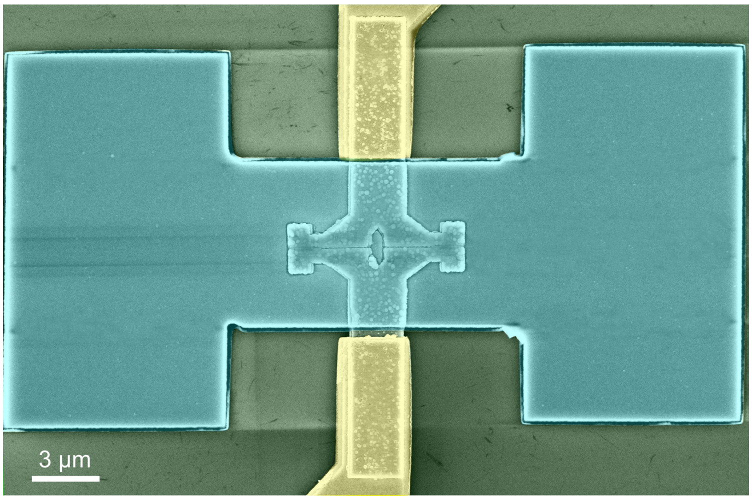

(b) After deposition of the superconducting plane

Figure 6.8: SEM micrographs of SQUID X-3 at two different stages of development: (a) before the deposition of the superconducting plane, and (b) after deposition (false-colouring). The Si_3N_4 layer and the overlying superconducting plane (in blue) are covering the SQUID visible underneath. The shape of the plane was chosen to maximise its area whilst not touching the gold leads (yellow) that were added in a previous step.

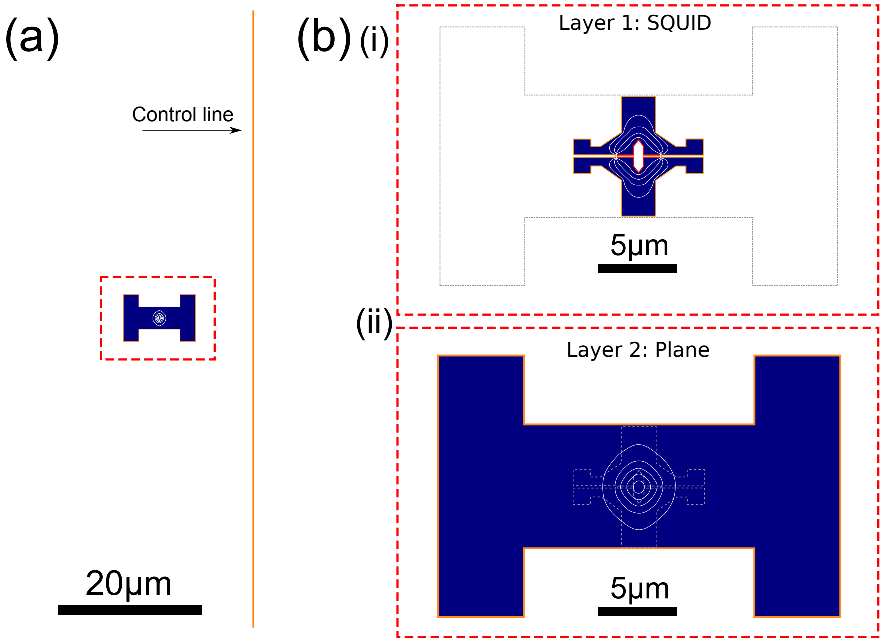

Figure 6.9: 3D-MLSI output after modelling the mutual inductance between the SQUID with the overlying superconducting plane and a control line. (a) shows the overall geometry and (b) shows magnified views of the two different layers: (i) the analysis for the SQUID layer with the plane greyed out for clarity (ii) equivalent analysis for the plane layer. The white lines are the current paths shown by the software.

λ for the superconducting plane. 3D-MLSI is limited to estimating the mutual inductance between two distinct materials only, referred to as *mat 1* and *mat 2* in the following, each having their respective thicknesses and penetration depths. In our model we therefore defined the SQUID as made of *mat 1*, whose penetration depth and thickness we set to match the values of the SQUID, respectively 740 μm and 200 nm. A plane of *mat 2* was then set to be located just above the device, whose thickness was 150 nm, corresponding to the aluminium thickness. The code to create this model can be found in Appendix B and the resulting 3D-MLSI schematic is shown in Figure 6.9. As we did previously in Chapter 5, we can consider that the field generated by a very long control line far enough from the SQUID will generate a magnetic field B constant over the area of SQUID. As $\Phi_{\text{SQUID}} = BA_{\text{eff}}$, it follows that M and A_{eff} are linearly proportional, related by $A_{\text{eff}} = 2\pi RM/\mu_0$. Using a computer script written in Python as a wrapper to 3D-MLSI enabled batch

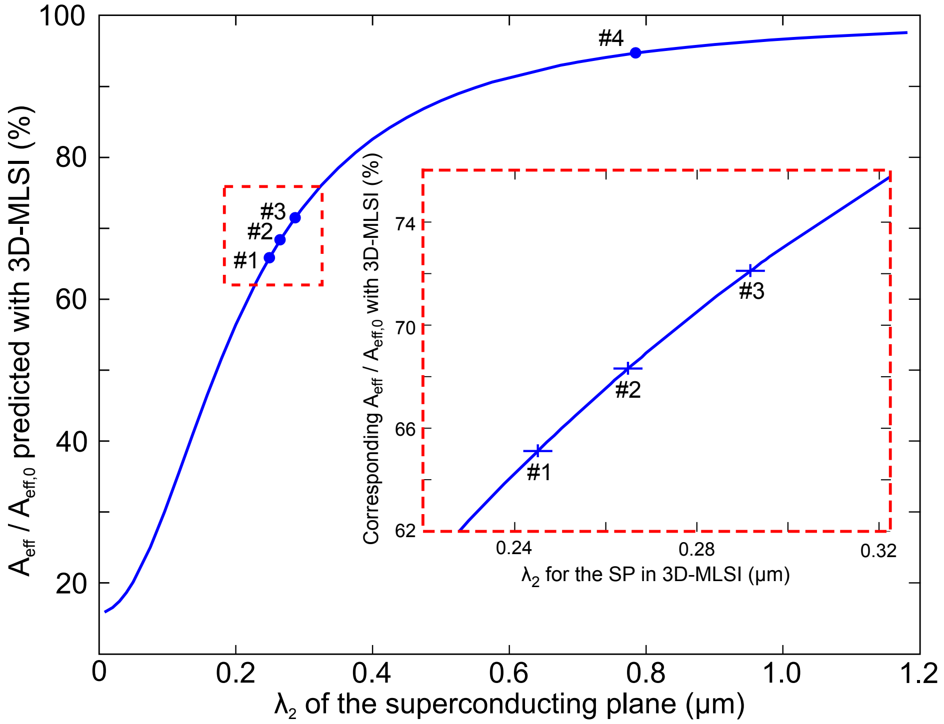

Figure 6.10: The predicted ratio $A_{\text{eff}}/A_{\text{eff},0}$ as a function of the penetration depth λ_2 of the 150 nm thick superconducting plane. The reference numbers (#) correspond to the values in the last column of Table 6.1. The insert is a zoomed-in region of the plot to make clearer the difference between the estimated values for the different input parameters. $A_{\text{eff},0}$ is the effective area of the device before the superconducting plane deposition.

calculations of the mutual inductance. We then generated a precise estimate of the corresponding change in A_{eff} as a function of the penetration depth λ_2 for the superconducting plane, as shown in Figure 6.10. In other words, using this graph we can match any measured change in effective area to a corresponding theoretical value for λ_2.

The model is insensitive to the exact thickness t_1 of the SQUID and its penetration depth λ_1: having $t_1 = 0.6\,\mu\text{m}$ in the model instead of $t_1 = 0.4\,\mu\text{m}$ results in a change of less than 0.3 % in A_{eff}. However, it is highly sensitive to the thickness t_2 of the superconducting plane. The error of the crystal monitor during the evaporation is estimated to be about ±2 % of the thickness for a standard evaporation which corresponds to an uncertainty in λ_2 of $\sim 4\,\text{nm}$. With the ±1 % error from the determination of the $V(B)$ period, we have an estimated total error $\sim \pm 14\,\mathrm{nm}$ in the estimate of λ_2. As a first approximation, we fitted λ_2 obtained as a function of temperature to the two-fluid model, $\lambda(T) = \lambda_0/\sqrt{1-(T/T_\mathrm{c})^4}$, with λ_0 and T_c as fitting parameters. The proximity effect has been reported to affect the temperature dependency of λ, especially at low temperatures [159], but taking this slight correction into account would require data for many additional temperatures. Nonetheless with the above assumption, the fit, shown in Figure 6.11, is excellent with $R^2 = 0.9994$, $T_\mathrm{c} = 466 \pm 10\,\mathrm{mK}$ and $\lambda_0 = 248 \pm 12\,\mathrm{nm}$. T_c is smaller than our prediction from the Martinis *et al.* model using a transmission coefficient of $t = 0.28$. Instead it corresponds to a transmission coefficient $t = 0.48$. This can probably be attributed to an improved quality of the interface compared to our early devices, as here we evaporated silver first then aluminium and used a higher, more controlled evaporation rate when we created the plane. The value we found for λ_0 can be compared to the somewhat simplistic theoretical value using the equation $\lambda_0 = \sqrt{\hbar\rho_0/\pi\mu_0\Delta_0}$ we used in Chapter 5 where ρ_0 is the resistivity of aluminium just above T_c and Δ_0 is the energy gap at $0\,\mathrm{K}$ assumed to be $1.76k_\mathrm{B}T_\mathrm{c}$ in the BCS approximation. This gives an estimated $\lambda_0 = 256\,\mathrm{nm}$ which is close to the fitted value. The same technique could be applied for many other thin materials with a weaker response, as will be discussed later in this chapter by taking the example of $\mathrm{SrTiO_3}$-$\mathrm{LaAlO_3}$ heterointerface.

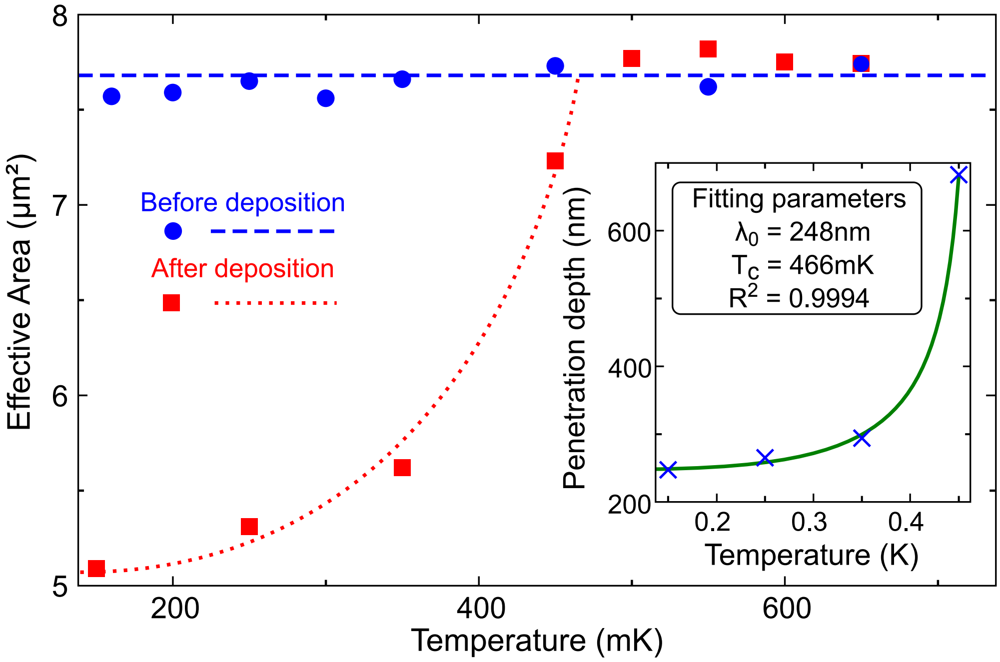

Figure 6.11: The effective area $A_{\text{eff}}(T)$ measured for SQUID X-4 with (red squares) and without (blue circles) an additional $2\,\mu\text{m} \times 2\,\mu\text{m}$ Al (150 nm) - Ag (80 nm) plane covering the device. The broken blue line is a guide to the eye and the red dashed line corresponds to the best fit to the two-fluid model for $\lambda_0 = 248\,\text{nm}$ for the island. The inset shows the theoretical form of $\lambda(T)$ for the island, the blue crosses are experimental data estimated from the measured effective area using 3D-MLSI and the solid line corresponds to the fit to the two-fluid model using the fitting parameters given.

6.1.3 Determination of the Penetration Depth of Superconducting Islands

Another configuration that can be envisaged for the measurement of superconducting layers is to have an island of the material located inside the hole of the SQUID [10]. In this section, we investigate the response of islands made of niobium and titanium/gold. As in the superconducting plane experiment, we deposited the island by EBL and lift-off after an initial characterisation of the bare SQUID. However, as the inner SQUID hole is only 400 nm × 150 nm, this is very technically challenging due to the reduced dimensions. Any slight misalignment of the new pattern would result in the island covering the SQUID. Our technical solution for this was to pattern very fine alignment markers (100 nm × 100 nm crosses) close to the SQUID during the same EBL patterning step of the devices. This enabled us to set the origin of the second pattern with an error below ~ 20 nm and allow the positioning of an island that is just slightly smaller than the SQUID hole, thus maximising the predicted response. The resulting device is shown in Figure 6.12.

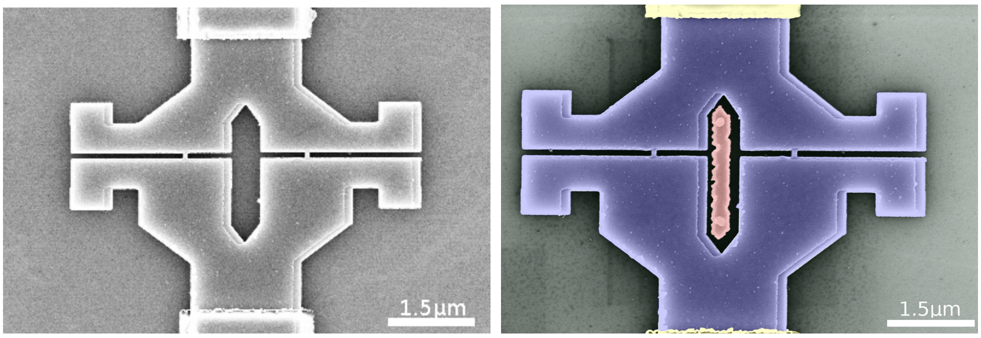

(a) Before deposition of the island (b) After deposition of the island

Figure 6.12: SEM micrographs of SQUID P-1 at two different stages of development: before (a) and after (b) deposition of a superconducting Nb island. False-colouring: the island is shown in red, the SQUID in blue, the substrate in pale green and the tracks in yellow.

Niobium Island

To ensure a visible shift in A_{eff}, we chose to deposit a 150 nm-thick niobium island whose small penetration depth ($\lambda \sim 100$ nm) was expected to strongly screen the magnetic flux. Despite the island being very small, our measurement on the SQUID with islands showed that the effective area was reduced by 1.4 % compared to the device before deposition of the island. The results before and after the Nb island deposition are shown in Tables 6.2 and 6.3 respectively. The effect is much smaller than we obtained with the superconducting plane. The difference is due to the fact that the inner SQUID hole is about 3 μm^2 whilst the SQUID effective area is about 10 μm^2 which means that only a small percentage of the applied flux ($< 33\,\%$) could be screened even if the island were infinitely thick. In order to offer an automated determination of the $V(B)$ period over many data files and to reduce any human bias when reading the graphs, we implemented an algorithm performing a Fast Fourier Transform (FFT) on each $V(B)$ curve and isolated the main frequency. This was written in Python and we used its modules SciPy and NumPy to analyse the spectrum and determine the main period. However, as our signal does not have to be analysed in real time, we can set a much higher resolution by heavily zero-padding the signal, i.e. adding a large number of zeros at the end of the signal. We chose to zero-pad to get $N = 2^{20}$ points. (This number of points enables the use of the extremely efficient split-radix FFT algorithm [160]). We chose a rectangular window over for instance a Hanning window as this minimises the uncertainty in the main harmonic determination even though it does not prevent spectral leakage, leading to the appearance of secondary lobes on either side of the harmonic. Figure 6.13 shows the typical shift in $V(\Phi)$ we obtained after island deposition, which directly corresponds to the shift of the main harmonic in the FFT. The values obtained using FFT are included in Table 6.3 as well.

From the tables, we can see that as expected FFT and measurement by eye give equivalent standard deviations, being both limited by the length of the signal and its sampling frequency. However, the FFT offers the option to automatise the analysis and perform batch-processing on many files which can be useful in future. It also removes any possible human bias. Even though the measured shift in frequency was large enough to be obviously significant, a precise determination

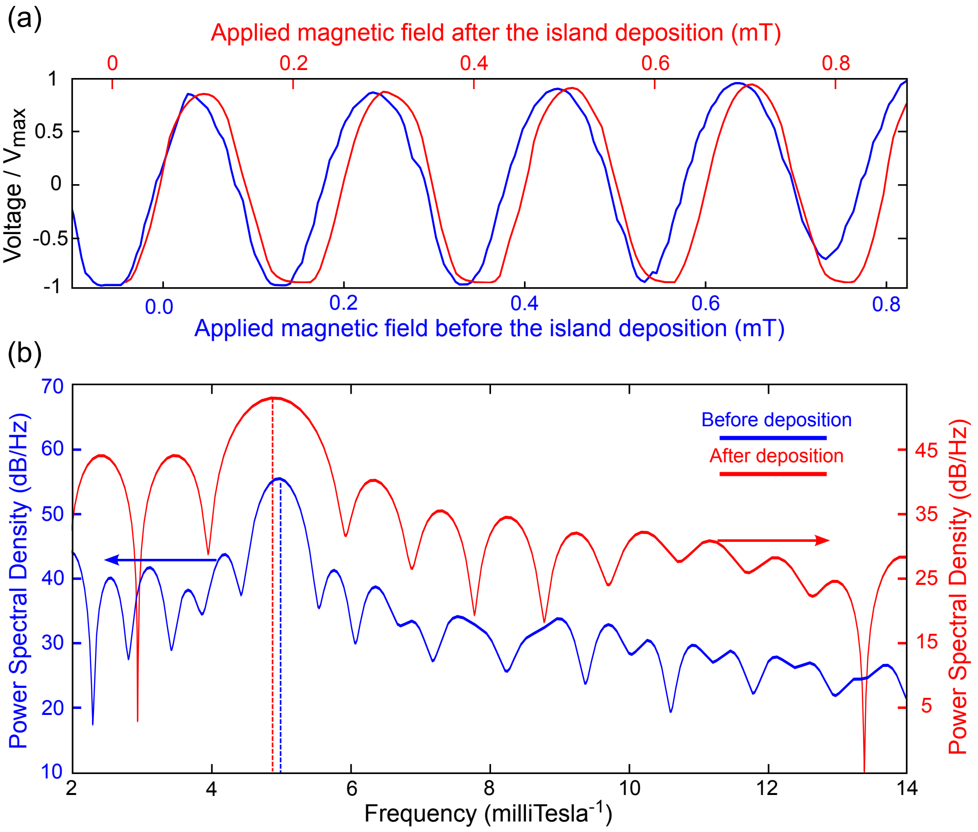

Figure 6.13: (a) Voltage across the SQUID as a function of applied magnetic field before (blue) and after (red) deposition of the Nb island. The red curve has been shifted to aid the comparison in periodicity and account for the slight shifts between cool-downs. (b) Power spectral density obtained by FFT of the zero-padded signal above. Only the positive part of the spectrum is shown. The values in blue are for the device without island and in red after the island has been deposited. The main peak shows a 1.4 % shift in frequency from $4.98\,\mathrm{mT}^{-1}$ to $4.91\,\mathrm{mT}^{-1}$ which translates into a shift in effective area from $10.32\,\mu\mathrm{m}^2$ to $10.17\,\mu\mathrm{m}^2$.

I_{bias} (µA)	T (K)	A_{eff} by eye (µm^2)	A_{eff} by FFT (µm^2)
0.16	11.4	10.32	10.352
0.2	11.4	10.28	10.219
0.2	12	10.34	10.311
0.25	8	10.22	10.209
0.28	8.7	10.30	10.339
0.3	8.7	10.29	10.294
0.38	8.4	10.37	10.392
Average		10.30	10.302
Std Deviation		0.048	0.0687

Table 6.2: Table presenting the effective area measured for SQUID P-1 before deposition of the niobium island at different temperatures and bias currents.

I_{bias} (µA)	T (K)	A_{eff} by eye (µm^2)	A_{eff} by FFT (µm^2)
0.15	6	10.13	10.090
0.15	9.2	10.23	10.291
0.15	9.4	10.13	10.267
0.15	9.6	10.18	10.116
0.25	9.6	10.18	10.161
Average		10.17	10.185
Std Deviation		0.0402	0.0899

Table 6.3: Table presenting the effective area measured for SQUID P-1 after deposition of the niobium island at different temperatures and bias currents.

of the statistical confidence interval for the estimate of λ requires a two-sample t-test on the two sets of data before and after deposition. To do this, we tested the validity of the null hypothesis "$\mu_{\mathrm{w/o}} = \mu_{\mathrm{isl}}$" where μ is the true mean (subscript "w/o" before deposition and "isl" after) by considering a parameter called the t-value based on the mean $\overline{x}$ and standard deviation $\hat{s}$ of the two sets of data (subscript "w/o" before deposition and "isl" after). As the standard deviations can be potentially different, we use Welch's t-test, which is a modified Student's t-test adapted for this case, which has a t-value

$$t = \frac{\left(\overline{x_{\mathrm{isl}}} - \overline{x_{\mathrm{w/o}}}\right) - \left(\mu_{\mathrm{isl}} - \mu_{\mathrm{w/o}}\right)}{\sqrt{\frac{\hat{s}^2_{\mathrm{isl}}}{n_{\mathrm{isl}}} + \frac{\hat{s}^2_{\mathrm{w/o}}}{n_{\mathrm{w/o}}}}}. \tag{6.6}$$

Then t-value has to be compared to the Student's t-distribution which is a form of normal distribution adjusted by the number of degrees of freedom ν. ν is a function of the number of entries available and their variances. Its expression is

$$\nu = \frac{\left(\dfrac{\hat{s}^2_{\mathrm{isl}}}{N_{\mathrm{isl}}} + \dfrac{\hat{s}^2_{\mathrm{w/o}}}{N_{\mathrm{w/o}}}\right)^2}{\dfrac{\hat{s}^4_{\mathrm{isl}}}{N^2_{\mathrm{isl}}(N_{\mathrm{isl}}-1)} + \dfrac{\hat{s}^4_{\mathrm{w/o}}}{N^2_{\mathrm{w/o}}(N_{\mathrm{w/o}}-1)}}. \tag{6.7}$$

The higher ν, the closer the Student t-distribution tends towards the normal distribution. We then calculate the theoretical t-value at ν degrees of freedom and an appropriate level of significance, typically 95 %. To conclude that the means are significantly different at this level of probability, the calculated t-value has to exceed the theoretical t-value. The two-tailed p-value can be calculated as well and represents the probability that these observations be made if the null hypothesis of same means holds true. The results for the t-test analysis are shown below in Table 6.4. The p-value is lower for the measurements by eye but even for the FFT it is below 5 % which indicates the difference in the means is statistically significant and is due necessarily to the effect of the island. Using 3D-MLSI we simulated the

	Manual	FFT
Degree of freedom	9.93	7.20
t value	4.30	2.44
p-value	0.0016	0.0439
$\overline{x}_{\mathrm{isl}} - \overline{x_0}$ (µm^2)	-0.1411	-0.116
Confidence interval at 95 % (µm^2)	[-0.214 , -0.068]	[-0.229 , -0.004]
Change in A_{eff} (%)	-1.36 %	-1.12 %
Confidence interval at 95 % (%)	[-2.08 % , -0.66 %]	[-2.22 % , -0.04 %]

Table 6.4: Table presenting the results of the t-test on the two sets of data in Table 6.2 (before Nb island deposition) and Table 6.3 (after).

change in effective area as a function of the penetration depth of the island. The curve is shown in Figure 6.14. A change in effective area of 1.4 % corresponds to an island made of a material whose penetration depth would be about 70 nm. The confidence interval at 95 %, which represents the interval having a 95 % probability to contain the true difference in effective area $\mu_{\mathrm{isl}} - \mu_{\mathrm{w/o}}$ is [-2.08 % , -0.66 %] which

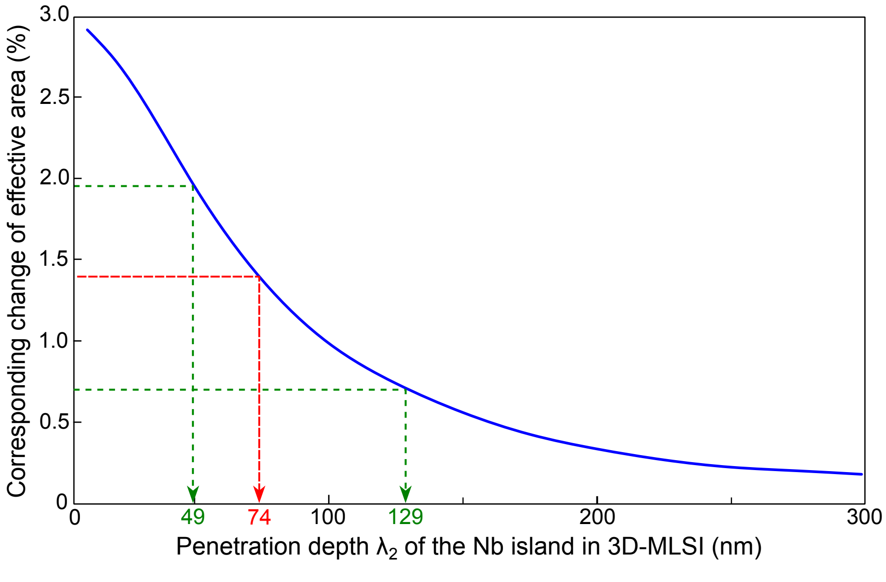

Figure 6.14: Estimated change in the effective area of SQUID P-1 after adding a 150 nm thick island as a function of the island's penetration depth. The red line indicates the mean measured (by eye). The green lines are the lower and upper bounds of the corresponding 95 % confidence interval where lies the true value of the mean measured by eye.

gives [$51\,\mathrm{nm}\,, 93\,\mathrm{nm}$] for λ_2. This is in excellent agreement with the values published for thin films of pure niobium $\sim 80\,\mathrm{nm}$. [161]

Titanium-gold island

Following the successful analysis of the niobium island, we decided to investigate a system with a weaker response: a titanium/gold island. By using a higher gold-to-titanium thickness ratio than for the SQUID, the critical temperature of the island would be lower. In an attempt to measure the change of effective area as a function of temperature as we did for the superconducting plane, we chose to deposit Ti (90 nm)/Au (35 nm). According to the 3D-MLSI model, the expected change in A_{eff} far below T_{c} is about 0.3 %, based on the estimate of λ_0 obtained in the previous chapter. This shift is very small and requires a standard deviation in determining the main frequency three times lower than for the Nb island. As we saw, either by eye or FFT, the error in reading is $\mathcal{O}(1/N_{\Delta B})$ where $N_{\Delta B}$ is the number of periods on the $V(\Phi)$. Our initial intent was to go up to $\sim 5\,\mathrm{mT}$ to collect about 20 periods but we found A_{eff} was only constant up to 1.5 mT before starting to increase which we attributed to the suppression of the bulk superconductivity in the film by the magnetic field. This experiment ideally requires a SQUID with a larger loop size to give accurate readings when operated in this way to get an improved significance.

We nonetheless observed a shift of the periodicity illustrated in Figure 6.15 showing the $V(\Phi)$ before and after island deposition along with the respective FFTs. The two sets of data for SQUID X-5 before and after island deposition are presented in Tables 6.5 and 6.6. On average, the frequency of the main harmonic shifts from $3.82\,\mathrm{mT}^{-1}$ to $3.77\,\mathrm{mT}^{-1}$ which translates into a corresponding shift in effective area from $7.89\,\mu\mathrm{m}^2$ to $7.80\,\mu\mathrm{m}^2$ which is about 0.9 %. To assess the significance of the data, we performed a t-test similar to that we used for the niobium island. The results are reported in Table 6.7.

The two-tailed p-value is equal to 0.14 by eye and 0.07 using the FFT. These results fail the t-test at 95 % significance but the FFT shows a 90 % significance

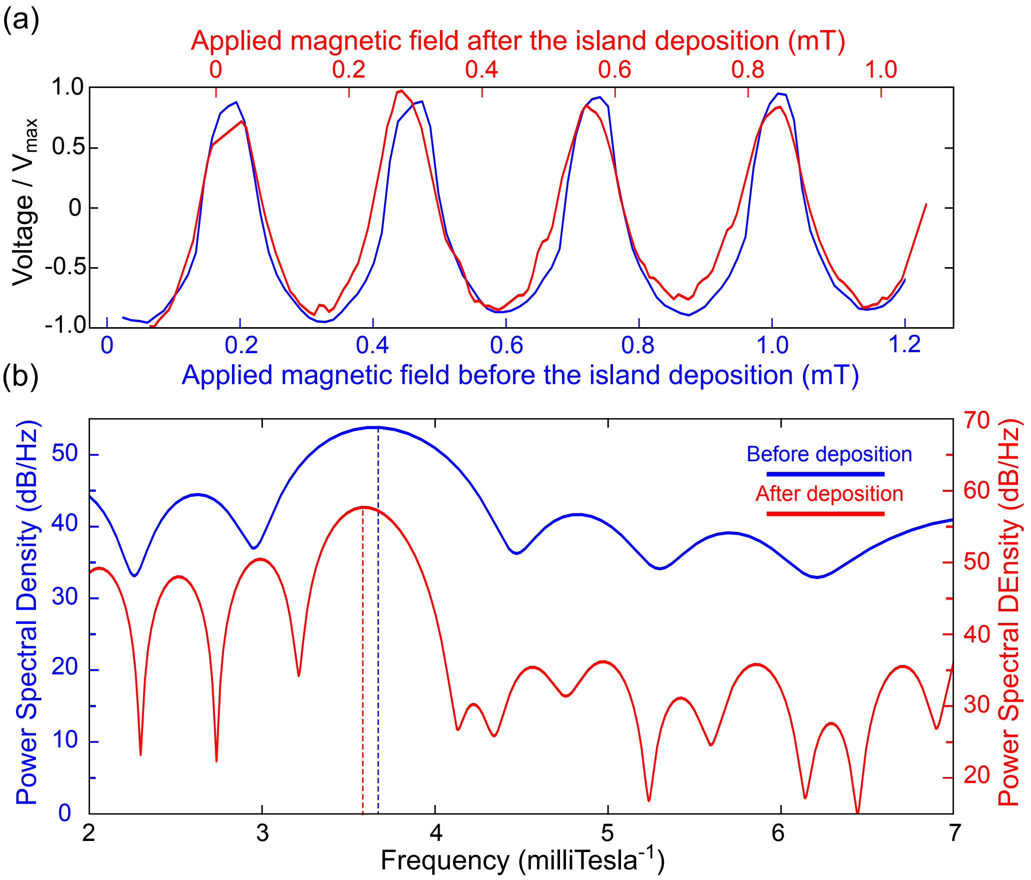

Figure 6.15: (a) Voltage across the SQUID as a function of applied magnetic field before (blue) and after (red) deposition of the Nb island. The red curve has been shifted to aid the comparison in periodicity and account for the different conditions between cool-downs (b) Power density obtained by FFT of the zero-padded signal above. Only the positive part of the spectrum is shown. The values in blue are for the device without island and in red after the island has been deposited. Between these two curves, the main harmonic frequency shifts by $0.05\,\mathrm{mT}^{-1}$ which indicates a change of effective area of $0.09\,\mu\mathrm{m}^2$, i.e.$\sim 0.7\,\%$.

T (K)	I_{bias} (µA)	A_{eff} (µm^2) (by eye)	A_{eff} (FFT)
0.16	5.8	7.42	7.467
0.2	6.2	7.53	7.477
0.2	6.5	7.59	7.586
0.2	6.7	7.56	7.456
0.2	6.9	7.49	7.493
0.2	8	7.60	7.509
0.2	8.5	7.60	7.519
0.2	8.9	7.52	7.332
0.25	7.5	7.53	7.627
0.25	7.8	7.57	7.653
0.25	8.2	7.57	7.609
Average		7.54	7.52
Std Deviation		0.056	0.092

Table 6.5: Table presenting the effective area measured for SQUID X-5 by eye and by FFT after deposition of the Ti/Au island at different temperatures and bias currents.

T (K)	I_{bias} (µA)	A_{eff} (µm^2) (by eye)	A_{eff} (FFT)
0.16	6	7.43	7.460
0.16	6.1	7.52	7.310
0.2	6	7.59	7.494
0.2	7	7.33	7.503
0.25	6	7.48	7.417
0.3	2.7	7.49	7.438
Average		7.47	7.437
Std Deviation		0.097	0.079

Table 6.6: Table presenting the effective area measured for SQUID X-5 by eye and by FFT after deposition of the Ti-Au island at different temperatures and bias currents.

	Manual	FFT
Degree of freedom	6.85	12.0
t value	1.675	1.977
p-value	0.14	0.071
$\overline{x}_{\mathrm{isl}} - \overline{x_0}$	-0.072	-0.084
Change in A_{eff} (%)	-0.96 %	-1.11 %
Confidence interval at 95 % ($\mu\mathrm{m}^2$)	[-0.174 , 0.03]	[-0.177 , 0.009]
Confidence interval at 95 % (%)	[-2.31 % , 0.39 %]	[-2.34 % , 0.11 %]

Table 6.7: Table presenting the results of the *t*-test on the data before and after titanium-gold island deposition on SQUID X-5.

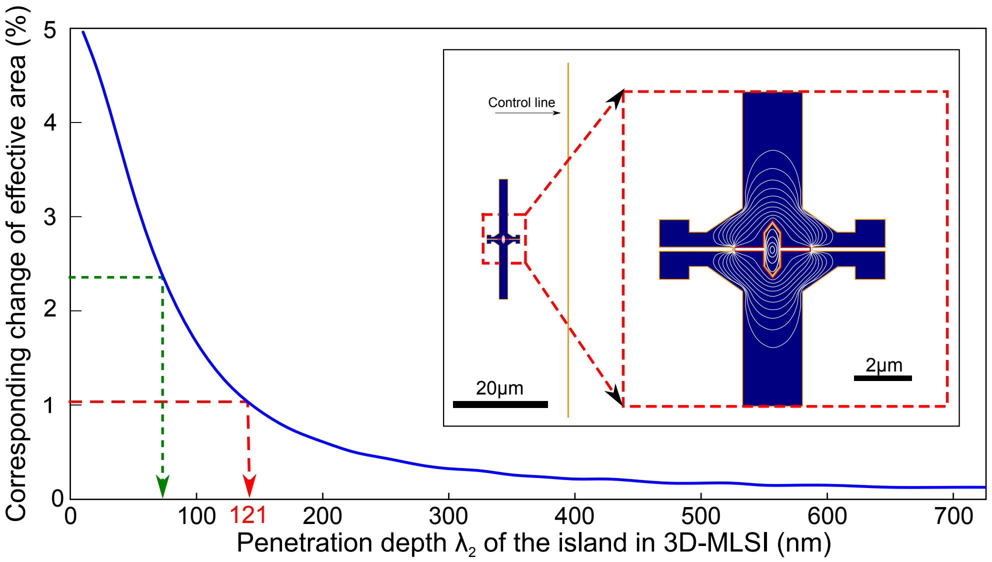

Figure 6.16: Using 3D-MLSI (model shown in inset) to estimate the change of the effective area of SQUID X-5 as a function of the penetration depth λ_2 set for a 80 nm-thick superconducting island deposited inside its loop. In red, λ_2 corresponding to the change in A_{eff} measured by FFT, in green the lower bound of the 95 % confidence interval.

which is satisfactory given the fact the island has a very small effect. As with the niobium island, we can plot the estimated change of effective area as a function of the penetration depth of the island using 3D-MLSI, which is shown in Figure 6.16. The measured shift would translate into a penetration depth of $\sim 120\,\mathrm{nm}$ for the island with a large standard deviation of several hundred nanometres and does not yield as much information as if we had measured more $V(\Phi)$ oscillations using a SQUID with an larger A_{eff}.

To conclude, we have demonstrated measurements of actual superconducting systems with a weak magnetic response by measuring the change in A_{eff} of our nanoSQUIDs. This technique works better by patterning the sample of interest as a plane. This is due to the fact the island dimension is limited to the inner hole size of the SQUID which given our current loop body represents about $30\,\%$ of the effective area. To be successful, measurements of an island would require an effective area at least three times larger ($\sim 30\,\mu\mathrm{m}^2$) to obtain sufficient signal periods, or a different ratio of inner hole area:effective area which could be achieved by having a narrower loop. Care would have to be taken as this would reduce I_{r} and I_{sat}. Additionally it is preferable to keep the area as small as possible to have a better spin coupling and flux noise so the superconducting plane seems the best option. In the following, we will consider the feasibility of measurements of other superconducting systems with very weak response that can be processed as planes.

6.2 Feasibility Study of Ultrathin Magnetic Systems – e.g. the $LaAlO_3/SrTiO_3$ Interface

In the previous chapters, we have demonstrated that we can successfully fabricate and operate devices down to 60 mK which opens the path towards the characterisation of ultrathin magnetic systems with a weak magnetic response that have intriguing properties in the millikelvin range. Such systems encompass topological insulators and heterointerfaces between peroskites. Such layers have been extensively studied by scanning SQUID magnetometry [6, 162, 163]. As the scanning SQUID is being hovered above the sample in a vacuum, there is no physical contact and therefore no issue with excess heat and the additional complications related to reprocessing the substrate such as possible contamination by chemicals or patterning beams. However, this comes at the expense of reduced magnetic coupling, limiting the resolution of such measurements. As our SQUIDs can be operated in a conventional way, independently of temperature and the lift-off process is very gentle to the surface, they could be easily integrated without adverse effects on many possible systems whilst yielding the maximum coupling.

In the following we study the feasibility of integration of our nanoSQUIDs with such ultrathin systems of interest. Without loss of generality, we focus our study on the heterointerface between $LaAlO_3/SrTiO_3$ (LAO/STO) as it is a very good example of such systems, sharing several characteristics with other materials of interest. Located at the interface between two very insulating perovskites, this sytem is very thin, a few unit cells, and exhibits a 2DEG at room temperature and superconductivity below 200 mK, properties that have attracted a lot of scientific interest. In this section, we discuss how our process could be adapted to such types of insulating substrates and estimate the response we would obtain with the configurations we discussed in the previous sections.

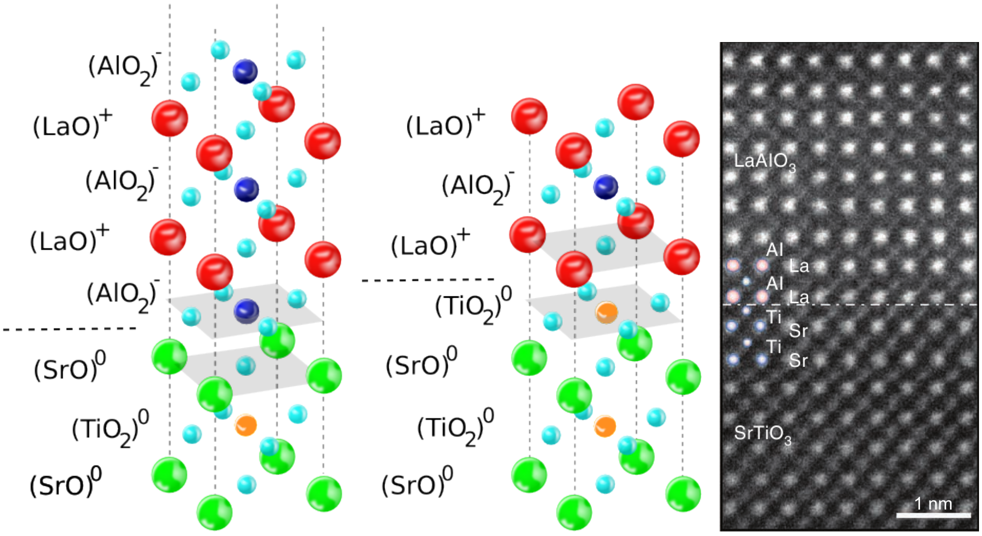

(a) STO-terminated (b) TiO-terminated (c) TEM

Figure 6.17: Schematic diagram showing the structures of the LAO/STO heterointerface for the two STO terminations: (a) SrO-terminated and (b) TiO_2-terminated. Only the latter exhibits a metallic interface displaying superconductivity at 200 mK. (c) TEM image of the heterointerface. Adapted from Park *et al.* [166].

6.2.1 Background: $LaAlO_3$/$SrTiO_3$ Heterointerface and its Properties

In 2004, a pionnering article from Ohtomo and Hwang [164] described the presence of a high-mobility 2D electron gas at the heterointerface of two perovskites: lanthanum aluminate $LaAlO_3$ and strontium titanate $SrTiO_3$ crystals. This heterointerface was grown using a Pulsed Laser Deposition (PLD) process carried out in an ultrahigh vacuum in the presence of a partial pressure of oxygen. The heated substrate on which the growth starts is $SrTiO_3$ as it is possible to choose its surface termination using a chemical treatment [165] after which the surface consists of atomically flat terraces. This is perfect for epitaxial growth as $LaAlO_3$ and $SrTiO_3$ have comparable lattice constants of 3.789 Å and 3.905 Å respectively.

Ohtomo and Hwang measured interesting properties depending on the termination of the $SrTiO_3$. The $(AlO_2)^-/(SrO)^0$ interface happened to be insulating whereas it was expected to be p-type. The $(LaO)^+/(TiO_2)^0$ interface was n-type and exhibited an unexpectedly high carrier mobility. However, there is still a debate in the physics community over the reasons causing this effect. Without going into details, three main hypothesis have been suggested: (i) electronic recombination from layer to layer to avoid the polar catastrophe scenario, which is the divergence with thickness of electric potential at heterointerfaces between materials made of highly polarised planes, described in detail by Nakagawa *et al.* [167, 168]; (ii) oxygen vacancies as different partial pressure of oxygen during the growth leads to different $R(T)$ profiles [169, 170]; (iii) interface intermixing [171]. Other relevant properties include the discovery in 2007 by Reyren *et al.* [172] that this heterointerface becomes superconducting below 200 mK, which they believed was proof of oxygen vacancies at the heterointerface. Unexpectedly, this superconductivity seems to coexist with ferromagnetism [162]. In 2007, Brinkman *et al.* reported a large magnetoresistance effect that they believed was due to the presence of magnetic moments [173]. Our nanoSQUIDs could be potentially used to measure this moments but such experiments would only be possible if (i) we can pattern the interface to suit our requirements; (ii) we are able to pattern a SQUID on top of this substrate. We discuss this in the following sections.

Patterning the Heterointerface To obtain $LaAlO_3$-$SrTiO_3$ samples, we collaborated with Dr Peter Petrov and his group: Clementine Walker, Dr Sean McMitchell and Dr Kevin Zou, from the Thin Film Technology Laboratory at Imperial College London, UK. This research group agreed to provide us samples grown by PLD under different partial oxygen pressure on $SrTiO_3$. These substrates were provided by Pi-kem ltd[2], and were of two types: either unterminated or already TiO_2-terminated and annealed using a proprietary technique. All samples presented the terraced surface clearly visible in the AFM image in Figure 6.18. Using wire-bonding with aluminium wires to create ohmic contacts [174, 175] to the heterointerface of these samples, we used evenly spaced contacts separated by $\sim 350\,\mu\text{m}$ and four-probe measurement to estimate the resistivity as described by Smits [176] as a function of temperature down to 60 mK. The resulting $R(T)$

---

[2] Pi-kem ltd, Staffordshire, UK

characteristics for a typical conducting sample are shown in Figure 6.19. The curve is very similar to what Ohtomo and Hwang reported for a partial pressure of oxygen $p_{O2} = 0.01\,\text{mTorr}$. The change of resistivity is nearly four orders of magnitude with a sharp decrease towards the low temperature as the phonon contribution is reduced. The best samples were fitted in the ADR for measurements down to 60 mK, the resistivity for one of them is shown in an inset of Figure 6.19(b). These results suggest that the sample exhibits the onset of superconductivity with a transition temperature of 210 mK as expected but without a fully zero-resistance state. The residual resistivity could be due to the resistance of the zone around the contacts, discontinuities between plateaus in the substrate and some microscopic non-uniformities in the film.

The heterointerface can be patterned using a method described by Schneider *et al.* [177]. This technique relies on the fact that the quasi-2DEG is created only if the thickness of $LaAlO_3$ is four unit cells or more. Two unit cells of crystalline $LaAlO_3$ are first deposited on the whole substrate. After this initial step, the regions that will be conducting are protected by resist and a layer of amorphous $LaAlO_3$ is deposited at room temperature as shown in Figure 6.20(b). After lift-off,

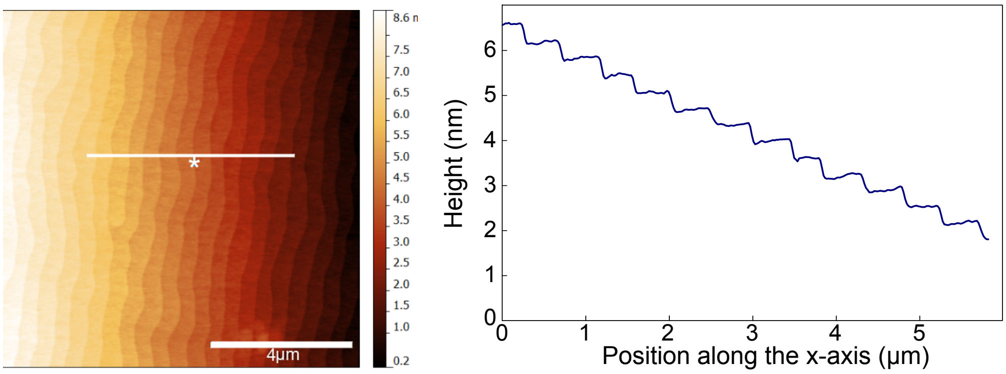

(a) (b)

Figure 6.18: (a) AFM micrograph of a SrO-terminated $SrTiO_3$ substrate. The white line indicates the direction of the scan whose profile is shown in image (b), showing the different flat terraces across the substrate. Courtesy of Clementine Walker.

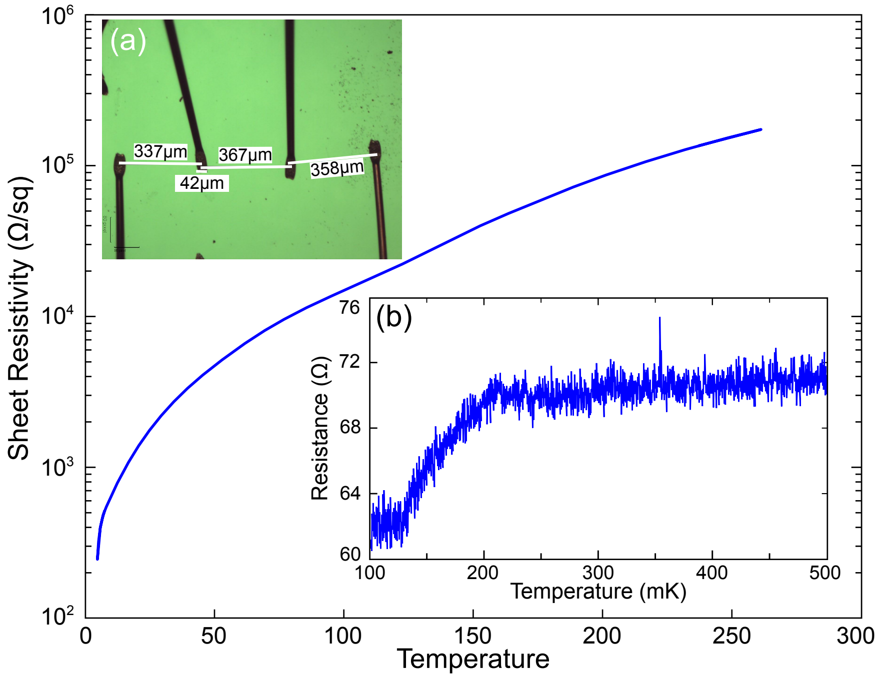

Figure 6.19: Main figure: Sheet resistivity as a function of temperature for a TiO_2-terminated $SrTiO_3$ sample with 6 unit cells of $LaAlO_3$ deposited at 0.02 mTorr. Insets: (a) Micrograph showing the evenly spaced aluminium contacts we made the substrate. (b) This set-up was used to measure the sheet resistivity of the heterointerface as a function of temperature using a helium dip-probe.

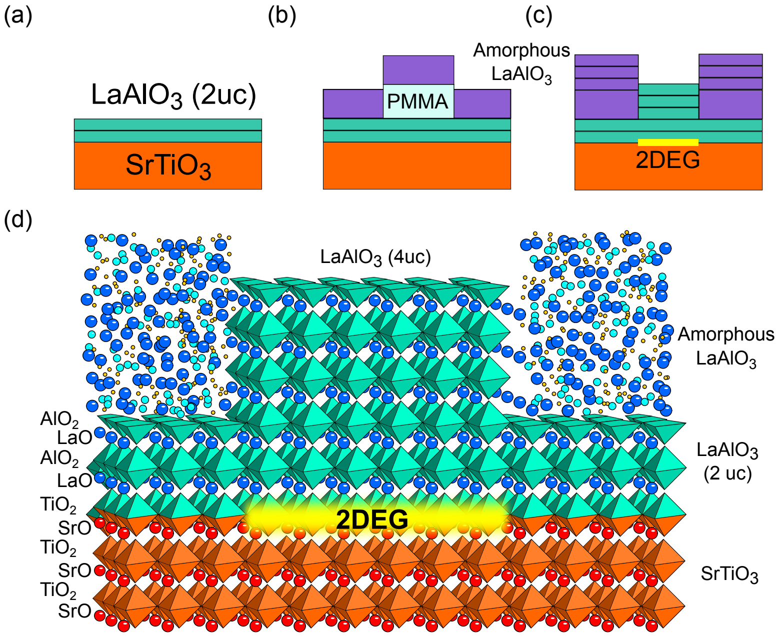

Figure 6.20: Schematic diagram presenting the technique used to create a localised island of the heterointerface between $SrTiO_3$ and $LaAlO_3$. (a) 2 unit cells of LAO are grown under epitaxial conditions on top of the TiO_2-terminated. (b) The area where the 2DEG should be located is covered by resist and amorphous $LaAlO_3$ is grown at room temperature. (c) After lift-off, several unit cells are grown under epitaxial conditions and grow as such on epitaxial parts, amorphously on amorphous parts, creating a located 2DEG. (d) Expanded view of the structure. Image adapted from Schneider *et al.* [177].

the sample is reprocessed under epitaxial growth conditions. Further $LaAlO_3$ grows epitaxially on top of the 2 u.c. of crystalline material and amorphously on top of the amorphous region. Depositing two additional unit cells or more activates the 2DEG at the heterointerface below the crystalline region. This patterning technique was successfully applied by Imperial College as shown by an AFM study in Figure 6.21 that clearly shows the distinction between the two regions. It should be noted Banerjee *et al.* [178] reported that patterning a 2DEG in this fashion does not alter its quality.

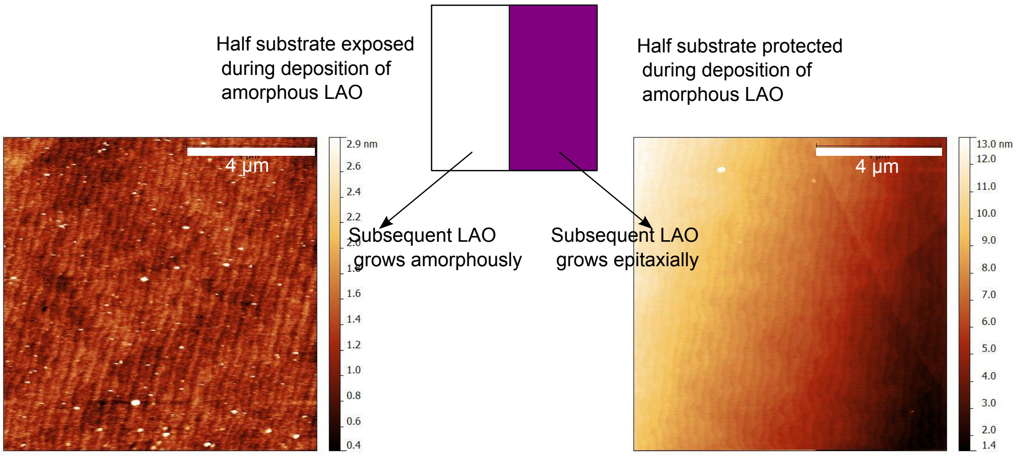

Figure 6.21: AFM images of crystalline and amorphous LAO after patterning. AFM images courtesy of Clementine Walker.

6.2.2 Fabrication of NanoSQUIDs by EBL on Highly Insulating Substrates

Strontium titanate and lanthanum aluminate are both highly insulating substrates with very high dielectric constants, respectively 100 – 20000 [179] and 27 [180]. These properties are interesting for future CMOS research including all-oxide electronics and spintronics. But from our fabrication point of view their use raises some technical issues. During the EBL process the surface of the substrate tends to charge resulting in distortion of patterns and drifting as shown in Figure 6.22, rendering the patterning of features smaller than 300 nm practically impossible. A conductive layer has to be added to limit the extent of this adverse effect and we tried several techniques to alleviate the issue: noble metal/PMMA bilayers, Resist/Gold 1 nm/Resist trilayers and PMMA/conductive polymer bilayers.

Noble metal/PMMA A common technique is to evaporate a very thin layer of noble metal, typically about 2 nm of gold, on top of the freshly spun and baked PMMA to dissipate subsequent charging. This layer is thin enough to let the beam through and expose the underlying PMMA. However, we found that it led to a broadening of the bridges of more than 150 % due to the large Bohr radius of gold which results to a strong scattering of incoming electrons. All other highly

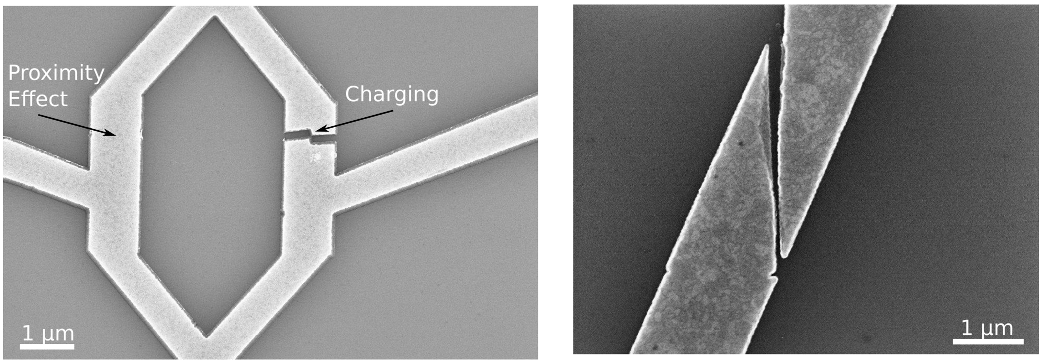

Figure 6.22: SEM micrograph showing the different issues when patterning an insulating sample by EBL. (a) shows a dummy device similar to SQUID G-1. On the left bridge the usual dose resulted in merged banks because of the proximity effect whilst the right bridge shows severe distortion due to local charging. (b) shows a track that is not continuous due to drifting during exposure.

conducting materials with a smaller Bohr radius such as copper, aluminium and silver are unfortunately prone to oxidation and are not suitable considering how thin the layer should be.

Resist/Gold/Resist It is not possible to evaporate gold directly on the sample as it would damage the features already in place. The only option is to sandwich the metal between two layers of resist such as LOR/Au/PMMA or PMMA 495 k/Au (1 nm)/PMMA 950 k. In both cases, the bottom layer protects the substrate. The LOR is an already-exposed resist unaffected by the electron beam and developed using TmaH-based developer whereas PMMA 495 k is a PMMA with shorter molecules and exposed more easily than PMMA 950 k. The 1 nm gold layer sits on top of this protecting layer and acts as a charge dissipater. It is itself covered by PMMA 950 k that will be patterned by the incoming beam at its full precision. After development of the top layer, the gold layer is etched in potassium iodine solution. The bottom layer is then developed as well, in both cases resulting in an undercut. However, whilst desirable in many situations, we noticed it was incompatible with the angled deposition needed for our nanoSQUIDs as it creates a parasitic shadow deposition between the banks after angling the sample as shown in Figure 6.23(b).

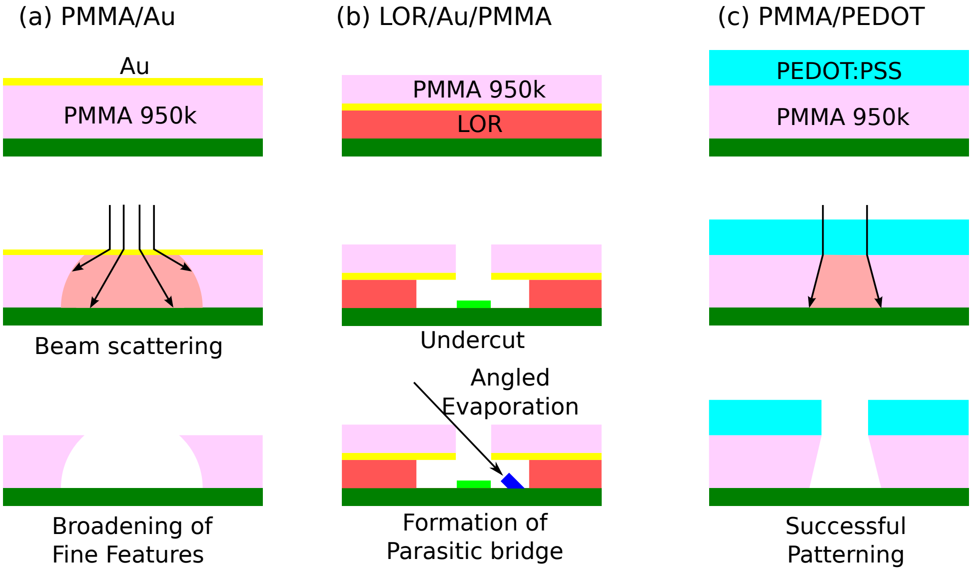

Figure 6.23: Schematic diagram showing the three possible ways to EBL pattern a highly insulating substrate. (a) PMMA/Au that leads to broadened fine features due to excessive beam scattering; (b) LOR/Au/PMMA which gives an undercut profile incompatible with the angled deposition by creating a phantom bridge; (c) PMMA/PEDOT:PSS that alleviates the charging without major side-effects.

PEDOT:PSS/PMMA The best results were achieved using the conductive polymer PEDOT:PSS[3] manufactured by Sigma-Aldrich Corporation, spun at 3000 RPM for 45 seconds and then baked at 180 °C for two minutes. The polymer is water-soluble and therefore does not affect in any way the underlying PMMA layer. The resulting layer was 40 nm thick and had a resistivity of 2 mΩ.m. The sample had to be loaded under filtered light as the polymer is highly UV-sensitive. Its conductivity proved to be sufficient to enable the EBL patterning of devices on a $SrTiO_3$ substrate, as demonstrated by Figure 6.24 which shows a successful patterning and lift-off of dummy SQUIDs with this technique. These different processes are summarised in Figure 6.23.

6.2.3 Foreseeable Measurements on the $SrTiO_3/LaAlO_3$ Heterointerface

In the following, we investigate the theoretical feasibility of two sorts of measurements. The first one is the estimation of the carrier density at the STO/LAO

---

[3] poly(3,4-ethylenedioxythiophene) poly(styrenesulfonate)

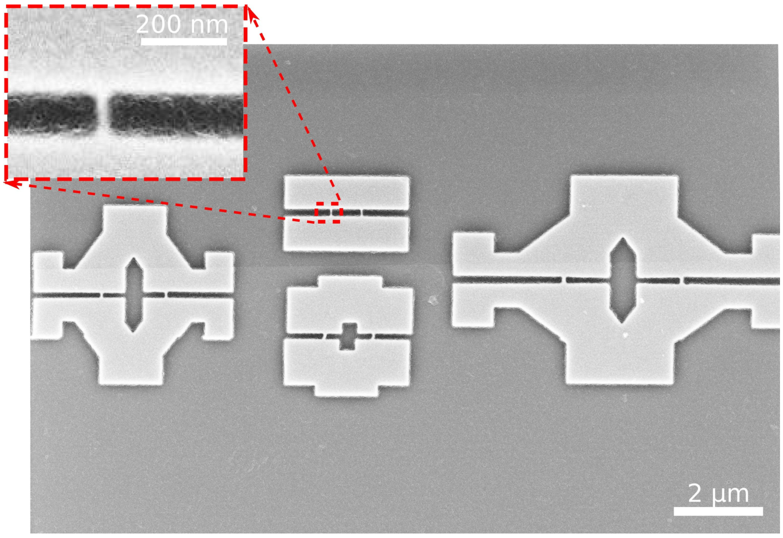

Figure 6.24: SEM micrograph of a dose test of dummy SQUID structures on a $SrTiO_3/LaAlO_3$ substrate. The conductive polymer, used to prevent charging during imaging, covers the entire sample and is also visible at higher magnification (inset).

heterointerface that could be achieved by monitoring ΔA_{eff}, and the direct measurements of magnetic dipole moments.

Estimation of carrier density

We have demonstrated that we can realistically pattern both the STO/LAO interface and a SQUID on top of this. In the following we discuss the response we can expect and assess if that would be measurable with our nanoSQUIDs. When dealing with very thin superconducting films, an important parameter is the Pearl length Λ, which is the spacing between vortex-type fluxoids occurring in thin films of a type II superconductor carrying a current [181]. This parameter is a function of the penetration depth $\Lambda = 2\lambda^2/t$ where t is the thickness of the superconducting layer. From the penetration depth of the heterointerface, we can estimate the sheet carrier density [163] using $n_s = 2m^*/\mu_0 e^2\Lambda$ where Λ is the Pearl length and m^* is the effective mass of electrons in the material, calculated to be $1.45\,m_e$ [182] in our case. There is a twofold uncertainty over the theoretical estimate for λ as the exact values of n_s and t are unknown. According to the polar catastrophe model [168], the carrier density should be $n_s = 3.3 \times 10^{14}\,\text{cm}^{-2}$, yielding $0.5\,e^-$ per unit cell, as it is the case for $SrTiO_3/GdTiO_3$ [183]. However, Hall measurements in the literature suggest it is one order of magnitude lower, estimates range from $n_s = 2.05 \times 10^{13}\,\mathrm{cm}^{-2}$ [163, 166, 174] to values closer to that predicted by the polar catastrophe, $1.0 \times 10^{14}\,\mathrm{cm}^{-2}$ [169]. Magnetic susceptibility measurements by scanning SQUID magnetometry [162] give much lower estimates, between 3×10^{11} and $1 \times 10^{12}\,\mathrm{cm}^{-2}$. The thickness and exact location of the 2DEG are also very debated in the literature. There is differing evidence that it forms in the $SrTiO_3$ and extends over a few unit cells [184], from 2 u.c (i.e. 0.78 nm), to 8 u.c ($\sim$ 3.1 nm) [185]. Using these intervals for d and n_s, we can estimate that Λ lies in the interval [25 μm,420 μm] implying λ is in the interval [100 nm,770 nm]. This uncertainty in the theoretical λ is a very important consideration. The 3D-MLSI model gives the correspondence reported in Figure 6.25 between the penetration depth for a superconducting plane and the estimated change in effective area of a nanoSQUID similar to those reported in Section 6.1.2 for the upper and lower bounds of the heterointerface thickness. The change of effective area would be 0.29 % in the least favourable case, which should be detectable by the SQUID using a careful setup, and 25 % in the best case ($\lambda = 100\,\mathrm{nm}$) which should be more easily measured.

Direct Measurements of Magnetic Moments

In this section we study the feasibility of experiments based on the direct measurement of flux by the nanoSQUIDs and not A_{eff}. In their susceptometry study using scanning SQUID technique, Bert *et al.* have reported the presence of ferromagnetic regions of areas $\sim 50\,\mu\mathrm{m}^2$ with magnetic moments up to the order of $10^8\mu_B$. The scan they obtained is shown in Figure 6.26. However, their spin sensitivity was quite poor $\sim 10^5 - 10^6\mu_B$ and the dipoles they observed are most likely to be due to defects in the film. An array of nanoSQUIDs with their much superior coupling would have a better resolution and yield more precise estimates for the carrier density. In the previous chapter, we estimated the flux noise density of our SQUIDs to be $0.2\,\mu\Phi_0/\sqrt{\mathrm{Hz}}$ at 100 mK, equivalent to 11 spins/$\sqrt{\mathrm{Hz}}$ in the centre of the loop using Granata *et al.*'s model for square filamentary SQUIDs [9].

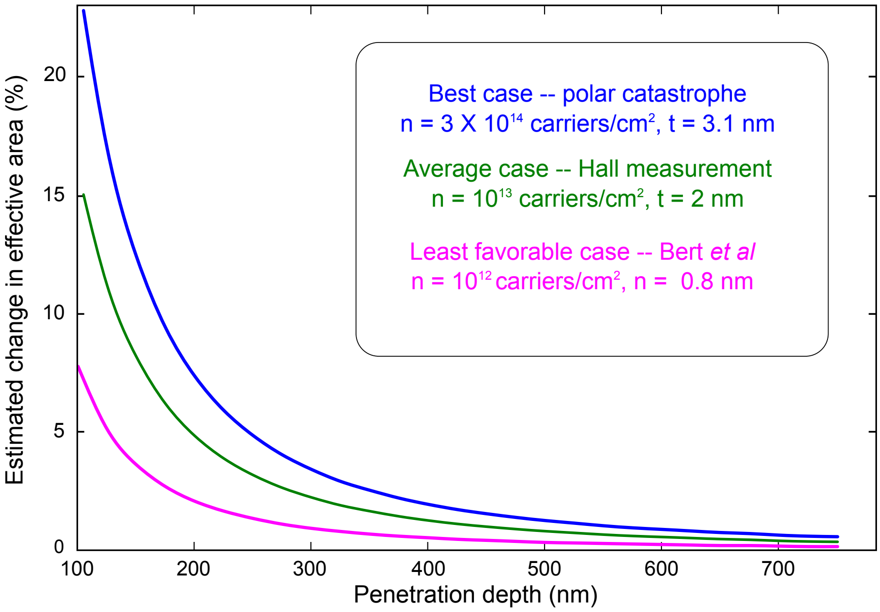

Figure 6.25: Estimated change in effective area using 3D-MLSI as a function of the penetration depth of a plane below the whole device in the similar arrangement as described in Section 6.1.2. The blue curve corresponds to the upper estimate for the heterointerface thickness (3 nm) while the magenta curve is the lower estimate 0.8 nm.

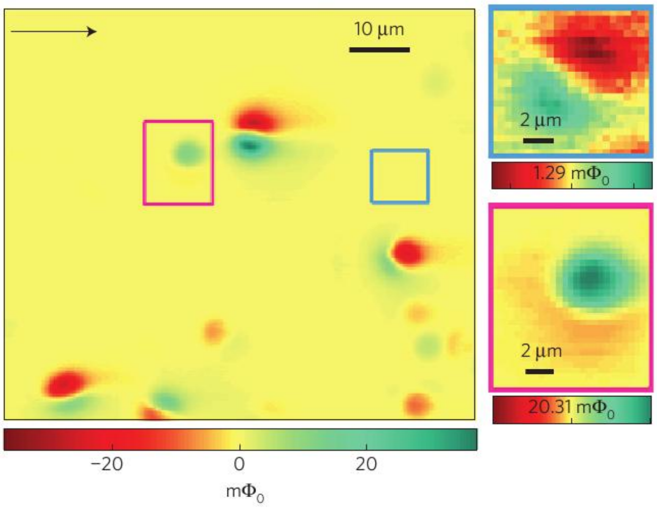

Figure 6.26: A scanning SQUID measurement of the susceptibility of a small island of heterointerface. Adapted from Bert *et al.* [162].

From the expressions described in Section 5.5.2, we can estimate the magnetic signal that would be coupled to the SQUID loop for any spin distribution.

Brinkman *et al.* [173] reported a large magnetoresistance, $R(30\,\mathrm{T})/R(0\,\mathrm{T}) = 1.3$, independent of the orientation of the field which they suggest is an effect related to spin physics. This, along with a logarithmic dependency of $R(T)$ at low temperatures – which can be interpreted as the Kondo effect – and a magnetoresistance hysteresis at 300 mK, suggests the presence of magnetic moments. XRD measurements indicate that there are less than 0.1 % oxygen vacancies in the sample which is three orders of magnitude too small to be the cause of this effect. The authors conclude that it is instead caused by electronic moments in the 3*d* shell of the Ti atoms. Further torque magnetometry measurements by Li *et al.* [186] seem to corroborate this finding and estimate the magnetic moment to $\sim 0.3\,\mu_B$ per unit cell. Pavlenko *et al.* [187] reported that the formation of the 2DEG results from the electronic reconstruction at the interface but that the magnetism is caused by electrons that are confined around oxygen vacancies.

To predict the total flux coupled by all the magnetic moments that we assume to be evenly spread, we use a Python script with SciPy to individually sum the contributions of every moment using the data above. The results for various SQUID edge lengths are tabulated in Table 6.8. If the magnetic moments are

SQUID edge length a (μm)	Total Flux coupled ($\mu\Phi_0$)
0.2	1136
0.3	1710
0.5	2836
1.0	5651
2.8	15775

Table 6.8: Table of the total flux coupled to a square filamentary nanoSQUID of edge length a calculated with the model by Granata *et al.* [9] using Python and SciPy to sum the individual spins assuming they are evenly spread inside the loop with density $\sim 0.3\,\mu_B$ per unit cell and perpendicular to the plane of the substrate.

evenly spread over the entire inner hole of a SQUID of area $2.8 \times 2.8\,\mu\mathrm{m}^2$ (A_{eff} of SQUID Y-1), and assuming they are perpendicular to the plane of the substrate, they would couple $15.7\,\mathrm{m}\Phi_0$ into the SQUID. If these spins can be flipped, this should be easily detectable given the flux noise density of our devices is typically below $1\,\mu\Phi_0/\sqrt{\mathrm{Hz}}$. Our measurements could include the study of the magnetisation reversal of these dipoles as described by Thirion *et al.* [3, 188] where a constant magnetic field is applied parallel to the substrate and SQUID and an rf pulse at the Larmor frequency is used to trigger the reversal. The critical field in a parallel field of a superconducting film is $H_{\mathrm{c}\|} = 2\sqrt{6}H_{\mathrm{c}}\lambda/t$ [189] where λ is the penetration depth of the film, t its thickness and H_{c} its bulk critical field. Taking values of a typical Ti nanoSQUID: $H_{\mathrm{c}} = 12\,\mathrm{mT}$, $t \sim 150\,\mathrm{nm}$ and $\lambda = 740\,\mathrm{nm}$, we estimate that $H_{\mathrm{c}\|} \sim 274\,\mathrm{mT}$. This is a slightly small magnetisation field but as we can operate the SQUID at temperatures as low as 60 mK, and probably even lower down to 10 mK using a dilution refrigerator, this should be sufficient to perform this sort of measurements.

6.2.4 Conclusion

To conclude, we have demonstrated that our nanoSQUIDs can fairly easily measure the relatively large magnetic signature of fabricated test samples. From this, we studied the feasibility of integrating our devices on systems of interest with a weaker response. As we showed, the patterning and deposition can be achieved even on difficult substrates, i.e. that are highly insulating. Measurements on substrates such as LAO/STO would obviously require very careful settings but theoretically our nanoSQUIDs could be successfully used to determine properties of ultrathin magnetic systems such as the carrier density or the presence and distribution of magnetic dipole moments. This could lead to a better understanding of the properties of many materials in future.

Chapter 7

Conclusion and Future Work

7.1 Conclusion

In the present project, we have demonstrated the successful operation of nanobridge-based nanoSQUIDs and magnetic measurements down to 60 mK. The advantage of our devices over rival technologies, involving e.g. carbon nanotubes [7] or DNA-templated nanowires [5] are their near-ideal electrical characteristics even at millikelvin temperatures, down to 60 mK and possibly lower, whilst operating the device with current biasing. This makes measurements a lot easier than alternative techniques relying on complex electronics as reported by e.g. Wernsdorfer *et al.* [66] or Levenson-Falk *et al.* [90].

As we saw, most devices optimised for operation at helium temperatures show hysteretic I-V characteristics when operated far below their T_c, i.e. in the millikelvin range, as the critical current of the bridges becomes larger than the retrapping current, the minimum current that allows the formation of a normal self-sustaining hotspot. Our solution to this issue was to use proximity bilayers involving a noble metal and a compatible superconductor with a lower T_c. Not only does the noble metal act as a thermal shunt that aids heat extraction as it has been reported before [10], but here it is also used in a novel way to further reduce T_c via the proximity effect. In order to guide the choice of the superconductor/normal metal we could use, and to optimise the thickness ratio, we developed a new thermal model by solving the heat flow equations for the case of a linear propagation of heat in the SQUID structure. We demonstrated that this form of heat propagation is closer to reality as the heat transfer coefficient to the substrate α is three to four orders of magnitude lower than that at 4.2 K. We showed that this explains the divergence between experiments and the models published in the literature. Our analysis showed that titanium/gold bilayers were the most suitable for millikelvin nanoSQUIDs as the gold layer does not need to be excessively thick: 23 nm of Au is needed for 100 nm of Ti, to remove the hysteresis in the I-V at any temperature.

To reveal the full potential of our devices, we then successfully tackled the issues of the excess heat and the large kinetic inductance that arise at millikelvin temperatures by adapting an angled evaporation method to our bilayer nanoSQUIDs. We therefore fabricated "3D nanoSQUIDs" whose banks were much thicker than the nanobridges – up to 250 % – which were characterised by highly sinusoidal $V(\Phi)$ curves and a kinetic inductance reduced by one order of magnitude. We further improved the devices by replacing the angled titanium by aluminium which, thanks to its shorter penetration depth and larger gap, led to a larger peak-to-peak modulation. Our best 3D nanoSQUID with an Al overlayer had an estimated white noise as low as $55\,\mathrm{n}\Phi_0/\sqrt{\mathrm{Hz}}$ at 200 mK which translates into a spin sensitivity of $11\,\mathrm{spins}/\sqrt{\mathrm{Hz}}$ at the centre of the SQUID loop, and $0.6\,\mathrm{spin}/\sqrt{\mathrm{Hz}}$ assuming a magnetic dipole moment in very close proximity (10 nm) to a nanobridge inside the SQUID hole. These figures compare well with those of the best devices fabricated by other groups as we described in Chapter 2.

We then used our nanoSQUIDs to characterise several fabricated test systems to further refine our understanding of their responses in terms of ΔA_{eff} and V_Φ. From these parameters, we then studied the feasibility of an integration and measurement on systems with a much weaker magnetic signature. The example of LAO/STO illustrates that we can couple our SQUIDs to a wide variety of substrates, including highly insulating materials. In the case of LAO/STO, we predicted even the least favourable magnetic signature could be detected by our nanoSQUID given its extreme sensitivity.

7.2 Suggestions for Future Work

In Chapter 6, we have already discussed in detail the feasibility of the integration onto LAO/STO substrates. Such an integration could be the object of future work to determine precisely the thickness and carrier concentration for this heterointerface and those of related perovskites such as $GaTiO_3/SrTiO_3$, doped $LaAlO_3/SrTiO_3$, or many other magnetic systems such as a small dot or nanoparticles of magnetic material. These need to show some remanence in their magnetic characteristics while having a coercive field low enough to be able to magnetise them without destroying the superconductivity of the SQUID. In this section, we will therefore focus our discussion towards the possible steps that would enable us to improve the performance of the nanoSQUIDs.

7.2.1 Reducing the Loop Size

As we saw in Chapter 5, the loop size is a crucial factor as a smaller loop results in a better flux sensitivity due to the reduction of inductance, and in a better spin sensitivity as the coupling is increased. As shown in Figure 7.1, it is possible using our technique to fabricate 3D nanoSQUIDs with extremely reduced dimensions. However, to have the effective area closer to this best achievable hole, the banks would have to be shaped to be quite narrow. The M-2 model could be used to determine how small the effective area can be before I_{sat} becomes an issue. Small changes in design such as creating slits in the cooling fins to prevent flux focussing into the SQUID loop, or a rounder geometry for the SQUID body, would easily decrease the effective area of our nanoSQUIDs without any negative impact in terms of L or I_{sat}.

7.2.2 S-N-S nanoSQUIDs

In Chapter 2, we saw that the minimum feature size depends on the thickness of PMMA used which needs to be proportional to the amount of metal to be

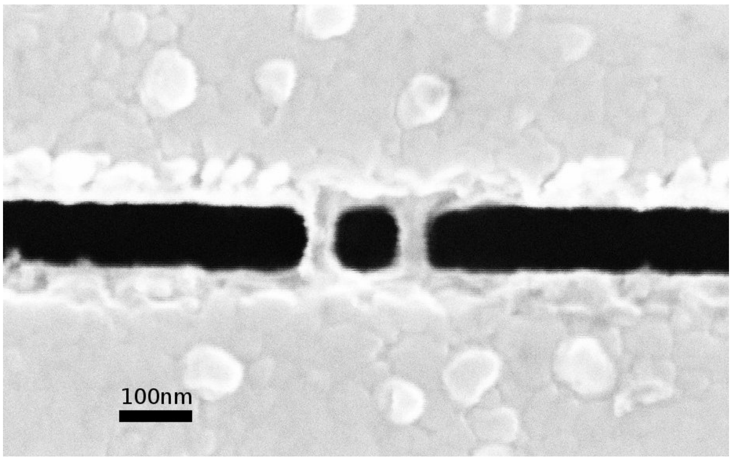

Figure 7.1: SEM micrograph of SQUID X-7 (not measured) showing the smallest loop hole we managed to pattern using our final EBL settings.

deposited. An idea to reduce the width of the bridge and to benefit from the very high conductivity of noble metals would be to fabricate an SNS SQUID. Gold nanowires of width 15 nm can be easily patterned with 30 kV and 30 nm of resist. After the gold deposition, the sample would be reprocessed and the SQUID body would be patterned on top of the nanowires. This principle is shown in Figure 7.2 for a Ti/Au SNS SQUID we fabricated (not measured). A variant of this technique would be to use the angled deposition to perpendicularly deposit the normal metal only and then the superconductor at an angle. In that case, it might be difficult to keep the separation between banks $\sim \xi_N$ as a thicker resist would have to be used.

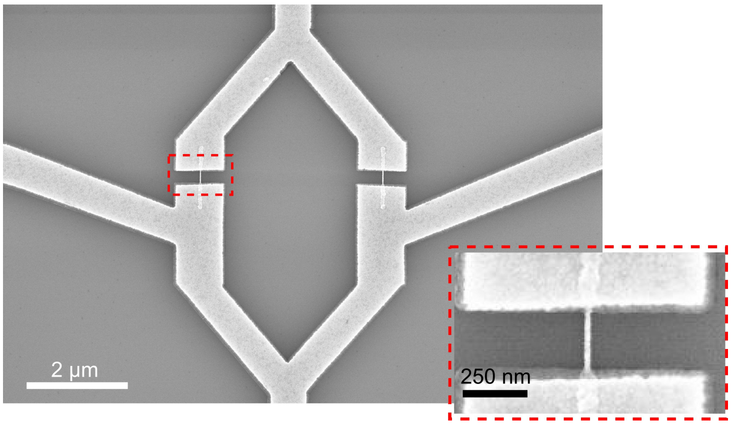

Figure 7.2: SEM micrograph of an S-N-S SQUID made of 30 nm Au for the bridges and 100 nm of Ti for the SQUID body. The dashed region is magnified in the inset.

7.2.3 Aluminium nanoSQUIDs

An inherent issue with the current Ti/Au bilayer is the mismatch between the resistivities of these two materials which leads to a large difference between $R_{\mathrm{n},0}$ and R_{n} as defined in Chapter 5. Due to a high $R_{\mathrm{n},0}$, I_{c} is small. In the meantime, R_{n} is small as well as gold is an excellent electrical conductor. This yields a small $I_{\mathrm{c}}R_{\mathrm{n}}$ product which is detrimental to the SQUID performance. To reduce this effect the resistivities of the normal metal and superconductor should match. Aluminium and silver are ideal in that regard as they both are highly conductive. The only issue would be to manage to remove the hysteresis in the millikelvin range. A prelimary study we performed on a Ag (50 nm)/Al (80 nm)/angled Al (60 nm) did not show any hysteresis down to 370 mK, the base temperature of the particular system we used to perform this I-V measurement, despite a critical current $\sim 100\,\mu$A.

7.2.4 Ne-FIB nanoSQUIDs

As we saw in Chapter 4, a typical nanobridge patterned by EBL and made from a niobium film is necessarily hysteretic at millikelvin temperatures. However, if we could pattern a bridge with much smaller dimensions, it might be possible to create a Nb-based or Pb-based nanoSQUID that would not non-hysteretic. This could be achieved for instance using LCN's new Neon/Helium Focussed Ion Beam (FIB) which theoretically allows patterning with a linewidth down to 5 nm. This is made possible by the use of light He and Ne ions which offers this resolution whilst avoiding the issue of ion poisoning which affects standard Ga-FIB patterning. This device could have a loop area similar to the device reported by Vasyukov *et al.* [89] which is a SQUID-on-a-tip, shown in Figure 7.3, with an excellent spin sensitivity of $0.55\,\mathrm{spin}/\sqrt{\mathrm{Hz}}$ 10 nm below the centre of the loop. However, as we would not be limited by the constraints due to their fabrication technique, we could have the loop much thicker as shown in Figure 7.4 with a kinetic inductance at least one order of magnitude lower. If the Ne-He FIB devices proved indeed non-hysteretic in the millikelvin range, we would be closer to the quantum noise and extrapolating from the flux noise reported by Vasyukov *et al.*, we would get a spin sensitivity better than $\sim 0.05\,\mathrm{spin}/\sqrt{\mathrm{Hz}}$ which would be an extremely useful tool.

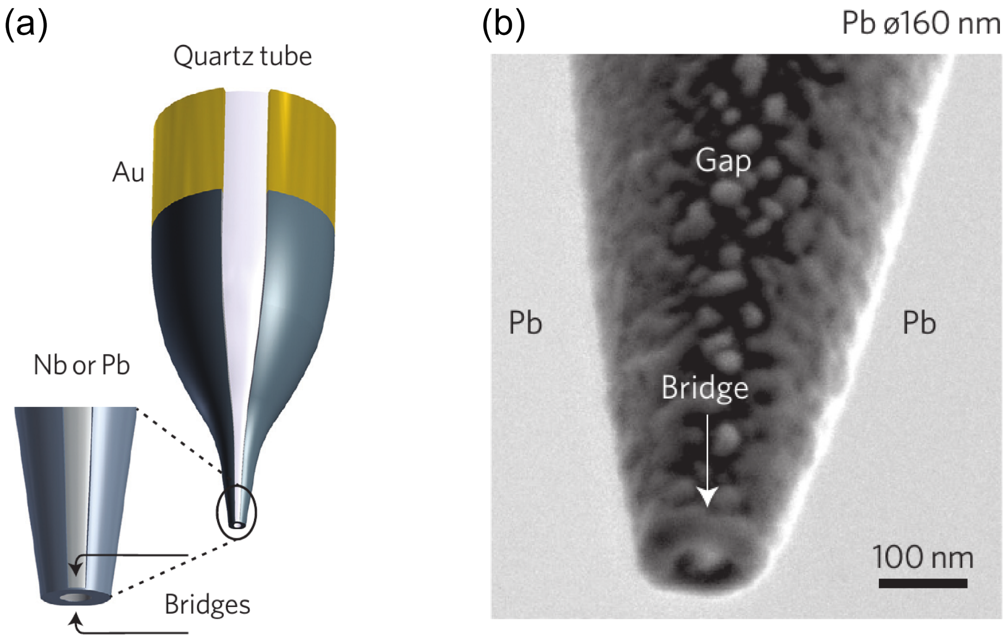

Figure 7.3: (a) Schematic diagram of a SQUID-on-a-tip showing the pulled quartz tube with the superconducting leads connected to Au electrodes. (b) SEM micrograph of a Pb-based SQUID-on-a-tip of radius 80 nm that sits on the apex of these quartz tube. Adapted from Vasyukov *et al.* [89].

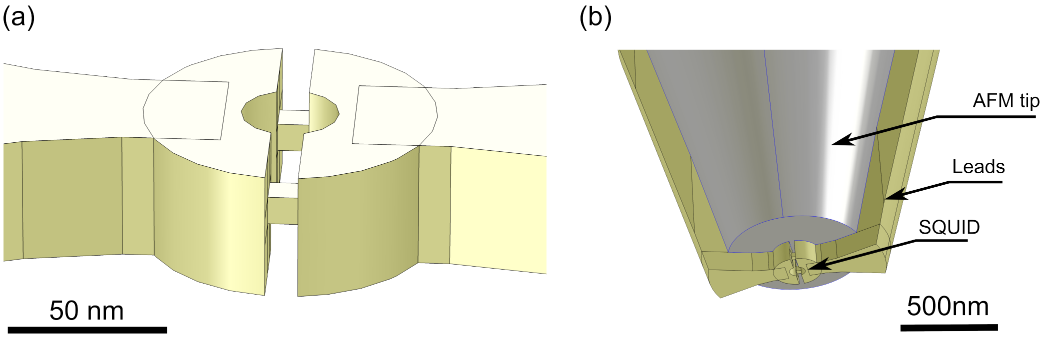

Figure 7.4: Artist's impression of an ultrasmall nanoSQUID that could be theoretically patterned using Ne/He FIB. Thanks to the FIB versatility, such a SQUID could even be patterned at the apex of an AFM tip to use for scanning SQUID magnetometry.

Appendices

Appendix A

Publication in Journal of Applied Physics

JOURNAL OF APPLIED PHYSICS **114**, 233907 (2013)

Proximity effect bilayer nano superconducting quantum interference devices for millikelvin magnetometry

A. Blois,[1,a)] S. Rozhko,[1] L. Hao,[2] J. C. Gallop,[2] and E. J. Romans[1]
[1]*London Centre for Nanotechnology, University College London (UCL), 17-19 Gordon Street, London WC1H 0AH, United Kingdom*
[2]*National Physical Laboratory, Hampton Road, Teddington, Middlesex TW11 0LW, United Kingdom*

(Received 20 August 2013; accepted 25 November 2013; published online 18 December 2013)

Superconducting quantum interference devices (SQUIDs) incorporating thin film nanobridges as weak links have sensitivities approaching that required for single spin detection at 4.2 K. However, due to thermal hysteresis they are difficult to operate at much lower temperatures which hinder their application to many quantum measurements. To overcome this, we have developed nanoscale SQUIDs made from titanium-gold proximity bilayers. We show that their electrical properties are consistent with a theoretical model developed for heat flow in bilayers and demonstrate that they enable magnetic measurements to be made on a sample at system temperatures down to 60 mK. © *2013 AIP Publishing LLC*. [http://dx.doi.org/10.1063/1.4843856]

Recently there has been a trend to develop nanoscale Superconducting QUantum Interference Devices (SQUIDs) with the aim to reach magnetic flux sensitivities sufficient to detect the flip of a single spin in close proximity. Potential applications range from investigating small spin populations in magnetic nanoparticles[1] and molecules[2] to readouts for flux qubits and nanomechanical resonators.[3] Various exotic techniques have been reported to create the Josephson elements in these SQUIDs including using carbon-nanotubes,[4] DNA-templated nanowires,[5] and films deposited on fine tips.[6] However most of the work has involved using either focused-ion-beam (FIB)[5,7,8] or electron-beam patterning[1,2,9–11] of superconducting thin films such as Nb and Al to form nanoscale constrictions which act as weak links when their dimensions are comparable to the Ginzburg-Landau coherence length $\xi_{GL}(T)$.

The remaining goal for these nanobridge-based devices is to extend their operating range down to millikelvin temperatures, both to take advantage of the lower thermal noise floor, but also to provide a uniquely sensitive tool for studying phase transitions and quantum phenomena at the nanoscale in coupled magnetic or superconducting systems at ultra-low temperatures. The main obstacle to this is that nanobridges usually have a large critical current I_c and a hysteretic I–V curve except very close to their transition temperature T_c ($\sim$9 K for Nb and 1.2 K for Al). Hysteresis occurs if the retrapping current I_r, i.e., the minimum current needed to sustain the normal state hotspot arising when I_c is exceeded, is smaller than I_c itself.[12] Hysteresis prevents the use of conventional SQUID readout methods involving current-biasing and makes fast, repeat measurements difficult.[13] More fundamentally excessive heat dissipation in the SQUID loop is clearly undesirable for studying samples of interest in close proximity since they may be directly affected by the heating or indirectly via other mechanisms that can lead to quantum decoherence. For Nb devices, several groups[1,7,8] have demonstrated that the use of a thin Au shunt layer can reduce the hysteresis close to T_c due to its higher thermal conductivity, but hysteresis still occurs below a significant fraction of T_c.

One way to extend the measurement range is to use a scanning SQUID system where the SQUID can be at a higher temperature than the sample.[14,15] However this involves a trade-off in sensitivity compared to an integrated device, so that is extremely beneficial to have a nanoSQUID that can operate at the sample temperature. To achieve this we have developed nanobridge-based devices fabricated from superconductor-normal metal proximity bilayers. Here in addition to providing a thermal shunt, the normal layer depresses T_c of the nanobridge region via the proximity effect so it can be tuned to match the desired operating temperature whilst avoiding hysteresis. For our desired measurement range (approximately 60–600 mK) we chose Ti as the superconductor (T_c (film) $\sim$ 760 mK) and Au as the normal metal. Ti/Au and related bilayers (e.g., Mo/Au, Mo/Cu, and Al/Ag) have also been developed by several groups[16] for transition edge bolometers operating at similarly low temperatures. Our choice of superconductor was governed by the relative ease of depositing high quality Ti films and the long term stability of Ti-based devices compared to, e.g., Al-based devices. In addition the higher resistivity and lower T_c of Ti compared to Al reduces the critical current of the nanobridges at the lowest temperatures reducing the Joule heating.

All our devices incorporate two Ti/Au nanobridges as shown in Fig. 1. The nanobridges are fabricated by lift-off using a Raith e-beam system with Ti/Au bilayers deposited *in situ* by e-beam evaporation on an oxidized Si wafer. Each nanobridge is 40 nm wide and 120 nm long, which is short enough compared to ξ_{GL} to give a predicted single-valued current-phase relation at all temperatures.[17] We chose the optimum Ti/Au thickness ratio for the nanobridges by extending to the bilayer case a thermal model recently developed by Hazra *et al.* (HPCG) for single layers.[18] The HPCG

[a)] Author to whom correspondence should be addressed. Electronic mail: a.blois@ucl.ac.uk

0021-8979/2013/114(23)/233907/5/$30.00

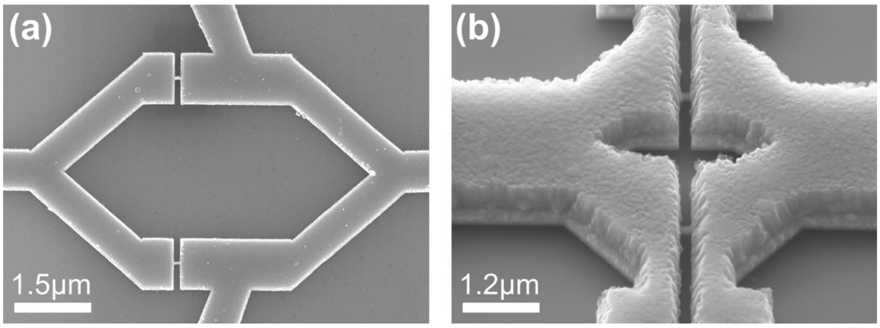

FIG. 1. Scanning Electron Microscope (SEM) images of Ti/Au bilayer nanoSQUIDs: (a) first generation; (b) second generation with thicker Ti layer, revised shape and additional cooling fins (partly visible at top and bottom of image).

model is itself based on an earlier thermal model[12] by Skocpol *et al.* (SBT), but with an additional approximation to allow for the rapid decrease in the thermal conductivity of the superconducting state below T_c due to the formation of Cooper pairs.

In SBT's analysis the retrapping current in bridges that are short compared to the thermal length scale $\eta = \sqrt{\kappa d/\alpha}$ is approximately $I_r = \sqrt{(\kappa d^2 T_c/\rho_N)(1-T/T_c)}$, where κ is the thermal conductivity, α is the heat transfer coefficient to the substrate, d is the film thickness and ρ_N is the normal state resistivity. In HPCG's analysis this current has to be found numerically from the minimum of the function $i_r^2(x_0) = \lambda x_0(1-t_b^3)K_1(\lambda x_0)/3[(\ln(x_0/x_1)+\beta)K_0(\lambda x_0)]$, where $i_r = I_r/I_c$, $t_b = T/T_c$, $x_1 = w/2\eta$, $x_0 = r_0/\eta$, $\lambda = (1+t_b+t_b^2)^{1/2}$, w is the width of the bridge, r_0 is the radial extent of the normal region in the banks, $\beta \approx (\pi/2)(1+l/w)$, and $K_{0,1}$ are modified Bessel functions of the second kind. As a check of which model was best applicable to our films and to check our estimates for κ and α, we first characterized a bare Ti device which was deliberately hysteretic over a wide temperature range. The $I_c(T)$ and $I_r(T)$ curves for this were measured inside an Adiabatic Demagnetization Refrigerator (ADR) and are shown in Fig. 2(a).

The $I_c(T)$ behavior follows the temperature dependence of the Kulik and Omelyanchuk (KO-1) model[17] which applies to short metallic weak links in the dirty limit. The value of R_N which can be extracted from the fit includes the unknown, but likely dominant contribution from the banks, and so we simply treat this as a fitting parameter. The I_r (T) behavior fits the HPCG model much better than the SBT model. From the best fit to the HPCG model we obtain $\alpha = 0.0043$ W/cm^2 K which is consistent with the magnitude we expect at these temperatures given the thermal boundary resistance R_b $(\equiv 1/\alpha)$ is generally found to scale rapidly as T^{-n} with $n \sim 3$ at typical metal-substrate interfaces.[19] We also find $\kappa(T_c) = 0.0163$ W/cm K, which is consistent with our estimate from the resistivity using the Wiedemann-Franz law. To predict I_c for the bilayer we assume that as a first approximation we can retain the KO-1 model and simply scale the gap function Δ by the transition temperature of the bilayer following the usual BCS expression in the weak-coupling limit, $\Delta(0) = 1.76\,k_B T_c$. We obtained the appropriate transition temperature from separate measurements (not shown) on bilayers with different superconductor-normal metal thickness ratios (d_S/d_N) which we fitted to the theory of Martinis *et al.* based on the Usadel equations for a bilayer.[20] The fit gave an interface transmission factor $t = 0.211$, comparable to that found by Martinis *et al.* for their best *in situ* interfaces, and a reasonable value for a high quality interface between dissimilar metals. To predict I_r for the bilayer we use HPCG's model but take the thermal conductivity as that of the parallel combination of the two layers. For the gold layer we use the Wiedemann-Franz law to estimate the thermal conductivity allowing for the increase in the resistivity we observe in ultrathin gold films (<20 nm). Fig. 2(b) shows the predicted I_c and I_r as a function of d_N for $d_S = 100$ nm at our lowest achievable temperature of 60 mK. As can be seen for $d_N < 23$ nm the

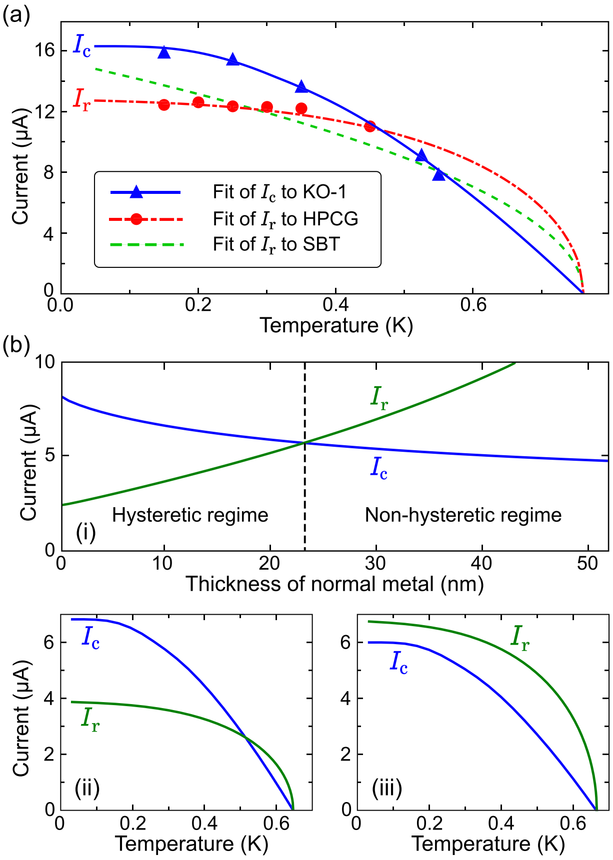

FIG. 2. (a) Fits to the measured critical current and retrapping current for a pure Ti device. (b)(i) The predicted I_r and I_c for a Ti/Au nanobridge at a fixed temperature of 60 mK as a function of the normal metal thickness d_N on a superconducting layer of thickness $d_S = 100$ nm. The device will be non-hysteretic down to 60 mK if $d_N > 23$ nm. Examples of the predicted temperature dependencies of I_c and I_r on either side of this threshold are shown in (ii) for $d_N = 10$ nm and in (iii) for $d_N = 25$ nm. The device with $d_N = 10$ nm shows hysteresis in the region where $I_r < I_c$. The device with $d_N = 25$ nm shows no hysteresis at any temperature.

device should be hysteretic at 60 mK whereas for $d_{\mathrm{N}} > 23\,\mathrm{nm}$ the device should be non-hysteretic over the full temperature range. As in-plane heat conduction is the dominant effect, the predicted value of I_{r} is only weakly sensitive to α: an order of magnitude change in α produces less than 1 μA change in I_{r}. In a similar way, we can assume that the minimum thickness of normal metal will be insensitive to the thermal boundary resistance at the Ti/Au interface since this is unlikely to be significantly larger than at the Ti/substrate interface given the high interface quality.[20]

Our initial nanoSQUID design is shown in Fig. 1(a). We chose to use $d_{\mathrm{N}} = 25\,\mathrm{nm}$ to allow for a margin of error in the above analysis whilst keeping $I_{\mathrm{c}}R_{\mathrm{N}}$ as large as possible. The loop size was chosen to allow easy characterization in a modest magnetic field rather than for maximum flux sensitivity. As predicted this type of device was found to be non-hysteretic down to our lowest measured temperature of 60 mK. The typical *I*–*V* curve and voltage modulation in an applied field at 100 mK are shown in Fig. 3(a) (this temperature was used to obtain long time thermal stability in the ADR). The device shows voltage modulation for bias currents I_{b} only in the range $I_{\mathrm{c}} < I_{\mathrm{b}} < 1.2\, I_{\mathrm{c}}$. We believe this is because above 1.2 I_{c} the normal hotspot has spread to the ends of the arms of the SQUID loop. Fig. 3(b) shows finite element simulations of the temperature distributions in the SQUID loop at bias currents below and above this threshold illustrating the growth of the hotspot. The simulation corroborates our estimated values for α and κ in our earlier analysis. The maximum peak-to-peak modulation measured was $\Delta V = 6.1\,\mu\mathrm{V}$. We can compare this with the theoretical prediction given the SQUID inductance *L*, the measured nanobridge critical current I_{c}, and normal resistance R_{N}. The inductance is dominated by kinetic inductance contributions since the penetration depth $\lambda \sim \lambda(0) = (0.18\hbar/\mu_0 k_{\mathrm{B}})^{1/2} (\rho_{\mathrm{N}}/T_{\mathrm{c}})^{1/2} \approx 1.2\,\mu\mathrm{m}$ is comparable or greater to the film thickness and the track widths. We estimate the total SQUID inductance $L \sim 510$ pH corresponding to a screening parameter $\beta_L = 2LI_{\mathrm{c}}/\Phi_0 \sim 0.81$. In this regime we expect[21] $\Delta V = I_{\mathrm{c}}R_{\mathrm{N}}/\ (1+\beta_L) = 6.4\,\mu\mathrm{V}$ which is slightly larger than measured but reasonable given the non-sinusoidal response. In order to improve the usable bias range and the voltage modulation characteristics, we made a second generation of devices with a much thicker Ti layer for the banks. This increases the heat extraction from the weak link regions and also reduces the kinetic inductance contribution of the loop, both directly via the increase in thickness itself and indirectly via the decreased penetration depth λ due to the increased T_{c} of the bilayer. In addition, we also made some changes to the loop geometry and added cooling fins to the side of the loop as shown in Fig. 1(b) to further help improve the usable bias range. When thickening the banks, it would be counter-productive to thicken the nanobridges at the same time, as this would lead to an increased I_{c} and greater Joule heating in the normal state. To avoid this we developed a technique where, after the original deposition of the nanobridges and SQUID loop, we add a further *in situ* step involving tilting the substrate and depositing up to an extra 450 nm of Ti. This thickens the superconducting loop but not the nanobridge regions which are shadowed by the tilt. This is similar to a more complicated process recently demonstrated by Vijay *et al.*[22] to thicken the banks of their aluminium nanoSQUIDs. In order to use this process we had to reverse the order of the original Au and Ti layers and introduce an ultrathin (1 nm) Ti adhesion layer between the Au and the wafer. As we noted above, providing we have good interface quality the thermal model should be insensitive to this change. We obtain a high yield of devices with similar characteristics and a spread in I_{c} on a single chip of less than 10%. We estimate the overall SQUID inductance is reduced to 212 pH corresponding to $\beta_L = 0.46$, the decrease being predominantly due to the thickening of the banks compared to the change in geometry.

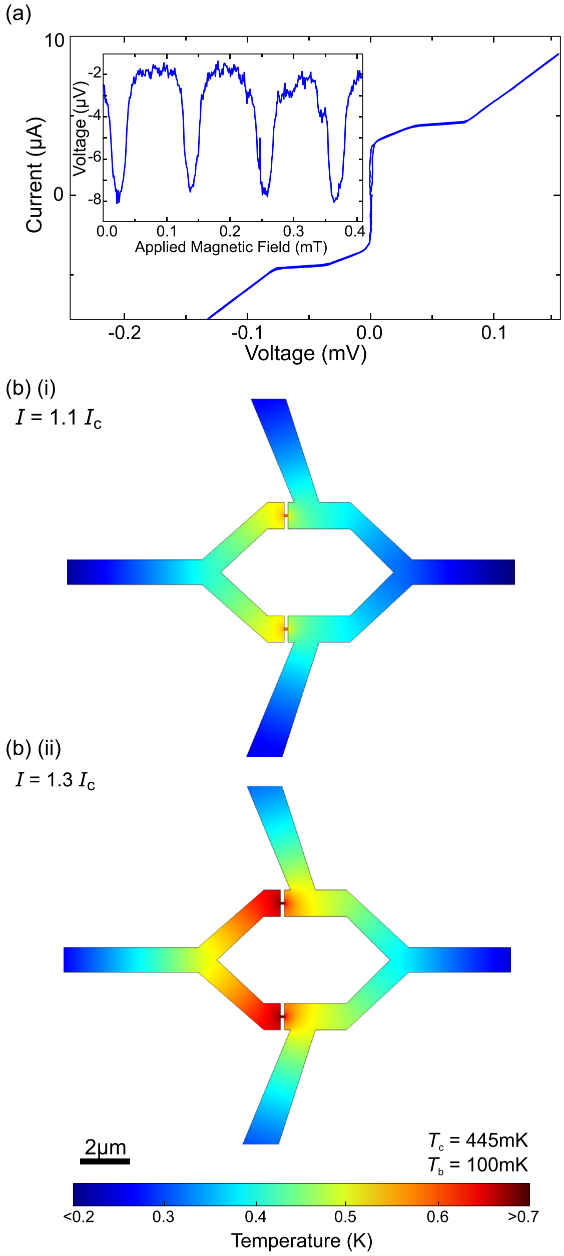

FIG. 3. (a) *I*–*V* curve and voltage modulation (inset) for the first generation device at 100 mK. The device only shows voltage modulation for bias currents in the small linear region just above the critical current I_{c} and below 1.2 I_{c}. (b) Finite element model of the temperature distribution at bias currents of (i) 1.1 I_{c} and (ii) 1.3 I_{c} showing the reason for the limited bias range at a base temperature of 100 mK. In (ii) the hotspots extend so far that the two arms of the SQUID loop are fully normal (>445 mK) thus preventing any SQUID modulation.

The I-V curve and voltage modulation of a second generation device are shown in Fig. 4(a). The device shows voltage modulation over a greater bias current range, $I_c < I_b < 4.6 I_c$. Finite element simulations showing this is consistent with the improved heat extraction are shown in Fig. 4(b). This allows us to achieve a more sinusoidal voltage modulation with a larger $\Delta V = 7.9\,\mu$V which is in good agreement with the estimated value of $\Delta V \approx I_c R_N/(1+\beta_L) = 8.25\,\mu$V. Given that $\Gamma = 2\pi k_B T/I_0\Phi_0 \ll 1$ and $\beta_L = 0.46$, we can estimate the ideal white noise floor (ignoring any hot electron effects[23]) as $S_\Phi^{1/2} \approx (16 k_B T R_N)^{1/2}/V_\Phi = 0.20\,\mu\Phi_0/\mathrm{Hz}^{1/2}$, using the measured transfer function $V_\Phi = 27.1\,\mu\mathrm{V}/\Phi_0$ at 100 mK. We were unable to confirm the actual flux noise was this low due to the lack of a perfectly matched cooled preamplifier, but using a preamplifier[24] with a slightly mismatched input sensitivity we found the SQUID noise was $<1.1\,\mu\Phi_0/\mathrm{Hz}^{1/2}$ without any excess noise down to 1 Hz. A key goal for these nanoSQUIDs is to be able to extract useful temperature dependent information from a coupled sample over a wide temperature range. A typical sample of interest might comprise a thin magnetic or superconducting layer, which have been extensively studied by scanning systems.[14,15] To simulate whether we can make local measurements on such layers we fabricated a test structure integrating a 2 μm × 2 μm superconducting island on top of one of our nanoSQUIDs, i.e., the inverted geometry of the scanning type measurements. The island was fabricated from an e-beam evaporated Al(150 nm)/Ag(80 nm) proximity bilayer which was electrically separated from the nanoSQUID by an 200 nm thick, sputter-deposited Si_3N_4 layer. We chose this particular bilayer to give a T_c (~470 mK) within our SQUID operating range, but also so that its penetration depth would be short enough that its change with temperature would be easily detectable. Fig. 5 shows the effective area $A_{\mathrm{eff}} = \Delta B(1\Phi_0)/\Phi_0$ of the nanoSQUID measured in a perpendicular magnetic field both before and after the island was added. As can be seen the SQUID itself has the advantage of almost constant A_{eff} over the temperature range since λ for Ti/Au is about 1.2 μm. This makes it straightforward to separate the effect of the island from the difference between the two curves. As a check that the measurements were consistent with theory we used the inductance modeling package 3D-MLSI to model the predicted effective area of the SQUID with the added island as a function of the island's penetration depth which we assumed simply followed the two-fluid model: $\lambda(T) = \lambda(0)(1-(T/T_c)^4)^{-1/2}$. We fitted this to the measured A_{eff} (T) curve and found a best fit for $\lambda(0) = 248 \pm 12$ nm. This seems reasonable given our naive estimate of $\lambda(0) = 256$ nm based on T_c and resistivity.

In summary we have demonstrated the use of a proximity bilayer solves the issue of sufficient heat extraction for nanobridge-based SQUIDs to remain non-hysteretic down to our lowest measurement temperature of 60 mK. This enabled us to make sensitive measurements over a very useful temperature range, and should lead to many more applications in the

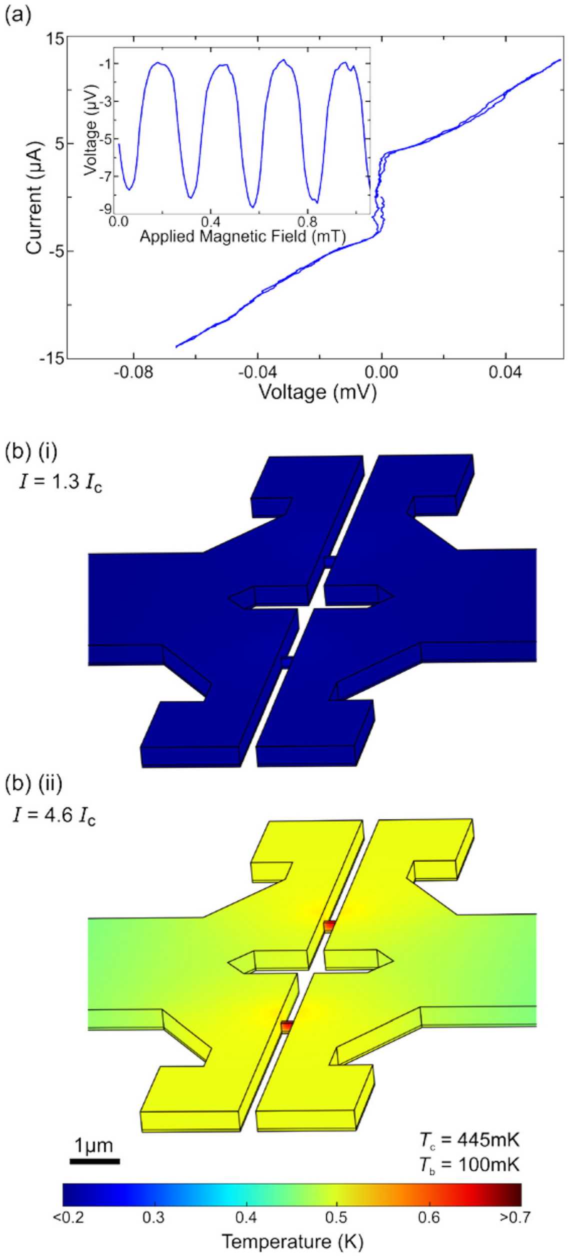

FIG. 4. (a) I–V curve and voltage modulation (inset) at 100 mK for a second generation device. The device shows modulation up to ~$4.6 I_c$ (beyond range shown in figure). (b) The modelled temperature distributions at bias currents of (i) 1.3 I_c and (ii) 4.6 I_c. In (i) the self-heating is negligible, whereas in (ii) the two arms of the SQUID loop have become normal.

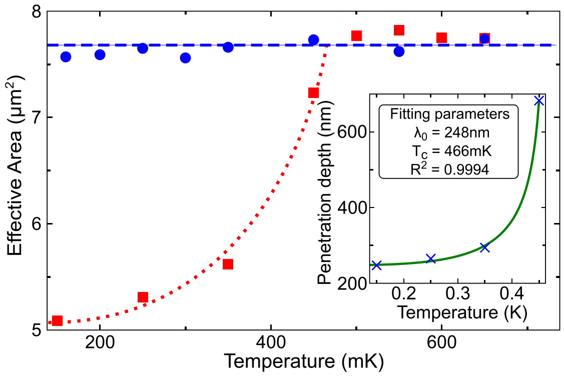

FIG. 5. The effective area A_{eff} (T) measured for a Ti/Au SQUID with (red squares) and without (blue circles) an additional Al/Ag superconducting island. The dashed blue line is a guide to the eye. The dotted red line is the best fit to a 3D-MLSI model for $\lambda(0) = 248$ nm for the island. The predicted form of $\lambda(T)$ for the island is shown in the inset.

future. Our theoretical flux noise of $\sim 0.2\,\mu\Phi_0/\mathrm{Hz}^{1/2}$ would correspond to an electron spin sensitivity of $\sim 11\,\mathrm{spins}/\mathrm{Hz}^{1/2}$ for spins located at the centre of a circular SQUID loop having the same effective area.[1] Optimisation of the magnetic coupling[7] and further reduction in our loop size should bring this sensitivity close to the single spin detection limit, which is comparable to that predicted for, e.g., carbon nanotube SQUIDs.[4]

[1] S. K. H. Lam and D. L. Tilbrook, Appl. Phys. Lett. **82**, 1078 (2003).

[2] C. Thirion, W. Wernsdorfer, and D. Mailly, Nature Mater. **2**, 524 (2003).

[3] L. Hao, D. Cox, J. Gallop, J. Chen, S. Rozhko, A. Blois, and E. Romans, IEEE Trans. Appl. Supercond. **23**, 1800304 (2013).

[4] J. Cleuziou, W. Wernsdorfer, V. Bouchiat, T. Ondarçuhu, and M. Monthioux, Nat. Nanotechnol. **1**, 53 (2006).

[5] D. S. Hopkins, D. Pekker, T.-C. Wei, P. M. Goldbart, and A. Bezryadin, Phys. Rev. B **76**, 220506 (2007).

[6] A. Finkler, Y. Segev, Y. Myasoedov, M. L. Rappaport, L. Ne'eman, D. Vasyukov, E. Zeldov, M. E. Huber, J. Martin, and A. Yacoby, Nano Lett. **10**, 1046 (2010).

[7] L. Hao, J. C. Macfarlane, J. C. Gallop, D. Cox, J. Beyer, D. Drung, and T. Schurig, Appl. Phys. Lett. **92**, 192507 (2008).

[8] A. G. P. Troeman, H. Derking, B. Borger, J. Pleikies, D. Veldhuis, and H. Hilgenkamp, Nano Lett. **7**, 2152 (2007).

[9] K. Hasselbach, C. Veauvy, and D. Mailly, Physica C **332**, 140 (2000).

[10] R. Russo, C. Granata, E. Esposito, D. Peddis, C. Cannas, and A. Vettoliere, Appl. Phys. Lett. **101**, 122601 (2012).

[11] E. M. Levenson-Falk, R. Vijay, N. Antler, and I. Siddiqi, Supercond. Sci. Technol. **26**, 055015 (2013).

[12] W. J. Skocpol, M. R. Beasley, and M. Tinkham, J. Appl. Phys. **45**, 4054 (1974).

[13] W. Wernsdorfer, Supercond. Sci. Technol. **22**, 064013 (2009).

[14] J. R. Kirtley, B. Kalisky, J. A. Bert, C. Bell, M. Kim, Y. Hikita, H. Y. Hwang, J. H. Ngai, Y. Segal, F. J. Walker, C. H. Ahn, and K. A. Moler, Phys. Rev. B **85**, 224518 (2012).

[15] J. A. Bert, B. Kalisky, C. Bell, M. Kim, Y. Hikita, H. Y. Hwang, and K. A. Moler, Nat. Phys. **7**, 767 (2011).

[16] For a review, see K. D. Irwin and G. C. Hilton in Topics Appl. Phys., Cryogenic Particle Detection **99**, 63–149 (2005).

[17] K. K. Likharev, Rev. Mod. Phys. **51**, 101 (1979).

[18] D. Hazra, L. M. A. Pascal, H. Courtois, and A. K. Gupta, Phys. Rev. B **82**, 184530 (2010).

[19] E. T. Swartz and R. O. Pohl, Rev. Mod. Phys. **61**, 605 (1989).

[20] J. M. Martinis, G. Hilton, K. Irwin, and D. Wollman, Nucl. Instrum. Methods Phys. Res. A **444**, 23 (2000).

[21] C. D. Tesche and J. Clarke, J. Low Temp. Phys. **29**, 301 (1977).

[22] R. Vijay, E. M. Levenson-Falk, D. H. Slichter, and I. Siddiqi, Appl. Phys. Lett. **96**, 223112 (2010).

[23] F. C. Wellstood, C. Urbina, and J. Clarke, Appl. Phys. Lett. **54**, 2599 (1989).

[24] SQUID Series Array manufactured by Magnicon GmbH, 22397 Hamburg, Germany.

Appendix B

3D-MLSI Model

```
cc SQUID X-3 Mutual inductance
rem 3D-MLSI for SQUID X-3, bridge 0.2umX0.04um. Overall thickness of 160
nc=2
pb=1
ah={0}
lmbd={1}
tol=1e-11

cond 0 0 0.2

rem --------------------------------------------------------
rem cond   form X1 Y1 X2 Y2
    ell 0  0 -0.5 0 0.5 0 t 1
    ell  0  0 0.5 0 0.5 0.5 b
    ell  0  0 0.5 0.5 1 1.25    b
    ell  0  0 1 1.25 1 1.75   b
    ell  0  0 1 1.75 0.5 1.75  b
    ell  0  0 0.5 1.75 0.5 1.9 b
    ell  0  0 0.5 1.9 1 1.9    b
    ell  0  0 1 1.9 1 2.4   b
    ell  0  0 1 2.4 0.5 3.15  b
    ell  0  0 0.5 3.15 0.5 3.65 b
    ell  0  0 0.5 3.65 -0.5 3.65 t 2
    ell  0  0 -0.5 3.65  -0.5 3.15 b
    ell  0  0 -0.5 3.15 -1 2.4  b
    ell  0  0 -1 2.4 -1 1.9   b
    ell  0  0 -1 1.9 -0.5 1.9    b
    ell  0  0 -0.5 1.9 -0.5 1.75 b
    ell  0  0 -0.5 1.75 -1 1.75  b
    ell  0  0 -1 1.75 -1 1.25   b
    ell  0  0 -1 1.25 -0.5 0.5    b
    ell  0  0 -0.5 0.5 -0.5 0 b

rem ------   The hole   ------------
```

```
rem cond form X1 Y1 X2 Y2
ell  0  0 0 1 -0.25 1.4   h 1
ell  0  0 -0.25 1.4 -0.25 1.75  h 1
ell  0  0 -0.25 1.75 -0.45 1.75 h 1
ell  0  0 -0.45 1.75 -0.45 1.9    h 1
ell  0  0 -0.45 1.9 -0.25 1.9   h 1
ell  0  0 -0.25 1.9 -0.25 2.25  h 1
ell  0  0 -0.25 2.25 0 2.6 h 1
ell  0  0 0 2.6 0.25 2.25 h 1
ell  0  0 0.25 2.25 0.25 1.9  h 1
ell  0  0 0.25 1.9 0.45 1.9   h 1
ell  0  0 0.45 1.9 0.45 1.75    h 1
ell  0  0 0.45 1.75 0.25 1.75 h 1
ell  0  0 0.25 1.75 0.25 1.4  h 1
ell  0  0 0.25 1.4 0 1   h 1

cond 1 0.25 {4} {2}

rem ---   The Control line   -----
rem cond form X1 Y1 X2 Y2
ell  1  0 {5} {7} {6} {7} t 3
ell  1  0 {6} {7} {6} {8}  b
ell  1  0 {6} {8} {5} {8} t 4
ell  1  0 {5} {8} {5} {7}    b

rem ------   Ground Plane  ------------
rem cond form X1 Y1 X2 Y2
ell  1  0 -1.5         0.1 1.05 0.1   b
ell  1  0 1.05 0.1 1.05 3.6  b
ell  1  0 1.05 3.6 -1.5 3.6 b
ell  1  0 -1.5         3.6 -1.5 0.1    b    b

tp 3->4
```

Bibliography

[1] M. B. Ketchen, T. Kopley and H. Ling. "Miniature SQUID susceptometer". *Applied Physics Letters*, **44**, 10, 1008–1010, 1984.

[2] S. K. H. Lam and D. L. Tilbrook. "Development of a niobium nanosuperconducting quantum interference device for the detection of small spin populations". *Applied Physics Letters*, **82**, 7, 1078–1080, 2003.

[3] C. Thirion, W. Wernsdorfer and D. Mailly. "Switching of magnetization by nonlinear resonance studied in single nanoparticles". *Nat Mater*, **2**, 8, 524–527, 2003.

[4] Jones P. J. et al. "Tunable electromagnetic environment for superconducting quantum bits". *Sci. Rep.*, **3**, 2013.

[5] D. S. Hopkins, D. Pekker, P. M. Goldbart and A. Bezryadin. "Quantum Interference Device Made by DNA Templating of Superconducting Nanowires". *Science*, **308**, 5729, 1762–1765, 2005.

[6] A. Finkler et al. "Nano-sized SQUID-on-tip for scanning probe microscopy". *Journal of Physics: Conference Series*, **400**, 5, 052004, 2012.

[7] J. Cleuziou et al. "Carbon nanotube superconducting quantum interference device". *Nature Nanotechnology*, **1**, 1, 53–59, 2006.

[8] S. K. H. Lam and S. Gnanarajan. "Hysteretic behaviour of nanoSQUIDs—prospective application as trapped-vortex memory". *Superconductor Science and Technology*, **22**, 6, 064005, 2009.

[9] C. Granata et al. "Performance of nano superconducting quantum interference devices for small spin cluster detection". *Journal of Applied Physics*, **106**, 2, 023925, 2009.

[10] L. Hao et al. "Measurement and noise performance of nano-superconducting-quantum-interference devices fabricated by focused ion beam". *Appl. Phys. Lett.*, **92**, 19, 192507, 2008.

[11] G. C. Tettamanzi, C. I. Pakes, S. K. H. Lam and S. Prawer. "Flux noise in ion-implanted nanoSQUIDs". *Superconductor Science and Technology*, **22**, 6, 064006, 2009.

[12] W. J. Skocpol, M. R. Beasley and M. Tinkham. "Self-heating hotspots in superconducting thin-film microbridges". *Journal of Applied Physics*, **45**, 9, 4054–4066, 1974.

[13] D. Hazra, L. M. A. Pascal, H. Courtois and A. K. Gupta. "Hysteresis in superconducting short weak links and μ-SQUIDs". *Phys. Rev. B*, **82**, 184530, 2010.

[14] R. Vijay, E. M. Levenson-Falk, D. H. Slichter and I. Siddiqi. "Approaching ideal weak link behavior with three dimensional aluminum nanobridges". *Applied Physics Letters*, **96**, 22, 223112, 2010.

[15] G. Ireson. *Discovering superconductivity an investigative approach.* Wiley, Chichester, West Sussex, 2012.

[16] K. Gavroglu. "James Dewar and the vanishing electrical resistance at absolute zero temperature". *Annalen der Physik*, **524**, 3-4, A61–A64, 2012.

[17] A. Matthiessen, K. C. Vogt and J. Tyndall. *On the influence of temperature on the electric conducting-power of Alloys.*, volume Philosophical transactions of the Royal Society of London, pages p. 167–200. London s. n., 1864.

[18] H. K. Onnes. "Further experiments with liquid helium. D. On the change of electric resistance of pure metals at very low temperatures, etc. V. The disappearance of the resistance of mercury,". *Comm. Phys. Lab. Univ. Leiden*, , 122b, 1911.

[19] P. Drude. "Zur Elektronentheorie der Metalle". *Annalen der Physik*, **306**, 3, 566–613, 1900.

[20] W. Meissner and R. Ochsenfeld. "Ein neuer Effekt bei Eintritt der Supraleitfähigkeit". *Naturwissenschaften*, **21**, 787–788, 1933.

[21] F. London and H. London. "The Electromagnetic Equations of the Supraconductor". *Proceedings of the Royal Society of London. Series A, Mathematical and Physical Sciences*, **149**, 866, pp. 71–88, 1935.

[22] J. G. Daunt, A. R. Miller, A. B. Pippard and D. Shoenberg. “Temperature Dependence of Penetration Depth of a Magnetic Field in Superconductors”. *Phys. Rev.*, **74**, 842–842, 1948.

[23] C. Gorter and H. Casimir. “On supraconductivity I”. *Physica*, **1**, 1–6, 306–320, 1934.

[24] E. A. Lython. *Superconductivity.* London, Methuen & Co., Ltd, methuen’s monographs on physical subjects edition, 1964.

[25] J. Bardeen, L. N. Cooper and J. R. Schrieffer. “Theory of Superconductivity”. *Phys. Rev.*, **108**, 1175–1204, 1957.

[26] H. Fröhlich. “Interaction of Electrons with Lattice Vibrations”. *Proc. Roy. Soc. (London), Ser. A*, 1952.

[27] A. C. Rose-Innes and E. H. Rhoderick. *Introduction to superconductivity.* Pergamon Press, Oxford; New York, 1978.

[28] F. W. Kus. “On the thermodynamics of weak-coupling superconductors”. *Journal of Physics F: Metal Physics*, **9**, 10, 2081, 1979.

[29] M. A. Biondi and M. P. Garfunkel. “Measurement of the Temperature Variation of the Energy Gap in Superconducting Aluminum”. *Phys. Rev. Lett.*, **2**, 143–145, 1959.

[30] I. Giaever. “Energy Gap in Superconductors Measured by Electron Tunneling”. *Phys. Rev. Lett.*, **5**, 147–148, 1960.

[31] I. Giaever and K. Megerle. “Study of Superconductors by Electron Tunneling”. *Phys. Rev.*, **122**, 1101–1111, 1961.

[32] C. Panagopoulos and T. Xiang. “Relationship between the Superconducting Energy Gap and the Critical Temperature in High- T_c Superconductors”. *Phys. Rev. Lett.*, **81**, 2336–2339, 1998.

[33] J. B. G Deutscher. “Short Coherence Length Superconductors and the Fermi Velocity Paradox”. *Chinese Journal of Physics*, **31**, 6S, 1993.

[34] J. G. Bednorz and K. A. Müller. “Possible high superconductivity in the Ba−La−Cu−O system”. *Zeitschrift für Physik B Condensed Matter*, **64**, 189–193, 1986.

[35] L. P. Gor'kov and T. K. Melik-Barkhudarov. "Microscopic derivation of the Ginzburg-Landau equations for an anisotropic superconductor". *J. Exptl. Theoret. Phys. (U.S.S.R)*, **45**, 1493–1498, 1963.

[36] W. H. . Keesom and A. P. Keesom. "On the Anomaly in the Specific Heat of Liquid Helium". *Communication from the Kamerlingh Onnes Laboratory at Leiden*, , 221d, 1932.

[37] G. Jaeger. "The Ehrenfest Classification of Phase Transitions: Introduction and Evolution". *Archive for History of Exact Sciences*, **53**, 1, 51–81, 1998.

[38] J. Šesták and P. Šimon. *Glassy, Amorphous and Nano-Crystalline Materials II: Reaction Dynamics and Thermal Analysis.* Hot topics in thermal analysis and calorimetry. Springer Netherlands, 2012.

[39] L. D. Landau. "On the theory of phase transition". *Phys. Z. Soviet*, **11**, 26, 545, 1937.

[40] V. L. Ginzburg and L. D. Landau. *Zh. Eksp. Teor. Fiz.*, **20**, 1064, 1950.

[41] A. A. Abrikosov. "On the magnetic properties of superconductors of the second group". *Soviet Physics JETP*, **5**, 6, 1174–1183, 1957.

[42] P. H. Smith, S. Shapiro, J. L. Miles and J. Nicol. "Superconducting Characteristics of Superimposed Metal Films". *Phys. Rev. Lett.*, **6**, 12, 686–688, 1961.

[43] H. Meissner. "Superconductivity of Contacts with Interposed Barriers". *Phys. Rev.*, **117**, 672–680, 1960.

[44] P. G. de Gennes. "Boundary Effects in Superconductors". *Rev. Mod. Phys.*, **36**, 225–237, 1964.

[45] N. R. Werthamer. "Theory of the Superconducting Transition Temperature and Energy Gap Function of Superposed Metal Films". *Phys. Rev.*, **132**, 2440–2445, 1963.

[46] L. Fabrega et al. "Mo-Based Proximity Bilayers for TES: Microstructure and Properties". *Applied Superconductivity, IEEE Transactions on*, **19**, 3, 460–464, 2009.

[47] B. D. Josephson. “Possible new effects in superconductive tunnelling”. *Physics Letters*, **1**, 7, 251–253, 1962.

[48] P. W. Anderson and J. M. Rowell. “Probable Observation of the Josephson Superconducting Tunneling Effect”. *Phys. Rev. Lett.*, **10**, 230–232, 1963.

[49] B. D. Josephson. “The discovery of tunnelling supercurrents”. *Rev. Mod. Phys.*, **46**, 2, 251–254, 1974.

[50] P. W. Anderson and A. H. Dayem. “Radio-Frequency Effects in Superconducting Thin Film Bridges”. *Phys. Rev. Lett.*, **13**, 6, 195–197, 1964.

[51] S. Shapiro. “Josephson Currents in Superconducting Tunneling: The Effect of Microwaves and Other Observations”. *Phys. Rev. Lett.*, **11**, 80–82, 1963.

[52] C. Enss and S. Hunklinger. *Low-Temperature Physics*. SpringerLink: Springer e-Books. Springer, 2005.

[53] D. E. McCumber. “Effect of ac Impedance on dc Voltage-Current Characteristics of Superconductor Weak-Link Junctions”. *J. Appl. Phys.*, **39**, 7, 3113–3118, 1968.

[54] W. C. Stewart. “Current-Voltage characteristics of Josephson junctions”. *Appl. Phys. Lett.*, **12**, 8, 277–280, 1968.

[55] A. B. Zorin et al. “Background charge noise in metallic single-electron tunneling devices”. *Phys. Rev. B*, **53**, 13682–13687, 1996.

[56] K. K. Likharev. “Superconducting weak links”. *Rev. Mod. Phys.*, **51**, 101–159, 1979.

[57] L. G. Aslamazov and A. I. Larkin. “Josephson Effect in Superconducting Point Contacts”. *JETP Lett.*, **9**, 87–92, 1969.

[58] V. Ambegaokar and A. Baratoff. “Tunneling Between Superconductors”. *Phys. Rev. Lett.*, **11**, 104–104, 1963.

[59] I. Kulik and A. Omelyanchuk. “”. *Sov. Phys. JETP*, **41**, 1071, 1975.

[60] I. Kulik and A. Omelyanchuk. “”. *Sov. J. Low Temp. Phys.*, **3**, 459, 1977.

[61] K. K. Likharev and L. A. Yakobson. *Zh. Tekh. Fiz.*, **46**, 1503, 1975.

[62] R. Jaklevic, J. Lambe, A. Silver and J. Mercereau. “Quantum Interference Effects in Josephson Tunneling”. *Physical Review Letters*, **12**, 7, 159–160, 1964.

[63] D. Drung et al. “Highly Sensitive and Easy-to-Use SQUID Sensors”. *IEEE Transactions on Applied Superconductivity*, **17**, 2, 699–704, 2007.

[64] De Bruyn Ouboter, R. and De Waele, A. Th. A. M. “Superconducting point contacts weakly connecting two superconductors”. *Rev. Phys. Appl. (Paris)*, **5**, 1, 25–31, 1970.

[65] C. D. Tesche and J. Clarke. “dc SQUID: Noise and optimization”. *Journal of Low Temperature Physics*, **29**, 301–331, 1977.

[66] W. Wernsdorfer. “From micro- to nano-SQUIDs: applications to nanomagnetism”. *Superconductor Science and Technology*, **22**, 6, 064013, 2009.

[67] W. Myers et al. “Calculated signal-to-noise ratio of MRI detected with SQUIDs and Faraday detectors in fields from 10uT to 1.5T”. *Journal of Magnetic Resonance*, **186**, 2, 182–192, 2007.

[68] B. Seeber. *Handbook of Applied Superconductivity.* vol. 2. Taylor & Francis, 1998.

[69] J. Clarke, W. M. Goubau and M. B. Ketchen. “Tunnel junction dc SQUID: Fabrication, operation, and performance”. *Journal of Low Temperature Physics*, **25**, 99–144, 1976.

[70] H. Weinstock. *Applications of Superconductivity*, volume 365 of *Applied Sciences.* Kluwer Academic Publishers, 2000.

[71] J. Clarke and A. I. Braginski. *The SQUID handbook.* Wiley-VCH, Weinheim, 2003.

[72] F. Ruede et al. “Readout System for NanoSQUID Sensors Using a SQUID Amplifier”. *Applied Superconductivity, IEEE Transactions on*, **21**, 3, 408–411, 2011.

[73] J. Martinis and J. Clarke. “Measurements of current noise in DC SQUIDS”. *Magnetics, IEEE Transactions on*, **19**, 3, 446–448, 1983.

[74] D. L. Tilbrook. “NanoSQUID sensitivity for isolated dipoles and small spin populations”. *Superconductor Science and Technology*, **22**, 6, 064003, 2009.

[75] J. Gallop et al. “Miniature dc SQUID devices for the detection of single atomic spin-flips”. *Physica C: Superconductivity*, **368**, 1–4, 109–113, 2002.

[76] R. P. Giffard, R. A. Webb and J. C. Wheatley. “Principles and methods of low-frequency electric and magnetic measurements using an rf-biased point-contact superconducting device”. *Journal of Low Temperature Physics*, **6**, 533–610, 1972.

[77] J. Pierce, J. Opfer and L. Rorden. “A broadband thin-film SQUID magnetometer pumped at 10 GHz”. *Magnetics, IEEE Transactions on*, **10**, 3, 599–602, 1974.

[78] M. B. Ketchen and R. F. Voss. “An ultra-low-noise tunnel junction dc SQUID”. *Applied Physics Letters*, **35**, 10, 812–815, 1979.

[79] M. W. Cromar and P. Carelli. “Low-noise tunnel junction dc SQUID’s”. *Applied Physics Letters*, **38**, 9, 723–725, 1981.

[80] R. Voss et al. “Ultra low noise Nb DC SQUIDs”. *Magnetics, IEEE Transactions on*, **17**, 1, 395–399, 1981.

[81] L. Hao et al. “Spatial Resolution Assessment of Nano-SQUIDs Made by Focused Ion Beam”. *Applied Superconductivity, IEEE Transactions on*, **17**, 2, 742–745, 2007.

[82] L. Hao et al. “Magnetic nanoparticle detection using nano-SQUID sensors”. *Journal of Physics D: Applied Physics*, **43**, 47, 474004, 2010.

[83] C. Granata et al. “NANO-SQUIDs based on niobium Dayem bridges for nanoscale applications”. *Journal of Physics: Conference Series*, **234**, 4, 042010, 2010.

[84] S. K. H. Lam, J. R. Clem and W. Yang. “A nanoscale SQUID operating at high magnetic fields”. *Nanotechnology*, **22**, 45, 455501, 2011.

[85] W. Wernsdorfer, D. Mailly and A. Benoit. “Single nanoparticle measurement techniques”. *Journal of Applied Physics*, **87**, 9, 5094–5096, 2000.

[86] M. Jamet et al. “Magnetic Anisotropy of a Single Cobalt Nanocluster”. *Phys. Rev. Lett.*, **86**, 4676–4679, 2001.

[87] R. Russo et al. “Nanoparticle magnetization measurements by a high sensitive nano-superconducting quantum interference device”. *Applied Physics Letters*, **101**, 12, 122601, 2012.

[88] A. Finkler et al. “Self-Aligned Nanoscale SQUID on a Tip”. *Nano Letters*, **10**, 3, 1046–1049, 2010.

[89] D. Vasyukov et al. “A scanning superconducting quantum interference device with single electron spin sensitivity”. *Nat Nano*, **8**, 9, 639–644, 2013.

[90] E. M. Levenson-Falk, R. Vijay, N. Antler and I. Siddiqi. “A dispersive nanoSQUID magnetometer for ultra-low noise, high bandwidth flux detection”. *Superconductor Science and Technology*, **26**, 5, 055015, 2013.

[91] M. Hatridge et al. “Dispersive magnetometry with a quantum limited SQUID parametric amplifier”. *Phys. Rev. B*, **83**, 134501, 2011.

[92] M. A. C. Beltran. “Development of a Josephson Parametric Amplifier for the Preparation and Detection of Nonclassical States of Microwave Fields”. Ph.D. thesis, University of Colorado, 2010 (thesis).

[93] S. Anders et al. “Sub-micrometer-sized, cross-type Nb–AlOx–Nb tunnel junctions with low parasitic capacitance”. *Superconductor Science and Technology*, **22**, 6, 064012, 2009.

[94] M. Schmelz et al. “Highly sensitive miniature SQUID magnetometer fabricated with cross-type Josephson tunnel junctions”. *Physica C: Superconductivity*, **476**, 0, 77–80, 2012.

[95] R. Wolbing et al. “Nb nano superconducting quantum interference devices with high spin sensitivity for operation in magnetic fields up to 0.5 T”. *Applied Physics Letters*, **102**, 19, 192601, 2013.

[96] T. Schwarz et al. “Low-Noise Nano Superconducting Quantum Interference Device Operating in Tesla Magnetic Fields”. *ACS Nano*, **7**, 1, 844–850, 2013.

[97] W. A. Little and R. D. Parks. “Observation of Quantum Periodicity in the Transition Temperature of a Superconducting Cylinder”. *Phys. Rev. Lett.*, **9**, 9–12, 1962.

[98] N. E. Staley and Y. Liu. “Manipulating superconducting fluctuations by the Little–Parks–de Gennes effect in ultrasmall Al loops”. *Proceedings of the National Academy of Sciences*, **109**, 37, 14819–14823, 2012.

[99] I. Sternfeld et al. “Magnetoresistance Oscillations of Superconducting Al-Film Cylinders Covering InAs Nanowires below the Quantum Critical Point”. *Phys. Rev. Lett.*, **107**, 037001, 2011.

[100] B. L. T. Plourde and D. J. V. Harlingen. “Design of a scanning Josephson junction microscope for submicron-resolution magnetic imaging”. *Review of Scientific Instruments*, **70**, 11, 4344–4347, 1999.

[101] A. Nakayama et al. “Measurement of trapped flux magnetic field near the superconducting film by the dependence of superconducting current through a Josephson junction sensor”. *Journal of Physics: Conference Series*, **234**, 4, 042023, 2010.

[102] J. M. Taylor et al. “High-sensitivity diamond magnetometer with nanoscale resolution”. *Nature Physics*, **4**, 10, 810–816, 2008.

[103] I. K. Kominis, T. W. Kornack, J. C. Allred and M. V. Romalis. “A subfemtotesla multichannel atomic magnetometer”. *Nature*, **422**, 6932, 596–599, 2003.

[104] M. Vengalattore et al. “High-Resolution Magnetometry with a Spinor Bose-Einstein Condensate”. *Phys. Rev. Lett.*, **98**, 200801, 2007.

[105] D. Maser et al. “Note: Detection of a single cobalt microparticle with a microfabricated atomic magnetometer”. *Review of Scientific Instruments*, **82**, 8, 086112, 2011.

[106] C. Lehrer et al. “Defects and gallium-contamination during focused ion beam micro machining”. In “Conference on Ion Implantation Technology”, pages 695–698. 2000.

[107] E. Kasper. “Basic properties, growth and preparation methods of group IV heterostructures”. In E. Kasper and C. Klingshirn, editors, “Optical Properties. Part 3”, volume 34C3 of *Landolt-Börnstein - Group III Condensed Matter*, pages 1–18. Springer Berlin Heidelberg, 2007.

[108] A. Hindmarch, D. Parkes and A. Rushforth. “Fabrication of metallic magnetic nanostructures by argon ion milling using a reversed-polarity planar magnetron ion source”. *Selected papers from the 20th Conference on Ion-Surface Interactions, Zvenigorod, Moscow Region 25 – 29 August 2011*, **86**, 10, 1600–1604, 2012.

[109] T. Hoss, C. Strunk and C. Schönenberger. “Nonorganic evaporation mask for superconducting nanodevices”. *International Conference on Micro- and Nanofabrication*, **46**, 1–4, 149–152, 1999.

[110] R. Dolata, H. Scherer, A. B. Zorin and J. Niemeyer. “Single electron transistors with high-quality superconducting niobium islands”. *Applied Physics Letters*, **80**, 15, 2776–2778, 2002.

[111] A. Sidorenko. *Fundamentals of Superconducting Nanoelectronics.* NanoScience and technology. Springer Berlin Heidelberg, 2011.

[112] Y. D. Park et al. “Comparative study of Ni nanowires patterned by electron-beam lithography and fabricated by lift-off and dry etching techniques”. *Journal of Vacuum Science & Technology B: Microelectronics and Nanometer Structures*, **18**, 1, 16–20, 2000.

[113] M. Süess, E. Mueller and R. Wepf. “Minimization of amorphous layer in Ar^+ ion milling for UHR-EM”. *Ultramicroscopy*, **111**, 8, 1224–1232, 2011.

[114] A. C. F. Hoole, M. E. Welland and A. N. Broers. “Negative PMMA as a high-resolution resist - the limits and possibilities”. *Semiconductor Science and Technology*, **12**, 9, 1166, 1997.

[115] A. E. Grigorescu and C. W. Hagen. “Resists for sub-20-nm electron beam lithography with a focus on HSQ: state of the art”. *Nanotechnology*, **20**, 29, 292001, 2009.

[116] S. Long et al. “Process study of ZEP520 positive electron-beam resist and its application in single-electron transistor”. *Proc. SPIE*, **5645**, 255–266, 2005.

[117] D. M. Tanenbaum et al. “High resolution electron beam lithography using ZEP`[U+2010]`520 and KRS resists at low voltage”. *Journal of Vacuum Science & Technology B*, **14**, 6, 3829–3833, 1996.

[118] M. Rooks et al. “Low stress development of poly(methylmethacrylate) for high aspect ratio structures”. *Journal of Vacuum Science Technology B: Microelectronics and Nanometer Structures*, **20**, 6, 2937–2941, 2002.

[119] W. W. Hu, K. Sarveswaran, M. Lieberman and G. H. Bernstein. "Sub-10 nm electron beam lithography using cold development of poly(methylmethacrylate)". *Journal of Vacuum Science & Technology B: Microelectronics and Nanometer Structures*, **22**, 4, 1711–1716, 2004.

[120] W. Henschel, Y. M. Georgiev and H. Kurz. "Study of a high contrast process for hydrogen silsesquioxane as a negative tone electron beam resist". *Journal of Vacuum Science & Technology B*, **21**, 5, 2018–2025, 2003.

[121] V. Sidorkin, E. van der Drift and H. Salemink. "Influence of hydrogen silsesquioxane resist exposure temperature on ultrahigh resolution electron beam lithography". *Journal of Vacuum Science & Technology B*, **26**, 6, 2049–2053, 2008.

[122] A. G. P. Troeman et al. "Temperature dependence measurements of the supercurrent-phase relationship in niobium nanobridges". *Phys. Rev. B*, **77**, 2, 024509, 2008.

[123] P. McGovern et al. "Characterization of an ultra high aspect ratio electron beam resist for nano-lithography". *Nanotech.*, **2**, 195–198, 2010.

[124] D. E. McCumber and B. I. Halperin. "Time Scale of Intrinsic Resistive Fluctuations in Thin Superconducting Wires". *Phys. Rev. B*, **1**, 1054–1070, 1970.

[125] E. Warburg. "Magnetische Untersuchungen". *Annalen der Physik*, **249**, 5, 141–164, 1881.

[126] W. F. Giauque. "A Thermodynamic treatment of certain magnetic effects. A proposed method of producing temperatures considerable below 1° absolute". *Journal of the American Chemical Society*, **49**, 8, 1864–1870, 1927.

[127] P. Debye. "Einige Bemerkungen zur Magnetisierung bei tiefer Temperatur". *Annalen der Physik*, **386**, 25, 1154–1160, 1926.

[128] W. F. Giauque and D. P. MacDougall. "Attainment of Temperatures Below 1° Absolute by Demagnetization of $Gd_2(SO_4)_3.8H_2O$". *Phys. Rev.*, **43**, 768–768, 1933.

[129] P. Wikus, G. Burghart and E. Figueroa-Feliciano. "Optimum operating regimes of common paramagnetic refrigerants". *Cryogenics*, **51**, 9, 555–558, 2011.

[130] G. W. Wilson and P. T. Timbie. “Construction techniques for adiabatic demagnetization refrigerators using ferric ammonium alum”. *Cryogenics*, **39**, 4, 319–322, 1999.

[131] W. R. Smythe. *Static and dynamic electricity.* McGraw-Hill, New York, 1967.

[132] P. R. Gray. *Analysis and design of analog integrated circuits.* Wiley, New York, 2009.

[133] J. S. Schilling. “Superconductivity in the alkali metals”. *High Pressure Research*, **26**, 3, 145–163, 2006.

[134] K. D. Irwin and G. C. Hilton. *Transition-Edge Sensors*, volume 99 of *Topics in Applied Physics*, chapter 3, pages 63–150. Springer Berlin / Heidelberg, 2005.

[135] U. Nagel et al. “Proximity effect in iridium-gold bilayers”. *Journal of Applied Physics*, **76**, 7, 4262–4266, 1994.

[136] W. E. Martinez, G. Gregori and T. Mates. “Titanium diffusion in gold thin films”. *Thin Solid Films*, **518**, 10, 2585–2591, 2010.

[137] D. J. Goldie, A. V. Velichko, D. M. Glowacka and S. Withington. “Ultra-low-noise MoCu transition edge sensors for space applications”. *Journal of Applied Physics*, **109**, 8, 084507, 2011.

[138] K. D. Irwin and J. M. Martinis. “Superconducting Transition Edge Sensor”. U.S. Patent 5880468, 1999.

[139] G. Brammertz et al. “Critical temperature of superconducting bilayers: Theory and experiment”. *Applied Physics Letters*, **80**, 16, 2955–2957, 2002.

[140] J. M. Martinis, G. Hilton, K. Irwin and D. Wollman. “Calculation of Tc in a normal-superconductor bilayer using the microscopic-based Usadel theory”. *Nucl. instrum. meth. A*, **444**, 1-2, 23–27, 2000.

[141] K. D. Usadel. “Generalized Diffusion Equation for Superconducting Alloys”. *Phys. Rev. Lett.*, **25**, 507–509, 1970.

[142] T. Heinzel. *Mesoscopic electronics in solid state nanostructures.* Wiley-VCH, Weinheim; Cambridge, 2003.

[143] S. Halas and T. Durakiewicz. “Work functions of elements expressed in terms of the Fermi energy and the density of free electrons”. *Journal of Physics: Condensed Matter*, **10**, 48, 10815, 1998.

[144] H. B. Michaelson. “The work function of the elements and its periodicity”. *Journal of Applied Physics*, **48**, 11, 4729–4733, 1977.

[145] E. T. Swartz and R. O. Pohl. “Thermal boundary resistance”. *Rev. Mod. Phys.*, **61**, 605–668, 1989.

[146] J. D. Vries. “Temperature and thickness dependence of the resistivity of thin polycrystalline aluminium, cobalt, nickel, palladium, silver and gold films”. *Thin Solid Films*, **167**, 1–2, 25–32, 1988.

[147] M. Fenn, G. Akuetey and P. E. Donovan. “Electrical resistivity of Cu and Nb thin films”. *Journal of Physics: Condensed Matter*, **10**, 8, 1707, 1998.

[148] A. E.-H. B. Kashyout et al. “Preparation and characterization of DC sputtered molybdenum thin films”. *Alexandria Engineering Journal*, **50**, 1, 57–63, 2011.

[149] S. V. Lotkhov et al. “Low hysteretic behavior of Al/AlO$_x$/Al Josephson junctions”. *Applied Physics Letters*, **89**, 13, 132115, 2006.

[150] F. Finkbeiner et al. “Fabrication of Superconducting Bilayer Transition Edge Thermometers and their Application for Spaceborne X-ray Microcalorimetry”. *IEEE T. Appl. Supercon.*, **9**, 2, 2940–2943, 1999.

[151] L. VJ et al. “Ultrasmooth Silver Thin Films Deposited with a Germanium Nucleation Layer”. *Nano Letters*, **9**, 1, 178–182, 2009.

[152] K. Masahiro and S. Noboru. “Effects of temperature, thickness and atmosphere on mixing in Au-Ti bilayer thin films”. *Journal of Materials Science*, **28**, 5088–5091, 1993.

[153] A. Peruzzi et al. “Investigation of the titanium superconducting transition as a temperature reference point below 0.65 K”. *Metrologia*, **37**, 3, 229, 2000.

[154] R. Meservey and P. M. Tedrow. “Measurements of the Kinetic Inductance of Superconducting Linear Structures”. *Journal of Applied Physics*, **40**, 5, 2028–2034, 1969.

[155] A. Kamlapure et al. “Measurement of magnetic penetration depth and superconducting energy gap in very thin epitaxial NbN films”. *Applied Physics Letters*, **96**, 7, 072509, 2010.

[156] M. M. K. Jr. “Extraction of inductances of plane thin film superconducting circuits”. *Superconductor Science and Technology*, **10**, 6, 389, 1997.

[157] R. Huebener et al. “Critical current density in superconducting niobium films”. *Journal of Low Temperature Physics*, **19**, 3-4, 247–258, 1975.

[158] H. Weinstock. *Squid Sensors: Fundamentals, Fabrication, and Applications.* NATO ASI series / E: NATO ASI series. Kluwer Academic Publishers, 1996.

[159] J. H. Claassen, J. E. Evetts, R. E. Somekh and Z. H. Barber. “Observation of the superconducting proximity effect from kinetic-inductance measurements”. *Phys. Rev. B*, **44**, 9605–9608, 1991.

[160] P. Duhamel and H. Hollmann. “‘Split radix’ FFT algorithm”. *Electronics Letters*, **20**, 1, 14–16, 1984.

[161] A. I. Gubin et al. “Dependence of magnetic penetration depth on the thickness of superconducting Nb thin films”. *Phys. Rev. B*, **72**, 064503, 2005.

[162] J. A. Bert et al. “Direct imaging of the coexistence of ferromagnetism and superconductivity at the LaAlO3/SrTiO3 interface”. *Nature Physics*, **7**, 10, 767–771, 2011.

[163] J. A. Bert et al. “Gate-tuned superfluid density at the superconducting $LaAlO_3/SrTiO_3$ interface”. *Phys. Rev. B*, **86**, 060503, 2012.

[164] A. Ohtomo and H. Y. Hwang. “A high-mobility electron gas at the LaAlO3/SrTiO3 heterointerface”. *Nature*, **427**, 6973, 423–426, 2004.

[165] M. Kawasaki et al. “Atomic Control of the SrTiO3 Crystal Surface”. *Science*, **266**, 5190, 1540–1542, 1994.

[166] J. Park et al. “Creation of a two-dimensional electron gas at an oxide interface on silicon”. *Nat Commun*, **1**, 94, 2010.

[167] S. Thiel et al. “Tunable Quasi-Two-Dimensional Electron Gases in Oxide Heterostructures”. *Science*, **313**, 5795, 1942–1945, 2006.

[168] N. Nakagawa, H. Y. Hwang and D. A. Muller. “Why some interfaces cannot be sharp”. *Nat Mater*, **5**, 3, 204–209, 2006.

[169] G. Herranz et al. “High Mobility in $LaAlO_3/SrTiO_3$ Heterostructures: Origin, Dimensionality, and Perspectives”. *Phys. Rev. Lett.*, **98**, 216803, 2007.

[170] L. Qiao et al. “Thermodynamic instability at the stoichiometric LaAlO3/SrTiO(001) interface”. *Journal of Physics: Condensed Matter*, **22**, 31, 312201, 2010.

[171] S. Chambers et al. “Instability, intermixing and electronic structure at the epitaxial heterojunction”. *Surface Science Reports*, **65**, 10–12, 317–352, 2010.

[172] N. Reyren et al. “Superconducting Interfaces Between Insulating Oxides”. *Science*, **317**, 5842, 1196–1199, 2007.

[173] A. Brinkman et al. “Magnetic effects at the interface between non-magnetic oxides”. *Nat Mater*, **6**, 7, 493–496, 2007.

[174] Y. Chen et al. “Metallic and Insulating Interfaces of Amorphous SrTiO3-Based Oxide Heterostructures”. *Nano Letters*, **11**, 9, 3774–3778, 2011.

[175] D. V. Christensen et al. “Controlling interfacial states in amorphous/crystalline LaAlO[sub 3]/SrTiO[sub 3] heterostructures by electric fields”. *Applied Physics Letters*, **102**, 2, 021602, 2013.

[176] F. M. Smits. “Measurement of sheet resistivities with the four-point probe”. *Bell System Technical Journal*, **34**, 711–718, 1958.

[177] C. W. Schneider et al. “Microlithography of electron gases formed at interfaces in oxide heterostructures”. *Applied Physics Letters*, **89**, 12, 122101, 2006.

[178] N. Banerjee, M. Huijben, G. Koster and G. Rijnders. “Direct patterning of functional interfaces in oxide heterostructures”. *Applied Physics Letters*, **100**, 4, 041601, 2012.

[179] H. Takashima et al. "Frequency Dependence of Dielectric Constant of Strontium Titanate Films with Single-Crystal-Like Behavior". *Ferroelectrics*, **335**, 1, 45–50, 2006.

[180] M. Suzuki. "Comprehensive Study of Lanthanum Aluminate High-Dielectric-Constant Gate Oxides for Advanced CMOS Devices". *Materials*, **5**, 3, 443–477, 2012.

[181] J. Pearl. "Current Distribution in Superconducting Films Carrying Quantized Fluxoids". *Applied Physics Letters*, **5**, 65–66, 1964.

[182] A. D. Caviglia et al. "Two-Dimensional Quantum Oscillations of the Conductance at $LaAlO_3/SrTiO_3$ Interfaces". *Phys. Rev. Lett.*, **105**, 236802, 2010.

[183] A. Janotti, L. Bjaalie, L. Gordon and C. G. Van de Walle. "Controlling the density of the two-dimensional electron gas at the $SrTiO_3/LaAlO_3$ interface". *Phys. Rev. Lett.*, **86**, 24, 241108, 2012.

[184] K. Yoshimatsu, R. Yasuhara, H. Kumigashira and M. Oshima. "Origin of Metallic States at the Heterointerface between the Band Insulators $LaAlO_3$ and $SrTiO_3$". *Phys. Rev. Lett.*, **101**, 026802, 2008.

[185] Z. Huang et al. "Conducting channel at the $LaAlO_3/SrTiO_3$ interface". *Phys. Rev. B*, **88**, 161107, 2013.

[186] L. Li, C. Richter, J. Mannhart and R. C. Ashoori. "Coexistence of magnetic order and two-dimensional superconductivity at $LaAlO_3/SrTiO_3$ interfaces". *Nat Phys*, **7**, 10, 762–766, 2011.

[187] N. Pavlenko et al. "Magnetic and superconducting phases at the $LaAlO_3/SrTiO_3$ interface: The role of interfacial Ti 3*d* electrons". *Phys. Rev. B*, **85**, 020407, 2012.

[188] M. Alba et al. "Spin-glass dynamics from magnetic noise, relaxation, and susceptibility measurements (invited)". *Journal of Applied Physics*, **61**, 8, 3683–3688, 1987.

[189] M. Tinkham. *Introduction to Superconductivity*, pages 119, 131, 288–293. McGraw Hill, 2 edition, 1996.